Ion Beam-Induced Defect Phenomena in Rock-Salt Crystals (MgO, NiO) for Optical and Electronic Device Applications

By

Sourav Bhakta

PHYS11201705005

National Institute of Science Education and Research, Bhubaneswar

A thesis submitted to the

Board of Studies in Physical Sciences

In partial fulfillment of requirements

for the Degree of

DOCTOR OF PHILOSOPHY

of

HOMI BHABHA NATIONAL INSTITUTE

June, 2024

Homi Bhaba National Institute

Recommendations of the Viva Voce Committee

As members of the Viva Voce Committee, we certify that we have read the dissertation prepared by **Sourav Bhakta** entitled **Ion Beam-Induced Defect Phenomena in Rock-Salt Crystals (MgO, NiO) for Optical and Electronic Device Applications** and recommend that it may be accepted as fulfilling the thesis requirement for the award of degree of Doctor of Philosophy.

Chairman - Prof. Bedangadas Mohanty		Date: 13/06/2024
Guide / Convener - Dr. Pratap Kumar Sahoo		Date: 13/06/2024
Examiner - Prof. Prahallad Padhan		Date: 13/06/24
Member 1 - Dr. Kartikeswar Senapati		Date: 13/06/2024
Member 2 - Dr. Ashis Kumar Nandy		Date: 13/06/2024
Member 3 - Prof. Tapobrata Som		Date: 13/06/24

Final approval and acceptance of this thesis is contingent upon the candidate's submission of the final copies of the thesis to HBNI.

I/We hereby certify that I/we have read this thesis prepared under my/our direction and recommend that it may be accepted as fulfilling the thesis requirement.

Date : 13/06/2024

Place : SPS, NISER

Signature of Guide

STATEMENT BY AUTHOR

This dissertation has been submitted in partial fulfillment of requirements for an advanced degree at Homi Bhabha National Institute (HBNI) and is deposited in the Library to be made available to borrowers under rules of the HBNI.

Brief quotations from this dissertation are allowable without special permission, provided that accurate acknowledgement of source is made. Requests for permission for extended quotation from or reproduction of this manuscript in whole or in part may be granted by the Competent Authority of HBNI when in his or her judgment the proposed use of the material is in the interests of scholarship. In all other instances, however, permission must be obtained from the author.

Sourav Bhakta

(Sourav Bhakta)

DECLARATION

I, hereby declare that the investigation presented in the thesis has been carried out by me. The work is original and has not been submitted earlier as a whole or in part for a degree/diploma at any other Institute/University.

Sourav Bhakta

(Sourav Bhakta)

List of Publications

Journals (Published and included in the thesis)

1. **Sourav Bhakta**, Subhadip Pradhan, Ashis K. Nandy, and Pratap K. Sahoo"Impact of MeV Ni Ion-Implanted Defects in Band Modification of MgO." Journal of Electronic Materials, 52,3, (2023).

2. **Sourav Bhakta**, and Pratap K. Sahoo. "Tuning optical bandgap of crystalline MgO by MeV Co ion beam induced defects." Applied Physics A 128,11 (2022).

3. **Sourav Bhakta**, and Pratap K. Sahoo. "Study of vibrational modes of MeV Ni ion implanted MgO crystal." Vibrational Spectroscopy, 129, 103603 (2023).

4. **Sourav Bhakta**, and Pratap K. Sahoo, "Tuning magnetocrystalline anisotropy by Au ion-induced defects in NiO thin films," Journal of Alloys and Compounds, 173844 (2024).

Journals (submitted and included in the thesis)

1. **Sourav Bhakta** and Pratap K. Sahoo, "Impact of Defects in 1D1R Resistive Switching in Au Ion Implanted NiO Thin Films."

2. **Sourav Bhakta**, Rudrashis Panda and Pratap K. Sahoo, "Third-order non-linear optical switching and threshold limiting of annealed NiO thin films."

Journals (to be submitted and included in the thesis)

1. **Sourav Bhakta** and Pratap K. Sahoo, "Analog to Digital Resistive Switching Transformation in Implanted NiO."

2. **Sourav Bhakta** and Pratap K. Sahoo, "Annealing effect of Improving the Resistive Switching in ITO/MgO/Ag bipolar memory device."

3. **Sourav Bhakta**, Amit Haldar, Shovon Pal, and Pratap K. Sahoo, "Defect induced Terahertz scattering in 100 keV Cu ion implanted NiO thin films."

Others publications: Not included in the thesis

1. **Sourav Bhakta**, Indra Sulania, S. Ojha, D. Kanjilal, and Pratap K. Sahoo; "Swift heavy ion beam stimulated epitaxial recrystallization of Si/SiO_2 heterostructure", Materials Letters, 308, 131153 (2022).

2. Mrinal K. Sikdar, Avanendra Singh, **Sourav Bhakta**, Madhusmita Sahoo, S. N. Jha, D. K. Shukla, D. Kanjilal, and Pratap K. Sahoo; "Modulation of intrinsic defects in vertically grown ZnO nanorods by ion implantation", Physical Chemistry Chemical Physics, 24, 30 (2022).

3. Km Surbhi, **Sourav Bhakta**, Anupa Kumari, Utkalika P. Sahoo, Pratap K. Sahoo, and Ritwick Das; "Impact of pauli-blocking effect on optical limiting properties of WSe2 thin films", Optical Materials, 129, 112479 (2022).

4. Km Surbhi, **Sourav Bhakta**, Pratap K. Sahoo, and Ritwick Das; "Impact of defects on the $\chi(3)$ optical nonlinearity of sputtered WSe_2 thin films in the optical communication band", Journal of Applied Physics 132, 24 (2022).

5. Subhashree Sahoo, Km. Surbhi, **Sourav Bhakta**, Ritwick Das, and Pratap K Sahoo; "Influence of defects on linear and nonlinear optical properties of Cu doped rutile TiO2 microflowers", Physical Chemistry Chemical Physics, 26, 13 (2024).

6. Chinmaya Kar, R. De, S. Jena, **S. Bhakta**, P. K. Sahoo, S. Pradhan, K. Divakar Rao, and D.V. Udupa,"Observation of Spatially Selective Absorption in Ag/SiO2/Ag based structure by oblique angle deposition of SiO2 layer", Nanotechnology, 35, 30, (2024).

Conferences

1. Defect induced band tuning in MeV Ni ion implanted MgO (100), **Sourav Bhakta** and Pratap K. Sahoo, 25th International Conference on Ion Beam Analysis and 17th International Conference on Particle Induce X-ray Emission and International Conference on Secondary Ion Mass Spectrometry (IBA/PIXE-SIMS 2021), 11-15 October, 2021.

2. Ion beam channeling patterns of swift heavy ion induced epitaxial recrystallized SiO2, **Sourav Bhakta** and Pratap K. Sahoo, 6th International Virtual Conference on Nanostructuring by Ion Beams (ICNIM 2021), October 5-8, 2021.

3. Vibrational mode analysis of MeV transition metal ion implantation on insulating MgO material, **Sourav Bhakta** and Pratap K. Sahoo, 11th International conference on Perspectives in Vibrational Spectroscopy (ICOPVS-2022), 13-17 December, 2022.

4. Ion Beam Induced Epitaxial Recrystallization of Si/SiO_2 Heterostructure by 100 MeV Ni^{7+} ions, **Sourav Bhakta**, S. Ojha, Indra Sulania, D. Kanjilal, and Pratap K. Sahoo, 7th International Conference on Ion Beams in Materials Engineering and Characterizations (IBMEC -2022), 16-19 November, 2022.

5. Defect mediated magnetic anisotropy of Au ion implanted NiO, **Sourav Bhakta** and Pratap K. Sahoo, 14th International Conference on Stopping and Manipulation of Ions and Related Topics (SMI-2023), 8-11 May, 2023.

6. Vacancy Modulated Resistive Switching Behaviour of 30 keV Au Ion Implanted NiO Thin Films, **Sourav Bhakta** and Pratap K. Sahoo, 1th International Conference on Materials for Advanced Technologies (ICMAT 2023), 26-30 June, 2023.

Sourav Bhakta

(Sourav Bhakta)

Dedicated to Lord Shri Krishna

ACKNOWLEDGEMENTS

I would like to express my deepest gratitude and humble acknowledgement to Almighty God, Lord Shri Krishna, the Creator of the universe and the source of all wisdom and guidance. In every endeavor, from the smallest to the greatest, I am grateful for the blessings, strength, and guidance that have been bestowed upon me. It is through Your infinite grace and mercy that I am able to navigate the challenges and triumphs of life. I recognize that every achievement, every success, and every moment of joy is a gift from You. Your divine presence has been a guiding light, illuminating my path and providing solace in times of difficulty.

I extend my sincere and deepest gratitude to my supervisor Prof. Pratap Kumar Sahoo, for his unwavering support, inspiring guidance, empathy, encouragement, care, and training throughout my Ph.D. journey. Working in his research group, Ion Beam and Nanomaterials Laboratory (IBNL), at the School of Physical Sciences, National Institute of Science Education and Research (NISER), Bhubaneswar, has been a privilege. His patience, diligence, enthusiasm, intelligence, experience, friendliness, and the freedom he allowed that make my research endeavors both smooth and delightful. I also want to express my appreciation to Prof. Kartik Senapati for engaging in discussions, sharing scientific knowledge, and offering valuable insights into my queries and doubts. I also thank Dr. Ashis Kumar Nandy and Mr. Subhadip Pradhan for their constant support and helping me during the DFT calculations, and for providing me the valuable suggestions to improve the analysis of the results. I am grateful to my doctoral committee members, Prof. Bedangadas Mohanty and Prof. Tapobrata Som, for their constructive suggestions and comments in the annual evaluation meetings. I especially express my sincere gratitude and appreciation to Prof. Bedangadas Mohanty for providing valuable guidance and encouraging me to delve into new physics, ultimately motivating me to complete my work expeditiously. I also acknowledge Dr. Abdelhak Chettah for teaching me about the thermal spike model and for hands-on training. I would like to thank my collaborators, Dr. Shovon Pal and Mr. Amit Haldar, for doing the tera-hertz measurement and for the fruitful discussions. I would like to thank my collaborator, Dr. Rudrashis Panda, for doing nonlinear measurements using the Z-scan technique. My heartfelt thanks go to NISER, the Department of Atomic Energy, Govern-

ment of India, for the financial support during my Ph.D. research. Special thanks to my lab seniors, Dr. Mrinal Kanti Shikdar and Dr. Gurupada Ghorai, Bidyadhar Das, Kalyan Ghosh, Subhashree Sahoo, Utkalika P. Sahoo, for their guidance in experimental techniques and discussion on various matters. Gratitude to our lab postdocs, Dr. Debi Prasad Datta, Dr. Nitul S. Rajput, Dr. Binaya K. Sahu, and Dr. Soumendra K. Das, for sharing their research experience and providing valuable suggestions. I also thank my Prof. Pratap Kumar Sahoo and Ma'am Madhusmita Sahoo for inviting us to their home for various events such as dinner party, the birthday party of Punyasloka Sahoo and Priyashraba Sahoo, the farewell party of Dr. Nitul S. Rajput. I especially thank my friends Prottay Das, Srish Mishra, Rahul Ghosh, and Shuvayu Roy for helping and supporting me in various prospects. I extend my thanks to all my friends, senior Ph.D. students, and batch-mates who have made my Ph.D. journey and life at NISER exciting and memorable.

My grandmother, Sabitri Sarkar (late), embodies a profound reservoir of wisdom, elegance, and enduring affection in my life. She was like a friend to me. I can express any incident of my life to her. I always miss her and her unconditional love. She stood with me always and took sides with me without any hesitation against any allegation of me. I will always remember the valuable advice that she gave to me. When I went to play cricket during the hot summer season in the holidays around mid-afternoon, she used to find me and force me to go home to take a bath and lunch. Her narratives are akin to cherished treasures, intricately woven with the strands of time, imparting invaluable lessons from the past and guiding me toward the future. I would like to acknowledge my mother, Maya Bhakta, for her unwavering support, hard work, countless sacrifices, vision, unconditional love, care, and advice through the ups and downs of my life. My mother has always guided me on the right path from childhood. She always tried to fulfill my wish if I asked her something. I miss the days when my mother took me to school under her umbrella, and I followed the path of shadow. Sometimes, I went out from the track, and she told me to come under the umbrella to be safe from the heat. I usually refused to take food during tiffin hour in my school days as I was always busy in playing games such as cricket, gollachut, pen fighting, pach er guti, chor pulish, dariabanda, kanamachi, sat chara, morog lorai, and many more. But she used to feed me forcefully. Whatever I have achieved in my life is due to the contribution of my mother and grandmother. I would like to thank my grandfather, Mr. Manindranath Sarkar

(late), for giving me his valuable advice and sometimes fighting with me. I usually roam with him around the local area. I thank my grandmother, Sebadashi Bhakta, for her love and affection for me. I also thank my father, Subhash Bhakta, for guiding me in case I did something wrong. I also thank my younger brother, Mr. Diganta Bhakta, for understanding, respecting, and supporting me. I also thank my family for their support and help during the hard situations.

Summary

This thesis delves into the exploration of rock salt materials, particularly MgO and NiO, for their potential applications in optical and electronic devices. The focus is on enhancing their properties through thermal annealing and low-energy ion-induced extrinsic defects to meet the demands of advanced miniaturized technology.

The first part investigates the modulation of optical properties in Ni and Co ion-implanted MgO single crystals, analyzing bandgap narrowing and induced color centers. Density functional theory (DFT) calculations aid in understanding the electronic characteristics of these modifications.

The second part explores the annealing effect on improving resistive switching (RS) properties in RF-sputtered-grown MgO thin films. The resistive random access memory (RRAM) devices are fabricated by sandwiching the MgO films between the bottom ITO and the top Ag electrode. The RRAM devices demonstrate enhanced memory window and endurance after annealing, attributed to the bulk-dominated vacancy filamentary model.

Subsequently, the thesis demonstrates the non-linear optical properties of NiO thin films through the Z-scan technique. In open aperture (OA) conditions, as-deposited and annealed NiO films exhibit saturable and reverse saturable absorption (RSA), respectively, where RSA is attributed to the two-photon absorption process. In contrast, the self-defocusing characteristics following the prefocal minima and post-focal maxima are observed in closed aperture (CA) measurements. The DFT calculations correlate the upward shifting of Ni-$d_{x^2-y^2}$ and Ni-d_{z^2} orbitals with the increase of bandgap, influencing the two-photon absorption process.

Then, the thesis examines the magnetocrystalline anisotropy and RS behavior of Au ion-implanted NiO thin films. Defects induced by ion implantation control the magnetic environment, influencing magnetocrystalline anisotropy and ferromagnetic responses. The changes in the depletion width and the Schottky barrier at the p-n junction and NiO/Au interface explain the tuning of RS properties in Si/NiO/Au RRAM devices.

The final study involves Cu ion implantation on NiO films deposited on ITO substrate, showing the transformation of analog RS into digital RS above a threshold fluence. The

Schottky interface at both ITO/NiO and NiO/Ag junctions plays a crucial role in analog current conduction, while digital switching is associated with the vacancy filamentary model. Along with RS property, this part also investigates the Tera Hertz (THz) conductivity in Cu ion implanted NiO thin films grown on Si/SiO_2 substrate. Crystal defects induced by implantation tune carrier concentration, affecting scattering time and plasma frequency. The DFT calculations aid in explaining the modulation of carrier concentrations with defect states to understand the THz optical conductivity.

List of Abbreviations

FESEM Field Emission Scanning Electron Microscope

XRD X-ray Diffraction

ECR Electron Cyclotron Resonance

UV Ultraviolet

PL Photoluminescence

CL Cathodoluminescence

LO Longitudinal Optical

PECVD Plasma Enhanced Chemical Vapor Deposition

DFT Density Functional Theory

GGA Generalized Gradient Approximation

PBE Perdew-Burke-Ernzerhof

PAW Projector Augmented Waves

DOS Density of States

PDOS Partial Density of States

RT Room Temperature

VB Valence Band

CB Conduction Band

NLOP Nonlinear Optical Properties

CA Closed Aperture

OA Open Aperture

TPA Two Photon Absorption

SA Saturable Absorption

RSA Reverse Saturable Absorption

RS Resistive Switching

RRAM Resistive Random Access Memory

AFM Atomic Force Microscopy

SQUID Superconducting Quantum Interference Device

SRIM Stopping and Range of Ions in Matter

TMO Transition Metal Oxide

ITO Indium Doped Tin Oxide

RF Radio Frequency

HRS High Resistance State

LRS Low Resistance State

VASP Vienna Ab initio Simulation Package

FM Ferromagnetic

ZFC Zero Field Cooled

FC Field Cooled

CCD Charged Coupled Device

List of Figures

1.1 The schematic of formation of various kinds of defects in the crystal. . . . 3

1.2 (a) The schematic of the construction of the RRAM device, and (b) the current-voltage mechanism in the bipolar mode of the RRAM device. . . . 4

1.3 The schematic of ion solid interactions, resulting in (a) the modification of target materials by (b) occurring collision cascade within the range of the incident ions. (c) represents the sputtering of host atoms during implantation. 6

1.4 The defect-free, vacancy, substitutional, and interstitial defect-associated rock salt crystal structure. 8

1.5 The schematic of (a,d) electron dynamics, (b,e) lattice dynamics, and (c,f) relaxing of atoms after the interaction with incident ions in thermal spike model for two scenarios when $S_e \gg S_n$ and $S_n \gg S_e$, respectively. 9

2.1 The schematic of RF Sputtering system for deposition of thin films. 23

2.2 Schematic of PECVD setup for thermal annealing of the sputtered grown films. 25

2.3 The diagram represents the tandem accelerator system for ion implantation used at IOP, Bhubaneswar. The components inside the red box represent the SNICS source. 27

2.4 The schematic of low energy ion implantation system at IOP, Bhubaneswar. 28

2.5 The schematic of LEIBF system for low energy ion implantation, at IUAC, Delhi [1]. 30

2.6 The schematic of RRAM with top (a) Au and (b) Ag electrode associated devices. 32

2.7 The schematic of FESEM system 33

2.8 The schematic of AFM system for investigating the surface morphology of the thin films. 35

2.9 The schematic of XRD system with a zoomed view of the Bragg's reflection from a periodic lattice. 36
2.10 The schematic of UV-Visible setup. 38
2.11 The schematic of PL emission for direct and indirect bandgap materials. . . 39
2.12 The schematic of PL setup. 40
2.13 The schematic of CL setup 42
2.14 The schematic represents the energy level diagram in Raman scattering. . . 44
2.15 The schematic diagram of ATR-FTIR system. 45
2.16 The schematic of detection coils used in SQUID. 46
2.17 The schematic of Z-scan setup. 47
2.18 The schematic of Tera Hertz setup. 48

3.1 SRIM simulations of ion range and deposited energy by one MeV (a) Ni and (b) Co in MgO. 57
3.2 The variation of the partial sputtering yield of Mg and O simulated using TRIDYN code for one MeV (a) Ni and (b) Co ion implantation in MgO with various ion fluences. 58
3.3 The UTS simulations to understand the rise of lattice temperature with different ion track radius of one MeV (a) Ni and (b) Co ion implanted MgO. . 59
3.4 The UV-Vis absorbance (a,d), the variation of concentration of (b,e) F center, and (c,f) bandgap with incident Ni and Co ion fluences, respectively. The inset of (c) shows the typical Tauc plot of pristine to calculate the bandgap. 61
3.5 Room temperature PL spectra of pristine, (a) Ni and (b) Co ion implanted MgO, The typical deconvoluted PL spectra at a fluence of 5×10^{14} ions/cm^2 of (b) Ni and (d) Co implanted samples. 65
3.6 The integrated intensity for (a-d) Ni and (e-h) Co ion implanted sample for the deconvoluted peaks as a function of ion fluence. 66
3.7 The proposed band model for electronic transitions 67
3.8 The CIE 1931 chromaticity plot of PL spectra for (a) Ni and (b) Co ion implanted MgO with the variation of ion fluences. 67

3.9 The atomic configuration of (a) pristine, (b) Mg vacancy, (c) O vacancy, (d) one Mg and two Oxygen vacancy, Mg substituted by (e) two Ni and (f) one Co defect associated MgO for the theoretical calculation. Green, Red, blue, and ash colors represent the Mg, O, Ni, and Co atoms, respectively. The green and black dashed circles indicate the Mg and O vacancy, respectively. 68
3.10 The calculated band structure of (a) pristine, (b) Mg vacancy, (c) O vacancy, (d) one Mg and two Oxygen vacancy, Mg substituted by (e) two Ni and (f) one Co defect associated MgO. The dashed line at 0 eV denotes the Fermi level. 69
3.11 The calculated DOS structure of (a) pristine, (b) Mg vacancy, (c) O vacancy, (d) one Mg and two Oxygen vacancy, Mg substituted by (e) two Ni and (f) one Co defect associated MgO. The dashed line at 0 eV denotes the Fermi level. 70
3.12 Raman spectra of pristine, (a) Ni and (b) Co implanted MgO for different ion fluences. 73
3.13 (a) pristine, (b) one Mg vacancy, (c) one oxygen vacancy, one Mg substituted by one (d) Ni, and (e) Co defect associated MgO structure for phonon band and DOS calculations. 74
3.14 The theoretical phonon dispersion band of (a) pristine, (b) one Mg vacancy, (c) one oxygen vacancy, one Mg substituted by one (d) Ni, and (e) Co-associated MgO. The different colors represent the band connection along the high symmetry points. 75
3.15 The total and partial phonon density of state calculation of (a) pristine, (b) one Mg vacancy, (c) one oxygen vacancy, one Mg substituted by one (d) Ni, and (e) Co-associated MgO. 76
3.16 FTIR spectra of pristine and Ni ion implanted crystalline MgO with different fluences in the range of (a) 450-800 cm^{-1}, (b) 800-1000 cm^{-1}, (c) 1000-1200 cm^{-1}, (d) 1200-1750 cm^{-1}, and (e) 2750-3000 cm^{-1}. 78
3.17 FTIR spectra of pristine and Co ion implanted crystalline MgO with different fluences in the range of (a) 450-800 cm^{-1}, (b) 800-1000 cm^{-1}, (c) 1000-1200 cm^{-1}, (d) 1200-1750 cm^{-1}, and (e) 2750-3000 cm^{-1}. 79

4.1 The XRD spectra of (a) pristine and (b) 350°C annealed MgO sample. . . . 90
4.2 The surface morphology of (a) pristine and (b) 350°C annealed MgO sample. The inset shows the magnified morphology of the MgO film in the respective graph. 91
4.3 The AFM images of (a) pristine and (b) 350°C annealed MgO sample. . . . 92
4.4 The UV-Visible spectra of (a) pristine and (b) 350°C annealed MgO sample. The inset shows the baseline corrected V center of pristine for clear vision. 92
4.5 (a) The schematic of the wire connection of the ITO/MgO/Ag memristor. (b) The comparison of the I-V curve of 1st cycle for pristine and 350°C annealed sample. The current-voltage curve of the 1st, 25th, 50th, 75th, and 100th cycles of (c) pristine, and (d) 350°C annealed sample. 93
4.6 (a) The linear fitting of the double logarithmic plot of the 1st cycle of the I-V curve of pristine sample. The I-V curve at a higher field deviates from linear behavior. (b) $\mathrm{Ln}(\frac{J}{T^2}) \propto \mathrm{V}^{\frac{1}{2}}$, (c) $\mathrm{I} \propto \mathrm{V}^2$, (d) $\mathrm{Ln}(\frac{J}{V}) \propto \mathrm{V}^{\frac{1}{2}}$, (e) $\mathrm{Ln}(\frac{J}{V^2}) \propto \mathrm{V}^{-1}$ and (f) $\mathrm{Ln}(\mathrm{J}) \propto \mathrm{V}$ plot along with linear fitting for 1st cycle of pristine. 95
4.7 The comparison of percentage change of $\frac{R_{HRS}}{R_{LRS}}$ with increasing cycle number at SET and RESETpoint for pristine and 350°C annealed sample at applied (a) positive and (b) negative bias. 98
4.8 The endurance performance of the memristor associated with (a) pristine and (b) 350°C annealed sample. 98
4.9 The schematic drawn of the filamentary model at (a) zero bias, (b) SET (complete filament formation), and (c) RESET (rupture of the filament) condition of the MgO-based RRAM device. 99

5.1 The NiO crystal structure of pristine, used in DFT calculation. 107
5.2 The surface morphology of (a) pristine and annealed samples at (b) 300, (c) 350, (d) 400, (e) 450 (f) 500°C. The inset of (a) shows the thickness of pristine sample. 108

5.3 (a) The XRD patterns of pristine and annealed NiO thin film at 300, 350, 400, 450, and 500°C, (b) The variation of crystallite size and microstrain with annealing temperature, (c) The decrement of lattice constant with annealing temperature. 109
5.4 (a) The UV-Vis absorbance spectra for pristine and annealed samples, the variation of (b) Urbach energy, and (c) indirect bandgap of NiO with annealing temperature. Inset of (C) shows the typical Tauc plot of as-grown sample. 111
5.5 (a) The PL spectra of pristine and annealed samples, (b) The typical deconvoluted spectra of pristine, The integrated intensity variation with annealing temperature for (c) 572 nm, (d) 524 nm and (e) 413 nm, respectively. 113
5.6 (a) The CL spectra of pristine and annealed samples, (b) The typical deconvoluted spectra of pristine, (c) The shifting of the 403 nm peak position with annealing temperature. 114
5.7 The electronic band structure calculation for (a) pristine, (b) 300, (c) 350, (d) 400, (e) 450, and (f) 500°C annealed samples. The black dashed line along zero indicates the Fermi level. 116
5.8 The total and partial (a and d), the Ni-d (b and e), and O-p (c and f) orbital decomposed DOS for pristine and 500°C annealed samples. The black dashed line along zero denotes the Fermi level. 119
5.9 Open aperture Z-scan of normalized transmittance of (a) pristine and annealed samples at (b) 300, (d) 400, (e) 450, and (f) 500°C, respectively. (c) The schematic of the TPA process. 120
5.10 Closed aperture Z-scan of normalized transmittance of (a) pristine and annealed samples at (b) 300, (c) 350, (d) 400, (e) 450, and (f) 500°C, respectively. 120

6.1 (a) The SRIM simulation of deposited energy and ion range vs. target depth, (b) The distribution of Au atomic percentage with target depth for different ion fluences, (c) The variation of dpa with sample depth for different ion fluences, calculated from SRIM simulations. The TRIDYN simulation for (d) surface recession, (e) partial sputtering yield, and (f) surface atomic fraction with ion fluences. 134
6.2 The surface morphology of (a) pristine, (b) 5×10^{14} ions/cm^2, (c) 1×10^{15} ions/cm^2, (d) 5×10^{15} ions/cm^2, (e) 1×10^{16} ions/cm^2, The inset shows the film thickness of the corresponding sample from (a-e), respectively, (f) The variation of NiO film thickness with ion fluences. 135
6.3 (a) The XRD pattern of pristine and ion implanted samples with fluences 5×10^{14} ions/cm^2 - 1×10^{16} ions/cm^2. The dashed line is for guiding the eye. (b) A plot of variation of crystallite size and strain with ion fluences. . 137
6.4 (a) The UV-Vis absorption spectra of pristine and implanted samples in the wavelength range of 200-550 nm for different ion fluences. (b) The variation of bandgap with ion fluences. A typical Tauc plot of pristine in the inset. 139
6.5 (a) The room temperature PL spectra in the wavelength range of 330 - 800 nm of pristine and Au ion implanted samples with different fluences. (b) The typical deconvoluted PL spectra of pristine. (c-f) The variation of integrated intensity with ion fluences for the deconvoluted peaks at 753 nm, 579 nm, 507 nm, and 428 nm. 140
6.6 The magnetic moment vs. field with ion fluences at (a) 5 K (b) 100 K, and (c) 300 K, respectively. The inset shows the magnified hysteresis in the respective plot. (d) The variation of coercivity with temperature for different ion fluences. 142
6.7 The magnetic moment vs. temperature at a fixed field of 200 Oe for (a) pristine, (b) 5×10^{15} ions/cm^2, and (c) 1×10^{16} ions/cm^2. (d) shows the typical baseline corrected ZFC curve of the fluence 1×10^{16} ions/cm^2 to find the blocking region. 144

6.8 The variation of magneton number with temperature for (a) 1×10^{16} ions/cm^2, (b) 5×10^{15} ions/cm^2, (c) 1×10^{15} ions/cm^2, (d) 5×10^{14} ions/cm^2, and (e) pristine samples. 145
6.9 (a) A typical M-H curve of pristine at 300 K with LAS fitting at the higher field region. (b) The variation of magnetocrystalline anisotropy constant with temperature (5K to 300K) for different incident ion fluences. 146
6.10 (a) Schematic of NiO-based RRAM device. The Current vs. voltage (I-V) graph of (b) pristine, (c) 5×10^{14} ions/cm^2, (d) 1×10^{15} ions/cm^2, (e) 5×10^{15} ions/cm^2, and (f) 1×10^{16} ions/cm^2 for 1st, 25th, 50th, 75th and 100th cycle at a compliance current of 20 mA. The inset in (b-f) shows I-V variation for the 1st cycle for pristine and 5×10^{14} - 1×10^{16} ions/cm^2 fluence samples for clear vision, respectively. 149
6.11 (a) The current vs. voltage graph of pristine, 5×10^{14} ions/cm^2, 1×10^{15} ions/cm^2, 5×10^{15} ions/cm^2, and 1×10^{16} ions/cm^2 for 100th cycle. Inset shows the current vs. voltage graph for pristine and 1×10^{16} ions/cm^2 fluence sample for better comparison. (b) Fluence-dependent RS ratio of the memristor. 150
6.12 The typical (a) ln (I) vs. ln (V) and (b) ln (I) vs. $V^{1/2}$ plot with linear fitting for the fluence of 1×10^{16} ions/cm^2 of 100th cycle. 151
6.13 Schematic of conduction mechanism of the Si/NiO/Au memristor of (a) zero bias, (b) forward bias, and (c) reverse bias. The band diagram of (d) pristine, (e) implanted samples at zero bias, (f) forward bias, and (g) reverse bias. 152

7.1 The crystal structure of (a) pristine NiO, (b) O vacancy, (c) Ni vacancy, (d) Ni substitution by Cu, and (e) Cu interstitial associated NiO, used for theoretical calculations. 165
7.2 The X-ray diffraction spectra of ITO substrate, pristine, and implanted samples. 167
7.3 (a) Crossectional FESEM images of pristine sample. The AFM images of the (b) pristine, (c) sample B, and (d) sample C. 168

7.4 (a) Schematic of ITO/NiO/Ag RRAM device for I-V measurements. The current-voltage curve of the 1st, 25th, 50th, 75th, and 100th cycles of (b) pristine and (c) sample B. (d) The variation of the current (1st cycle) with an applied bias voltage of pristine and implanted samples with increased ion fluences 169
7.5 (a) The double logarithmic I-V plot and (b) ln(I) vs $V^{1/2}$ plot with liner fitting for first positive voltage scan of pristine. 171
7.6 The variation of Schottky barrier with the increase of number of cycles in (a) pristine, (b) sample B for positive and negative voltage scan. (c) The schematic of Schottky contact at NiO/Ag interface. 172
7.7 (a) The current-voltage curve of the 1st, 25th, 50th, 75th, and 100th cycles of sample C, (b) The LRS and HRS state with an increasing number of cycles for the endurance test of sample C. The HRS and LRS was read at 0.3 V. 173
7.8 The schematic of the proposed filamentary model for the (a) zero bias, (b) SET, and (c) RESET process in digital resistive switching of sample C. . . 174
7.9 (a) The variation of displacement per atom with respect to target depth for different ion fluence, calculated using SRIM simulations. The inset shows the SRIM simulated deposited energy and ion range vs. target depth. The TRIDYN simulation for (b) partial sputtering yield, (c) surface recession, and (d) surface atomic fraction with ion fluences. 176
7.10 The surface morphology of (a) pristine, (b) 5×10^{14} ions/cm^2, (c) 5×10^{15} ions/cm^2, (d) 1×10^{16} ions/cm^2, and (e) 2×10^{16} ions/cm^2. (f) shows the cross-sectional FESEM to get the thickness of pristine. 177
7.11 (a) The XRD spectra of pristine and implanted samples in the fluence range of 5×10^{14} ions/cm^2 - 2×10^{16} ions/cm^2, (b) The variation of crystallite size and microstrain with ion fluences, (c-e) The shifting of the XRD peak position of 62.89°, 43.28°, and 37.25° with increasing ion fluences, respectively. 178
7.12 (a) The PL spectra of pristine and implanted samples, (b) The typical deconvoluted PL spectra of pristine, The variation in integrated intensity with ion fluences for the peak position at (c) 429, (d) 510 and (e) 574 nm. 180

7.13 (a) The CL spectra for pristine and implanted samples, (b) The typical deconvoluted CL spectra for pristine, (c-e) The integrated CL intensity of the deconvoluted peak at 445, 481, and 652 nm, respectively, The shifting of intense CL peak at (f) 481 and (g) 445 nm with ion fluences. 182
7.14 The room temperature Raman spectra of pristine and Cu ion implanted samples in the fluence range of 5×10^{14} ions/cm^2 to 2×10^{16} ions/cm^2. 183
7.15 (a) The THz transmission spectra for pristine and implanted samples in the fluence range of 5×10^{14} - 2×10^{16} ions/cm^2 at room temperature, (b) The real optical conductivity with THz frequency for pristine and implanted samples, found from transmission spectra. 185
7.16 The variation of (a) scattering time and (b) plasma frequency for free and bound charges with ion fluences 186
7.17 The calculated band structure of (a) pristine, (b) O vacancy, (c) Ni vacancy, (d) Ni substituted by Cu, and (e) Cu interstitial associated NiO, respectively. The black dashed line along zero is the Fermi level. 186
7.18 The calculated total, orbital, and Ni-d orbital decomposed DOS of (a,b) pristine, (c,d) O vacancy, (e,f) Ni vacancy, (g,h) Ni substituted by Cu, and (i,k) Cu interstitial associated NiO, respectively. 187

List of Tables

5.1 The DFT calculated bandgap values (with experimental lattice constant value) for different U values, matching with experimental values. The variation of calculated bandgap values for fixed U value. 118
5.2 The evaluated β and n_2 values for pristine and annealed samples 121

6.1 Structural parameters: Peak position (2θ), full-width half maxima (FWHM), lattice constant (a), crystallite size (D), strain (ϵ), and dislocation density (δ) 138
6.2 Magnetic parameters: Magnetic coercivity (H_c), Remanence (M_r), Saturation magnetization (M_s) 143

Contents

1 Introduction **1**

1.1 RRAM devices 4

1.2 Ion Solid Interactions 5

1.3 Thermal Spike model 7

1.4 Optical and electronic properties of Rock salt crystal (MgO, NiO) 10

1.5 Outline of the Thesis 14

2 Experimental methods & characterization techniques **22**

2.1 Sample preparation 22

2.1.1 Substrate cleaning 22

2.1.2 Thin film depositions 23

2.1.3 Thermal annealing in PECVD 24

2.2 Ion Implantation 26

2.2.1 Tandem accelerator at IOP 26

2.2.2 Low Energy Implantation at IOP 28

2.2.3 LEIBF at IUAC 29

2.3 RRAM device fabrication 31

2.3.1 RRAM device 31

2.4 Characterization techniques 33

2.4.1 Field emission scanning electron microscopy 33

2.4.2 Atomic Force Microscope 35

2.4.3 X-ray diffraction 36

2.4.4 Ultraviolet-visible near-infrared spectroscopy 37

2.4.5 Photoluminescence spectroscopy 39
2.4.6 Cathodoluminescence 41
2.4.7 Raman spectroscopy 42
2.4.8 Fourier Transform Infrared (FTIR) spectroscopy 43
2.4.9 Superconducting quantum interference device (SQUID) 45
2.4.10 Z-scan technique 47
2.4.11 Tera-Hertz Time Domain Spectroscopy technique 48
2.4.12 Basics of Density Functional Theory 49

3 Tuning electronic and optical properties of Ni and Co ion implanted s-MgO 53

3.1 Introduction 53
3.2 Experimental details 55
3.3 Computational Details 56
3.4 Ion Beam Simulations 57
3.5 Optical Properties 60
3.5.1 UV-Visible Absorption Studies 60
3.5.2 Photoluminescence Studies 63
3.5.3 Theoretical DFT Study 68
3.5.4 Raman study 72
3.5.5 FTIR study 77
3.6 Summary 81

4 Resistive switching effect in ITO/MgO/Ag devices 88

4.1 Introduction 88
4.2 Experimental details 89
4.3 Structural and Morphological Studies 90
4.4 Optical Studies 92

4.5 Resistive Switching Studies 93
4.6 Summary 101

5 Third order non-linear optical properties of NiO thin films 104

5.1 Introduction 104
5.2 Experimental details 105
5.3 Computational Details 107
5.4 Surface Morphology and Structural Analysis 108
5.4.1 SEM study 108
5.4.2 XRD Analysis 108
5.5 Optical Studies 111
5.5.1 UV-Vis Analysis 111
5.5.2 PL Analysis 112
5.5.3 CL Analysis 114
5.5.4 Theoretical Analysis 115
5.5.5 Non-linear Optical Properties 118
5.6 Summary 124

6 Magnetocrystalline Anisotropy and Resistive Switching in 30 keV Au implanted NiO thin films 129

6.1 Introduction 129
6.2 Experimental details 131
6.3 Ion Beam Simulations 132
6.4 Morphological and structural studies 135
6.4.1 FESEM 135
6.4.2 XRD Spectra 136
6.5 Optical studies 138

6.5.1 UV-visible spectroscopy 138
6.5.2 PL spectroscopy 139
6.6 Magnetic Properties 141
6.7 Resistive Switching studies 149
6.8 Summary 155

7 Resistive switching and Terahertz conductivity in 100 keV Cu ion implanted NiO thin films 162

7.1 Introduction 162
7.2 Experimental Details 164
7.3 Computational Details 165
7.4 First Part: Resistive Switching 166
7.5 Second Part: Optical Properties and THz Dynamics 175
7.5.1 SRIM and TRIDYN Simulations 175
7.5.2 Surface Morphology and Structural Analysis 177
7.5.3 Optical Properties 179
7.5.4 THz Properties 184
7.6 Summary 189

8 Summary and future prospects 195

8.1 Summary 195
8.2 Future prospects 200

Chapter 1

Introduction

Over the past few decades, thin film deposition technology has gained significant attention from researchers and industries, particularly in sectors such as solar, semiconductor, and optical devices. This interest stems from the potential applications of thin films in protective coatings, optics, biomedical devices, and microelectronic solid-state devices. Thin films, with thickness ranging from a few nanometers to a few micrometers, exhibit distinct surface properties compared to conventional bulk materials, owing to a remarkable increase in surface-to-volume ratio. The optical, mechanical, thermal, and electrical properties of thin films differ significantly from their bulk counterparts due to the introduction of defects during the film growth process. Despite having the same elemental compositions, thin films play a crucial role in various applications, including diffusion barriers, stain repellents, antimicrobial coatings, anti-fogging layers, corrosion-resistant films, photo-catalytic materials, photovoltaics, thin-film batteries, insulators, conductors, optics, low-friction coatings, and wear-resistant surfaces. Thin films have become indispensable in modern life, influencing science and technology across electronic, optical, mechanical, and biological domains. Notably, electronic and optical thin film-based devices have dominated advancements in fields ranging from laser technology to memory devices. The popular thin film optical devices are anti-reflection (AR) coating, highly reflecting (HR) dielectric mirrors, beam reflectors, beam combiners, beam dividers, band pass or edge pass filters, broadband AR or HR coatings, Q switching, passive mode locking, electro-optical devices [1], active [2] and passive [3] waveguides and so on.

In the pursuit of high-performance and miniaturized electronic devices, from smart-

phones, laptops, and automobiles to thermostats and toaster ovens, there is a growing demand for innovative solutions, such as resistive random-access memory (RRAM) devices, which can address issues like Joule heating, low-speed, high power consumption, and storage limitations in tiny chips. Techniques like doping and ion implantation can be employed to modulate the optical and electronic properties of polycrystalline and single-crystal thin films, affecting the intrinsic and inducing the extrinsic defects that enhance the functionality of devices for a wide range of technological applications.

In the realm of materials science, MgO and NiO thin films stand out among various rock salt structures due to their potential capability in optical and electronic device applications. Both materials are non-toxic, environmentally friendly, thermally stable, and share a similar face-centered cubic (FCC) crystal structure. The wide bandgap properties of MgO (7.8 eV) and NiO (3.6 eV) make them suitable for use in resistive memory devices as insulating or semiconducting layers, respectively. This property also allows broad luminescence from the near-infrared to the ultraviolet range based on the different recombination levels in the bandgap. The wide luminescence capability in the broadband white light region reveals NiO as white light emitters without the help of phosphors or quantum well structures, benefiting the LED industries. The third-order non-linear behavior of rock salt materials is also useful in optical Q-switching and mode-locking applications. Depending on the applications, thin films of MgO and NiO are grown using various thin film growth techniques such as Vacuum Evaporation, radio frequency sputtering, dc sputtering, magnetron sputtering, Plasma-Enhanced Chemical Vapor Deposition, Atomic Layer Deposition, pulsed laser deposition, molecular beam epitaxy etc. The optical and electrical conductivity properties of grown MgO and NiO thin films using various techniques can be finely tuned depending on growth conditions and intrinsic defects, as well as intentionally added extrinsic defects in the matrix by doping or ion implantation. The schematic of different kinds of defect production in the crystal is shown in Fig. 1.1.

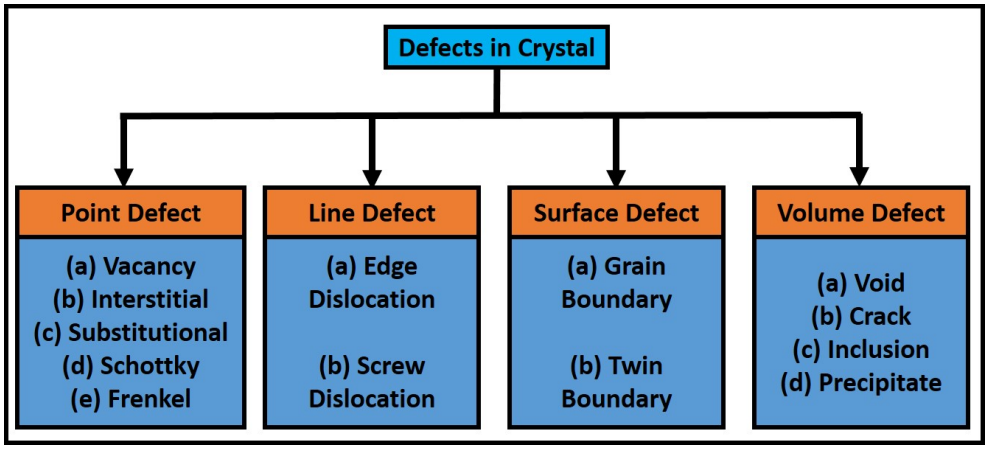

Figure 1.1: The schematic of formation of various kinds of defects in the crystal.

Point defects arise when one or more lattice atoms leave their site and/or the foreign or lattice atoms occupy the interstitial position within the crystal. Vacancy defects occur when a lattice atom leaves its original position. The foreign atom can take place at the interstitial position and/or substitute the original lattice atom, forming interstitial and/or substitutional defects in the crystal, respectively. Schottky defect forms by creating the anionic and cationic vacancy defects simultaneously. In contrast, the Frenkel defect is associated with the movement of the original lattice atom to the interstitial position, leaving a vacancy position there. Line defects, like edge and screw dislocations, result from irregularities along periodically arranged lattice atoms. Surface defects, such as grain and twin boundaries, can form during crystal growth. The volume defects like voids (vacancies), cracks (lattice fractures), inclusions (foreign particles immersed in the lattice), and precipitation can appear during annealing or film deposition. Line, surface, and volume defects primarily emerge during crystal growth, influenced by growth conditions. Conversely, point defects induced by doping or implantation can be tailored as needed. Exploring defect production through ion-solid interactions in rock salt materials like MgO and NiO presents a vast and captivating research area in physics and chemistry, with potential applications in diverse optical and electronic devices such as RRAM devices.

1.1 RRAM devices

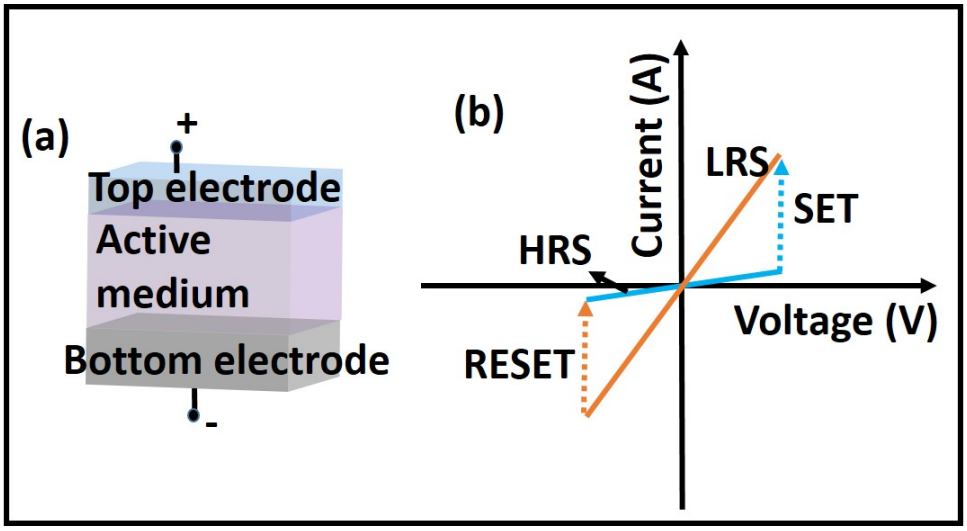

Figure 1.2: (a) The schematic of the construction of the RRAM device, and (b) the current-voltage mechanism in the bipolar mode of the RRAM device.

Various kinds of defects in semiconductor or insulating layers (active medium) play a crucial role in changing the RRAM properties. RRAM is a type of non-volatile memory that leverages a material's resistance change to store data. Unlike traditional memory technologies like DRAM and flash memory, RRAM operates by changing the resistance of an insulating or dielectric material, which is typically an oxide sandwiched between two metal electrodes. The typical construction of an RRAM device is shown in Fig 1.2 (a). The active medium is usually an oxide material such as MgO, NiO, or others. The bipolar mode of the RRAM device is illustrated in Fig 1.2 (b). A bias voltage is applied on the top electrode. A SET voltage is an applied voltage across the electrodes when the charge carriers face a less resistive path in the active layer, and the current suddenly jumps at that voltage. Hence, SET voltage creates a low-resistance state (LRS), representing a binary '1'. A RESET voltage is an applied voltage when the charge carriers face a high resistive path in the active layer, and the current drops down. The system moves from LRS to a high-resistance

(HRS) state, representing a binary '0'. When the SET and RESET operations occur within the same polarity region, it indicates a unipolar RRAM device. Conversely, when SET and RESET operations occur in opposite polarity regions, it indicates a bipolar RRAM device. The resistance state is maintained even after the power is switched off, providing non-volatile storage. Several mechanisms, such as the bulk-dominated filamentary model, charge trapping effect, and interface mechanism, etc., are proposed to explain the current conduction at SET and REST voltage in an active medium. These mechanisms highlight the diverse ways RRAM can operate, depending on the active materials, electrodes, and structures employed. Along with this, various kinds of defects, mainly vacancies, assist the filament formation in the active medium to improve the performance of the RRAM device. Ion implantation can be a suitable technique for introducing defects into the active layer, necessitating a thorough understanding of ion-solid interactions.

1.2 Ion Solid Interactions

Ion implantation is a popular and widely adopted technique to modify the surface and interior of the target lattice by creating various kinds of defects in the materials. The modification of various optical and electrical properties of the host lattice depends extensively on incident ion angle, ion species, and energies. The energetic ion interacts with the target in two ways: elastic collisions with nuclei and inelastic collisions with target electrons. Fig. 1.3 shows the various processes involved in ion-solid interaction during implantation. Figure 1.3(a) depicts the ion implantation process, where the concentration of the incident ions increases in the implanted area, leading to alterations in lattice composition and structures. The damage to the target material and the distribution of ions rely on incident ion energies. The damages through collision cascade by ions are shown in Fig. 1.3(b). The displacement of the host atoms primarily occurs due to the nuclear energy loss process through elastic col-

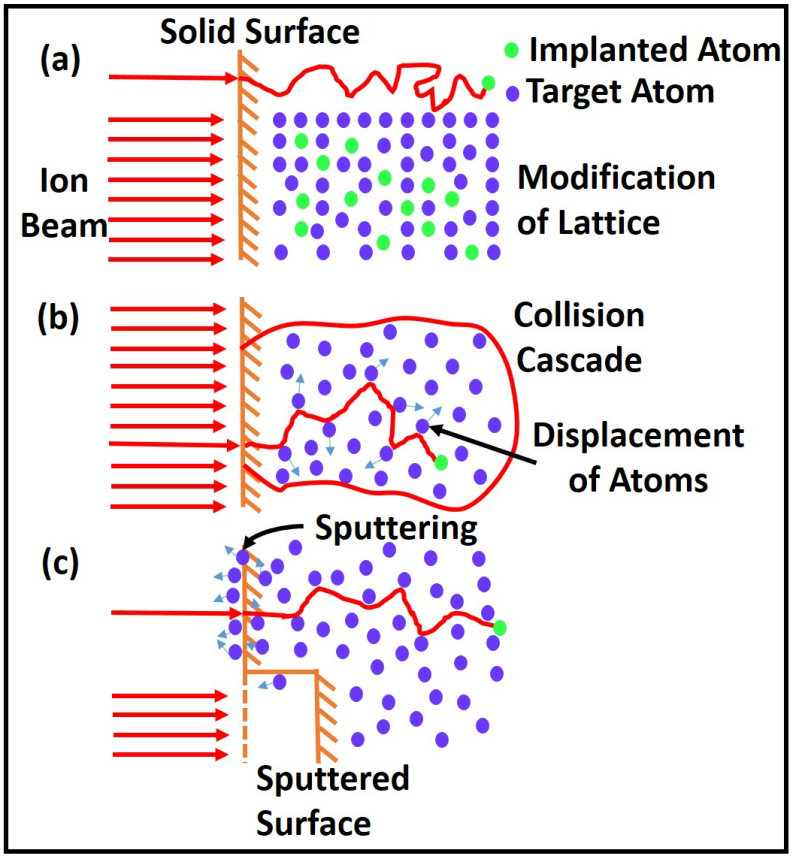

Figure 1.3: The schematic of ion solid interactions, resulting in (a) the modification of target materials by (b) occurring collision cascade within the range of the incident ions. (c) represents the sputtering of host atoms during implantation.

lisions between the incident and target nuclei along the ion track. Fig. 1.3(c) exhibits the surface atom ejection process of the target through elastic collision through the momentum exchange between target nuclei and incident ions, known as "Sputtering" [4]. The sputtering is possible when the incident ion has sufficient energy to break the chemical bonding of the target materials. The sputtering yield (Y) is defined as the mean number of target atom ejections per incident ions:

$$Y = \frac{\alpha N S_n(E)}{E_B} \tag{1.1}$$

The parameter α depends on the geometry of the materials. N denotes the atomic den-

sity of the target materials. E_B is the binding energy of surface atoms, and S_n is nuclear energy loss. Thus, sputtering depends on the kinetic energy of incident ions, binding energy, and stoichiometry of the materials [5]. The expression suggests that if the number of incident ions is large, the number of sputtered atoms will also be large. For multi-component systems, the sputtering can behave differently for different elemental constituents. For example, the sputtering of lighter atoms is preferable than the heavier ones, which can result in acquiring different stoichiometry near the surface compared to bulk materials [6, 7]. On the other hand, the total energy loss by the ions in target materials is composed of two basic energy transfer mechanisms: nuclear and electronic (S_e) energy loss. The S_n is associated with elastic collisions between target nuclei and incident ions, whereas S_e is the consequence of inelastic excitations and ionizations of the electrons [8, 9]. The nuclear collision dominates in the case of low-energy (keV) ion implantation. On the other hand, the governing inelastic collision at high-energy (MeV) implantation leads to lattice modifications and deep-layer implantation. The sputtering of surface atoms is also minimal in high-energy ion irradiation compared to low-energy irradiation. The synergetic effect of both elastic and inelastic collision happens when S_n is comparable to S_e.

Low-energy ion implantation predominantly centers on the collision cascade occurring within the material as a result of elastic collisions with substantial nuclear energy loss. In this thesis, various vacancy, interstitial, and substitutional defects are introduced through implantation in the rock salt structure depending on the ion energy and species, as illustrated in Fig. 1.4.

1.3 Thermal Spike model

The inelastic thermal spike (i-TS) model stands out as a highly effective tool for describing damage produced by swift heavy ions, finding widespread application across various target

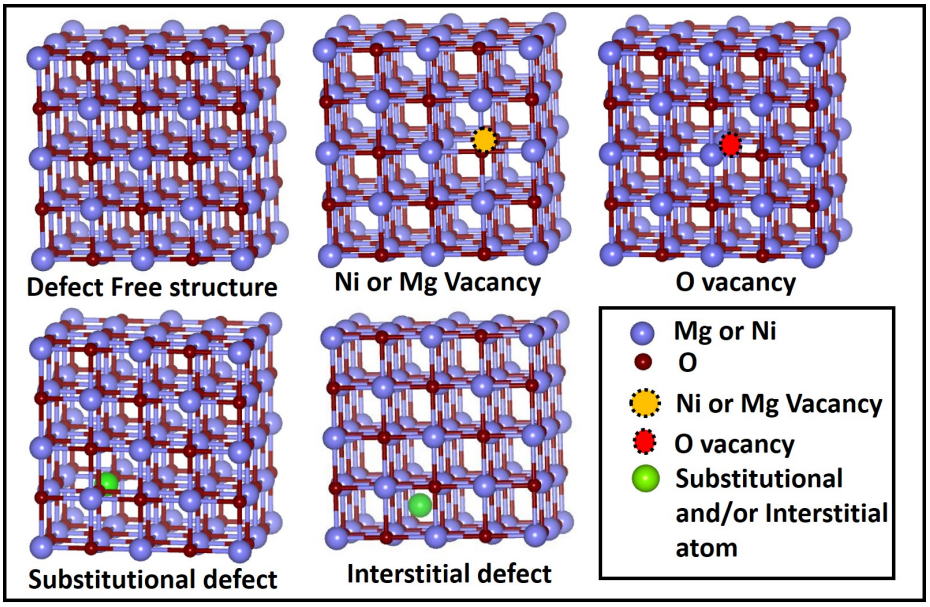

Figure 1.4: The defect-free, vacancy, substitutional, and interstitial defect-associated rock salt crystal structure.

materials, including metals, semiconductors, and insulators. The processes involved in the thermal spike model are illustrated in Fig. 1.5. Fig. 1.5(a-c) and Fig. 1.5(d-f) describe the electron dynamics, lattice dynamics, and relaxation of lattices for dominating high and low energy incident ion cases, respectively. Initially, the incident ions impart their energy to the target's electrons through ion-electron collisions. Subsequently, electron-electron collisions facilitate the redistribution of this energy among other cold electrons. Thirdly, the energy is transmitted to the lattice via electron-phonon coupling. Finally, the energy dissipates among the atoms, resulting in a spike along the ion trajectory. The energy is deposited in the electrons within the ultrafast timeframe of 10^{-16} to 10^{-15} seconds, followed by its transfer to the lattice atoms occurring within the range of 10^{-13} to 10^{-11} seconds. The following two coupled differential equations [10] of heat diffusion used in i-TS model describe heat transfer with time (t) and space (r) in electronic and lattice subsystems in cylindrical coordinates.

$$C_e(T_e)\frac{\partial T_e}{\partial t} = \frac{1}{r}\frac{\partial}{\partial r}[rK_e(T_e)\frac{\partial T_e}{\partial r}] - g(T_e - T_a) + A(r) \tag{1.2}$$

$$C_a(T_a)\frac{\partial T_a}{\partial t} = \frac{1}{r}\frac{\partial}{\partial r}[rK_a(T_a)\frac{\partial T_a}{\partial r}] - g(T_e - T_a) \tag{1.3}$$

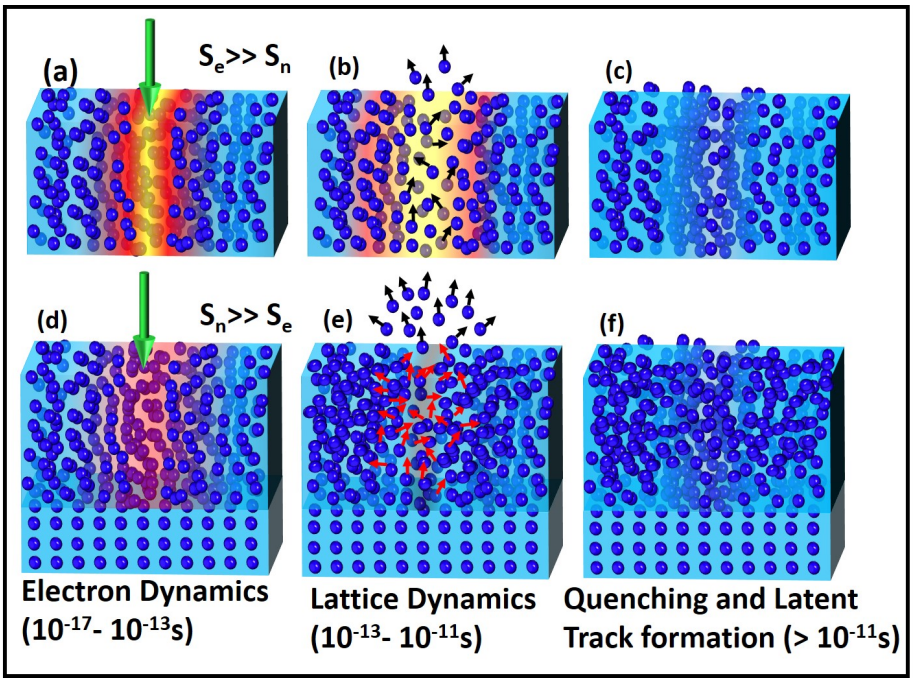

Figure 1.5: The schematic of (a,d) electron dynamics, (b,e) lattice dynamics, and (c,f) relaxing of atoms after the interaction with incident ions in thermal spike model for two scenarios when S_e » S_n and S_n » S_e, respectively.

Where $T_{e,a}(r,t)$, $C_{e,a}(r,t)$ and $K_{e,a}(r,t)$ represents the temperature, the specific heat and the thermal conductivity of the electronic (e) and lattice (a) subsystem, respectively. A(r) is the energy deposition in the electronic subsystem [11]. The electron-phonon coupling strength g is the only free parameter in this model.

For low-energy cases, nuclear energy deposition by ions dominates over the electronic energy loss process and requires the unified thermal spike model (U-TSM). Hence, the energy deposition through elastic collision can not be neglected, and the solution of the two coupled differential equations would be modified according to U-TSM and solved by adding

the nuclear energy deposition term B(r) in equation 1.3 in the low-energy ion bombardment process. The equation 1.3 will be modified as follows:

$$C_a(T_a)\frac{\partial T_a}{\partial t} = \frac{1}{r}\frac{\partial}{\partial r}[rK_a(T_a)\frac{\partial T_a}{\partial r}] - g(T_e - T_a) + B(r) \tag{1.4}$$

A large amount of heat generation along the ion path in an ultrafast time scale helps to displace the atom from the lattice position to create different kinds of defects in the system.

1.4 Optical and electronic properties of Rock salt crystal (MgO, NiO)

The rock salt material exhibits remarkable optical and electronic properties attributed to its wide bandgap, encompassing a semiconducting gap for NiO and an insulating gap for MgO. The exciton properties within this bandgap vary depending on the concentration of intrinsic and extrinsic defects. Opting for ion implantation as a technique offers advantages over chemical doping, providing a favorable method to introduce extrinsic defects into the rock salt material with precise control over their concentration and location. This allows the modulation of optical and electronic properties to meet various optical and electronic device applications.

MgO is a promising rock salt material with unique electronic and optical properties, which has widespread applications in optoelectronics, microelectronics, adsorbents, sensors, catalysis, refractory material, paints, fluoride remover, and luminescence devices [12–16]. The conduction band (CB) minima and valence band (VB) maxima of defect-free MgO in electronic band structure lie along the same Γ points, indicating the direct bandgap nature of MgO. The VB and CB primarily consist of O-p and Mg-s and Mg-p orbitals, respectively [17]. The electronic transition from CB minima to VB maxima is triggered by UV light absorption, and subsequent de-excitation results in the near-band emission of MgO. Some-

times, the defects, such as F, F_2, F^+, and V centers, during crystal growth are reflected in excitation through UV light. The electron in the defect center gets excited and moves to CB, and the de-excitation from CB to various defect states emits photon energy corresponding to the gap between CB and defect states. Depending upon the concentration of the color centers, the bandgap of MgO can be altered. MgO serves as an advantageous insulator with a wide bandgap of 7.8 eV [18]. Due to having a high dielectric constant (6–10), a high thermal conductivity, and a high breakdown field (12 MV/cm), MgO thin films show potential interest in adequate band offsets and reduction of leakage currents in device applications [19]. Furthermore, MgO can be employed as an insulating oxide layer in RRAM devices [20, 21]. MgO can be an ideal candidate to substitute SiO_2 as the gate dielectric in Metal Oxide Semiconductor (MOS) devices both for low and high-power applications [21]. The various optical and electrical properties can be enhanced by extrinsic defect creation in the films, although defects are generally considered imperfections of the matrix. They are not always disadvantageous; rather, they modulate system properties. Chemical doping is one of the options to introduce defects in MgO. However, ion implantation can be the most effective and widely used surface modification method in insulators and ceramics. Metallic ion implantation in insulators shows optical features linked to optical extinction at the surface plasmon resonance frequency, which is crucial for the creation of novel optical devices with increased nonlinear parameters. 150 keV Kr ion implantation in MgO gives rise to damage and lattice disorder at the surface, which are created after the collision cascade. The quasi-amorphous region required less energy to regrowth during thermal annealing compared to removing the extended defects [22]. The magnetic properties are introduced in 64 keV Ni ion implanted single crystal MgO (s-MgO) [23]. The giant enhancement of the F-type color center is achieved by 3 MeV Ne ion bombardment in MgO, where much of the coloration is associated with the displacement type lattice damage [24]. F centers are one of the crucial crystallographic point defects in the lattice. These

defects form when the anionic vacancies in the lattice are occupied by unpaired electrons. These defects act as electron trap centers, which can play a role in current conduction in RRAM devices. MgO's microstructure and optical absorbance behave differently for 60 keV N and 40 keV Fe ion implantation [25]. N impurity concentration affects very little to change the optical absorbance. 30 keV Pt ion implantation in MgO displaces 40 lattice atoms permanently per ion, creating radiation damage in the system [26]. The channeling and backscattering results help to explain the catalysis behavior of MgO. The strong correlation between lattice disorder, the defect-dependent optical density, and the variation of color centers are investigated by 200 keV and 1 MeV Ni ion implantation in MgO [27]. The electrical conductivity (orders of magnitude = 14 and 7) is enhanced in the 175 keV Li ion implanted region compared to the unimplanted area at 293 and 450 K [28]. The 1.5 MeV H ion implantation also increases the electrical conductivity with the increase of doses due to the escalation of the defects (oxygen vacancies and interstitials) in the system [29]. Although MgO is an insulating material with a high bandgap, 100 keV Fe ion implantation increases the conductivity rapidly to a value of 100 $\Omega^{-1}.cm^{-1}$ at 1×10^{17} ions/cm^2 [30]. The above investigation shows that the different ion implantation with various energies and fluences influence the optical and electrical properties of MgO by creating damage in the desired area.

NiO is another auspicious p-type semiconducting rock salt material with outstanding optical and electronic properties that provides potential applicability in many emerging fields of technological research. The optical, chemical, and electrical stability of NiO thin films are suitable for various applications such as photocathodes for p-type dye-sensitized solar cells [31], resistive switching memory devices [32], magnetoresistance [33, 34], buffer layer in organic solar cells [35], light emitting diode [36], electrochromic devices [37], hydrogen sensing [38, 39], humidity sensing [40], smart windows [41], photoelectrochemical water splitting [42], organic photovoltaics [43], antiferromagnetism [44], optoelectronic de-

vices [45], etc. The emerging linear and non-linear optical properties of NiO-based micro and nanostructures provide the advancement of future research opportunities in lighting devices, optical microresonators, waveguides, optical power limiters, saturable absorbers, and neuromorphic applications which still remain scarcely explored from an optical perspective [46]. The heterojunction formation of p-type NiO and n-type oxide (examples: ZnO, TiO_2) demonstrates the excellent photodiode characteristics for the application as a photodetector [47, 48]. The band engineering of NiO shows that the lowest CB states of NiO material form with Ni-3d orbitals and the highest VB states by O-2p orbitals [49]. The near-band emission of NiO in the UV region is observed when the electronic transition between VB maxima and CB minima occurs either along the same high symmetry k points or different k points inside the Brillouin zone [50]. As a wide bandgap material (3.6 eV), the luminescence of NiO from near IR to UV region is observed due to different recombinational levels, which is associated with Ni deficiency, d–d transitions, and defect or impurity levels in the bandgap [46]. The high transparency in visible regions with large hole conductivity and large charge carrier density make NiO a better choice than other transition metal oxides for optoelectronic applications. Although NiO in its stoichiometric form is antiferromagnetic (Neel temperature 523 K) low-conducting material with high resistivity up to $10^{13}\ \Omega/cm$ [51], the electrical conductivity can be improved by inducing vacancy and interstitial defects either by the chemical doping or controlled ion implantation method. The ion implantation can be a suitable technique to tune the optical and electronic properties of NiO over doping due to the precise creation of defects at the desired depth with a controlled amount of concentration. 100 keV Ni ion implantation in NiO decreases the optical transmittance and bandgap with ion fluences [52]. The low dose of 500 keV Cu ion implantation in NiO increases the crystallinity of the film compared to the high dose [53]. Similarly, the optical bandgap narrows for low doses and becomes wider at high-dose implantation. 60 keV O ion implantation in Ni crystal forms the NiO material, providing a new path of crystal

growth using implantation [54]. The optical and electronic properties are modulated by 80 MeV O ion irradiation in Fe:SnO_2/Li:NiO p–n junctions [55]. The suppression of rectifying characteristics of ZnO/NiO and acquiring the Ohmic behavior with increasing ion fluences are achieved by 200 MeV Ag ion irradiation on the heterojunction [56]. The controlled defect stabilizes the switching performance of the RRAM devices. The resistive switching hysteresis characteristic of 100 MeV Ag ion irradiated Li-doped NiO is developed from the near linear I-V behavior [57]. The conductivity is greatly improved to $2.8 \times 10^{-6}\ (\Omega cm)^{-1}$ by 40 keV Li ion implantation in NiO single crystals compared to the unimplanted crystal ($2 \times 10^{-10}\ (\Omega cm)^{-1}$) [58]. The small polaron motion of NiO has been obtained through Li-ion implantation. Hence, the above discussion suggests that different ion implantation with various energies can be the crucial parameter to introduce the defect in the NiO thin films to improve the optical and electrical behavior for achieving better NiO-based optical and electronic devices.

1.5 Outline of the Thesis

In this thesis, the impact of ion implantation on single-crystal MgO and RF-sputtered-grown NiO and MgO thin films are investigated to tailor their optical and electronic behaviors for various device applications. Additionally, the lattice temperature rises during low-energy ion implantation due to elastic collisions between the target nuclei and incident ion. Hence, understanding the modulation of electronic and optical properties in rock salt thin films through thermal annealing is also another focal point.

Chapter 1 explicitly outlines the motivation to regulate the optical and electronic properties of implanted and annealed rock salt (MgO and NiO) thin films for different applications. The detailed explanation of ion-solid interaction provides a clear idea about the defect creation in the matrix and sputtering at the surface to modify the target during implantation.

The thermal spike model explains the rise of temperature along the ion path for both low and high incident ion energy cases. This chapter also narrates the fundamentals of optical and electronic properties of rock salt materials, investigating the effect of ion implantation and thermal annealing.

Chapter 2 explains the experimental technique and characterization methods employed in the thesis. It covers the growth of MgO and NiO thin films using an RF sputtering system, subsequent thermal annealing in vacuum using a PECVD system, and low-energy ion beam sources for ion implantation. The deposition of Au thin films for making electrodes was achieved by the thermal evaporation technique. The working principles of different characterization techniques such as FESEM, SQUID, AFM, XRD, PL, CL, Raman, Tera Hertz (THz), FTIR, UV-visible spectroscopy, and Z-scan are briefly described. The chapter also provides a basic understanding of Density Functional Theory (DFT).

Chapter 3 delves into the band modification and vibrational mode analysis induced after one MeV Ni and Co ion implantation in s-MgO. The origin of experimental band narrowing and induction of vibrational modes due to defect creation of implanted samples compared to pristine is correlated with the help of DFT.

Chapter 4 reports the annealing effect of sputtered-grown MgO for improving the RRAM properties. The RRAM device is fabricated by sandwiching MgO between the bottom conducting ITO substrate and the top Ag electrode. The better endurance was sustained in the annealed sample than in the as-deposited sample for higher cycles of ITO/MgO/Ag devices.

Chapter 5 describes the third-order non-linear optical properties of various thermally annealed NiO thin films. In the OA condition, SA and RSA are observed in pristine and annealed samples, respectively, where RSA is linked with the TPA process. In contrast, the self-defocusing signature is exhibited in CA conditions. In our case, the TPA process was favored more over the plasmonic effect due to the increasing indirect bandgap with

annealing temperature. The DFT calculations give the insight reason for increasing the bandgap by showing the upward shifting of Ni-$d_{x^2-y^2}$ and Ni-d_{z^2} orbitals in CB, which is correlated to the nonlinear optical properties (NLOP).

Chapter 6 narrates the magnetocrystalline anisotropy and RRAM characteristics of 30 keV Au ion implanted NiO thin films. The ion beam simulation predicts the ion range, damage, and sputtering of the films. The role of defects is correlated to the origin of FM nature in NiO and magnetocrystalline anisotropy. Additionally, the analog behavior of Si/NiO/Au RRAM devices with ion fluences is elucidated based on the interface-dominated behavior with the changes in the depletion width and the Schottky barrier at Si/NiO (p-n junction) and NiO/Au interface, respectively.

Chapter 7 elucidates the transformation of analog to digital RRAM characteristics in 100 keV Cu ion implanted ITO/NiO/Ag devices with various fluences. The analog current conduction in pristine and low fluence (5×10^{15} ions/cm^2) samples is associated with interface-dominated Schottky characteristics. In contrast, the bulk-dominated vacancy filamentary model elucidates the digital current flow mechanism at the highest fluence sample (2×10^{16} ions/cm^2). This chapter is also dedicated to observing the THz conducting effect in 100 keV Cu ion implanted NiO thin films. Ion implantation modulates the carrier concentration and strain of the films, influencing THz transmission and optical conductivity. The variation of THz scattering and plasma frequency is correlated to the carrier concentration and defect states between CB and VB and explained using DFT calculations.

Finally, **chapter 8** serves as a comprehensive summary and outlines the future prospects of the research. The conclusion emphasizes the effectiveness of integrating diverse defects into MgO and NiO thin films, showcasing their potential for manipulating optical and electronic properties to enhance device functionality.

Bibliography

[1] Ş. Korkmaz, S. Pat, N. Ekem, M. Z. Balbağ, S. Temel, *Vacuum* **86**, 1930 (2012).

[2] M. Zevin, R. Reisfeld, *Optical Materials* **8**, 37 (1997).

[3] R. Brenier, C. Urlacher, J. Mugnier, M. Brunel, *Thin Solid Films* **338**, 136 (1999).

[4] P. Sigmund, *Nuclear Instruments and Methods in Physics Research Section B: Beam Interactions with Materials and Atoms* **27**, 1 (1987).

[5] P. Sigmund, R. Behrisch, *Topics in Applied Physics* **47**, 9 (1981).

[6] Z. Liau, J. Mayer, W. Brown, J. Poate, *Journal of Applied Physics* **49**, 5295 (1978).

[7] H. H. Andersen, H. L. Bay, *Journal of Applied Physics* **46**, 2416 (1975).

[8] U. Littmark, J. F. Ziegler, *Handbook of range distributions for energetic ions in all elements* (Pergamon Press Incorporated, Elmsford, NY, 1980).

[9] J. F. Ziegler, *Handbook of stopping cross-sections for energetic ions in all elements* (Pergamon Press Incorporated, Elmsford, NY, 1980).

[10] I. M. Lifshitz, M. I. Kaganov, L. V. Tanararov, *J Nucl Energy A* **12**, 69 (1960).

[11] M. Waligorski, R. Hamm, R. Katz, *International Journal of Radiation Applications and Instrumentation. Part D. Nuclear Tracks and Radiation Measurements* **11**, 309 (1986).

[12] S. Balamurugan, L. Ashna, P. Parthiban, *et al.*, *Journal of nanotechnology* **2014**, 1 (2014).

[13] M. Sterrer, T. Berger, O. Diwald, E. Knözinger, *Journal of the American Chemical Society* **125**, 195 (2003).

[14] A. J. Haes, S. Zou, G. C. Schatz, R. P. Van Duyne, *The Journal of Physical Chemistry B* **108**, 109 (2004).

[15] S.-W. Bian, J. Baltrusaitis, P. Galhotra, V. H. Grassian, *Journal of Materials Chemistry* **20**, 8705 (2010).

[16] X.-Y. Yu, *et al.*, *The Journal of Physical Chemistry C* **115**, 22242 (2011).

[17] S. Bhakta, S. Pradhan, A. K. Nandy, P. K. Sahoo, *Journal of Electronic Materials* **52**, 1937 (2023).

[18] N. F. Chayed, N. Badar, R. Rusdi, N. Kamarudin, N. Kamarulzaman, *AIP Conference Proceedings* (American Institute of Physics, 2011), vol. 1400, pp. 328–332.

[19] E. Miranda, *et al.*, *Microelectronics Reliability* **49**, 1052 (2009).

[20] D. J. J. Loy, P. A. Dananjaya, X. L. Hong, D. Shum, W. Lew, *Scientific reports* **8**, 14774 (2018).

[21] M. Menghini, *et al.*, *physica status solidi (c)* **12**, 246 (2015).

[22] E. Friedland, *Nuclear Instruments and Methods in Physics Research Section B: Beam Interactions with Materials and Atoms* **85**, 316 (1994).

[23] S. Zhu, X. Xiang, X. Zu, L. Wang, *Nuclear Instruments and Methods in Physics Research Section B: Beam Interactions with Materials and Atoms* **242**, 114 (2006).

[24] B. Evans, *Physical Review B* **9**, 5222 (1974).

[25] C.-M. Liu, *et al.*, *Chinese Physics B* **20**, 047505 (2011).

[26] A. Turos, P. Rabette, O. Meyer, *et al.*, *Journal of Physics C: Solid State Physics* **14**, 3333 (1981).

[27] T. Mitamura, *et al.*, *Journal of nuclear materials* **271**, 15 (1999).

[28] M. Tardío, *et al.*, *Nuclear Instruments and Methods in Physics Research Section B: Beam Interactions with Materials and Atoms* **218**, 164 (2004).

[29] A. M. E. Raj, *et al.*, *Nuclear Instruments and Methods in Physics Research Section B: Beam Interactions with Materials and Atoms* **266**, 2564 (2008).

[30] A. Perez, J. Bert, G. Marest, B. Sawicka, J. Sawicki, *Nuclear Instruments and Methods in Physics Research* **209**, 281 (1983).

[31] C.-Y. Hsu, *et al.*, *Electrochimica acta* **66**, 210 (2012).

[32] G. Ma, X. Tang, Z. Zhong, H. Zhang, H. Su, *Microelectronic engineering* **108**, 8 (2013).

[33] J. Fischer, *et al.*, *Physical Review B* **97**, 014417 (2018).

[34] H. D. Chopra, D. X. Yang, P. Chen, D. Parks, W. F. Egelhoff Jr, *Physical Review B* **61**, 9642 (2000).

[35] D. Nguyen, *et al.*, *Applied surface science* **311**, 110 (2014).

[36] X. L. Zhang, *et al.*, *Thin Solid Films* **567**, 72 (2014).

[37] S. Pereira, *et al.*, *Solar energy materials and solar cells* **120**, 109 (2014).

[38] P.-C. Chou, *et al.*, *International Journal of Hydrogen Energy* **40**, 729 (2015).

[39] I. Sta, *et al.*, *Journal of Alloys and Compounds* **626**, 87 (2015).

[40] D. Das, M. Pal, E. Di Bartolomeo, E. Traversa, D. Chakravorty, *Journal of Applied Physics* **88**, 6856 (2000).

[41] G. Bodurov, P. Stefchev, T. Ivanova, K. Gesheva, *Materials Letters* **117**, 270 (2014).

[42] J. P. Kollender, B. Gallistl, A. I. Mardare, A. W. Hassel, *Electrochimica Acta* **140**, 275 (2014).

[43] K. X. Steirer, *et al.*, *Organic Electronics* **11**, 1414 (2010).

[44] H. Ohldag, N. Weber, C. Bethke, F. Hillebrecht, *Journal of Electron Spectroscopy and Related Phenomena* **114**, 765 (2001).

[45] Y. Zhang, *Applied Surface Science* **344**, 33 (2015).

[46] M. Taeño, D. Maestre, A. Cremades, *Nanophotonics* **10**, 1785 (2021).

[47] H. Hakkoum, *et al.*, *Optical Materials* **108**, 110434 (2020).

[48] H. Li, *et al.*, *Optics express* **23**, 27683 (2015).

[49] C. Park, *et al.*, *Applied Science and Convergence Technology* **24**, 72 (2015).

[50] M. Shkir, V. Ganesh, S. AlFaify, I. Yahia, H. Zahran, *Journal of Materials Science: Materials in Electronics* **29**, 6446 (2018).

[51] M. Napari, *et al.*, *InfoMat* **2**, 4 (2020).

[52] R. Nongjai, K. Asokan, *AIP Conference Proceedings* (AIP Publishing, 2020), vol. 2265.

[53] A. Masood, *et al.*, *Ceramics International* **49**, 4435 (2023).

[54] M. Tošić, *et al.*, *Nuclear Instruments and Methods* **182**, 303 (1981).

[55] B. V. Mistry, D. Avasthi, U. Joshi, *Applied Physics A* **122**, 1 (2016).

[56] P. Das, *et al.*, *Materials Research Express* **6**, 106413 (2019).

[57] U. Joshi, *et al.*, *Journal of Applied Physics* **105**, 7 (2009).

[58] R. Benenson, V. Tikku, M. Brown, J. Savi, R. MacCrone, *Nuclear Instruments and Methods* **182**, 769 (1981).

Chapter 2

Experimental methods & characterization techniques

This chapter provides a concise overview of the experimental methods and characterization techniques implemented in this thesis. The deposition of MgO and NiO thin films is accomplished through the RF-sputtering method, followed by post-annealing using the Plasma Enhanced Chemical Vapor Deposition (PECVD) system. Defects are introduced into the samples through ion implantation methods. Structural and morphological analysis of the thin films is conducted using XRD, FESEM, and AFM characterization techniques. Optical properties and defects of the thin films are characterized through various spectroscopic tools, including UV-visible, PL, CL, and Raman spectroscopy. SQUID is employed for magnetic measurements, while electrical measurements are carried out using a Keithley 2450 source meter. The non-linear optical properties and THz transmission of ion-implanted samples are investigated using the Z-scan and THz techniques, respectively.

2.1 Sample preparation

2.1.1 Substrate cleaning

Si, Si/SiO_2, glass, and ITO substrates were utilized in this thesis for the deposition of MgO and NiO thin films. Prior to the deposition process, standard cleaning of the substrates was carried out. The substrates underwent a 10-minute ultrasonication cycle in acetone, followed by isopropyl alcohol and then deionized water. Subsequently, the substrates were dried using pure N_2 gas.

2.1.2 Thin film depositions

RF Sputtering:

In this thesis, the rock salt thin films are deposited using the RF sputtering system (a physical vapor deposition (PVD) technique). Fig. 2.1 shows the schematic of the RF sputtering system involved in depositing the thin films.

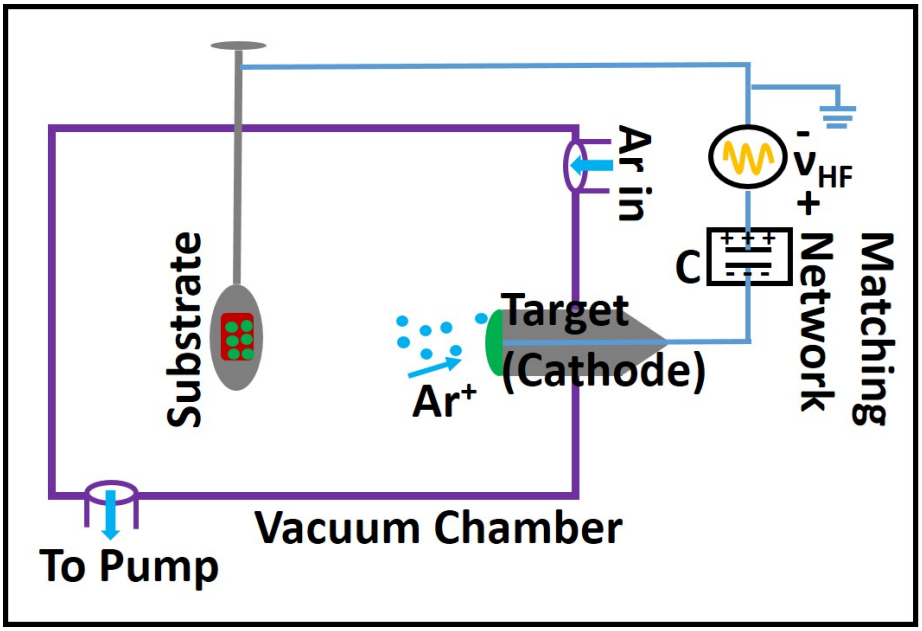

Figure 2.1: The schematic of RF Sputtering system for deposition of thin films.

In RF sputtering, there exists a cathode (representing the target) and an anode arranged in series, along with a blocking capacitor (C) incorporated into the circuit. This capacitor is an essential component of an impedance-matching network designed to facilitate effective power transfer from the RF source to the plasma discharge. The power supply is a high-voltage RF source typically operating at a fixed high frequency. The inclusion of the blocking capacitor C in the circuit is crucial for generating the pivotal DC self-bias, and a matching network is employed to optimize the transfer of power from the RF source to the plasma. RF sputtering offers distinct advantages over DC sputtering, notably enabling the sputtering of electrically insulating targets.

The following step-by-step process is taken care of depositing the rock salt thin films using the above RF sputtering system.

1. Target Material Selection: First, a desired solid target material for thin film deposition (MgO and NiO in this instance) is chosen and mounted in the chamber.

2. Vacuum Environment: The deposition process is accomplished within a high vacuum chamber to eliminate interference from air molecules.

3. Introduction of Inert Gas: An inert gas, such as argon, is introduced into the chamber, serving as the sputtering agent and contributing to the formation of a plasma.

4. RF Power Supply: Utilizing a radio-frequency power supply, a high-frequency electric field is generated within the chamber. This electric field ionizes the inert gas, leading to the creation of a plasma.

5. Ionization and Acceleration: The electric field propels positively charged ions from the plasma toward the target material. These accelerated ions collide with the target surface, sputtering atoms or molecules from the target.

6. Deposition on Substrate: The sputtered material from the target is deposited onto a nearby substrate at room temperature, forming a thin film.

RF sputtering offers advantages such as precise control over film thickness, uniform deposition, and the capability to deposit a diverse array of materials. Widely employed in the semiconductor industry, it plays a crucial role in fabricating various thin-film devices for both research and industrial applications.

2.1.3 Thermal annealing in PECVD

Following the RF sputtering deposition, the subsequent annealing of the thin films was conducted using the PECVD system, as illustrated in Fig. 2.2. The success of the annealing process relied on the following key components crucial for the vacuum heating of the deposited samples.

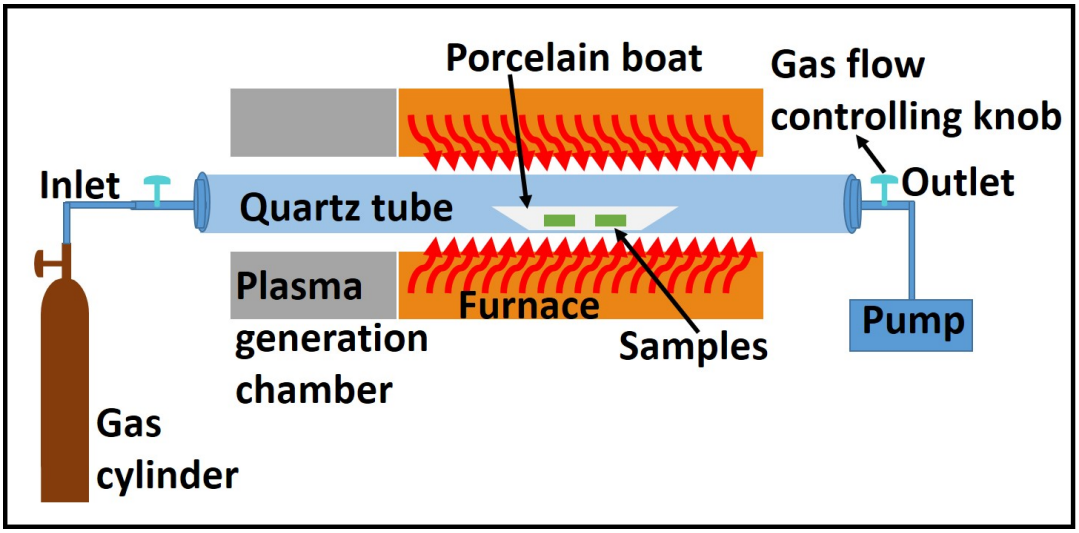

Figure 2.2: Schematic of PECVD setup for thermal annealing of the sputtered grown films.

1. **Reactor Chamber (Furnace):** The furnace serves as the primary vessel for the PECVD system, facilitating the annealing process. Its design allows the maintenance of the required temperature, pressure, and gas flow rates during both annealing and deposition.

2. **Heating System:** Attached to the furnace, the heating coil provides the necessary heat for sample annealing. The desired annealing temperature, in our case ranging from 300 to 500°C, is achieved and consistently maintained.

3. **Vacuum System:** A quartz tube, mounted through the plasma generation chamber and furnace, acts as a vacuum chamber. This tube accommodates a porcelain boat containing the samples. Connected to a gas cylinder at one end and a pump at the other, the tube facilitates the vacuuming environment of the samples. This vacuum chamber prevents unwanted external gases from outside to react with samples during annealing.

4. **Substrate Holder:** In this scenario, a porcelain boat serves as the sample holder, capable of withstanding high temperatures. Positioned centrally in the furnace, the boat ensures uniform sample heating.

5. **Gas Delivery System:** Gas cylinders linked to the gas delivery system play a vital

role in controlling the gas flow rate into the reactor chamber during operation. For vacuum annealing, N_2 gas is employed at a flow rate of 100 cc for purging the tube multiple times during vacuum, ensuring the removal of environmental reagents. Following purging, the gas flow controlling knob at the inlet side is tightly closed, preventing further gas flow, while the knob at the outlet side is left open for tube vacuuming.

6. Pressure Control System: Maintaining the chamber pressure is crucial during vacuum annealing to prevent unwanted reactions with the samples. The pressure is carefully regulated at approximately 10^{-2} mbar throughout the annealing process.

Upon completing the required annealing duration, the heating coil is turned off. The chamber is then left undisturbed, allowing it to cool naturally. After reaching room temperature, the chamber is opened, and the annealed samples are collected.

2.2 Ion Implantation

The low-energy ion implantation to create the damage in the rock salt thin films is accomplished by the low-energy ion beam facility at the Institute of Physics (IOP), Bhubaneswar, 3 MV tandem accelerator at IOP, Bhubaneswar, and low energy ion beam facility (LEIBF) at Inter-University of Accelerator Center (IUAC), New Delhi.

2.2.1 Tandem accelerator at IOP

The one MeV ion implantation experiment detailed in this thesis utilized a 3 MV Tandetron accelerator, as depicted in the schematic diagram (Fig. 2.3). The accelerator employs tandem acceleration, where ions undergo two stages of acceleration utilizing the same high voltage applied at the middle of the accelerating tube.

Negative ions generated by the ion source are initially accelerated by the high-voltage terminal at the middle of the tube. In a stripper canal filled with nitrogen gas, these negative ions are converted into positive ions. Subsequently, the positive ions are accelerated again

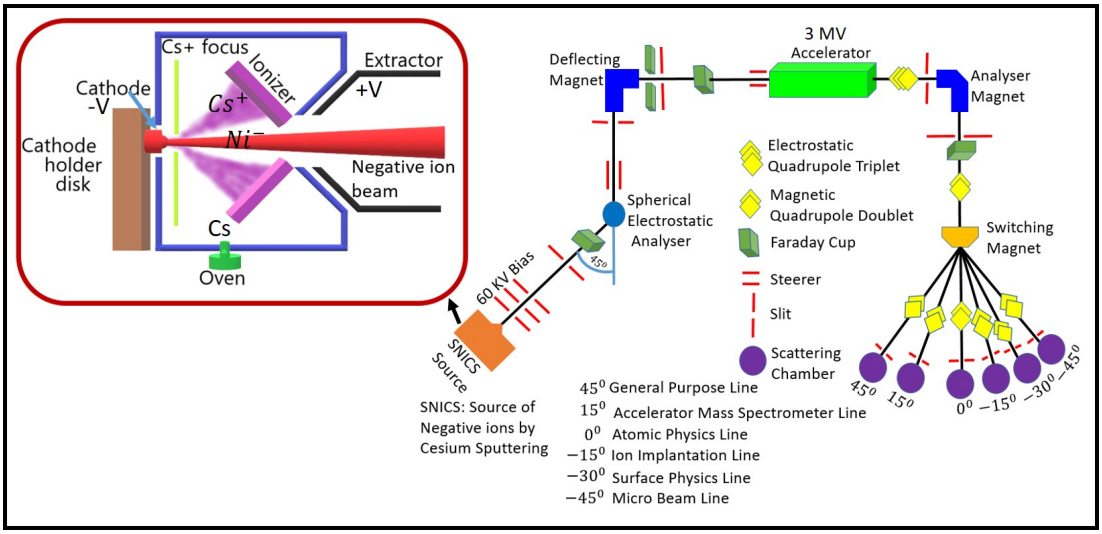

Figure 2.3: The diagram represents the tandem accelerator system for ion implantation used at IOP, Bhubaneswar. The components inside the red box represent the SNICS source.

by the same high voltage terminal towards ground potential. The maximum energy (E) of positive ions, transformed from negative ions with charge (q) and accelerated by a terminal voltage (V), is given by the equation E = V(1+q). This configuration offers the advantage of having both the ion injection system and the target at ground potential. The accelerator features two ion sources for beam injection: (i) a duoplasmatron ion source producing H^+ and He^+ ions, and (ii) a Source of negative ions by cesium sputtering (SNICS) sputter source capable of generating negative ions for almost all elements. A 90° mass analyzing magnet with a resolution of approximately 190 facilitates beam injection for both ion sources.

The entire accelerating structure is high-voltage insulated using a tank by enclosing it in a pressure vessel filled with SF6 gas at 6 kg/cm^2. A turbo-molecular pump, installed at the high voltage terminal, maintains an ultra-high vacuum of 10^{-7} mbar in the accelerating tubes and recirculates the stripper gas.

A Cockroft-Walton type solid-state power supply generates a high voltage in the range of 100 kV to 3 MV with high stability ($\pm$100 V). Accelerated ions undergo focusing by an electrostatic quadruple lens before a high-energy switching magnet analyzes the beam's

energy and directs it to experimental ports located at -15° angular positions.

At the -15° port of the switching magnet, an implantation beam line, equipped with a beam sweep system, neutral trap, beam profile monitor, and retractable slits for beam collimation, has been installed. Finally, an ultra-high vacuum-compatible chamber at the end of the beamline was used for one MeV ion implantation presented in this thesis.

2.2.2 Low Energy Implantation at IOP

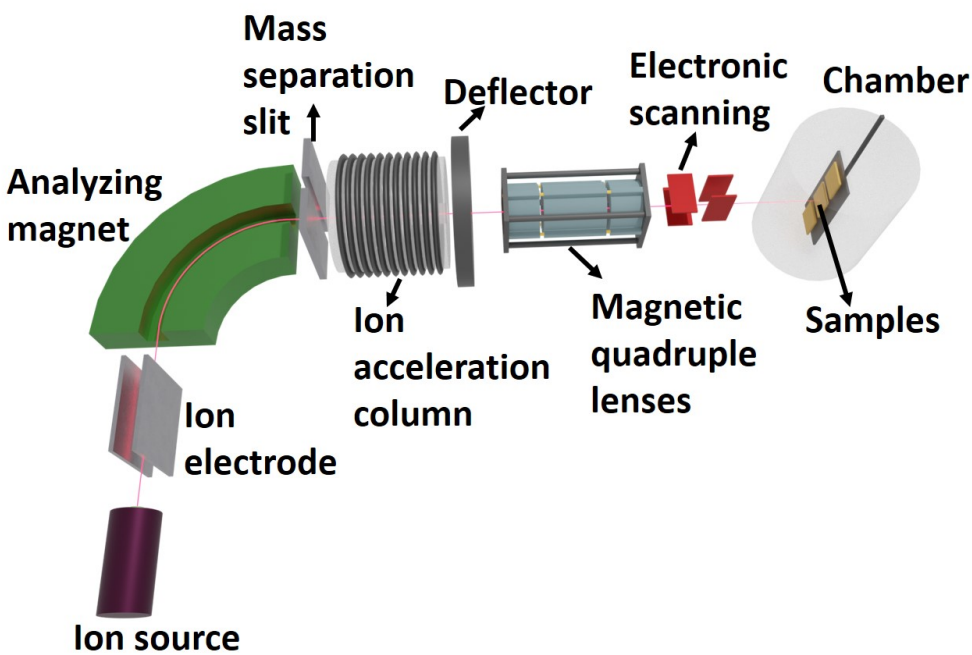

Figure 2.4: The schematic of low energy ion implantation system at IOP, Bhubaneswar.

The current thesis utilizes a low energy negative ion implanter facility, based on a Cs sputter source (SNICS-II, NEC, USA), established at IOP. This facility is employed for investigating keV ion-induced modifications of NiO thin films. Typically, such an implanter comprises an ion source for generating the necessary ions, an acceleration stage to increase their energy, and a mass/energy selector for choosing ions with specific characteristics. Additionally, the system includes components for beam steering, focusing, and monitor-

ing. Ensuring uniform implantation over an area larger than the beam size necessitates a beam-scanning arrangement. Implantation experiments are conducted in a high vacuum chamber (approximately 10^{-7} mbar) equipped with facilities for sample manipulation and current measurements. A visual depiction of the low-energy negative ion implanter is presented in Fig. 2.4. In contrast to most ion implanters that deliver energetic positive ions, this facility specializes in providing negative ions at energies of a few tens of keV. Negative ion implantation offers the advantage of nearly charge-free implantation into isolated electrodes and insulators. Unlike positive ion implantation, which often necessitates external charge compensation to mitigate sample charge-up issues, negative ion implantation effectively addresses this problem. The technique minimizes surface charging concerns by balancing the incoming negative charge of implanted ions with the outgoing negative charge of secondary electrons. Consequently, surface charging voltage remains relatively stable, typically within $\pm$ 10 V for isolated conductive materials and insulators, and is devoid of spatial and temporal fluctuations. Although differences exist between negative- and positive-ion implantations concerning beam transport and secondary electron emission factors, projected ion ranges in the target show little disparity.

2.2.3 LEIBF at IUAC

The LEIBF at the IUAC is designed to generate multiple charged ions spanning a wide range of energies, from tens of keV to a few MeV, catering to experiments in atomic, molecular, and materials science. Figure 2.5 provides a schematic diagram of the LEIBF at IUAC. The facility features a 10 GHz Nanogun-type Electron Cyclotron Resonance (ECR)-based ion source installed on a high voltage deck to produce positively charged ions [1, 2].

The ion source, along with all other components of the implanter, including a high-power ultra-high-frequency transmitter, power supplies for the extractor, and einzel lens, are positioned on the high voltage deck, controlled through optical fiber communication.

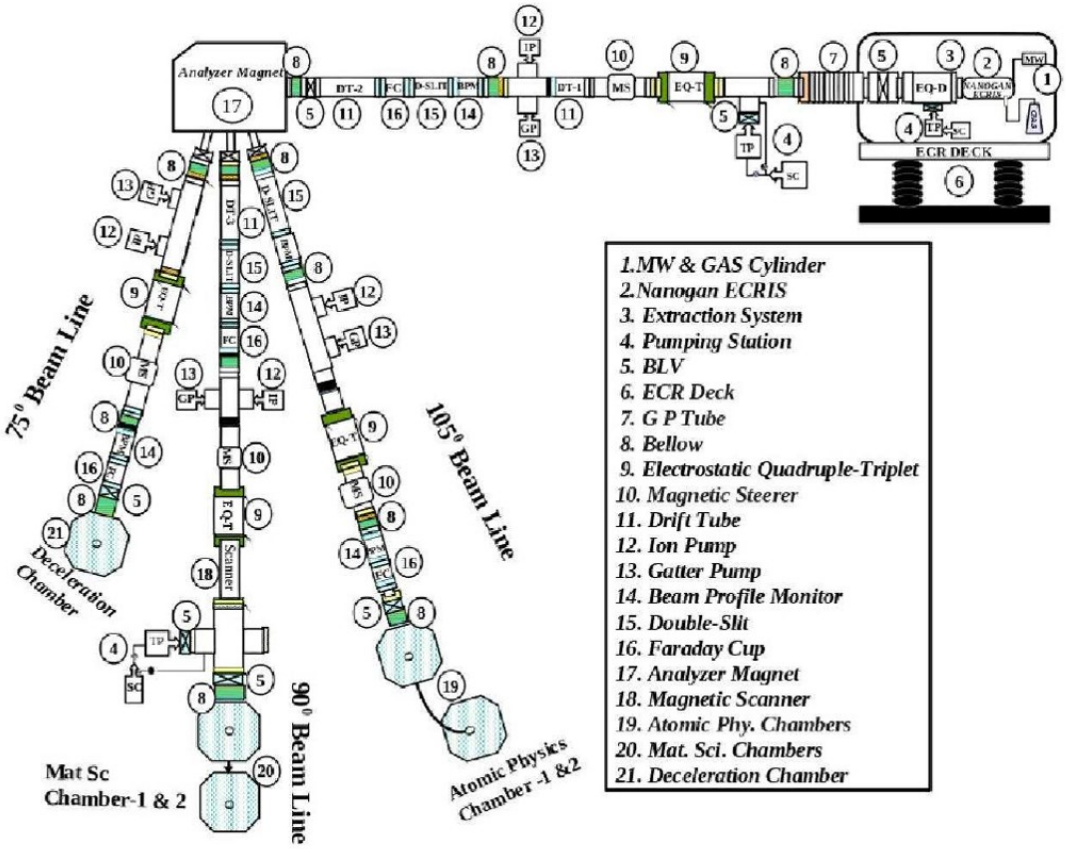

Figure 2.5: The schematic of LEIBF system for low energy ion implantation, at IUAC, Delhi [1].

The voltage differential between the high potential deck and the ground, distributed over the accelerating tube to the beamline end, imparts the necessary kinetic energy to the ions. Vacuum levels inside the ion source chamber, extraction chamber, and accelerating tube are maintained below 10^{-6} mbar by a pumping station comprising a turbo pump backed by a rotary pump.

An electrostatic steerer is employed to adjust the beam, while double slits control the beam size. A beam profile monitor determines the distribution of ions in the x- and y-directions within the ion beam. Ion selection is achieved using a mass analyzer with the application of a specific magnetic field. An electric quadrupole triplet is utilized to focus

the ions onto the sample surface. During beam tuning, the ion beam is focused into a fine circular spot. Subsequently, the beam is electrostatically scanned over the sample area using a beam scanner, ensuring homogeneous implantation.

Samples are mounted on a copper ladder to facilitate efficient heat dissipation generated during the impingement of the ion beam on the sample [1]. In the current thesis, implantation involving 100 keV Cu ions on NiO thin films, with ion fluences up to 2×10^{16} ions/cm^2, was conducted using this ion source at room temperature.

2.3 RRAM device fabrication

The annealed and ion-implanted samples are used for resistive switching measurements.

2.3.1 RRAM device

The RRAM device is constructed by sandwiching the rock salt oxide film between the top and bottom electrodes. We used Si and ITO substrates (upon which the film was grown) as the bottom electrode. After the consequent annealing and implanting (according to requirement) of the samples, the top electrode was grown on the film. We chose Au and Ag as the top electrodes. Au electrode is accomplished using the thermal evaporation technique, while the Ag electrode is achieved by conducting Ag paste. The schematic of the RRAM device is shown in Fig. 2.6.

Thermal Evaporation Technique:

Thermal evaporation is a type of physical vapor deposition (PVD) method employed to deposit thin films. In this process, materials are deposited onto a substrate by heating the material source until it reaches its vaporization temperature. The vaporized or sublimated material then condenses onto the substrate, forming a thin film. This technique finds widespread application across various industries, including electronics, optics, and materi-

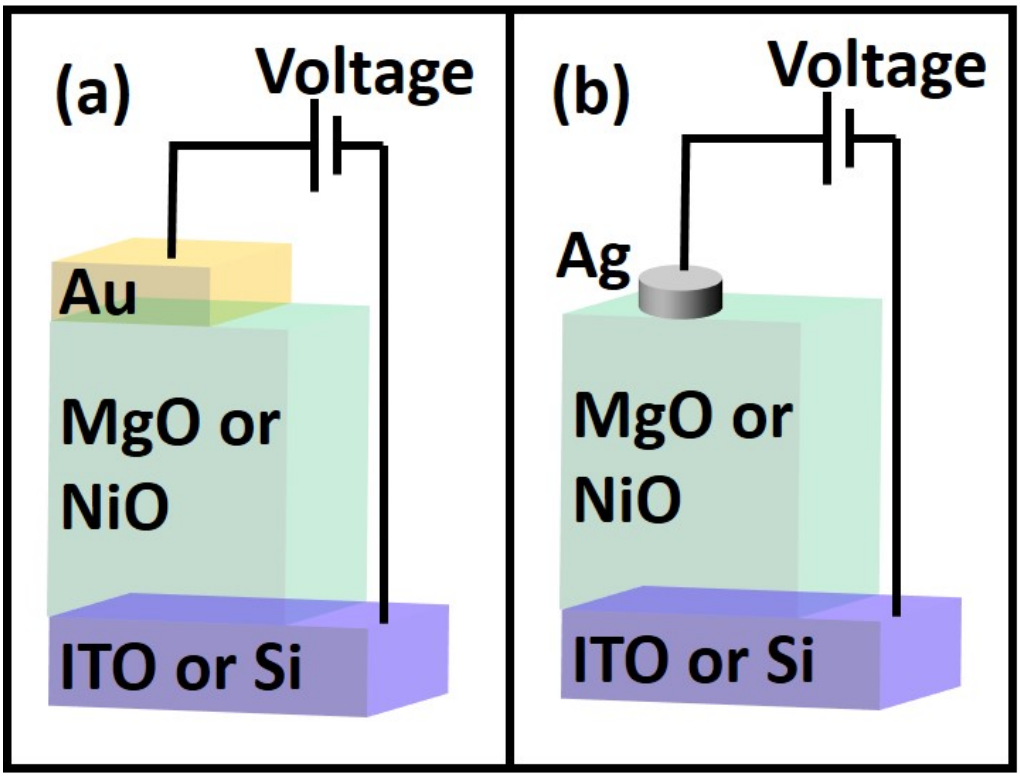

Figure 2.6: The schematic of RRAM with top (a) Au and (b) Ag electrode associated devices.

als science. Here's an overview of the thermal evaporation process: The material intended for deposition is kept on the thermal evaporation pocket. After that, the high vacuum of the depositing chamber is achieved by the combination of rotary and turbo molecular pumps to eliminate the interference of air molecules and prevent contamination for depositing high-purity film. After achieving the required vacuum, the high current passing through the sources undergoes heating of the material. Once the material attains its vaporization temperature, it transforms into a vapor or gas phase. Then, the evaporated material condenses onto the surface of the substrate, giving rise to form a thin film. The deposition of the film thickness at a slow rate is controlled by a thickness control monitor associated with quartz crystal. The substrate holder was rotated slowly at 20 rpm for uniform film growth. Following the completion of the deposition, the substrate and the newly formed thin film are

cooled down to room temperature to prevent the stresses in the film.

2.4 Characterization techniques

2.4.1 Field emission scanning electron microscopy

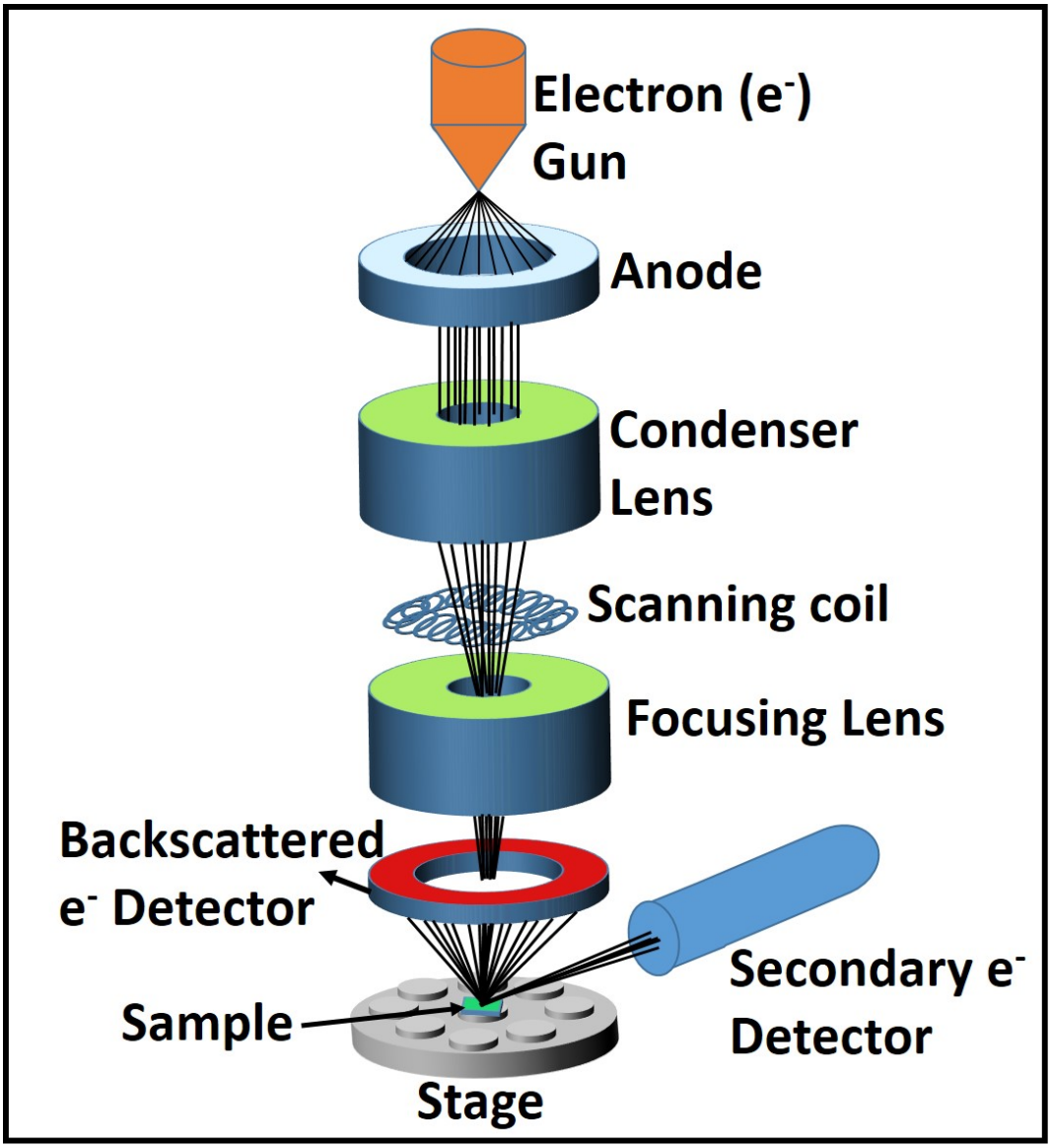

Figure 2.7: The schematic of FESEM system

Scanning Electron Microscopy (SEM) is a widely utilized technique for studying the

surface morphology and topography of samples [3]. In the current study, the morphology of the thin films was investigated using a Field Emission Scanning Electron Microscopy (FESEM) (Carl-Zeiss Sigma model) system. Figure 2.7 illustrates a schematic diagram outlining the typical construction of a FESEM. In FESEM, an energetic beam of electrons is directed at the sample, leading to various interactions that result in the emission of secondary electrons, back-scattered electrons, Auger electrons, transmitted electrons, X-rays, and more. The emissions arising from these interactions are collected by the specialized detectors incorporated into the system. The selection of appropriate detector signals allows for the gathering of specific information from the samples. The electron gun responsible for generating the electron stream can be categorized into two types: thermionic electron gun and field emission electron gun. Our system is associated with a field emission electron gun where the thermionic emission occurs from the electrically heated filament (usually tungsten or lanthanum hexaboride). However, due to the various limitations of thermionic sources, including low spatial resolution, brightness, and high-temperature requirements, in modern SEM systems, Field Emission (FE) guns are employed. FESEM offers several advantages to overcome these limitations. The process involves accelerating electrons by applying an extraction voltage to the anode. The electron gun produces a divergent beam, which is then converged using the condenser lens. Subsequently, the focusing lens further focuses the beams. The vacuum level within the chamber column is maintained in the range of 5×10^{-5} mbar to approximately 10^{-6} mbar, while the electron gun is kept at a vacuum level of $\approx 2 \times 10^{-9}$ mbar. When conducting secondary electron imaging in FESEM, the in-lens detector plays a crucial role by capturing low-energy secondary electrons emitted from the top few nanometers of the sample surface. This process yields intricate details about the surface morphology. To improve image quality and sensitivity, the in-lens detector amplifies the detected signals. Subsequently, the amplified signals undergo processing to produce a high-resolution image of the sample surface. The resulting image exhibits the

topographical information, unveiling nanoscale surface features and structures.

2.4.2 Atomic Force Microscope

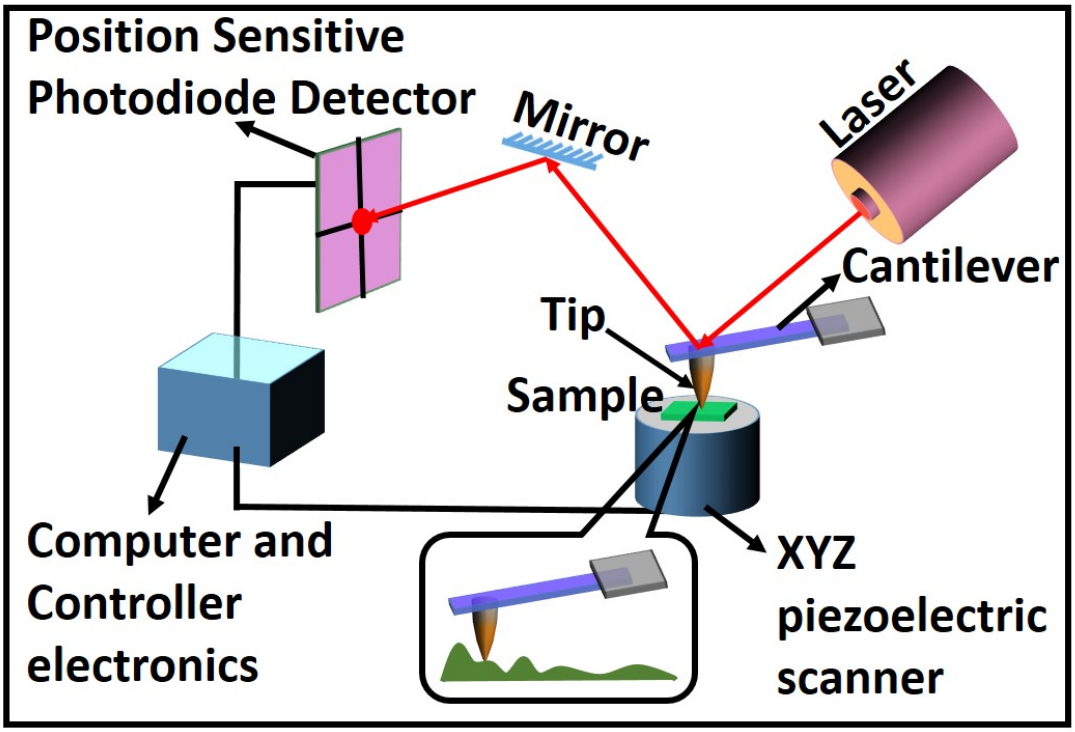

Figure 2.8: The schematic of AFM system for investigating the surface morphology of the thin films.

In the current research, the surface morphology investigations were also conducted using an AFM system (Fig. 2.8) equipped with Nanoscope IIIa from Bruker, featuring quadrature capabilities. All 2D and 3D morphology images of the surface of thin films presented in this thesis were obtained in tapping mode. The analysis was carried out using the Nanoscope software. In tapping mode, the cantilever undergoes oscillation near its resonance frequency, akin to the non-contact mode. However, the amplitude of this oscillation is notably larger, typically ranging from 100 to 200 nm. As the tip approaches the surface, various forces such as Van der Waals, dipole-dipole, and electrostatic forces between the atoms of the tip and the sample can alter the cantilever's vibration amplitude. In this

mode, the surface is scanned with a constant reduction in oscillation amplitude instead of maintaining constant deflection. Consequently, during the scan, no physical contact is established between the tip and the surface. The recorded feedback amplitude and the vertical adjustments of the piezo scanner serve as the basis for generating a height image.

2.4.3 X-ray diffraction

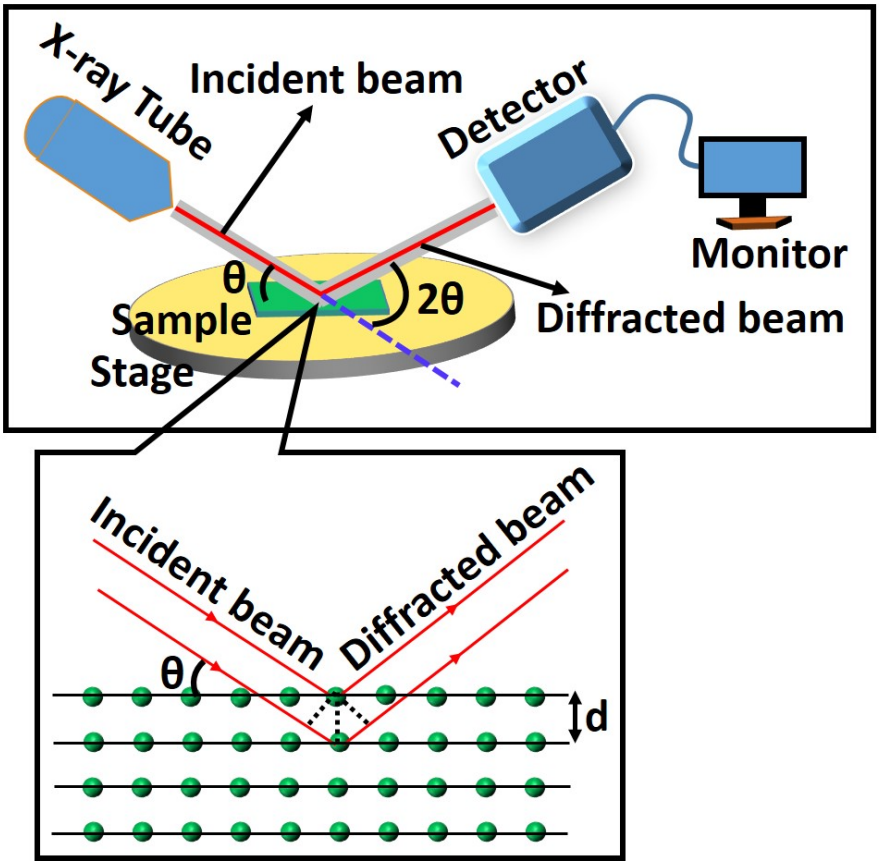

Figure 2.9: The schematic of XRD system with a zoomed view of the Bragg's reflection from a periodic lattice.

The study of crystal structure and phase identification of the materials is usually carried out through the popular and well-established XRD technique [4]. The schematic of the Rigaku Smartlab XRD system is presented in Fig. 2.9. The Cu K_α source in the X-ray tube

generates X-ray having a wavelength of 1.54 Å. The χ-ϕ stage was used for mounting the samples. The target materials are irradiated by the monochromatic parallel beam of X-rays. Subsequently, the diffracted beams produced after the scattering from the lattice atom of the materials are collected by the detector. The constructive interference of the scattered beam is satisfied when the path difference of beams coming from two adjacent planes is an integer multiple of incident wavelength (λ). The condition of Bragg's law for constructive interference is as follows,

$$2d\sin\theta = n\lambda$$

Where, n is an integer number, d = the distance between the atomic planes. θ-2θ, and grazing angle, etc modes are available in the XRD system. In this thesis, we employed θ-2θ, and grazing angle according to the different sample's requirements for getting the constructive diffraction to identify the single or multiple phases of the materials.

2.4.4 Ultraviolet-visible near-infrared spectroscopy

UV-Vis spectroscopy stands as a pivotal technique for characterizing the optical properties of materials, offering valuable insights into electronic transitions within molecular levels. The absorption of visible and ultraviolet light by the materials when electromagnetic radiation falls on them, resulting in the absorption, reflection, and transmission of light depending on the nature of materials [5]. This method gauges the attenuation of radiation as it traverses a sample, where the absorption is influenced by electronic transitions between different molecular levels within the material. The wavelength of maximum absorption and the degree of absorption yield crucial details about the molecule's structure and the concentration of the absorbing species, respectively. The principles governing absorption are encapsulated in two laws: Beer's and Lambert's Law. The combination of Beer's and Lambert's laws results in the formulation of the 'Beer-Lambert Law' [6], expressed as:

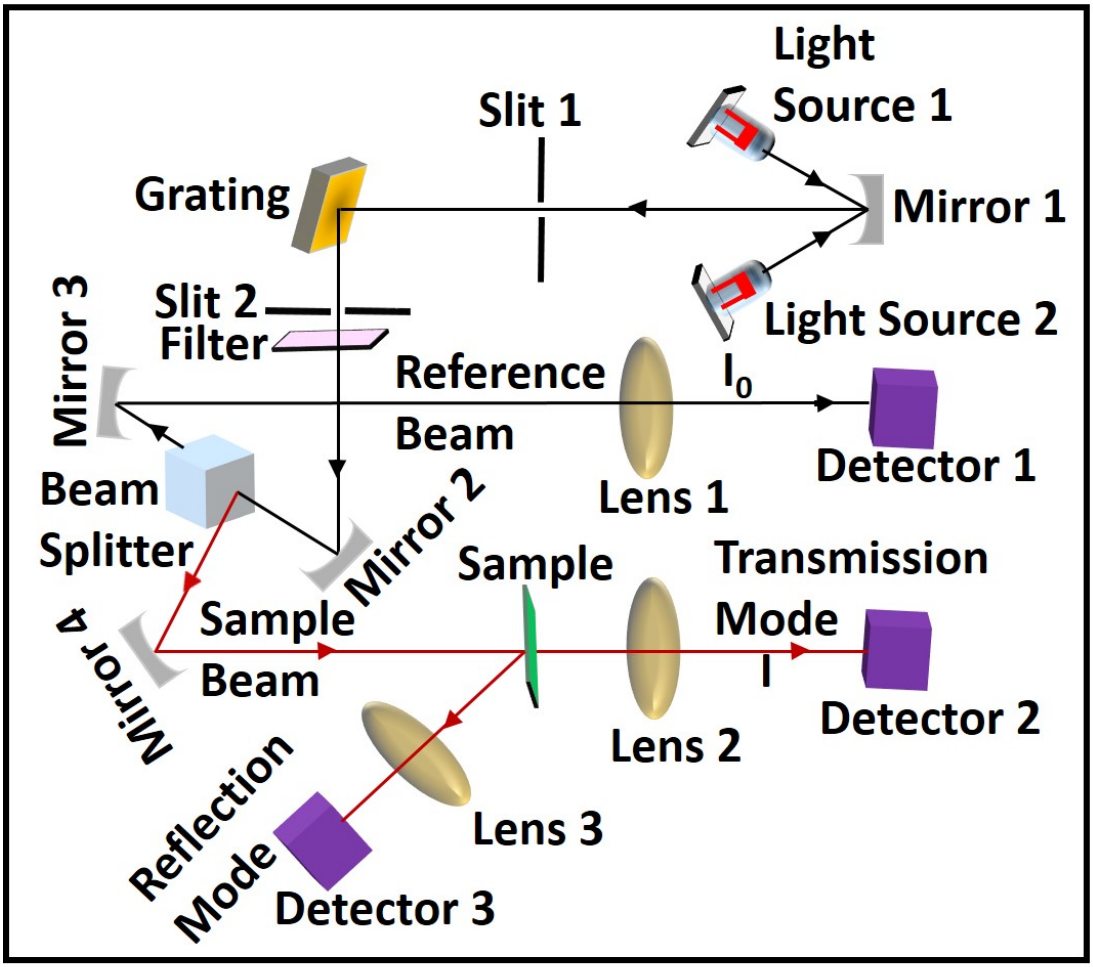

Figure 2.10: The schematic of UV-Visible setup.

$$A = log_{10}(\frac{I_0}{I}) = \alpha \cdot l \tag{2.1}$$

Here, A represents absorbance, l is the thickness of the substance, and α is the absorption coefficient of the material. I_0 is the irradiated light intensity, and I is the radiation intensity after traversing the substance. Now, if the sample is transparent, $R \approx 0$, and $A = \log_{10}(I_0/I)$ and $T = I/I_0$; and for an opaque sample $T \approx 0$, $A = \log_{10}(I_0/I)$ and $R = I/I_0$.

The UV-visible spectra taken in this thesis are achieved using the Agilent Carry-5000

UV-VIS-NIR spectrometer. Figure 2.10 provides a visual representation of the UV-Vis spectrometer setup employed in this research, showcasing its ability to operate in both UV and visible regions. The UV-visible spectrophotometer employed in measuring the photo-absorption spectrum utilizes two light sources: a deuterium arc discharge lamp for UV measurements and a tungsten lamp for visible region measurements. The system seamlessly switches between the two lamps automatically. The instrument's design and optical components are optimized for efficient stray light rejection. A beam splitter divides the incident light into two beams, one passing through the sample and the other through the reference cell. The detector captures the signal difference across all wavelengths, providing the absorbance spectrum.

2.4.5 Photoluminescence spectroscopy

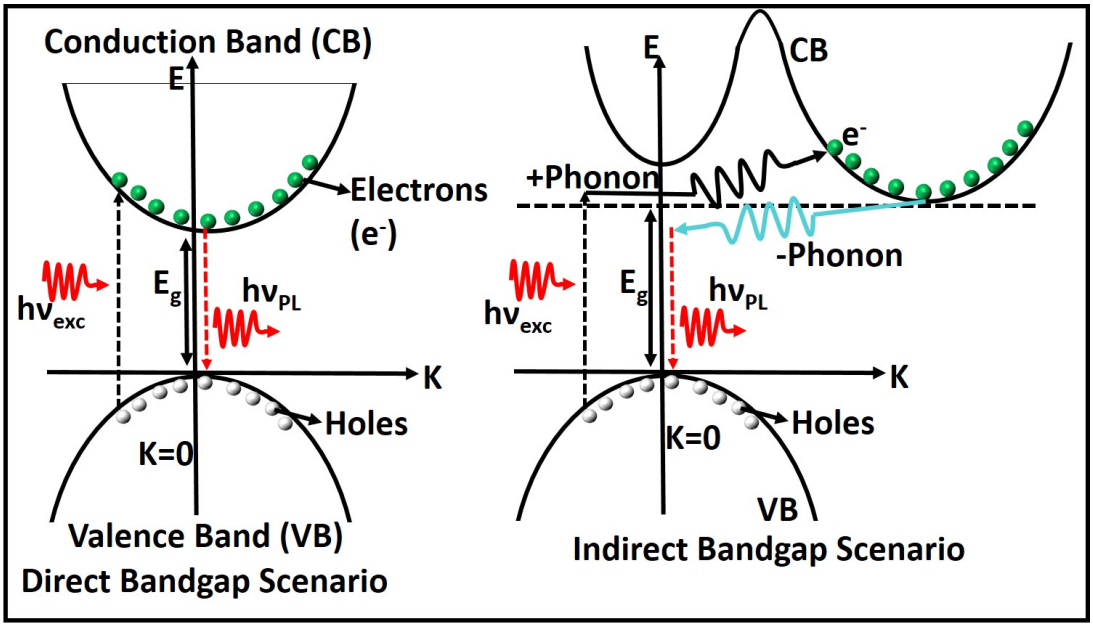

Figure 2.11: The schematic of PL emission for direct and indirect bandgap materials.

Photoluminescence (PL) stands out as a useful and non-destructive spectroscopic method employed extensively to investigate the optical properties of the materials. Additionally,

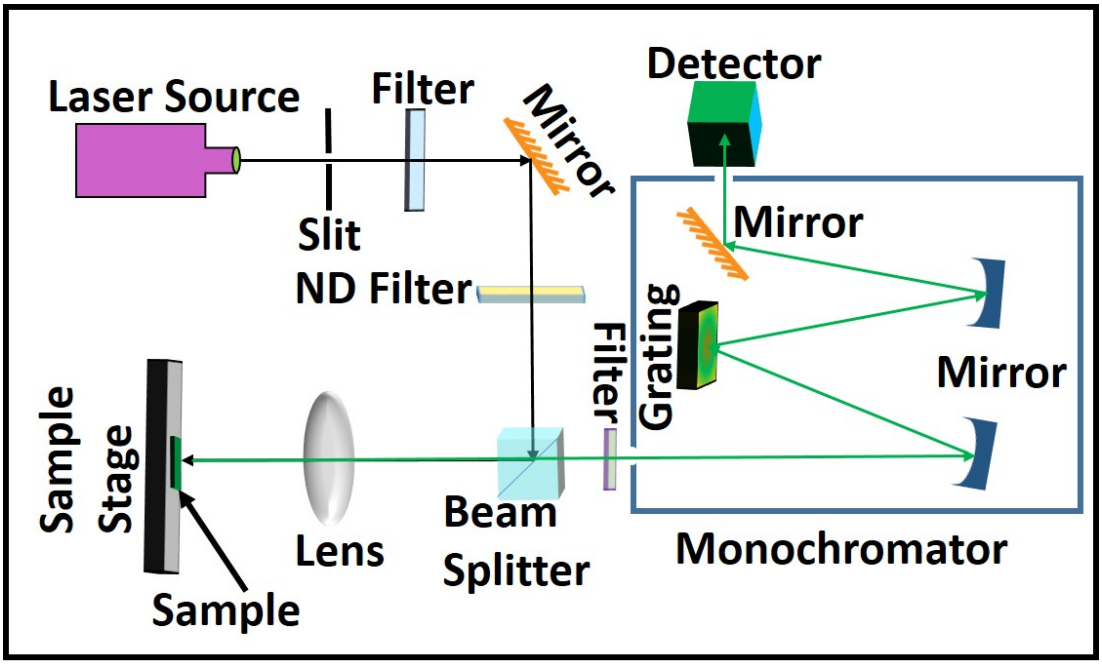

Figure 2.12: The schematic of PL setup.

it serves as a valuable tool for monitoring impurity or defect levels within a material. PL refers to the irradiation of energetic light on the material for photo excitation and subsequent de-excitation for the radiative emission of light. The excitation of the material is usually done using a monochromatic laser source with photon energy greater than or equal to the bandgap. The excitation of electrons from the VB to CB through laser light leaves a hole in the VB. These electron-hole pairs undergo rapid thermalization, establishing a quasi-equilibrium distribution. Ultimately, recombination of electron-hole occurs, resulting the emission of radiative photon, which is detected as photoluminescence. The entire process spans a time period ranging from femtoseconds to milliseconds. The recombination of electron-hole pairs for direct and indirect bandgap materials are presented in Fig. 2.11. In an indirect band gap material, for radiative recombination to take place, the process necessitates the absorption or emission of a phonon. This phonon must possess a momentum equal to the difference between the momentum of the electron and the hole. The PL peak

position allows for the estimation of the band gap energy, while the peak intensity contributes to the relative rates of radiative and non-radiative recombination processes. The excitation of electrons from the impurities and native defect states to CB and subsequent de-excitation within the material provides the PL emission of defect levels. The schematic of the PL setup is shown in Fig. 2.12. The instrument comprises an excitation source, typically a laser, a spectrometer, and a detector. In this thesis, all the PL measurements are acquired at room temperature. We used a He-Cd laser as the optical excitation source, which has a wavelength of 325 nm. The PL measurements were accomplished using the Horiba Jobin Yvon triple system equipped with a monochromator to resolve the spectra and detected using the UV-sensitive charged coupled detector (CCD).

2.4.6 Cathodoluminescence

Cathodoluminescence (CL) refers to the characteristic emission of photons from a material when subjected to an incident of high-energy electron [7]. Notably, the energy of the incident primary electrons exceeds the threshold required for the direct excitation of electrons. Instead, a cascade of scattering events by the primary electron irradiation generates secondary electrons, Auger electrons, and X-rays. This cascade effect can lead to the excitation of electrons from the VB to the CB. Subsequent relaxation of these electrons back to the VB results in the emission of photons with corresponding energy. During this process, electrons may undergo a temporary trapped state, lasting for microseconds, facilitated by intrinsic or extrinsic defects. The associated transition of photons will exhibit reduced energy due to the loose of energy by electrons during vacating the traps. One notable advantage of CL is that the incident electron energy is not constrained by the bandgap of the material under investigation. In this study, a Monarc CL Detector (Gatan Inc.) was utilized which is integrated with a FESEM system. The schematic mirror arrangement of the CL setup for collecting the emission is depicted in Fig. 2.13. The attached spectrograph resolved the

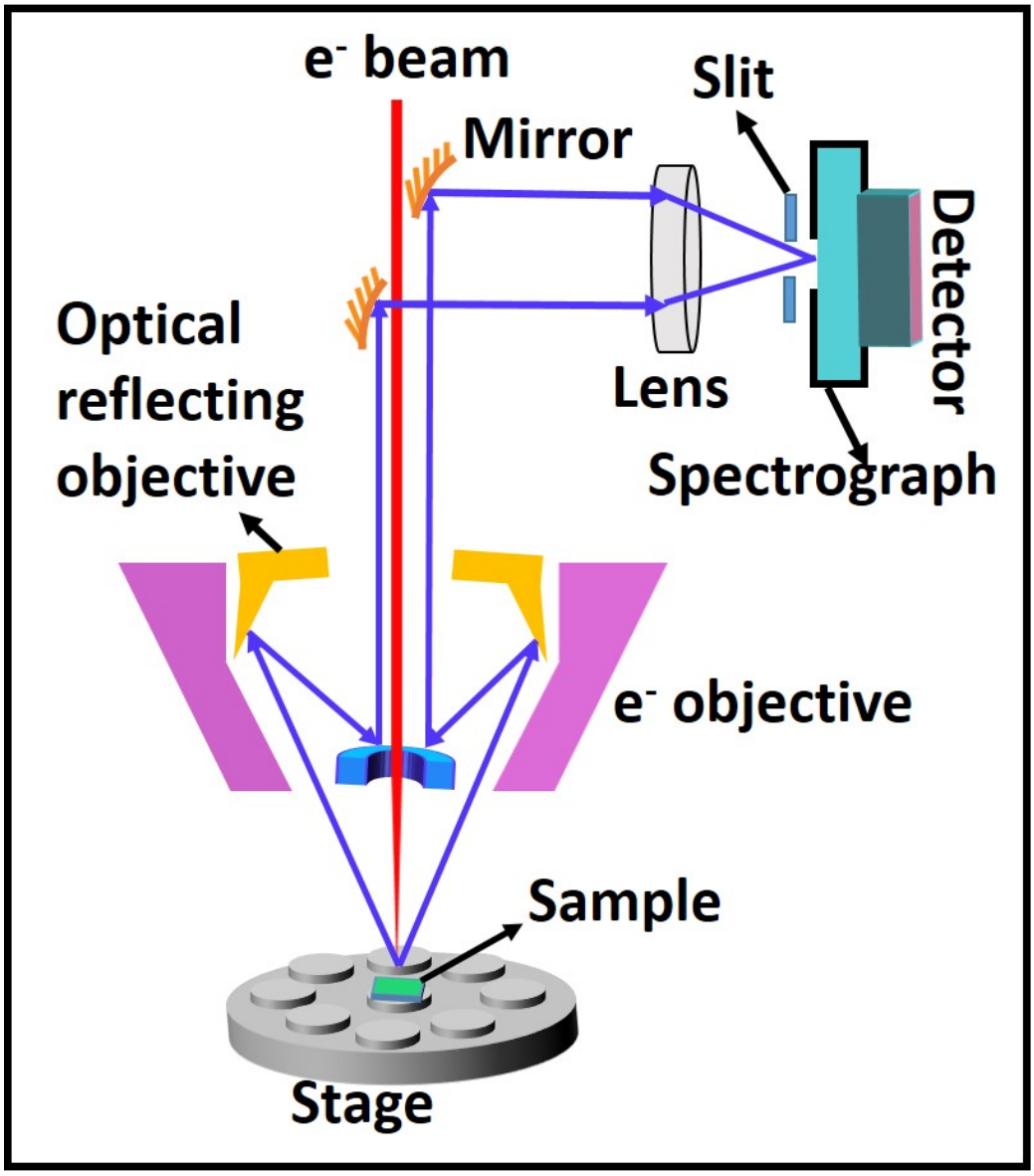

Figure 2.13: The schematic of CL setup

emitted spectra and then detected using a detector coupled to the spectrograph.

2.4.7 Raman spectroscopy

Raman spectroscopy is a versatile and non-destructive spectroscopic technique which describes the inelastic scattering of light with matter. This method offers several distinct

advantages, including simple operation, easy sample preparation, and the ability to conduct experiments under normal ambient conditions. Raman spectroscopy is widely utilized to examine the vibrational and rotational modes of molecules, composition, phase, and crystallinity of the materials. When a molecule absorbs photons, it is promoted to a virtual state from its ground electronic state, as illustrated in Fig. 2.14. Typically, after elastic scattering, the molecule de-excited and returned back to its ground state by emitting photons with the same frequency as the incident photons, known as Rayleigh scattering. In contrast, for the inelastic scattering process, the observed frequency difference between the incident and scattered photons arises when the molecule comes back into a different vibrational level rather than the ground state, known as the Raman shift. This shift, being an intrinsic property of the molecule of the materials, is independent of the excitation frequency. The probability of the Raman scattering is minuscule compared to incident photons (≈ 1 in 10^7), resulting in a weak intensity of the Raman shift compared to the Rayleigh shift. Two types of Raman scattering are observed: Stokes scattering, where the scattered photons are shifted to longer wavelengths region, and the shifting due to anti-Stokes scattering occurs towards shorter wavelengths. The schematic diagram in Figure 2.14 illustrates the three scattering processes: Rayleigh, Stokes, and anti-Stokes Raman scattering. In Raman spectra, the intensity of scattered light is plotted against the Raman shift (in terms of wave number). The Rayleigh peak is typically cut off from the spectrum to observe Raman peaks. In this thesis, Raman spectra are taken at room temperature using the Horiba Jobin Yvon LabRam HR Evolution system coupled with a CCD detector. The excitation source used for Raman scattering was a 532 nm green diode laser.

2.4.8 Fourier Transform Infrared (FTIR) spectroscopy

The Fourier Transform Infrared (FTIR) spectrometer is a powerful analytical tool used in various scientific fields for the qualitative and quantitative analysis of materials based on

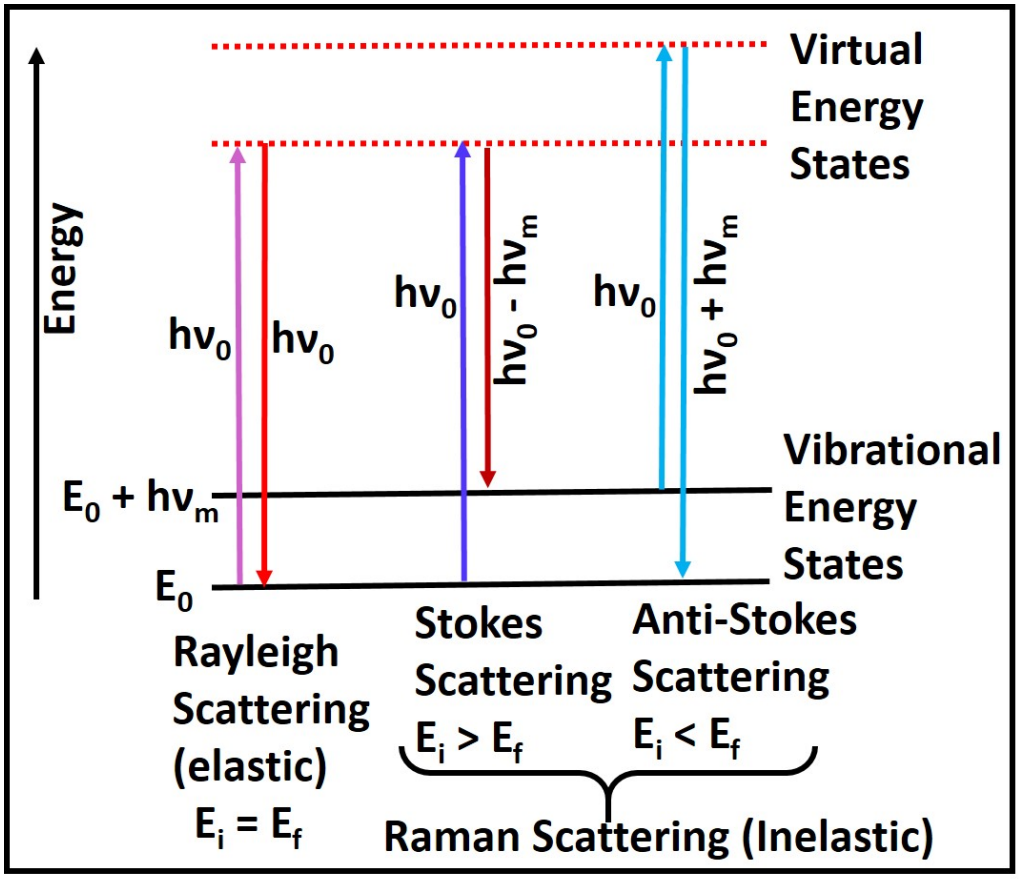

Figure 2.14: The schematic represents the energy level diagram in Raman scattering.

their infrared absorption properties. Its working principle relies on the interaction between infrared radiation and the sample being analyzed. Attenuated Total Reflection (ATR) is an integral component of Fourier Transform Infrared (FTIR) spectrometers, enhancing their capabilities for material analysis. In ATR-FTIR spectroscopy, as shown in Fig. 2.15, infrared (IR) radiation is directed into a sample through an internal reflection element (IRE) made of a material with a high refractive index, such as diamond or zinc selenide. The IR radiation undergoes multiple total internal reflections within the IRE, creating an evanescent wave that extends into the sample. As the evanescent wave interacts with the sample, it undergoes attenuated total reflection, resulting in the absorption of specific wavelengths of IR light by the sample. By measuring the intensity of the attenuated radiation using a de-

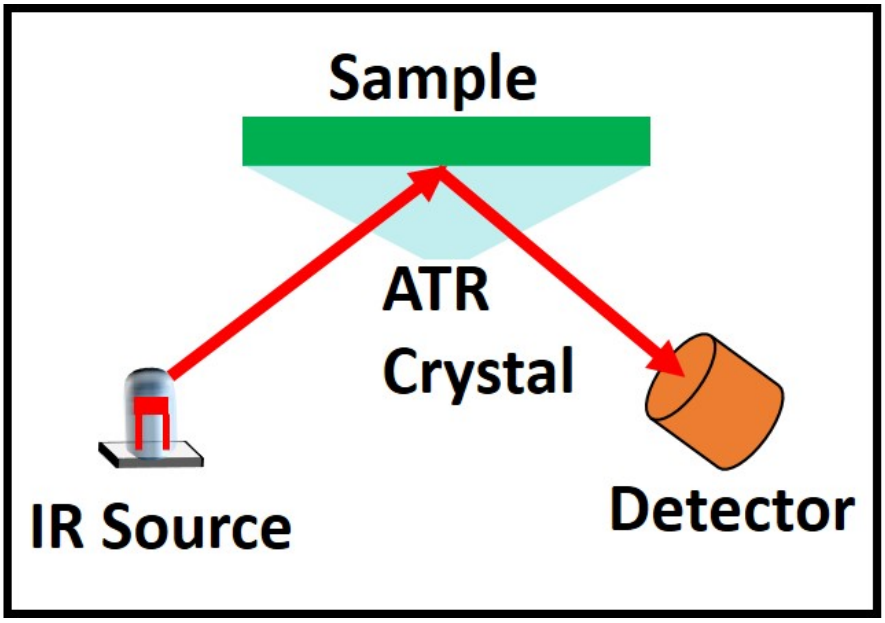

Figure 2.15: The schematic diagram of ATR-FTIR system.

tector, valuable information about the sample's chemical composition, molecular structure, and surface properties can be obtained without the need for extensive sample preparation. ATR-FTIR spectroscopy finds applications in fields such as materials science, pharmaceuticals, forensics, and environmental analysis.

2.4.9 Superconducting quantum interference device (SQUID)

SQUID serves as an exceptionally sensitive magnetometer utilized for the precise measurement of extremely subtle magnetic fields, relying on superconducting loops incorporating Josephson junctions. The following six essential components are the core of the SQUID system:

1. Temperature Control System
2. Magnetic Field Control System
3. Motion Control System
4. SQUID Detection System

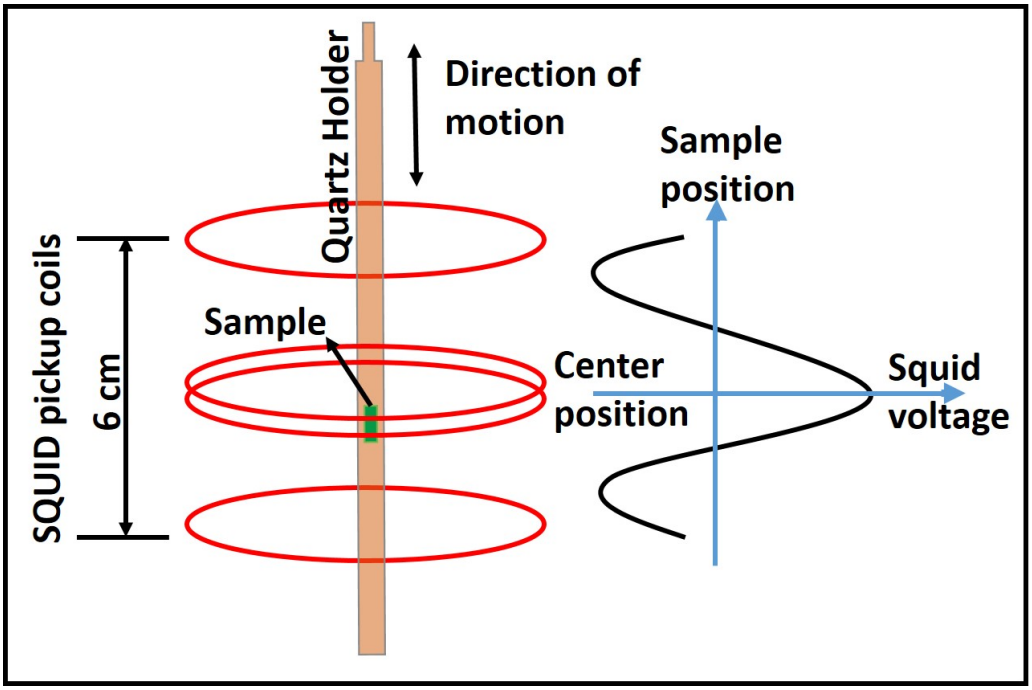

Figure 2.16: The schematic of detection coils used in SQUID.

5. Chamber Atmosphere Control System

6. Cryogen Monitoring System

Liquid helium is required in the SQUID system to cool the superconducting Niobium Titanium (NbTi) solenoid. The solenoid provides the magnetic field to the instrument. Liquid helium also cools the many associated components, such as superconducting electrical leads, quick switches, superconducting quantum interference devices, magnetic shields, detection coils, etc. The sensitivity to magnetic moments is facilitated by the superconducting quantum interference device. The SQUID detection system comprises superconducting detection coils inductively coupled to a magnetically shielded SQUID, as shown in Fig. 2.16. During standard measurements, the sample is positioned at the center of the detection coils using a quartz holder. During centering, the movement of the sample is controlled using the motion control system inside the detection coils with the help of a Vibrating Sample Magnetometer (VSM). Magnetic measurements in the presented thesis were conducted us-

ing the Quantum Design SQUID VSM system [8], sweeping in a temperature range of 5 K to 300 K and a magnetic field range of -3 to +3 kOe, with a sensitivity of moment of 10^{-8} emu.

2.4.10 Z-scan technique

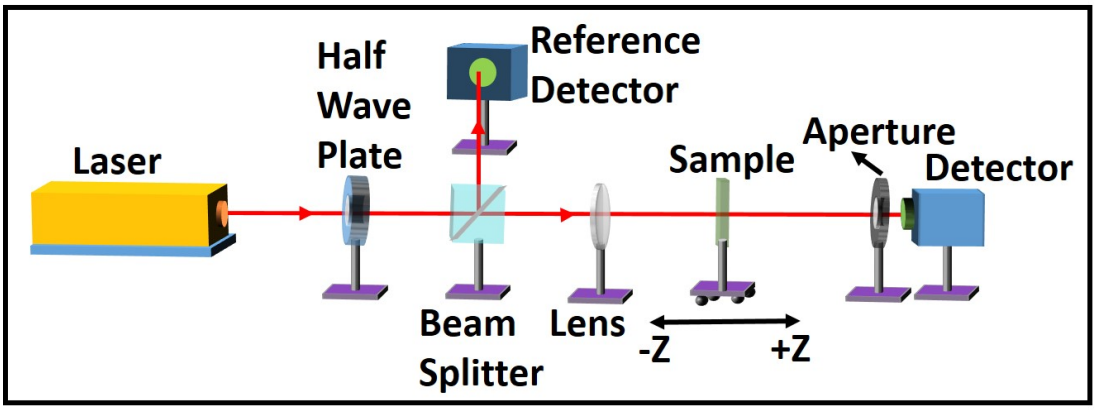

Figure 2.17: The schematic of Z-scan setup.

The non-linear optical properties, such as nonlinear absorption and nonlinear refractive index, are estimated utilizing the z-scan technique [9]. The schematic diagram of the z-scan setup is depicted in Fig. 2.17. In this method, the sample is irradiated by the laser source, which has a Gaussian beam profile. The laser light passes through the transmitted samples. During the measurements, the samples are translated from -z to +z direction using the motorized translation stage around the focal plane (z = 0) of the converging lens. In open aperture conditions, the aperture is completely removed or significantly enlarged in front of the detector, ensuring that the entire transmitted light reaches the detector. Any variations observed in the transmitted light are attributed to the nonlinear absorption coefficient (β). Conversely, in the closed aperture conditions, a small aperture is kept in front of the detector, permitting only the central region of the transmitted light to reach the detector. The tiny variation in transmitted light indicates the material's nonlinear refraction (n_2).

2.4.11 Tera-Hertz Time Domain Spectroscopy technique

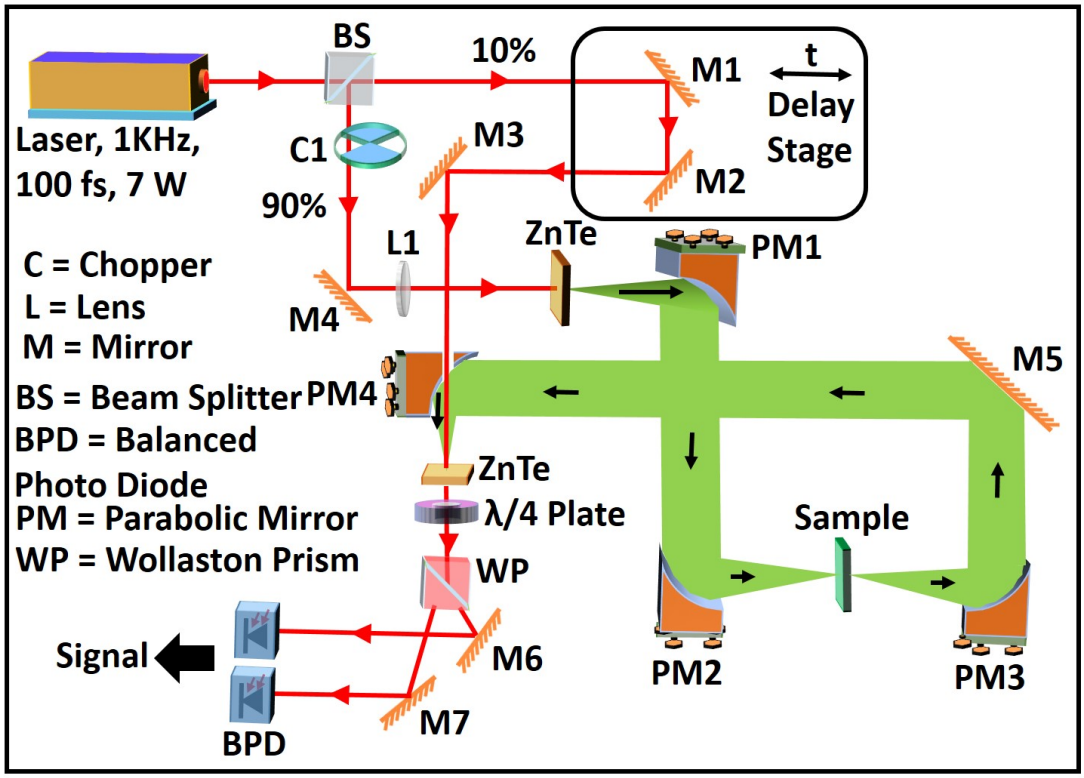

Figure 2.18: The schematic of Tera Hertz setup.

The THz technique is extensively employed for examining various material properties, such as optical transmission, optical conductivity, and scattering, within the THz time domain [10]. The schematic representation of the THz setup is depicted in Fig. 2.18. Ti:Sapphire laser source was used in this study. The laser output from the laser source with a repetition rate of 1 KHz (pulse width = 100 fs, wavelength = 800 nm, energy = 7mJ/pulse) is divided into two parts using a beam splitter. 10% of the beam passes through a delay stage (used as a gating pulse) while the major part (90%) traverses the 0.5 mm thick ZnTe crystal (110-cut) to generate a THz signal via optical rectification. The generated THz signal is then directed onto the sample. Since the THz signal can transmit through our sample, a transmission setup was employed to observe the THz transmittance characteristics in the THz

time-domain spectroscopy. The transmitted signal and gating pulse are then co-propagated through another optically active ZnTe detection crystal (110-cut, thickness = 0.5 mm). The optically inactive ZnTe crystal (100-cut, 2 mm thickness) was bonded optically with the detection crystal to increase the thickness. This modification causes a temporal shift in the Fabry-Perot fringes originating from the crystal thickness. The THz pulse induces birefringence, resulting in ellipticity in the co-propagating sampling beam. The $\lambda/4$ waveplate, Wollaston prism, and a balanced photodiode were utilized to analyze the co-propagating sampling beam. The Si/SiO_2 substrate was used for the reference measurement. All the measurements were done at room temperature.

2.4.12 Basics of Density Functional Theory

Density Functional Theory (DFT) is a robust theoretical quantum mechanical framework for studying the electronic structure of many-body systems, primarily in the field of condensed matter physics and quantum chemistry [11]. The DFT framework serves to investigate the electronic characteristics of atoms, molecules, and solids. The use of electron density rather than the electron wave function is the fundamental idea in DFT. The solution of the Schrodinger equation for a many-body system is extremely complicated and nearly impossible to solve numerically and computationally when the interaction energy between an electron and collection of nuclei and the electron-electron interaction of different nuclei is taken into consideration. For example, the wave function for a cluster of 100 Pt atoms essentially becomes a 23000 dimension-associated problem! To overcome this problem, Hohenberg and Kohn proposed a theorem which states as follows:

1. The ground state energy of the Schrodinger equation gives a distinct functional of electron density, where the density of electrons n(**r**) at a position in space r is defined as,

$$n(\mathbf{r}) = 2\sum_i \psi_i^*(\mathbf{r})\psi_i(\mathbf{r}) \tag{2.2}$$

So, according to the theorem, the ground state energy can be written as E[n(**r**)], which is a function of a function. Hence, the name density functional theory. The second theorem of Hohenberg and Kohn defines the characteristics of the functional, stated as follows:
2. The true electron density for the complete solution of the Schrodinger equation is the density which minimizes the energy of the overall functional.

The two theorems make life easier. However, the further difficulty of DFT is overcome by Kohn and Sham. They showed that the true electron density can be found by solving the set of equations where each equation is associated with a single electron. The Kohn and Sham equation has the following form:

$$\left[\frac{h^2}{2m}\nabla^2 + V(\mathbf{r}) + V_H(\mathbf{r}) + V_{XC}(\mathbf{r})\right]\psi_i(\mathbf{r}) = \epsilon_i\psi_i(\mathbf{r}) \tag{2.3}$$

The solution of equation 2.3 will provide the single electron wavefunction, which is a function of r only. Hence, the system with N electrons is reduced to a 3-dimensional problem instead of 3N dimensions. The first term represents the kinetic energy of the electrons. V(r) is the interaction between electrons and the collection of nuclei. V_H is the Hartree potential. V_{XC} is the exchange-correlation potential, which is defined as the functional derivative of exchange-correlation energy.

$$V_{XC}(\mathbf{r}) = \frac{\delta E_{XC}(\mathbf{r})}{\delta n(\mathbf{r})} \tag{2.4}$$

Different approaches have been taken to find out the exchange-correlation potential. Among them, the local density approximation (LDA) and generalized gradient approximation (GGA) are the two popular and widely approached methods for finding the exchange-correlation energy. LDA considers that n(**r**) is constant at all points in space, similar to a uniform electron gas system. The exchange-correlation potential takes the form of uniform electron gas as follows:

$$V_{XC}(\mathbf{r}) = V_{XC}^{\text{electron gas}}(\mathbf{r})[n(\mathbf{r})] \tag{2.5}$$

Electron density is a crucial parameter in real systems because it defines chemical bonding in the system to exhibit interesting properties. Hence, GGA is one of the widely used methods to find the functional which take into account the effect of local electron density and local gradient of electron density. The Perdew–Wang (PW91) and Perdew–Burke–Ernzerhof (PBE) functional are the most common and immensely utilized GGA functionals among various kinds of GGA functionals. The exchange energy in GGA method exhibits as follows:

$$E_{XC}^{GGA} = E_{XC}^{LDA} + \int \nabla n(\mathbf{r}) d^3\mathbf{r} \tag{2.6}$$

The Kohn and Sham equation with the appropriately chosen exchange-correlation potential according to the system can be solved using an iterative method which is self-consistent. In this thesis, we took the PBE functional for solving the Kohn and Sham equation implemented in the Vienna Ab-initio Simulation Package (VASP).

Bibliography

[1] D. Kanjilal, *et al.*, *Ind. Jour. Pure Appl. Phys.* **39**, 25 (2001).

[2] P. Kumar, *et al.*, *Pramana* **59**, 805 (2002).

[3] N. Brodusch, H. Demers, R. Gauvin, *Field Emission Scanning Electron Microscopy* (Springer Singapore, 2018), first edn.

[4] B. D. Cullity, *Elements of X-ray diffraction* (Addison-Wesley Pub. Co., Reading, Mass., 1956).

[5] M. J. K. Thomas, *Ultraviolet and Visible Spectroscopy* (Wiley India Pvt. Limited, 2008), second edn.

[6] J. Ingle, S. Crouch, *Spectrochemical Analysis; Prentice Hall: New Jersey, NJ, USA* (1988).

[7] B. G. Yacobi, D. B. Holt, *Cathodoluminescence Microscopy of Inorganic Solids* (Springer US, 1990), first edn.

[8] *Magnetic Property Measurement System SQUID VSM Users Manual, Part Number 1500-100, C0.*

[9] M. Sheik-Bahae, A. Said, T.-H. Wei, D. Hagan, E. Van Stryland, *IEEE Journal of Quantum Electronics* **26**, 760 (1990).

[10] D. Yang, *et al.*, *Physical Review Applied* **20**, 014023 (2023).

[11] D. S. Sholl, J. A. Steckel, *Density functional theory: a practical introduction* (John Wiley & Sons, 2022).

Chapter 3

Tuning electronic and optical properties of Ni and Co ion implanted s-MgO

3.1 Introduction

Ion beam implantation stands as a reliable and widely adopted technique for inducing significant modifications in the electrical, vibrational, and optical properties of insulators and semiconductors, making them applicable in various industrial contexts. This method allows the precise implantation of ions into target materials, influencing their properties based on the incident ion species and energies [1, 2]. Concurrently, ion implantation introduces different types of point defects within the material at specified depths, distinct from conventional chemical routes [3]. Both doped and undoped MgO emerge as environmentally friendly, sensitive, and non-toxic candidates with numerous interesting and potential applications. These applications encompass photoelectric solar cells, catalysts, optoelectronics, toxic waste remediation, microelectronics, and as a window layer in heterojunction solar cells [4–7]. Single crystal MgO, a compelling ceramic material, is extensively used as a substrate for various device applications. Researchers aspire to create high-quality MgO ceramics due to their outstanding mechanical, thermal, and optical properties without undergoing phase transformations during heating [8]. The MgO ceramic properties have been advanced with various ceramic developing techniques that exhibit persistent luminescence emission due to the presence of F^+ centers [9]. The controlled defect formation in MgO by ion implantation is suitable in different technological applications such as adsorbents, sensors, refractory material, paint, fluoride remover, and luminescence devices[10–13]. The

ionic model of solid and interatomic potentials based on the modified electron-gas model suggests that each oxygen site incorporated with effective 2- electronic charge compensated by the nearest Mg site associated with effective 2+ electronic charge in MgO[14]. Depending on the impurity ion incorporation in MgO, the vacancies and defects are of different kinds (such as F, F_2, and V-type color centers). The charge neutrality in the doped MgO affects the optical and magnetic properties depending on the implanted ions or chemically doped elements [15–18]. The electronic and optical absorption spectrum strongly depends on various types of color centers. The dramatic change of optical properties can be tuned by the formation of small metallic clusters on the surface of the lattice, which absorb light in different frequency limits [19]. In this case, the impurity concentration is tuned by Ni and Co ion implantation. When one MeV Ni and Co ions are implanted in crystalline MgO, a large number of vacancy defects are created by removing O or Mg atoms from the host lattice, and these vacancy centers are stable and neutral with respect to charge [20]. The different vibrational behavior of Ni and Co ion-induced defect structures can be studied and well understood using different vibrational spectroscopy techniques such as infrared absorption and Raman scattering. Most of the vibrational spectroscopic studies have been done for non-magnetic ion-doped MgO single crystals, thin films, and nanoparticles. Instead of non-magnetic ions, the implantation of magnetic ions can effectively induce vibrational modes along with magnetism in the system. The nature of the defect and color centers act as the mediator of electronic states inside the bandgap of MgO. The majority of optical studies have focused on samples implanted with low-energy (keV) ions, where S_n dominates, and S_e is considerably small. However, one MeV Ni and Co ions exhibit substantial electronic energy loss (S_e) in addition to S_n, resulting in distinct defect production compared to low-energy cases. The contribution of S_e leads to an increase in the sample's temperature during implantation due to electron-phonon coupling, which is also taken into account in modulating the optical properties of MgO.

The chapter explores bandgap narrowing and the induced vibrational modes due to the formation of various point defects with the rising of significant lattice temperature in MgO single crystal by MeV Ni and Co ion implantation. We correlate the observed bandgap narrowing and the origin of the vibrational modes with the modifications in the electronic band structure, density of states (DOS), and phonon band and DOS using the DFT, respectively.

3.2 Experimental details

Single crystalline MgO (100) substrates with a thickness of 0.5 mm were used for implantation. The cleaned (as described in Chapter 2) and polished surface was irradiated by one MeV Ni ions at room temperature at a fluence range from 5×10^{14} ions/cm^2 to 1×10^{16} ions/cm^2. The low flux of 1×10^{12} ions/cm^2/s was used to avoid beam heating for all the irradiation. The focused beam was scanned over 10 mm$\times$10 mm on the sample surface using the electrostatic scanner for uniform irradiation. We have used a UV-Vis-NIR spectrometer (Cary 5000 - Agilent) to measure the optical absorption spectra of the damaged region in the spectral region of 192-800 nm (1.55 - 6.46 eV). The measurement was carried out using a dual-beam configuration. The variation of bandgap with ion fluences is procured from Tauc plotting. Steady-state PL spectra were collected using a 325 nm He-Cd laser at room temperature in the 350-630 nm wavelength range. The sample was excited through an achromatic UV objective (LMU-UVB) with 40$\times$ magnification. The backscattered emission was collected through the same objective, using a CCD detector coupled to the spectrometer. On the other hand, the Raman spectra were taken using the 532 nm laser source. An ATR-FTIR spectrometer was utilized to observe the infrared absorption spectra and identify the functional group in the samples.

3.3 Computational Details

The theoretical band structure and DOS calculations for pristine, one Mg vacancy, one O vacancy, both Mg and O vacancy, and Mg substituted by Ni and Co defect associated in MgO structures are performed using DFT by implementing VASP code [21, 22]. The projector-augmented Wave (PAW) method [23] is used to describe the interaction between electrons and ions. MgO belongs to a cubic structure with a space group of Fm$\bar{3}$m. Pristine consists of a large supercell with 32 formula units. One Mg atom substituted by one Co or Ni atom in the supercell produced 1.56% doping in the matrix. In our calculation, all the structures are fully relaxed using the GGA scheme in order to implement exchange–correlation potential with the PBE functional [24]. A fixed cut-off energy of 600 eV for pristine and Mg and O vacancy structure was considered for a plane-wave basis set, whereas 1000 eV for substitutional defects. The utilities of Monkhorst–Pack method [25] for the generation of $12 \times 12 \times 12$ k-point meshes are implemented for achieving the required convergence of the structures within 10^{-7} eV per atom. The optimization of the structures is accomplished with respect to volume, shape, and atomic position. The relaxation of the structures was considered to be completed when the forces reached a sufficiently smaller value than 0.0001 eV/Å for each atom. The most stable and converged structures are used for the band structure and DOS calculations. The total energy and DOS calculations are performed using the linear tetrahedron method with Blochl corrections [26]. The band gap found in our DFT calculation for pristine matches well with other theoretical calculations [27, 28]. The vibrational phonon bands and DOS for pristine (containing four formula units), one Mg, one oxygen vacancy, and one Mg substituted by one Ni and Co defect-associated MgO cubic cell are calculated under the scheme of density functional perturbation theory (DFPT) by taking the most stable structure. The replacement of one Mg by implanted ions gives rise to 12.5% doping in MgO. The cut-off energy for phonon calculation was fixed at 500 eV. The

Monkhorst–Pack method of 5 × 5 × 5 k-point meshes was taken. The irreducible representation found from the phonon band and DOS provides the information of phonon modes associated with defect structure.

3.4 Ion Beam Simulations

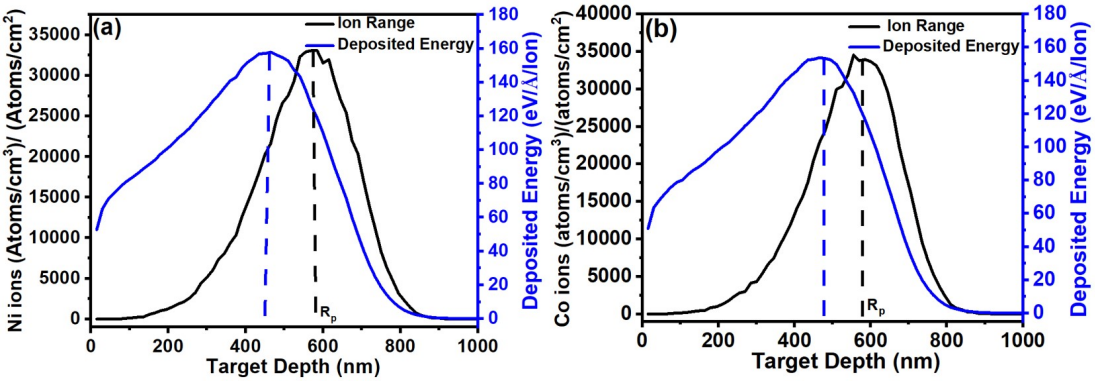

Figure 3.1: SRIM simulations of ion range and deposited energy by one MeV (a) Ni and (b) Co in MgO.

The Stopping and Range of Ions in Matter (SRIM) simulation is very useful for the ion beam community to observe the range and energy deposition by the incident ions in the target materials [29]. The option " Detailed Calculation with full Damage Cascades" was implemented for simulation in the version 'SRIM 2013'. The SRIM simulation for one MeV Ni and Co ion implantation in MgO is shown in Fig. 3.1(a) and 3.1(b), respectively. The projected range (R_p) for Ni and Co ions is 574 and 577 nm, respectively. The maximum implanted ion will be distributed around R_p. The calculated electronic (S_e) and nuclear (S_n) energy loss are 1.06 and 0.68 keV/nm and 1.08 and 0.65 keV/nm for one MeV Ni and Co in MgO, respectively. The comparable S_e and S_n values for Ni and Co ions will affect the energy depositions in MgO. The deposited energy (F_d) is calculated from the SRIM simulation using the following equation:

$$F_d = E_d \times (2 \times (Mg_{vacancy} + O_{vacancy}) + NOVAC) \tag{3.1}$$

Where E_d is the sum of the displacement energy of Mg, and O, $Mg_{vacancy}$ and $O_{vacancy}$ are the vacancies of Mg and O, respectively, and NOVAC is the 'Number' of vacancies. The deposited energy initially increases with the target depth for both the ions and becomes maximum at a depth of 470 and 478 nm with a value of 153 and 157 eV/Å·ion for Ni and Co ions, respectively, and then it decreases gradually. The deposited energy of the ions is quite high near the projected range. Hence, the damage production by the ion will be maximum near the depth of R_p due to elastic and inelastic collisions between the incident ions and host lattice atoms. So, the construction of the defect states near R_p can significantly affect electronic and optical properties in the implanted samples apart from pristine sample.

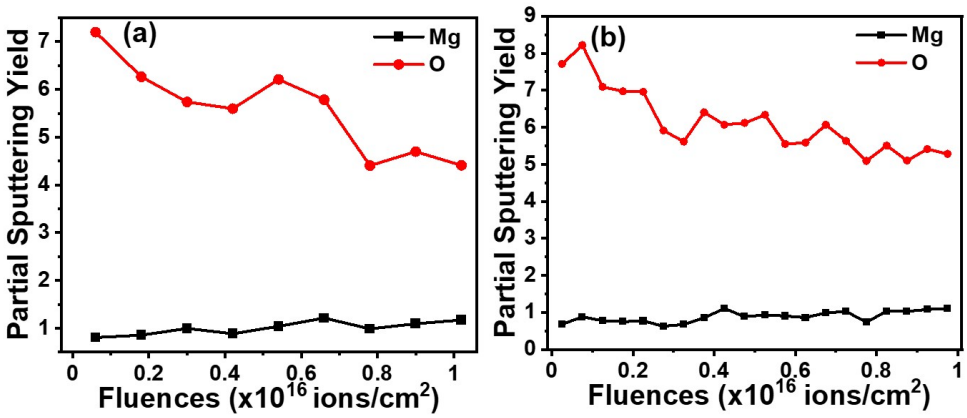

Figure 3.2: The variation of the partial sputtering yield of Mg and O simulated using TRIDYN code for one MeV (a) Ni and (b) Co ion implantation in MgO with various ion fluences.

The fluence-dependent dynamic change of thickness and/or composition of the target during ion implantation can be well understood by sputtering yield calculation. The partial sputtering yield simulation of Mg and O atoms using TRIDYN for incident Ni and Co ions in MgO is shown in Fig. 3.2(a) and 3.2(b), respectively. The statistical quality of the

TRIDYN simulation depends on the value of MAXCHA, which should be less than 0.05 for better results. In our case, the values of MAXCHA are 0.003 and 0.004, respectively, which suggests that, statistically, the simulation is quite good. It is observed from Fig. 3.2 that the sputtering yield of Mg increases from 0.80 to 1.17 and 0.68 to 1.11 with Ni and Co ion fluences while it decreases from 7.20 to 4.41 and 7.70 to 5.28 for oxygen atoms, respectively. The sputtering yield of O is still very high compared to the Mg atom at the highest fluence of 1×10^{16} ions/cm^2, and there is no signature of steady state condition observed at this fluence. This suggests that the composition of the Mg atom is proportionately larger than the O atom near the surface. Hence, the surface modification by ion implantation (Ni and Co) can be another factor for tuning the electronic and optical properties of MgO.

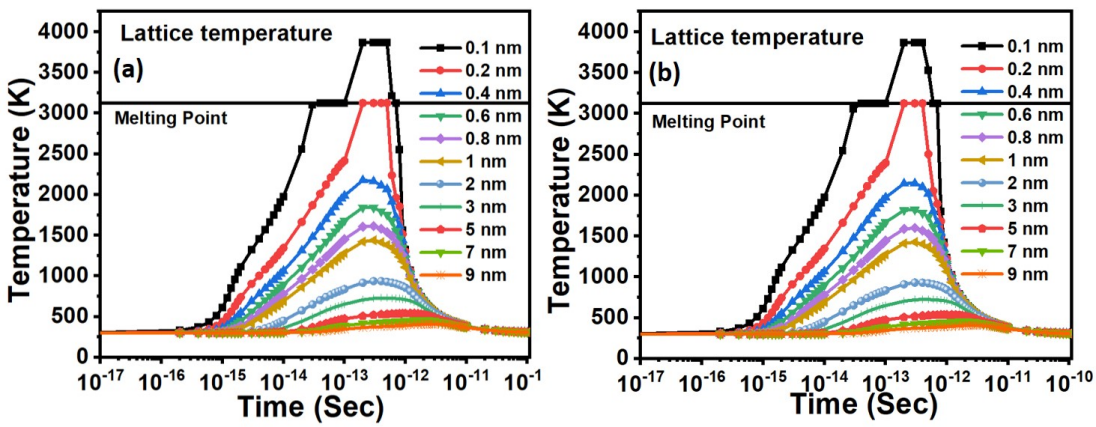

Figure 3.3: The UTS simulations to understand the rise of lattice temperature with different ion track radius of one MeV (a) Ni and (b) Co ion implanted MgO.

The UTS model was employed to calculate the rise of lattice temperature around different ion track radii for one MeV Ni and Co ion implantation in MgO, as shown in Fig. 3.3(a) and 3.3(b), respectively. The melting temperature of MgO is 3125 K. Due to having a high melting point (MP), the temperature rises above the MP around the 0.1 nm ion tract radius for both ions. The temperature just reaches the MP around 0.2 nm of the ion track. This signifies that the melting of the lattice is confined along the ion track only. The tem-

perature goes below 500 K after a 5 nm ion track radius. The rising and distribution of such huge temperatures along the ion path help to displace the lattice atom to create different kinds of defects in the matrix. The induced defects can modulate the material's optical and electronic properties.

3.5 Optical Properties

3.5.1 UV-Visible Absorption Studies

Optical absorption spectra are a sensitive method to understand the defect center and bandgap of a material. The UV-Vis absorption spectra of pristine and MeV Ni and Co ion implanted MgO single crystal are shown in Fig. 3.4(a) and 3.4(d), respectively. The maximum absorption occurs near 5.04 - 4.98 eV (246 - 249 nm), which is identified as an F-type defect center incorporated with F^+ centers [30]. The two weak absorption peaks around 4.01 - 3.97 (309 - 312 nm) and 3.46 - 3.54 eV (358 - 360 nm) are due to the transition of the oxygen defect center, which is assigned to $1A_{1g} \rightarrow 1E$(electron donation from $1s \rightarrow 2p_x$ or $2p_y$) and $1A_{1g} \rightarrow 1A_{1g}$(electron donation from $1s \rightarrow 2p_z$) respectively [31]. The small peak of F_2 type defect [32] center formed at 358 - 360 nm in the implanted sample is due to the oxygen di-vacancy center. The absorption peak observed at 575 nm is assigned by the Mg vacancy center (V center) [19].

The O_2 vacant center, F_2, and V-type defect centers are not observed in pristine, as seen in Fig. 3.4(a) and 3.4(d), respectively. These defect centers are induced and become prominent with Ni and Co ion fluences. When the highly energetic Ni and Co ions incident on a crystalline MgO, the Mg atom can be substituted by the implanted ions. Devaraja et al. mentioned that the substitution is possible when the difference in the percentage of radius (D_r) between the doped and substituted ions does not exceed 30 %. The radius percentage difference is calculated from the following equation [33]:

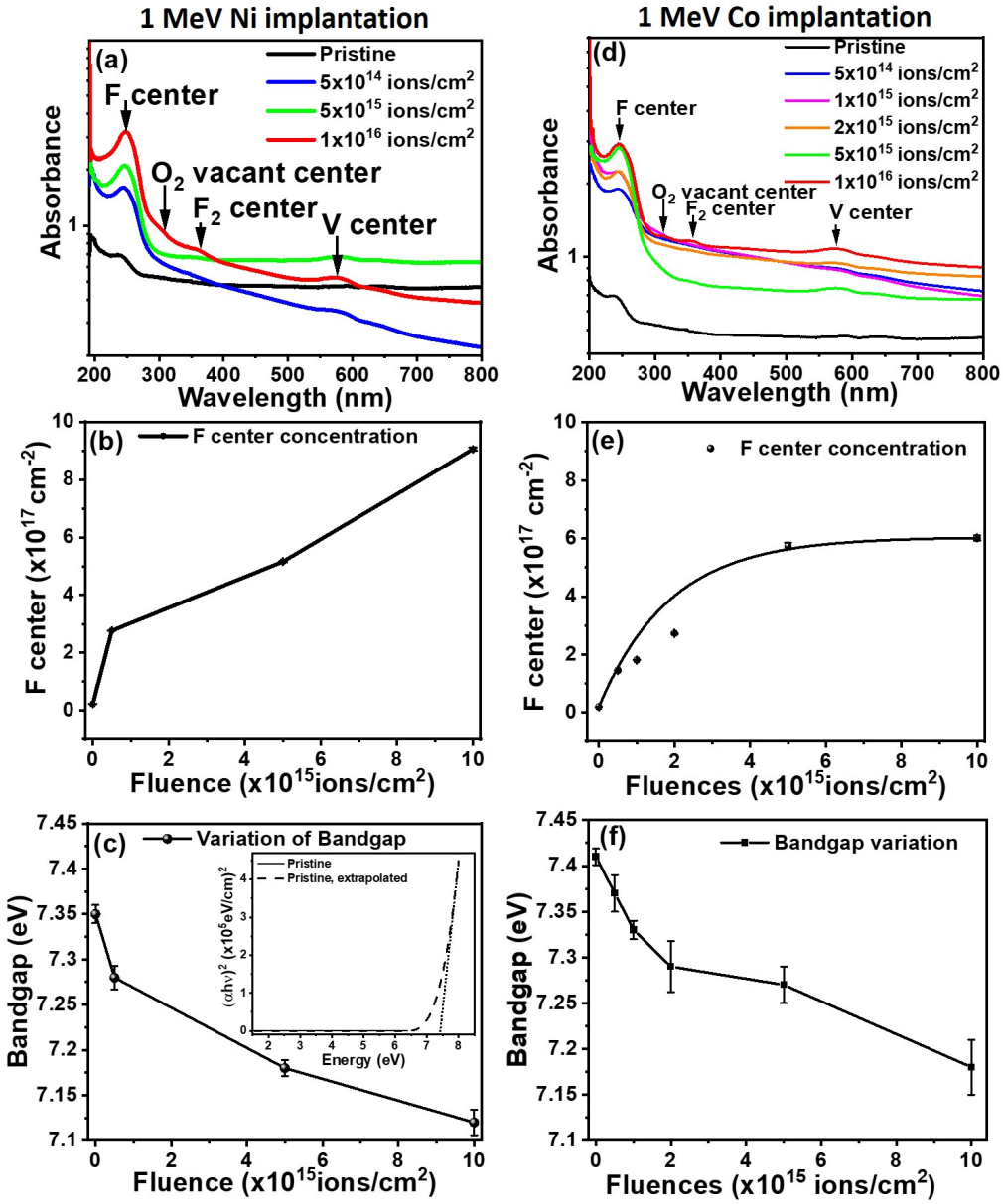

Figure 3.4: The UV-Vis absorbance (a,d), the variation of concentration of (b,e) F center, and (c,f) bandgap with incident Ni and Co ion fluences, respectively. The inset of (c) shows the typical Tauc plot of pristine to calculate the bandgap.

$$D_r = \frac{Rm(CN) - Rd(CN)}{Rm(CN)} \tag{3.2}$$

Where, CN = Co-ordination number, Rm(CN) = Radius of host cation (Mg^{2+}), Rd(CN)

= Radius of implanted ions. The D_r for substituting the Mg by Ni and Co are 4.16% and 9.72%, which is much lower than 30%. This confirms that Ni and Co can substitute Mg. On the other hand, if the radius of the cation in the host lattice is much larger than the implanted ions, the implanted ions will always sit at the interstitial site [34]. The substitution depends on the relative ionic radius and relative oxygen affinity between the host and implanted ions. In this case, Ni and Co ions can't substitute the O^{2-} ions because D_r is high due to the large ionic radius of O^{2-} than the implanted ions.

The F center can be quantified using Smakula–Dexter equation [35–37] to calculate the defect accumulation number (n_F) in the matrix, which is as follows,

$$n_F = B \times 10^{15} \times 2.3 \times I_{max} \tag{3.3}$$

Where B is a constant that takes into account the oscillator strength (0.8 for MgO), full-width half maximum of the color center, and refractive index of MgO (1.74). I_{max} is the maximum absorbance at defect centers. The fluence-dependent concentration variation of the F center of Ni and Co implanted MgO is presented in Fig. 3.4(b) and 3.4(e), respectively. The concentration of F center in the order of 10^{16} cm^{-2} in pristine is observed due to intrinsic defects during crystal growth. The mean concentration of strong F center increases with the increase of Ni ion fluences. The F center starts to saturate at 5×10^{15} ions/cm^2 in the Co implanted sample. The F center concentration remains nearly the same (5.7-6.0 $\times 10^{17}$ cm^{-2}) for the fluence 5×10^{15} and 1×10^{16} ions/cm^2, respectively, showing clear saturation signal. But, in the Ni ion implantation case, the high fluence (> 1×10^{16} ions/cm^2) is required to exhibit the saturation signature. This signifies that the continuous increasing of the color center (F center) even after 1×10^{16} ions/cm^2, one MeV Ni ion implantation can decrease the bandgap more than the Co ion implantation. Hence, F-type defect centers may play a crucial role in lowering the bandgap.

The optical bandgap is calculated using the Tauc plot [38]. The following relation between the absorption coefficient (α) and incident photon energy (h ν) is used in the Tauc plot:

$$(\alpha h\nu)^n = C(h\nu - E_g) \tag{3.4}$$

Where C is a constant and E_g = energy gap. The value of n represents the nature of transition, and the direct bandgap nature has been found for MgO. The bulk bandgap of MgO is reported to be 7.8 eV[39]. Due to the limitation of energy scan by the detector in the UV-Vis spectrometer, we have used a third-order polynomial extrapolation to the Tauc plot in order to get the energy above 6.46 eV. A typical Tauc plot for pristine is shown in the inset of Fig. 3.4(c). Nefedova et al. [40] reported the bandgap of MgO and Cr-doped MgO as 7.16 and 5.36 eV, respectively. In our case, the extension of the linear part of the extrapolated line intersects the x-axis, giving the bandgap of pristine of 7.35$\pm$0.01 eV. The bandgap of MgO decreases to 7.18$\pm$0.03 eV for the Co ion fluence 1×10^{16} ions/cm^2 (Fig. 3.4(f)). On the other hand, the Ni implantation narrows the gap to 7.12$\pm$0.014 eV at the same fluences (Fig. 3.4(c)). The bandgap of MgO decreases more due to Ni ion implantation compared to Co ion, as anticipated. Bandgap can vary due to changes in the crystal structure, lattice strain, surface, and interface effect. The SRIM and TRIDYN simulation shows that the defect states form in the matrix, imparting lattice strain, and the sputtering modifies the surface. In our case, the gradual decrease of the optical bandgap with the increment of the incident ion fluences arises mainly due to the increase of defect concentration and surface modifications. The bandgap reduction due to defect states is further investigated through DFT calculation.

3.5.2 Photoluminescence Studies

The room temperature PL spectra of pristine and one MeV Ni and Co ion implanted MgO in the fluence range of 5×10^{14} - 1×10^{16} $ions/cm^2$ are shown in Fig. 3.5(a) and 3.5(c), re-

spectively. The PL spectra of the implanted samples are deconvoluted into four bands at 388 (Violet), 419 (Blue), 514 (Green), and 563 (red) nm to understand the different color centers. The typical deconvoluted spectra of Ni and Co ion at a fluence of $5 \times 10^{14}\ ions/cm^2$ are shown in Fig. 3.5(b) and 3.5(d), respectively. The high intensity and prominent peaks observed at 417/419 and 518/514 nm are assigned to V and F centers, respectively [41, 42]. The integrated intensity vs fluence of the PL spectra is presented in Fig. 3.6(a-d) and 3.6(e-h) for Ni and Co ion implanted samples, respectively. The PL peak around 387/388 nm is not observed in pristine, as seen in Fig. 3.6(d) and 3.6(e), respectively. This peak may originate from Ni or Co defect states in the matrix. The rise of such a metal-assisted defect band is further explored by theoretical DFT calculation, discussed in the next section. The decreasing tendency of integrated intensity with ion fluence indicates the diminishing of the population of electron occupancy in the defect states. The peak around 565/563 nm is identified as F^- color center, which originated due to oxygen vacancy filled by one electron [41]. The excitation behavior of the F center can be understood and explained in two different routes. When the F-type defect states are illuminated by UV light, the electrons become excited due to the absorption of sufficient photon energy and move to either F^+ or the excited states of the F center (F^*). The electron from F^* states de-excite by emitting a photon energy of 2.39/2.41 eV. The electron experiences a radiative transition via a metastable F^+ state from the F center. The F^+ states are metastable states with relatively higher lifetime than the F^* states. So, the F^+ needs a different path to de-excite by emitting a similar photon energy of 2.39/2.41 eV.

The formation of different defect states and the electronic transition between defect states and CB and VB can be explained by the proposed band model, as shown in Fig. 3.7. When the incident UV light of wavelength 325 nm excites the F center, it tries to de-excite by releasing electrons. The released electrons move to the CB via the F^+ center and become free there. The free electrons in CB can recombine with different defect states. The

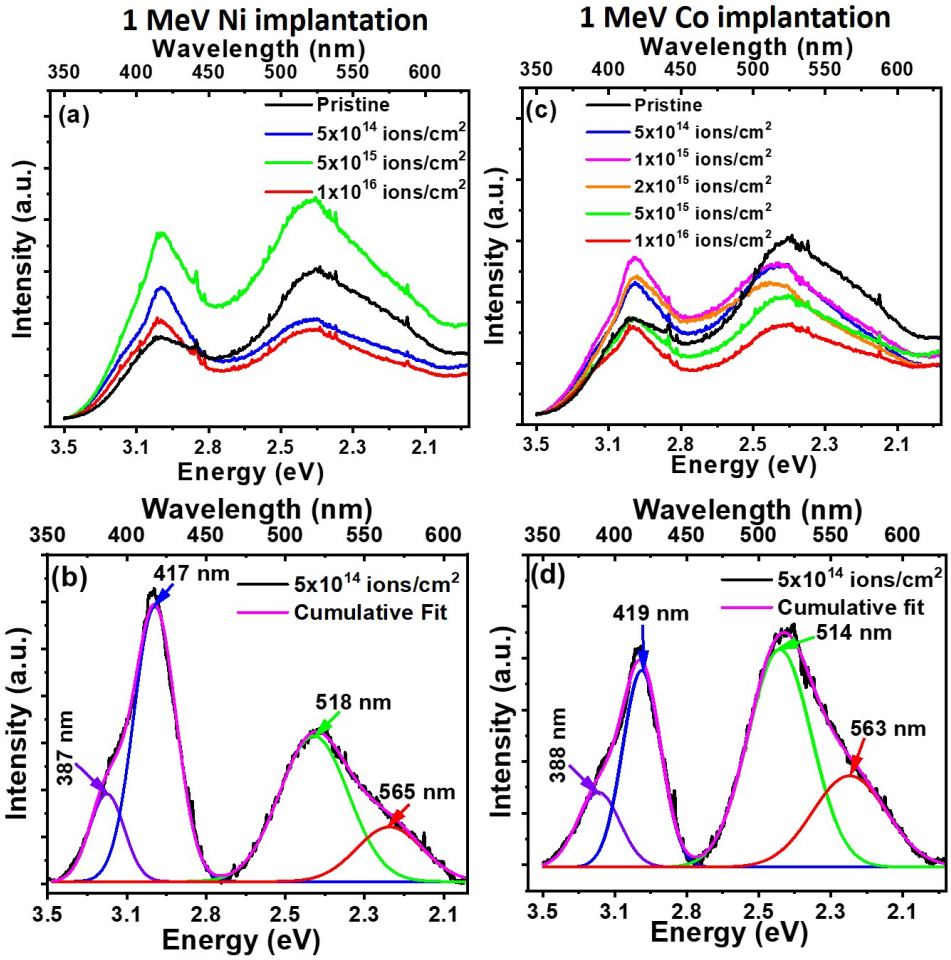

Figure 3.5: Room temperature PL spectra of pristine, (a) Ni and (b) Co ion implanted MgO, The typical deconvoluted PL spectra at a fluence of 5×10^{14} ions/cm^2 of (b) Ni and (d) Co implanted samples.

released photon corresponds to the wavelength of 518/514 nm when the recombination occurs between the CB and F centers. When the electron jumps to the oxygen vacancy center, the released energy corresponds to the wavelength of 565/563 nm. Pathak et al. reported that the recombination of conduction band electron is not possible with V center [43], and this defect center can lie near the valence band maximum [44]. It is also energetically unfavorable to recombine an electron to V center with the chemical potential of conduction band minimum because the electron gains almost the entire bandgap energy in this jump

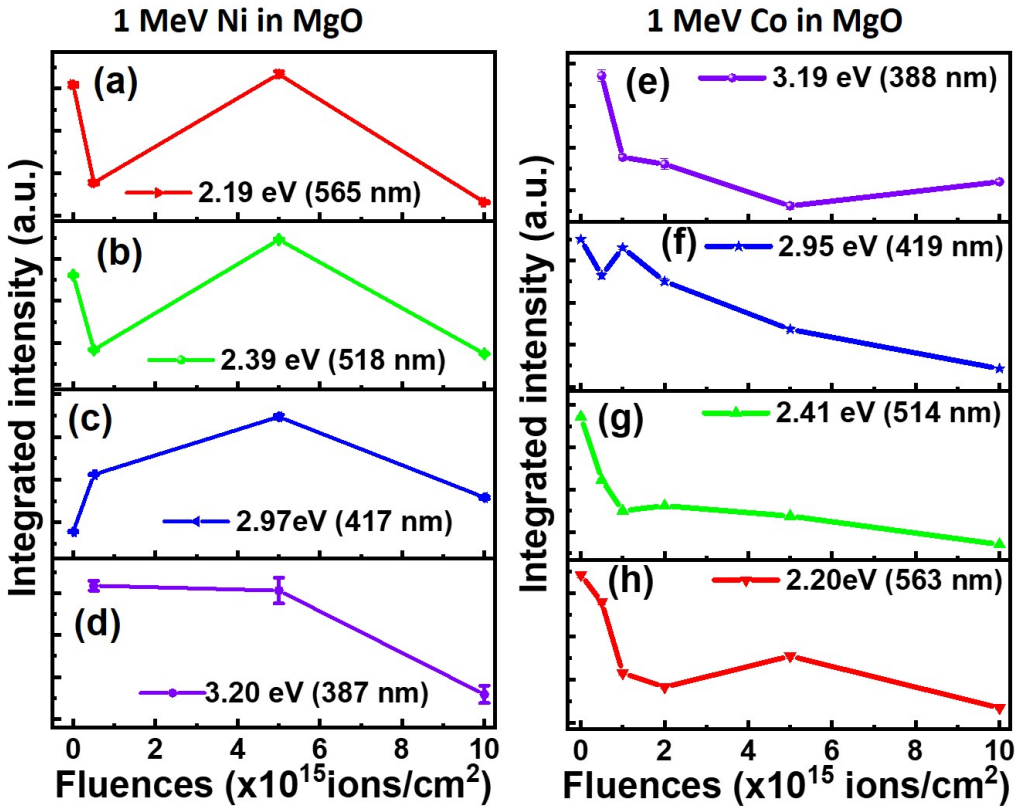

Figure 3.6: The integrated intensity for (a-d) Ni and (e-h) Co ion implanted sample for the deconvoluted peaks as a function of ion fluence.

[44]. On the other hand, the excited electrons from the valence band can move to the V center. Subsequently, the de-excitation emits energy corresponding to the wavelength of 417/419 nm. The PL spectra suggest the formation of the Ni/Co defect state near the conduction band. The lower excited electron moves to the metal-assisted defect state and then de-excites by releasing energy corresponding to the wavelength of 388 nm.

The PL spectra plotted in chromaticity coordinates for Ni and Co implanted samples, according to Commission Internationale l'Eclairage (CIE) 1931, are shown in Fig. 3.8(a) and 3.8(b), respectively. The dark spots on the graph depict the color observed in the PL spectra. The luminescent signal spot of MgO remains relatively unchanged when subjected

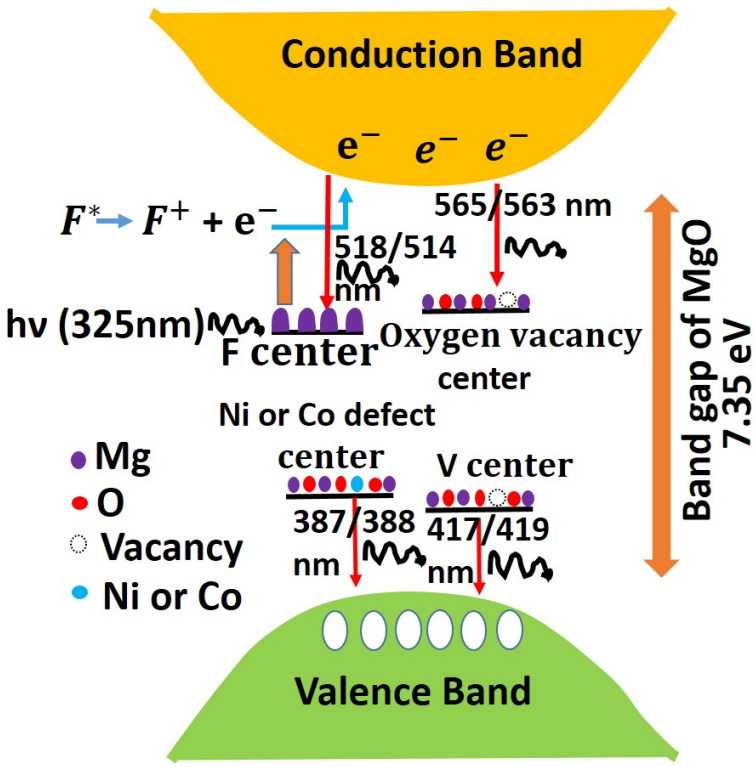

Figure 3.7: The proposed band model for electronic transitions

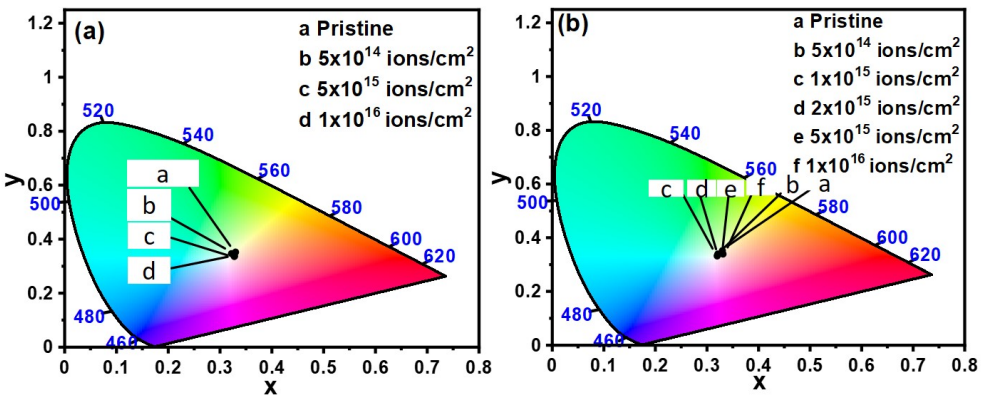

Figure 3.8: The CIE 1931 chromaticity plot of PL spectra for (a) Ni and (b) Co ion implanted MgO with the variation of ion fluences.

to Ni and Co ion implantation. This observation indicates that both untreated and implanted samples can generate predominantly white light when excited by 325 nm UV light. The CIE

graph of PL spectra tells that the emission of white light in ion-implanted MgO opens up possibilities for its utilization in optical devices. Additionally, it can serve as a valuable material for substrates or insulating layers in the construction of LED device structures.

3.5.3 Theoretical DFT Study

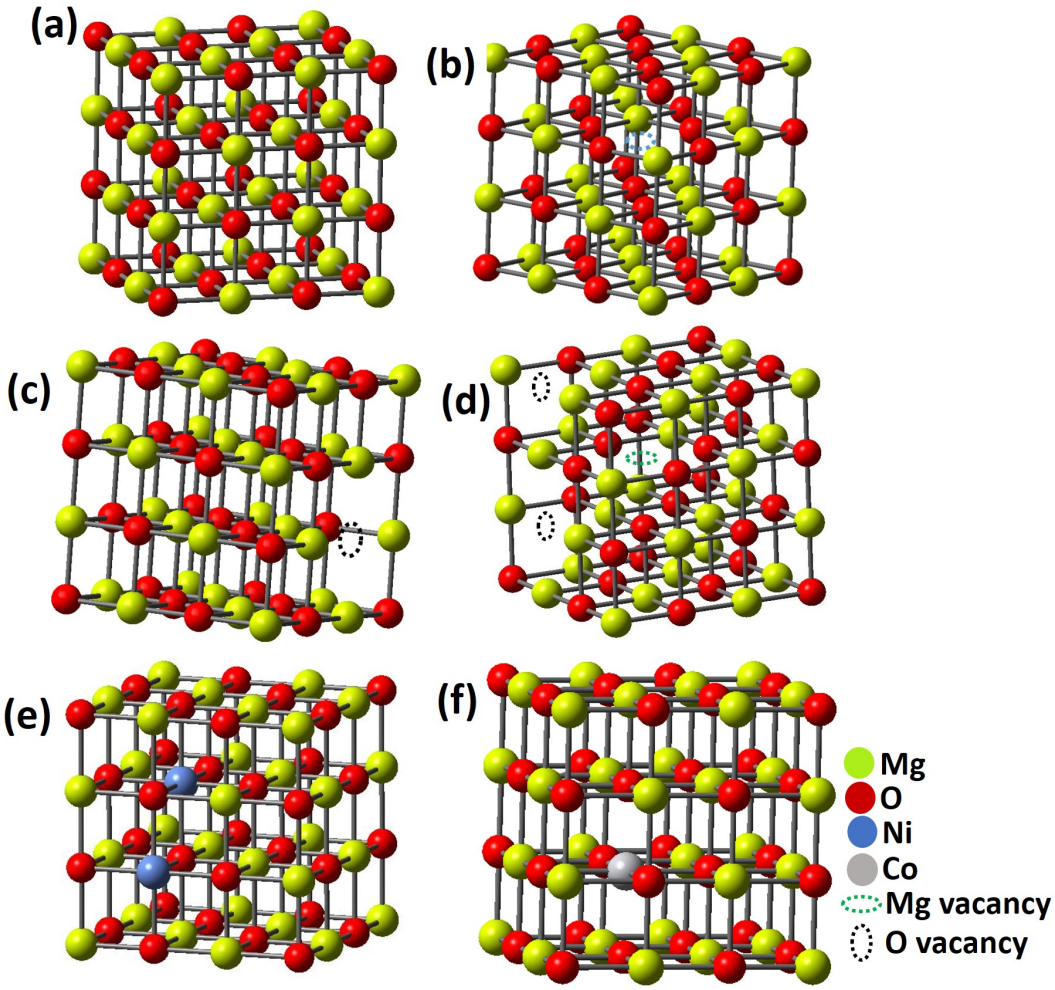

Figure 3.9: The atomic configuration of (a) pristine, (b) Mg vacancy, (c) O vacancy, (d) one Mg and two Oxygen vacancy, Mg substituted by (e) two Ni and (f) one Co defect associated MgO for the theoretical calculation. Green, Red, blue, and ash colors represent the Mg, O, Ni, and Co atoms, respectively. The green and black dashed circles indicate the Mg and O vacancy, respectively.

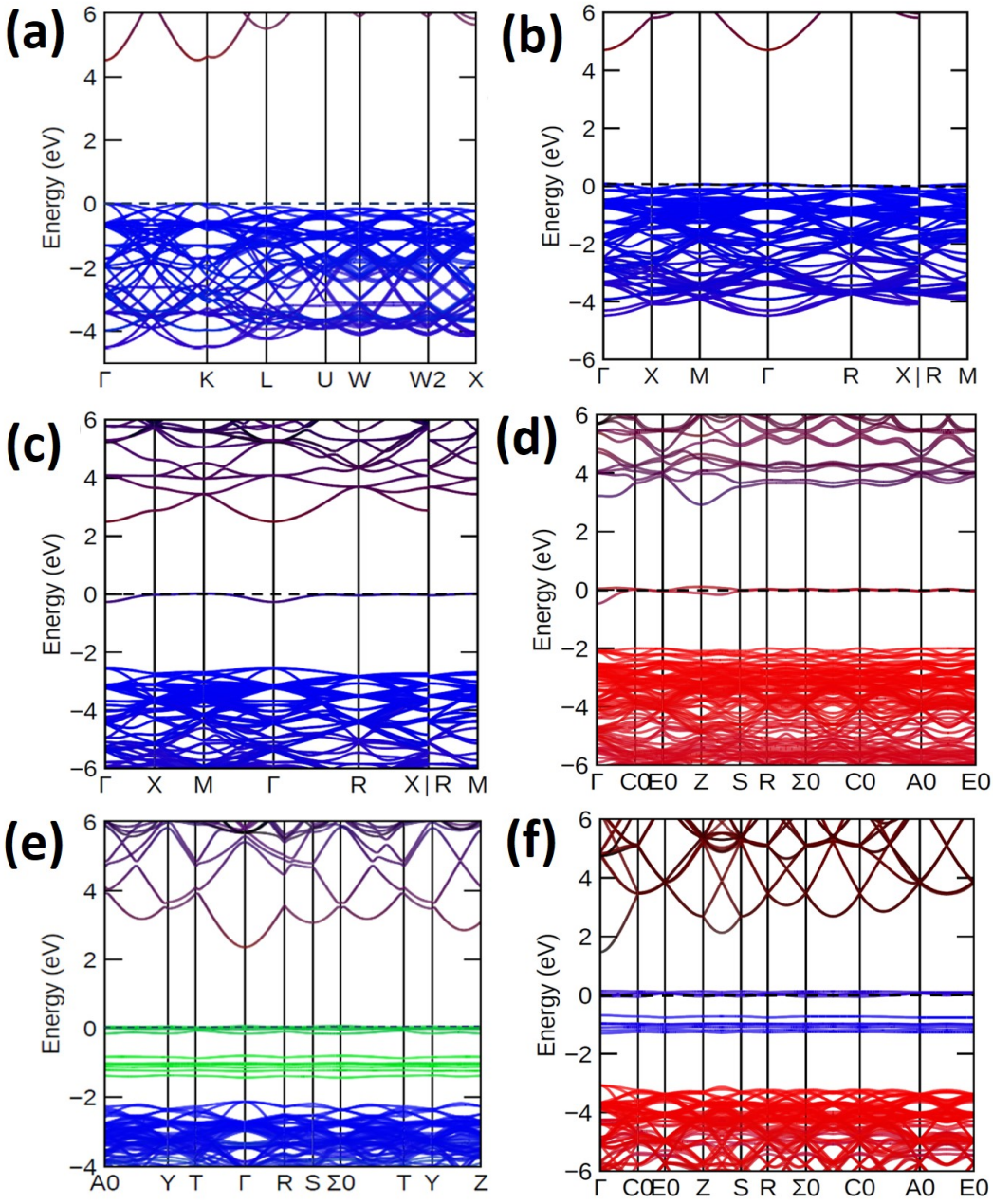

Figure 3.10: The calculated band structure of (a) pristine, (b) Mg vacancy, (c) O vacancy, (d) one Mg and two Oxygen vacancy, Mg substituted by (e) two Ni and (f) one Co defect associated MgO. The dashed line at 0 eV denotes the Fermi level.

The atomic configuration of cubic super-cell containing 32 formula units of pristine, Mg vacancy, O vacancy, one Mg and two Oxygen vacancy, Mg substituted by two Ni and

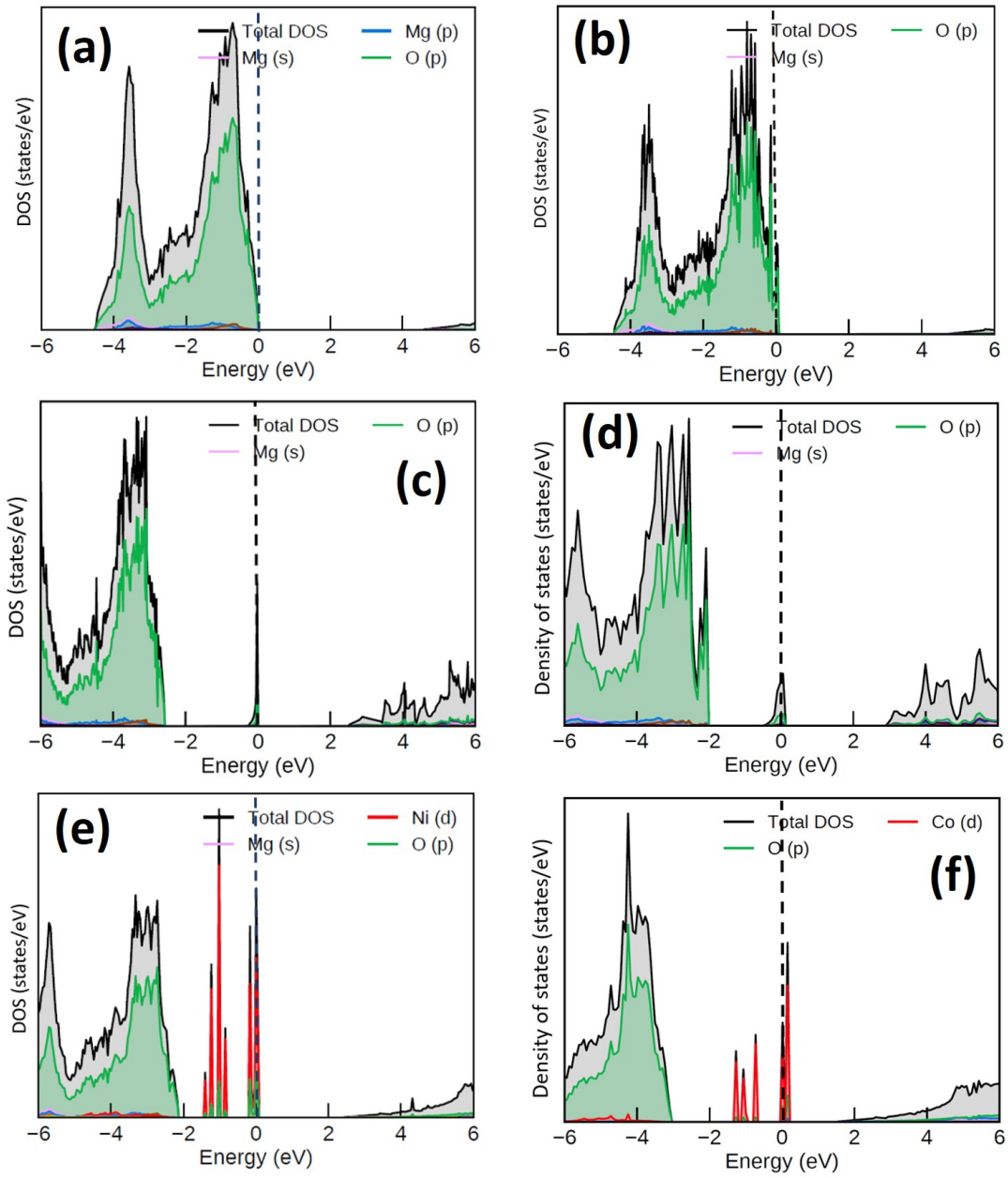

Figure 3.11: The calculated DOS structure of (a) pristine, (b) Mg vacancy, (c) O vacancy, (d) one Mg and two Oxygen vacancy, Mg substituted by (e) two Ni and (f) one Co defect associated MgO. The dashed line at 0 eV denotes the Fermi level.

one Co for DFT calculation is shown in Fig. 3.9(a-f), respectively. The theoretical band structure for pristine, Mg vacancy, O vacancy, one Mg and two Oxygen vacancy, and Mg

substituted by two Ni and one Co defect associated MgO are shown in Fig. 3.10(a-f), respectively. The DFT calculated bandgap for pristine is found to be 4.50 eV. The introduction of vacancy and substitutional defects in MgO produces the defect band states around the Fermi level, as shown in Fig. 3.10(b-f). The creation of defect states influences to vary the bandgap. The Mg vacancy in MgO doesn't play a role in creating defect states near the Fermi level (Fig. 3.10(b)), whereas one oxygen vacancy creates a defect state around Fermi level (Fig. 3.10(c)). For further confirmation, the combined effect of Mg and O vacancy is justified (Fig. 3.10(d)). The two defect bands at the Fermi level correspond to the O vacancy (more clear in PDOS calculations), and no signature of the Mg vacancy-associated band is observed. On the other hand, since the number of oxygen vacancy defects is proportional to the number of production of oxygen defect states (Fig. 3.10(c) and 3.10(d)), the large intensity for oxygen vacancy defects in absorption spectra confirms that most of the defect states are associated with oxygen vacancy states. The Mg vacancies (V centers) can only play a role in the movement of oxygen vacancy defect states around the Fermi level to reduce the bandgap (observed in Fig. 3.10(c) and 3.10(d)). The formation of different defect states between CB and VB agrees with our proposed model for taking all the defect states between CB and VB. The CB minimum and VB maximum occur at the same gamma point in pristine, confirming the direct bandgap property of MgO, which was considered in the Tauc plot.

We further calculated the total DOS and projected DOS (PDOS) to understand the orbital information about the defect bands. The total DOS and PDOS for pristine, Mg vacancy, O vacancy, one Mg and two Oxygen vacancy, Mg substituted by two Ni and one Co defect associated MgO are shown in Fig. 3.11(a-f), respectively. The majority contribution in forming CB and VB comes from the Mg-p, Mg-s, and O-p orbitals. The O-p, Ni-d, and Co-d orbitals mainly contribute to forming the O vacancy, Ni, and Co defect states in MgO, respectively (Fig. 3.11(c-f)). These defect states can be filled fully or partially by electrons

and become free after moving to the CB by external excitation, as discussed in the proposed model (Fig. 3.7). The deconvoluted PL band around 387/388 nm arises due to defect creation by high-energy Ni or Co ions in MgO. Ni-d and Co-d orbital mainly contributed to creating this defect band. This confirmed the presence of metal-assisted defect bands in implanted samples. Hence, the bandgap variation with ion fluences is well justified from the band structure and DOS calculations.

3.5.4 Raman study

The observation and analysis of Raman spectra are very useful for understanding the nature of the vibration of atoms and molecules in finite crystals. The Raman spectra of pristine and Ni and Co ion implanted MgO with different fluences are shown in Fig. 3.12(a) and 3.12(b), respectively. In this case, pristine doesn't exhibit the Raman active modes, as clearly seen in Fig. 3.12. But, the Raman scattering peaks are induced in the implanted samples at 237, 346, 409, 444, 499, 648, and 1566 cm^{-1}. Most of the peaks arise in the D bands region, which is also known as breathing mode [45]. The peaks under this band region lie below 1500 cm^{-1}. The broad peak observed at 1566 cm^{-1} signifies the overlapping between the D and G bands [46]. This overlapping is absent in the lower fluence samples due to a lack of sufficient defect states. The overlapping becomes prominent ($\geq 5 \times 10^{15}$ ions/cm^2) with the increase of Ni and Co ion fluences. The Raman shift around 444 cm^{-1} originates due to the contribution of transverse optical (TO) phonon mode. The small peak at 499 cm^{-1} arises due to the symmetrical stretching vibration of Mg and O [47]. The radial breathing mode of vibrational peaks is identified around 237, 346, and 409 cm^{-1} [48]. Now, to understand the root of the observed Raman shift, we performed the phonon band and DOS calculations.

Fig. 3.13(a-e) shows pristine, one Mg, one oxygen vacancy, and one Mg substituted by one Ni and one Co defect-associated MgO structure for phonon band and DOS calculations, respectively. The theoretical phonon dispersion, total DOS, and PDOS calculation of

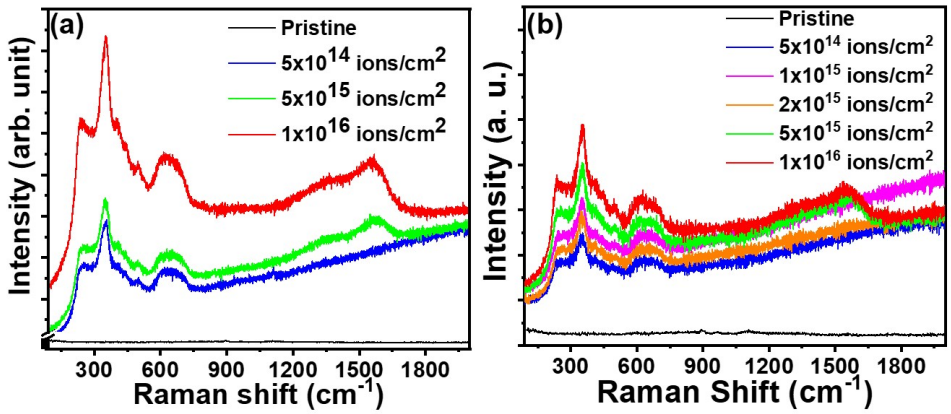

Figure 3.12: Raman spectra of pristine, (a) Ni and (b) Co implanted MgO for different ion fluences.

pristine, one Mg, one oxygen vacancy, and one Mg substituted by one Ni and one Co defect-associated MgO are shown in Fig. 3.14(a-e) and 3.15(a-e), respectively. The Raman active modes of MgO with a space group of Fm$\bar{3}$m are A_{1g}, E_g, T_{2u} and T_{2g}. Besides, T_{1u} can be either Raman or IR active. Hence, it is important to calculate the irreducible representation of pristine and defect-attributed MgO to confirm the active modes. The irreducible representation for the phonon bands at Γ points for pristine, one Mg, one oxygen vacancy, and one Mg substituted by Ni and Co defect-associated MgO are $3T_{1u} + 3T_{1u}$, $3T_{1u} + 3T_{2u} + 3T_{1u} + 3T_{1u} + 3T_{1u} + 3T_{2u} + 3T_{1u}$, $3T_{1u} + 3T_{1u} + 3T_{2u} + 3T_{1u} + 3T_{1u} + 3T_{2u} + 3T_{1u}$, $3T_{1u} + 3T_{1u} + 3T_{2u} + 3T_{1u} + 3T_{1u} + 3T_{1u} + 3T_{2u} + 3T_{1u}$, and $3T_{1u} + 3T_{1u} + 3T_{1u} + 3T_{2u} + 3T_{1u} + 3T_{1u} + 3T_{1u} + 3T_{2u}$ respectively. In this case, all the T_{2u} modes are Raman active mode, but T_{1u} mode can be either Raman or IR active. The calculation for pristine sample shows (Fig. 3.14(a)) that it won't have any Raman active mode, matching with our experimental results. In pristine, the 1st T_{1u} (0.005 THz) peak is inactive, and the 2nd T_{1u} peak arises at 11.16 THz (372 cm^{-1}), which we didn't observe experimentally. The peak at 11.16 THz corresponds to both Mg and O vibration, but the vibrational contribution of the O atom dominates over the Mg atom (Fig. 3.15(a)). The experimentally found Raman

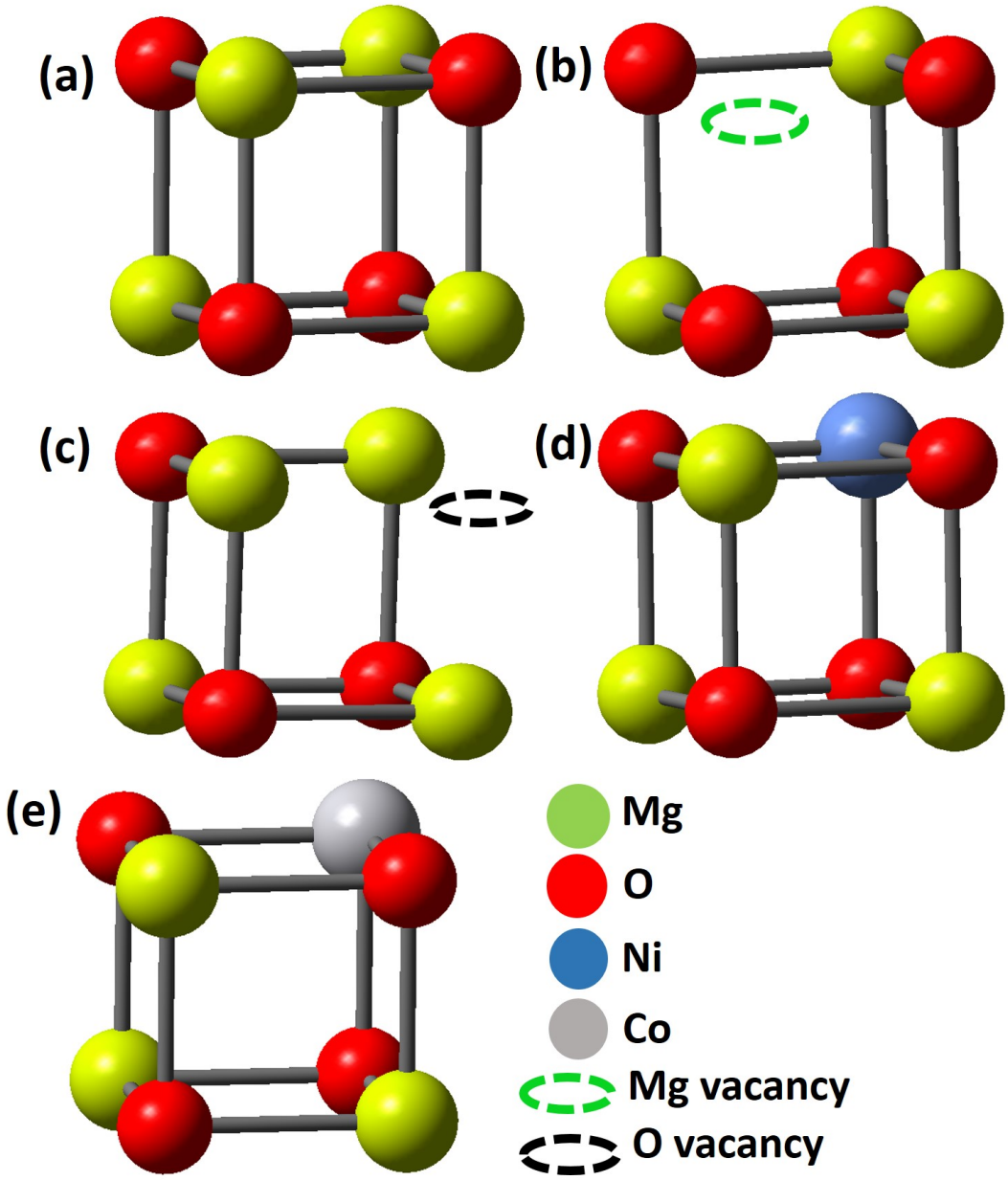

Figure 3.13: (a) pristine, (b) one Mg vacancy, (c) one oxygen vacancy, one Mg substituted by one (d) Ni, and (e) Co defect associated MgO structure for phonon band and DOS calculations.

shift at 237 cm^{-1} agrees well with the theoretically observed band peak around 7.38 (246 cm $^{-}1$) and 6.90 THz (230 cm^{-1}) for one Mg and O vacancy associated MgO, as shown in Fig. 3.14(b) and 3.14(c), respectively. This peak is associated with T_{1u} active mode, which

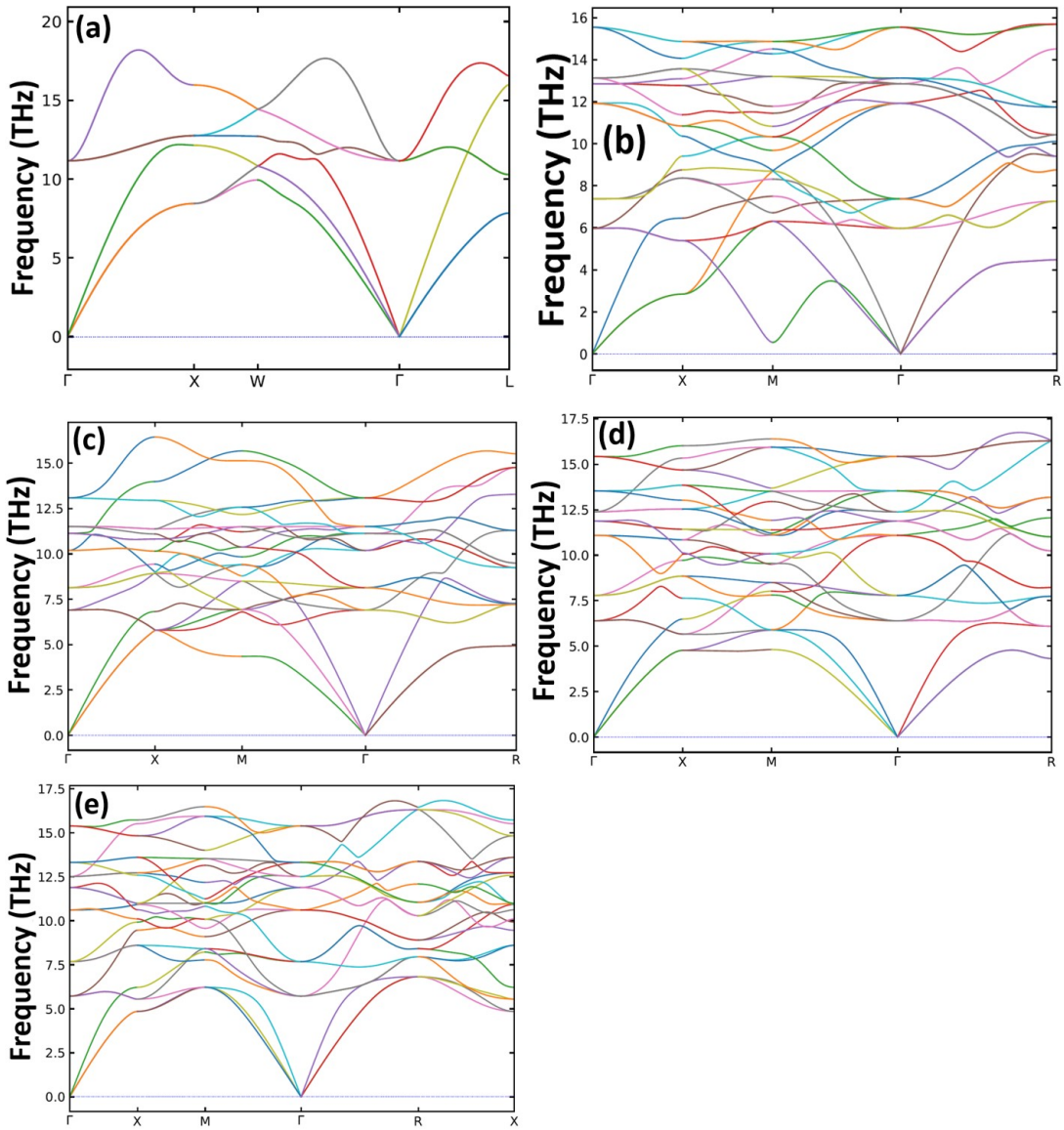

Figure 3.14: The theoretical phonon dispersion band of (a) pristine, (b) one Mg vacancy, (c) one oxygen vacancy, one Mg substituted by one (d) Ni, and (e) Co-associated MgO. The different colors represent the band connection along the high symmetry points.

forms due to the vibration of Mg and oxygen atoms, as seen in Fig. 3.15(b) and 3.15(c), respectively. The vibrational contribution for constituting this mode by Mg dominates over oxygen, comparing the phonon DOS in Fig. 3.15(b) and 3.15(c), respectively. The prominent peak at 346 cm^{-1} matches with the active peak found at 10.19 THz (340 cm^{-1}), as

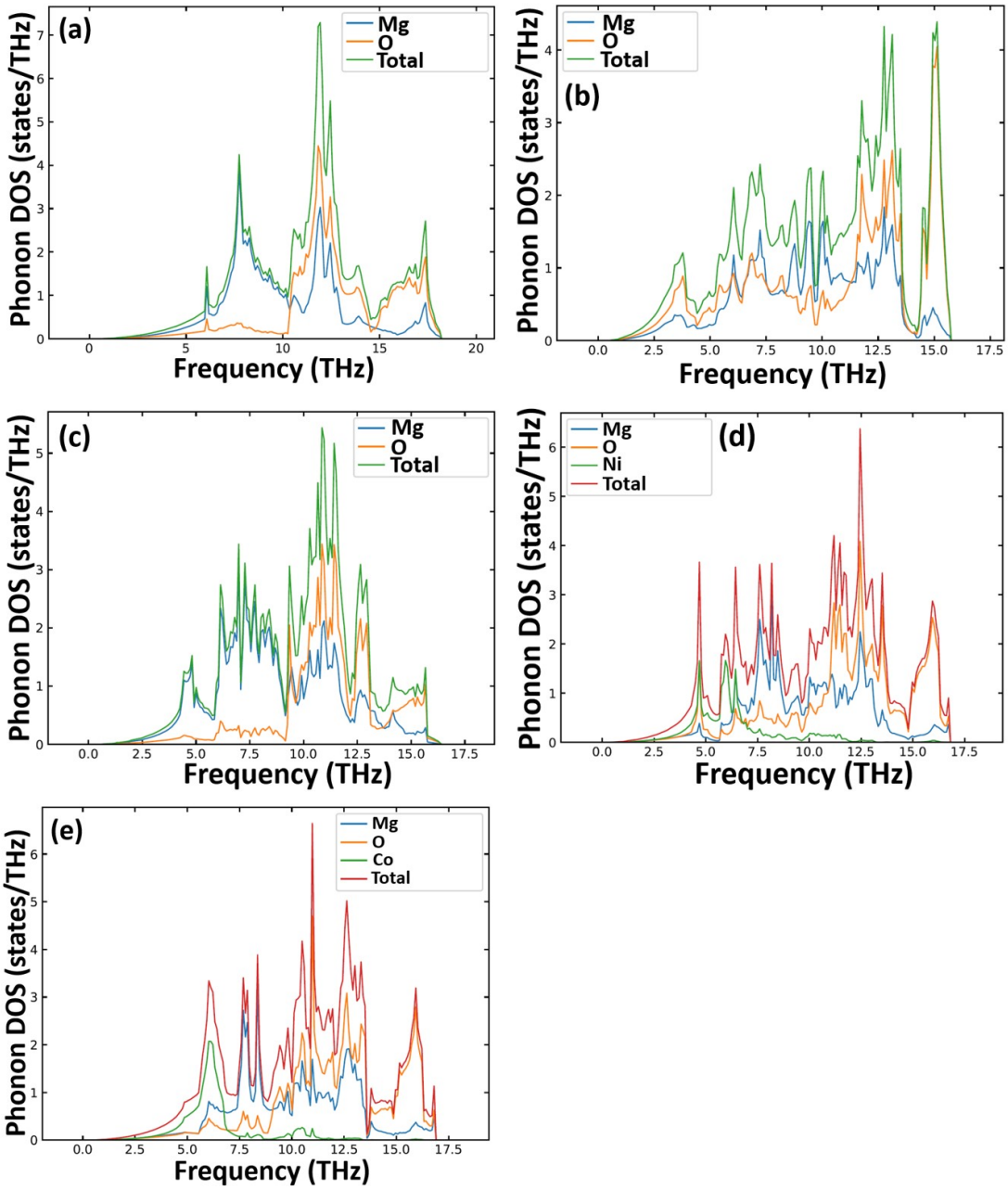

Figure 3.15: The total and partial phonon density of state calculation of (a) pristine, (b) one Mg vacancy, (c) one oxygen vacancy, one Mg substituted by one (d) Ni, and (e) Co-associated MgO.

shown in Fig. 3.14(c). The creation of oxygen vacancy in an enormous number in MgO due to Ni and Co ion implantation plays a significant role in forming this active T_{1u} mode.

Fig. 3.15(c) further apprised that the most vibrational contribution comes from the oxygen compared to the Mg atom. The prominent peak at 12.37 (413 cm^{-1}) THz (Fig. 3.14(d) and 3.15(d)) is related to T_{1u} mode. This peak originates only after inducing the Ni atom in the matrix. The vibrational intensity of oxygen atoms is more than that of Mg atoms (Fig. 3.15(d)). The vibrational effect from the Ni atom is negligible compared to the O atoms to induce the peak at 413 cm^{-1}. But for Co implanted samples, this peak arises at 12.51 THz (417 cm^{-1}) (Fig. 3.14(e) and 3.15(e)). The other experimental Raman active peak around 444 and 499 cm^{-1} is associated with T_{2u} (13.53 THz) and T_{1u} (15.42 THz) mode in Ni implanted samples. On the other hand, T_{1u} (13.31 THz) and T_{2u} (15.38 THz) modes are responsible for the peak at 444 and 499 cm^{-1} in Co implanted samples. The peaks around 13.12 (438 cm^{-1}) and 15.54 (518 cm^{-1}) in Mg vacancy-associated MgO also agree well with the experimental peak at 444 and 499 cm^{-1}. The combined vibrational effect of Mg vacancy and substitutional defect contributed to the origin of the 444 and 499 cm^{-1} in Ni and Co implanted samples, respectively (Fig. 3.15(b), 3.15(d), and 3.15(e)). The partial DOS suggests that the vibrational contribution from oxygen atoms takes the larger responsibility for arising these Raman shifts compared to the Mg atoms in defect-associated MgO.

3.5.5 FTIR study

FTIR spectroscopy is one of the advantageous techniques for identifying the functional group and analyzing the different vibrational features of the materials. The typical FTIR spectra of pristine and Ni and Co ion implanted MgO are shown in Fig. 3.16 and 3.17, respectively. Fig. 3.16(a) and 3.17(a) show that the broad absorption peak ranging from 561-608 cm^{-1} arises due to the stretching vibration of Ni-O, Co-O [49]. The broadness signifies the formation of nanocrystals in the matrix. The broad absorption peak observed at 840-841 cm^{-1} (Fig. 3.16(b) and 3.17(b)) arises due to the stretching vibration of Mg-O-

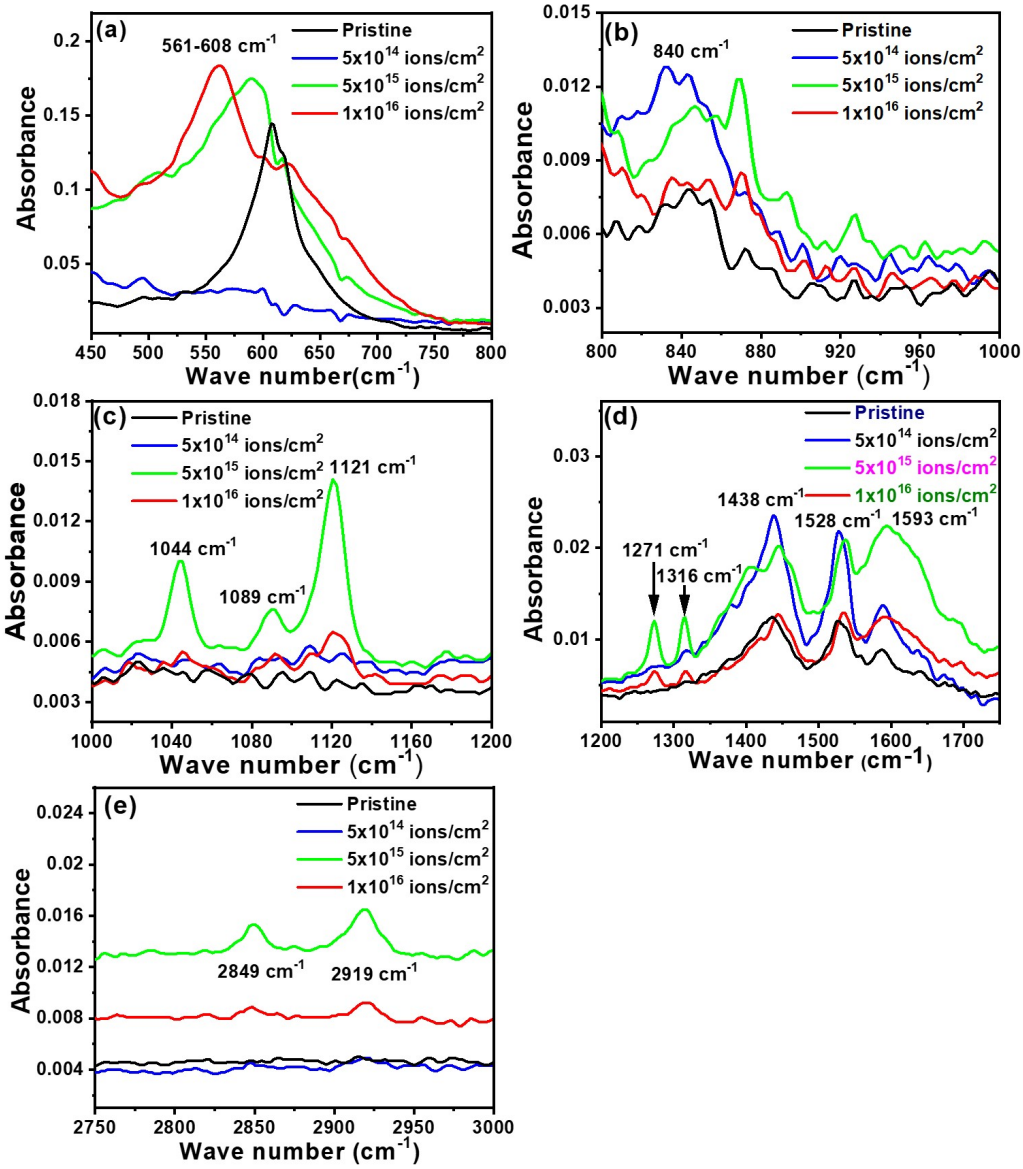

Figure 3.16: FTIR spectra of pristine and Ni ion implanted crystalline MgO with different fluences in the range of (a) 450-800 cm^{-1}, (b) 800-1000 cm^{-1}, (c) 1000-1200 cm^{-1}, (d) 1200-1750 cm^{-1}, and (e) 2750-3000 cm^{-1}.

Mg bonds [50]. The peak at 840-841 cm^{-1} is allowed by the sum modes of W_2' and W_3'' along the Z symmetry through the critical point at W [51]. We observed three peaks around 1044, 1089-1092, and 1121-1122 cm^{-1} in this range of 1000-1200 cm^{-1} for Ni and Co im-

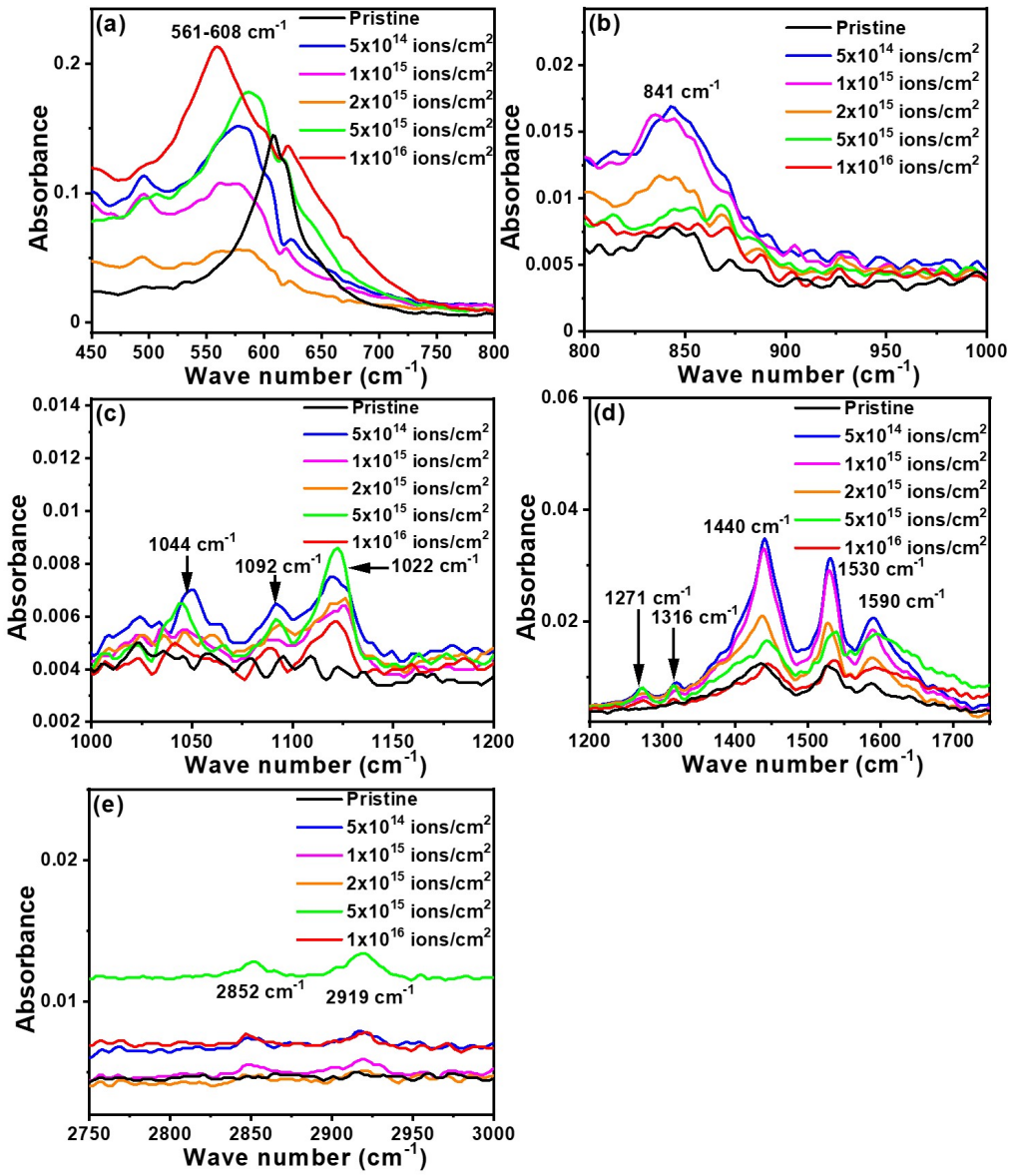

Figure 3.17: FTIR spectra of pristine and Co ion implanted crystalline MgO with different fluences in the range of (a) 450-800 cm^{-1}, (b) 800-1000 cm^{-1}, (c) 1000-1200 cm^{-1}, (d) 1200-1750 cm^{-1}, and (e) 2750-3000 cm^{-1}.

planted samples (Fig. 3.16(c) and 3.17(c)). Earlier, we showed that Ni/Co ion implantation produces different types of vacancy and substitutional defects in the matrix. These defects on the surface can absorb the atmospheric constituents (e.g., CO_2, H_2O, O_2, H_2, N_2, etc.)

to modify the defect center and can produce different vibrational modes [52]. The 1044 cm^{-1} peak occurs due to the vibration of C-O bending vibration. C-O stretching vibration is responsible for the assigning of 1089-1092 cm^{-1} peak. The peak at 1121-1122 cm^{-1} is also due to the stretching vibration of C-O bond [53]. Fig. 3.16(d) and 3.17(d) show the absorption spectra in the range of 1200-1750 cm^{-1} for Ni and Co implanted samples, respectively. We pointed out a peak around 1271 cm^{-1}, referring due to Ni-O stretching vibration or O-Ni-O bending vibrations. When the MgO sample was exposed to the atmosphere, chemisorption of CO_2 happens onto the MgO sample [16]. The absorption peak at 1316 cm^{-1} is associated with the δ (OC=C) modes [31]. The adsorption band peaks around 1438-1440 cm^{-1} for different fluences originate due to the chemisorption of carbonate (CO_3^{2-}) groups and the stretching vibration of this group over the MgO surface [54, 55]. The absorbance at 1593 and 1590 cm^{-1} is associated with the stretching vibration of Mg-OH bonds [56]. This -OH bond comes from the atmospheric water molecule adsorbed on the MgO surface. The presence of C=C bending vibration may be another reason for observing this adsorption band peak, which is assigned to the presence of aromatic group [57]. The FTIR spectra in Fig. 3.16(e) and 3.17(e) show the two small peaks in Ni and Co implanted samples. The observed peaks around 2849-2852 and 2919 cm^{-1} are assigned due to the stretch of the surface -OH group that comes from the dissociated state of hydroxyl groups. C–H stretch of organic residue may be another reason for observing these peaks [53].

This chapter, tuning the bandgap of MgO due to the induction of defects with ion fluences, motivates the making of MgO-based advanced RRAM devices. MgO is a potential binary metal oxide candidate that can be applied as an insulating layer in transition metal oxide (TMO) based RRAM device due to its large bandgap property [58]. It is reported that the trap states in MgO films come from the F centers, the trapping center for electron [59]. Besides, in this chapter, we showed that most of the vacancy defects are due to oxygen

vacancies, and the concentration of these vacancy defects is much higher than the other defects and increases with the increase of ion fluences. So, these anionic vacancies can be applied to form the filament in RRAM device to improve the device's functionality. Since an enormous amount of heat is generated along the ion track during implantation, the effect of annealing on improving the MgO-based RRAM device must be explored.

3.6 Summary

In summary, we have investigated the creation of different kinds of vacancy and substitutional defects in crystalline MgO after one MeV Ni and Co ion implantation. The UV-Vis absorption spectra identified F, F_2, other O_2 vacant center, and V-type color center in the matrix. We found that the F center is more prominent than the V center. The mean concentration of F-type defect states increases with ion fluences. The PL spectra also confirm the existence of the F and V centers. We demonstrated that Ni and Co ion fluence can be used as a controlling knob to tune the defect states to decrease the bandgap of MgO. The metal-assisted defect center is identified from deconvoluted PL spectra, which were absent in pristine. Further, the root cause of the bandgap tuning is understood using band and DOS calculation on the basis of DFT. The electronic transition is also explained with the help of a proposed band model.

We also analyzed the origin of different vibrational modes of pristine and Ni and Co ion-implanted MgO samples. The role of the identified defects from UV-Vis and PL spectra in implanted MgO to induce the vibrational modes is also investigated. The Raman spectra confirm that the Raman scattering peaks come mainly from the breathing modes of D bands. The overlapping of D and G bands becomes prominent with the increment of Ni and Co ion fluences. The DFT calculations confirm that 237, 346, 409, 444, 499 cm^{-1} peaks arise in the implanted samples due to Mg, O vacancy, and Mg substitution by Ni and Co atoms in

the matrix. The phonon band and DOS also yield information about the active mode and the contribution of individual atoms in producing these vibrational peaks. The stretching and bending vibration between Mg, O, and Ni atoms, the identification of functional groups, and the bond criterion are scrutinized by analyzing the FTIR spectra.

Bibliography

[1] C. White, C. McHargue, P. Sklad, L. Boatner, G. Farlow, *Materials science reports* **4**, 41 (1989).

[2] V. Markevich, *Materials science in semiconductor processing* **9**, 589 (2006).

[3] S. Azzaza, *et al.*, *Materials Chemistry and Physics* **143**, 1500 (2014).

[4] A. Akhtar, R. Pilevarshahri, M. R. Benam, *Physica B: Condensed Matter* **502**, 61 (2016).

[5] U. Sharma, P. Jeevanandam, *Journal of Sol-Gel Science and Technology* **75**, 635 (2015).

[6] P. Jeevanandam, K. Klabunde, *Langmuir* **18**, 5309 (2002).

[7] S. F. Bdewi, O. G. Abdullah, B. K. Aziz, A. A. Mutar, *Journal of Inorganic and Organometallic Polymers and Materials* **26**, 326 (2016).

[8] K. Itatani, T. Tsujimoto, A. Kishimoto, *Journal of the European Ceramic Society* **26**, 639 (2006).

[9] T. Kato, G. Okada, T. Yanagida, *Ceramics International* **42**, 5617 (2016).

[10] M. Sterrer, T. Berger, O. Diwald, E. Knözinger, *Journal of the American Chemical Society* **125**, 195 (2003).

[11] X.-Y. Yu, *et al.*, *The Journal of Physical Chemistry C* **115**, 22242 (2011).

[12] A. J. Haes, S. Zou, G. C. Schatz, R. P. Van Duyne, *The Journal of Physical Chemistry B* **108**, 109 (2004).

[13] S.-W. Bian, J. Baltrusaitis, P. Galhotra, V. H. Grassian, *Journal of Materials Chemistry* **20**, 8705 (2010).

[14] P. Tasker, E. Colbourn, W. Mackrodt, *Journal of the American Ceramic Society* **68**, 74 (1985).

[15] J. W. Lee, J.-H. Ko, *Journal of Information Display* **15**, 157 (2014).

[16] N. C. S. Selvam, R. T. Kumar, L. J. Kennedy, J. J. Vijaya, *Journal of Alloys and Compounds* **509**, 9809 (2011).

[17] H. Wu, *et al.*, *Physical review letters* **105**, 267203 (2010).

[18] S. Ramachandran, J. Narayan, J. Prater, *Applied physics letters* **90**, 132511 (2007).

[19] X. Xiang, X. Zu, S. Zhu, C. Zhang, L. Wang, *Nuclear Instruments and Methods in Physics Research Section B: Beam Interactions with Materials and Atoms* **250**, 229 (2006).

[20] A. Gibson, R. Haydock, J. P. LaFemina, *Physical Review B* **50**, 2582 (1994).

[21] G. Kresse, J. Furthmüller, *Physical review B* **54**, 11169 (1996).

[22] G. Kresse, J. Furthmüller, *Computational materials science* **6**, 15 (1996).

[23] P. E. Blöchl, *Physical review B* **50**, 17953 (1994).

[24] J. P. Perdew, K. Burke, M. Ernzerhof, *Physical review letters* **77**, 3865 (1996).

[25] H. Monkshort, J. Pack, *Phys. Rev. B* **13**, 5188 (1976).

[26] P. E. Blöchl, O. Jepsen, O. K. Andersen, *Physical Review B* **49**, 16223 (1994).

[27] E. Ertekin, L. K. Wagner, J. C. Grossman, *Physical Review B* **87**, 155210 (2013).

[28] F. Tran, P. Blaha, *Physical review letters* **102**, 226401 (2009).

[29] J. F. Ziegler, M. Ziegler, J. Biersack, *Nuclear Instruments and Methods in Physics Research Section B: Beam Interactions with Materials and Atoms* **268**, 1818 (2010).

[30] L. A. Kappers, R. L. Kroes, E. B. Hensley, *Physical Review B* **1**, 4151 (1970).

[31] N. Budiredla, A. Kumar, S. Thota, J. Kumar, *International Scholarly Research Notices* **2012** (2012).

[32] T. Mitamura, *et al.*, *Journal of Nuclear Materials* **271-272**, 15 (1999).

[33] P. Devaraja, *et al.*, *Journal of Radiation Research and Applied Sciences* **8**, 362 (2015).

[34] D. Misra, S. K. Yadav, *Scientific reports* **9**, 1 (2019).

[35] C. Trautmann, M. Toulemonde, K. Schwartz, J. Costantini, A. Müller, *Nuclear Instruments and Methods in Physics Research Section B: Beam Interactions with Materials and Atoms* **164**, 365 (2000).

[36] G. Baubekova, *et al.*, *Nuclear Instruments and Methods in Physics Research Section B: Beam Interactions with Materials and Atoms* **463**, 50 (2020).

[37] K. Schwartz, *et al.*, *Nuclear Instruments and Methods in Physics Research Section B: Beam Interactions with Materials and Atoms* **266**, 2736 (2008).

[38] R. A. Ismail, Y. Najim, M. Ouda, *e-Journal of Surface Science and Nanotechnology* **6**, 96 (2008).

[39] D. Roessler, W. Walker, *Physical Review* **159**, 733 (1967).

[40] V. Nefedova, *et al.*, *Applied Physics Letters* **118**, 201103 (2021).

[41] O. Diachenko, *et al.*, *Acta Physica Polonica A* **130**, 805 (2016).

[42] C. Janet, B. Viswanathan, R. Viswanath, T. Varadarajan, *The Journal of Physical Chemistry C* **111**, 10267 (2007).

[43] N. Pathak, P. S. Ghosh, S. K. Gupta, R. M. Kadam, A. Arya, *RSC advances* **6**, 96398 (2016).

[44] A. Gibson, R. Haydock, J. P. LaFemina, *Physical Review B* **50**, 2582 (1994).

[45] T. Athar, A. Hakeem, W. Ahmed, *Advanced Science Letters* **7**, 27 (2012).

[46] A. Weibel, D. Mesguich, G. Chevallier, E. Flahaut, C. Laurent, *Carbon* **136**, 270 (2018).

[47] L. Chen, C. Xu, X.-F. Zhang, *Journal of Molecular Structure: THEOCHEM* **863**, 55 (2008).

[48] H. I. Kurt, E. Ergul, N. F. Yilmaz, M. Oduncuoglu, *Materials Research Express* **6**, 0850f1 (2019).

[49] H. Qiao, Z. Wei, H. Yang, L. Zhu, X. Yan, *Journal of Nanomaterials* **2009** (2009).

[50] G. Balakrishnan, R. Velavan, K. M. Batoo, E. H. Raslan, *Results in Physics* **16**, 103013 (2020).

[51] J. Gourley, W. Runciman, *Journal of Physics C: Solid State Physics* **6**, 583 (1973).

[52] M. Foster, M. Furse, D. Passno, *Surface science* **502**, 102 (2002).

[53] A. Kumar, J. Kumar, *Journal of Physics and Chemistry of Solids* **69**, 2764 (2008).

[54] L. Sharma, R. Kakkar, *ACS applied materials & interfaces* **9**, 38629 (2017).

[55] P. Gao, *et al.*, *Environmental Science: Nano* **3**, 1416 (2016).

[56] N. Jamil, M. Mehmood, A. Lateef, R. Nazir, N. Ahsan, *Advanced Materials-TechConnect Briefs* **1**, 353 (2015).

[57] C. W. Wong, *et al.*, *Journal of Cluster Science* **31**, 367 (2020).

[58] D. Loy, P. Dananjaya, X. Hong, D. Shum, W. Lew, *Scientific reports* **8**, 1 (2018).

[59] F.-C. Chiu, W.-C. Shih, J.-J. Feng, *Journal of Applied Physics* **111**, 094104 (2012).

Chapter 4

Resistive switching effect in ITO/MgO/Ag devices

4.1 Introduction

Advancements in computing performance are essential for the evolution of the next-generation data-driven economy. The data center serves as a repository for vast amounts of data, while personal electronic devices rely on efficient local storage. Therefore, the enhancement of speed and performance in memory devices is crucial to meet the growing demand in today's rapidly advancing information technology landscape. Due to various limitations, such as architecture, switching speed, and density of silicon-based flash memory, researchers and industries have shifted their focus away from such devices. Various alternative systems, including ferroelectric random access memory (RAM) [1], magnetoresistance RAM [2], and RRAM [3, 4], have been proposed to address these limitations and challenges. Among these alternatives, RRAM has garnered significant attention due to its simple fabrication structure, highly scalable cross-point design, fast operation, high-density integration, and the potential for multilevel stacking of structures [5–7]. The operation of the RRAM device is based on abrupt resistance changes, such as those observed in transition metal oxides (TMO), particularly in MgO, transitioning from a high-resistance state (HRS) to a low-resistance state (LRS) and from LRS to HRS. MgO, with its wide bandgap (7.42 eV) [8, 9] and high dielectric constant (9.90) [10], is a promising TMO candidate for use as an insulator layer in memory devices. The wider bandgap of the MgO film is advantageous for achieving sufficient band offset and reducing leakage current in the device. The conduction mechanism in

dielectric-based RRAM is complex, and various models have been proposed to understand the current-voltage behavior [11–14]. Previous studies have demonstrated high retention in annealed MgO-based RRAM devices [15]. Their research explored the impact of annealing on resistance variation, retention, and conduction mechanisms in Ru/MgO/Ta and Ru/MgO/Cu devices. Since RRAM behavior depends on the oxide layer, type of electrodes, and growth mechanism of the active layer, this chapter explores the RRAM properties with the annealing effect in ITO/MgO/Ag devices.

This chapter presents bipolar resistive switching in an ITO/MgO/Ag device, where the oxide layer grown through the RF sputtering technique is sandwiched between the bottom ITO and the top Ag electrode. Both pristine and annealed samples exhibit lower LRS fluctuation than in the HRS state. The annealed sample demonstrates an improvement in the memory window and better endurance over cycles compared to pristine sample. Additionally, the current voltage characteristic is elucidated with the help of the vacancy filamentary model.

4.2 Experimental details

The cleaned ITO substrate was mounted to the RF sputtering system perpendicular to the MgO target (2-inch diameter, 99.99% purity) to deposit the thin films. The substrate-to-target distance was kept fixed at 12 cm during the deposition time. Sputtering parameters, including RF power, reflectance, Ar gas flow rate, base pressure, and deposition pressure, were set at 110 W, 0 W, 15 sccm, 5.27 $\times 10^{-6}$ mbar, and 7 $\times 10^{-3}$ mbar, respectively. Following deposition, one of the as-grown samples (pristine) underwent annealing at 350°C (annealed sample) using a PECVD system at a vacuum of 6.75 $\times 10^{-2}$ mbar. Phase identification of both pristine and annealed MgO samples was carried out using a Rigaku Smartlab X-Ray diffractometer with a Cu K_α source (λ = 1.5418 Å). The top and bottom electrodes

were composed of Ag and conductive ITO, respectively. For electrical characterization, a two-terminal Keithley 2450 source meter was employed to apply voltage pulses, and the current was measured in an ITO/MgO/Ag memory cell with a voltage sweep step of 40 mV. We repeat the I-V measurement up to the 100th cycle to understand the resistive switching and endurance of the device.

4.3 Structural and Morphological Studies

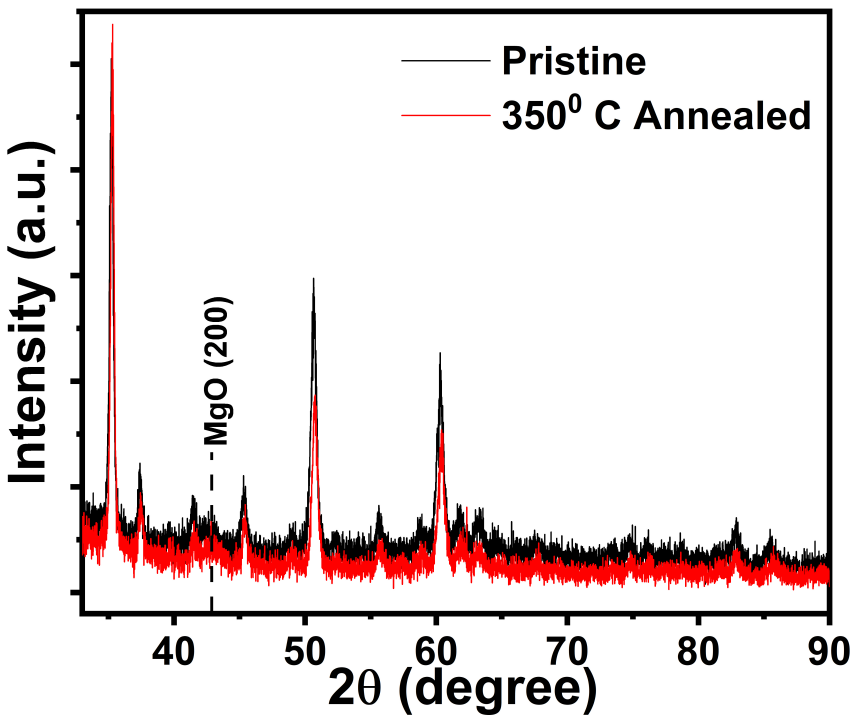

Figure 4.1: The XRD spectra of (a) pristine and (b) 350°C annealed MgO sample.

Figure 4.1 shows the XRD spectra of pristine and 350°C annealed MgO sample. Both the samples exhibit a peak around 42.86°. This indicates the growth of the cubic structure of MgO thin films, confirmed by the JCPDS number 790612. The space group and lattice

parameter are identified as Fm$\bar{3}$m and 4.21 Å, respectively. The other peak corresponds to the ITO substrate upon which the samples are deposited.

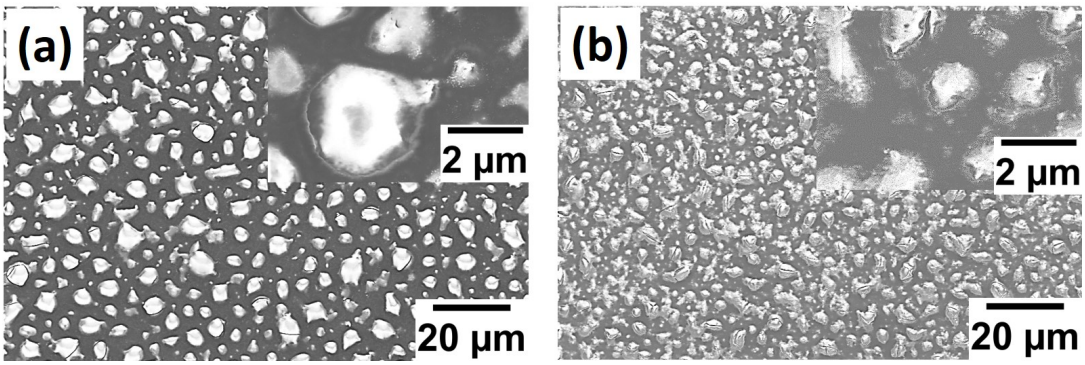

Figure 4.2: The surface morphology of (a) pristine and (b) 350°C annealed MgO sample. The inset shows the magnified morphology of the MgO film in the respective graph.

The surface morphology of pristine and 350°C annealed MgO thin films is checked by FESEM images, as depicted in Fig. 4.2(a) and Fig. 4.2(b), respectively. The MgO cluster forms in both samples. Pristine shows a relatively bigger cluster than the annealed samples. The density of the cluster increases in the annealed samples compared to pristine sample. So, the change in the morphology of MgO thin film after annealing can show different switching behavior than pristine, which is to be investigated.

The surface morphology of pristine and annealed samples is further investigated using AFM images, illustrated in Fig. 4.3(a) and 4.3(b), respectively. The images were taken using the tapping mode over a large-scale area scan of 10 $\mu m \times$ 10 μm. The figure shows that the film is continuous between the clusters all over the surface. The increase in the density of the cluster can be a factor that plays a role in changing the current in the ITO/MgO/Ag device.

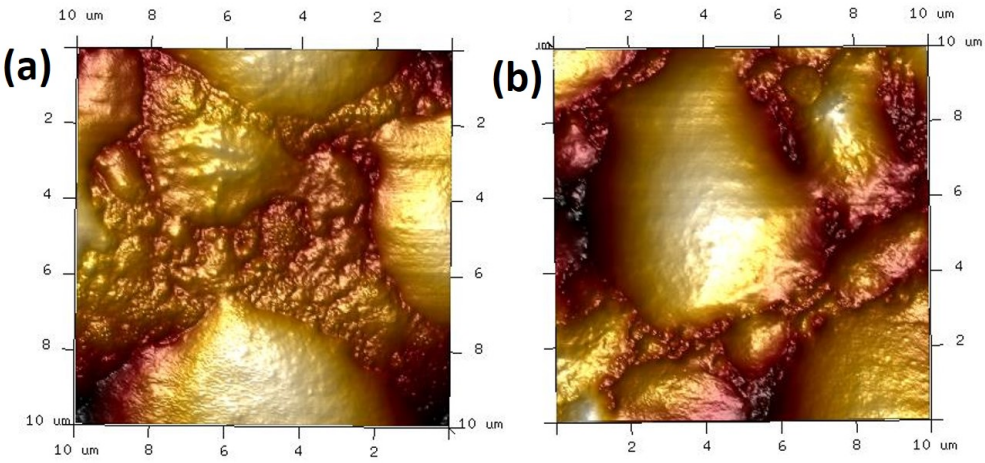

Figure 4.3: The AFM images of (a) pristine and (b) 350°C annealed MgO sample.

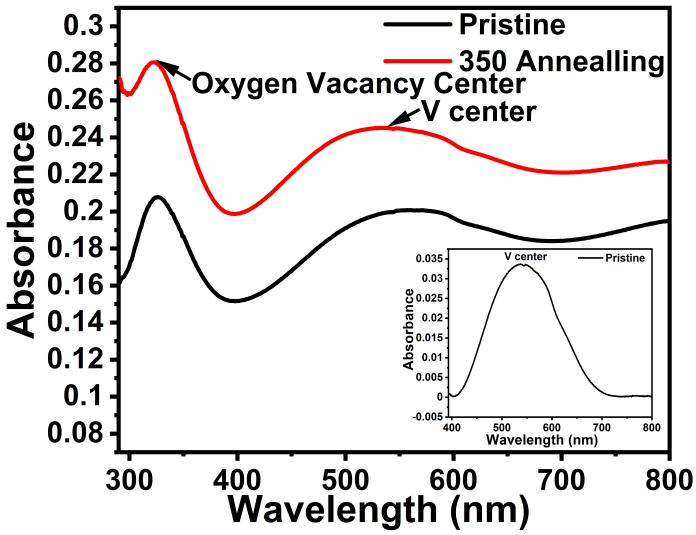

Figure 4.4: The UV-Visible spectra of (a) pristine and (b) 350°C annealed MgO sample. The inset shows the baseline corrected V center of pristine for clear vision.

4.4 Optical Studies

Figure 4.4 shows the UV-visible absorption spectra of pristine and 350°C annealed MgO samples. The two broad absorption peaks at 322 and 550 nm are identified as oxygen and

Mg vacancy center (V center) [8, 9]. The inset shows the V center of pristine after baseline correction. The UV-Vis absorption is improved in the annealed sample. These defects arise in the films during crystal growth. The presence of these defects in the oxide layer can modulate the switching characteristics.

4.5 Resistive Switching Studies

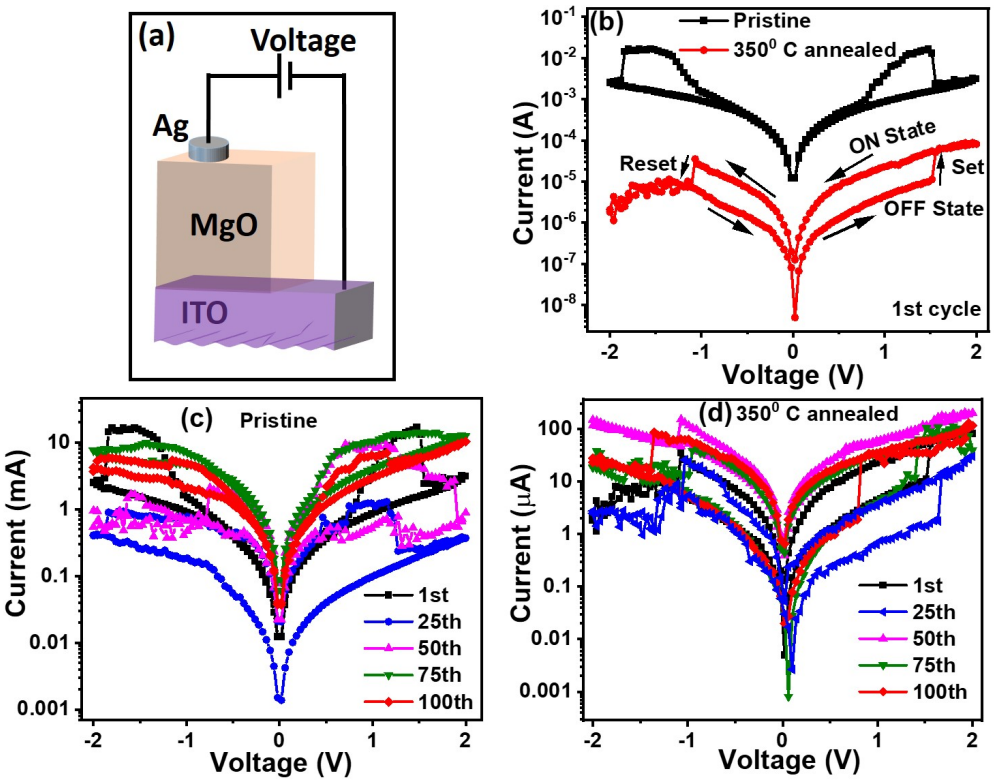

Figure 4.5: (a) The schematic of the wire connection of the ITO/MgO/Ag memristor. (b) The comparison of the I-V curve of 1st cycle for pristine and 350°C annealed sample. The current-voltage curve of the 1st, 25th, 50th, 75th, and 100th cycles of (c) pristine, and (d) 350°C annealed sample.

The schematic of the wire connection of the ITO/MgO/Ag device is presented in Fig. 4.5(a). The top electrode was stressed by bias voltage, and the bottom electrode was kept

grounded. The I-V variation for 1st cycle of pristine and annealed samples is shown in Fig. 4.5(b). The voltage was swept from -2 V $\rightarrow$ 0 V $\rightarrow$ 2 V and 2 V $\rightarrow$ 0 V $\rightarrow$ -2 V. The arrows show the current direction of the device. The device exhibits digital bipolar switching behavior. Pristine shows the clockwise switching, whereas the annealed sample exhibits the anticlockwise switching. We measured the I-V sweeping for bare ITO substrate in the same voltage region, and no switching was observed. This confirms that the resistive switching occurs from the oxide layer. In annealed samples, under positive voltage sweep, the abrupt increase in current from the OFF state to the ON state where the device switches from HRS to LRS is defined as a SET process, observed in Fig. 4.5(b). The device moves to the initial HRS from LRS in the RESET process. The reverse scenario for SET and RESET transition is observed in pristine. The reason may depend on the crystal quality and growth condition. The current reduces from mA to μA order in the annealed sample. The current flow through the top and bottom electrode interface is associated with various conduction mechanisms, and the process is complicated. The possible reason for the decreasing current in the annealed sample is discussed in the current conduction mechanism section. Figures 4.5(c) and 4.5(d) show the typical I-V curves of the 1st, 25th, 50th, 75th, and 100th cycles for pristine and annealed samples, respectively. The memory window is well maintained with digital switching even at the 100th cycle in annealed samples. But, at this cycle, the switching window becomes negligible in pristine (the SET-RESET point is not clear). This indicates the good reproduction of the memory window in the annealed sample. Again, the switching at SET voltage after the forming process is not also reproducible. This signifies that the structural changes that occurred during the forming process after applying the bias can not be fully reversed. The signature of the SET and RESET process becomes weak in pristine sample with increasing the number of cycles. However, the signature was sustained in the annealed sample even at the 100th cycle, as seen in Fig. 4.5(d). The consistency of the digital switching in μA current range up to 100 cycles in the annealed sample signifies

that the annealing improved the device functionality as compared to pristine sample.

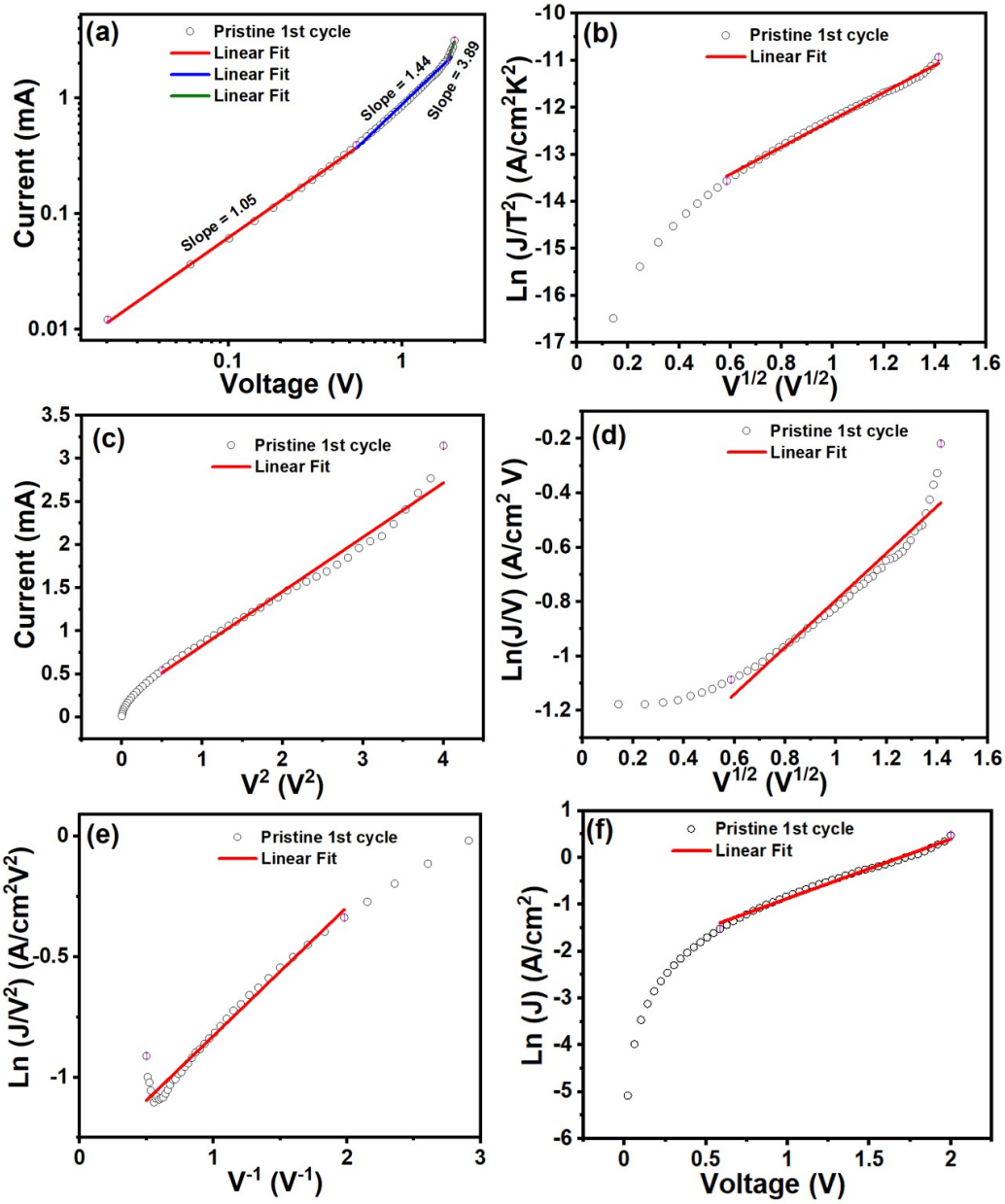

Figure 4.6: (a) The linear fitting of the double logarithmic plot of the 1st cycle of the I-V curve of pristine sample. The I-V curve at a higher field deviates from linear behavior. (b) $\mathrm{Ln}(\frac{J}{T^2}) \propto \mathrm{V}^{\frac{1}{2}}$, (c) $\mathrm{I} \propto \mathrm{V}^2$, (d) $\mathrm{Ln}(\frac{J}{V}) \propto \mathrm{V}^{\frac{1}{2}}$, (e) $\mathrm{Ln}(\frac{J}{V^2}) \propto \mathrm{V}^{-1}$ and (f) $\mathrm{Ln(J)} \propto \mathrm{V}$ plot along with linear fitting for 1st cycle of pristine.

Now, several mechanisms have been proposed to understand the conduction mechanism

through the insulator/metal interface. The popular conduction mechanisms [16, 17] such as, Ohmic conduction ($I \propto V$), Schottky conduction ($ln(\frac{J}{T^2}) \propto \sqrt{V}$), Space Charge Limited Current (SCLC) ($I \propto V^2$), Poole Frenkel (P-F) conduction ($ln(\frac{J}{V}) \propto \sqrt{V}$), Fowler Nordheim (F-N) tunneling ($ln(\frac{J}{V^2}) \propto V^{-1}$), and hopping conduction ($ln(J) \propto V$) are shown in Fig. 4.6(a-f), respectively. The good linear relation between current and voltage (slope = 1.05) at the lower voltage region (0 V to 0.55 V) indicates that ohmic conduction dominates in this voltage sweep region. The Ohmic conduction follows as [18]:

$$I = qA\mu N_c E \exp\left[\frac{-(E_c - E_f)}{kT}\right] \tag{4.1}$$

Where A = conduction area, μ = electron mobility, N_c = effective density of states in the conduction band, E = $\frac{V}{d}$ = applied electric field, d = film thickness, E_c = Energy level at the bottom of the conduction band, E_f = Fermi energy level, k = Boltzman constant, T = Absolute temperature. The Ohmic conduction arises at this lower voltage region due to the generation of a small number of mobile charge carriers in the conduction band by thermal excitation. The deviation from linear behavior at higher voltage sweeping region (0.55 V to 2 V) confirms that the other mechanism dominates over the ohmic behavior. The switching from HRS to LRS occurs in the high-voltage sweeping region that can fall in the hopping conduction region. Good linear fitting, as shown in Fig. 4.6(f), signifies that hopping conduction can occur. The hopping conduction is a bulk-dominated mechanism. In this mechanism, the trapped electron tunnels from one trap state to other trap states in thin dielectric films. On the other hand, the electrode-dominated Schottky relation shows a better linear fitting in the high-voltage region compared to SCLC, P-F, and F-N mechanism, as seen in Fig. 4.6(b). Besides, in the present study, a low electric field ($8 \times 10^6\ Vm^{-1}$) was stressed, which is lower than the limiting value to start the F-N conduction over the whole bias sweeping region. This rules out the F-N conduction mechanism. Hence, the Schottky emission (SE) plays a role in resistive switching at the MgO/Ag interface when

the thermally activated electrons jump to the conduction band (CB) after gaining sufficient energy. The following relation governs the current conduction in SE:

$$I = AD^{*}T^{2}exp\left[-q\phi_{B} + \frac{q}{kT}\sqrt{\frac{qE}{4\pi\epsilon_{i}}}\right] \tag{4.2}$$

Where, D^{*} = Effective Richardson constant ($\frac{4\pi q m_{n}^{*} k_{0}^{2}}{h^{3}}$), q = electric charge, ϕ_{B} = Schottky barrier, ϵ_{i} Dielectric constant of MgO. The Schottky barrier in pristine is 0.35 eV. The ϕ_{B} value increases to 0.51 eV in the annealed sample. The increase of the barrier height and the modification of surface morphology after annealing, as observed in the AFM images, may be incorporated into the decrease in the current in annealed samples. Day et al. [19] reported that the majority of charge carriers in MgO are positive, which are considered as holes. The Schottky junction formed at the ITO/MgO interface, observed by Jambois et al. [3]. So, in our case, the symmetric behavior of the resistive switching curve for both polarities suggests that the active bulk layer is mainly contributing to the current limitation and not by the electrode. Also, the forming step strongly depends on the thickness of the oxide layer. Hence, the above discussion suggests that the sudden increase in current at the SET voltage occurs due to the formation of conductive filaments in dielectric MgO.

The cycle-dependent percentage of resistive switching (RS) ratio at the positive and negative voltage for pristine and annealed samples are shown in Fig. 4.7(a) and 4.7(b), respectively. The figure shows that the RS ratio decreases for pristine at both positive and negative bias. However, the RS abruptly increases at cycle number 25th, decreases at the 50th cycle, and then continuously increases in the annealed sample for both positive and negative polarity. The nonlinear behavior of RS suggests that the rapid variation in RS ratio is incorporated with the bulk effect of MgO. This can also be associated with vacancies in the vicinity of the interface during conduction in the filamentary model [20]. So, these results suggest that the bulk-dominated RS happens due to the formation and rupture of

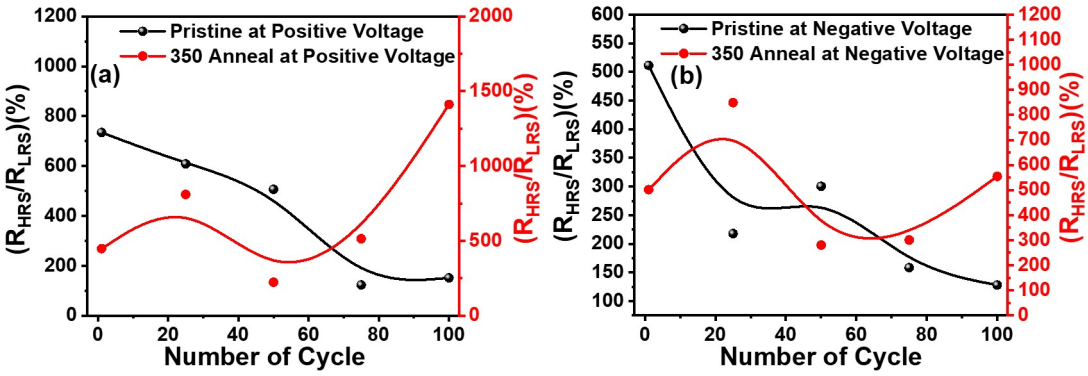

Figure 4.7: The comparison of percentage change of $\frac{R_{HRS}}{R_{LRS}}$ with increasing cycle number at SET and RESETpoint for pristine and 350°C annealed sample at applied (a) positive and (b) negative bias.

vacancy filament in MgO.

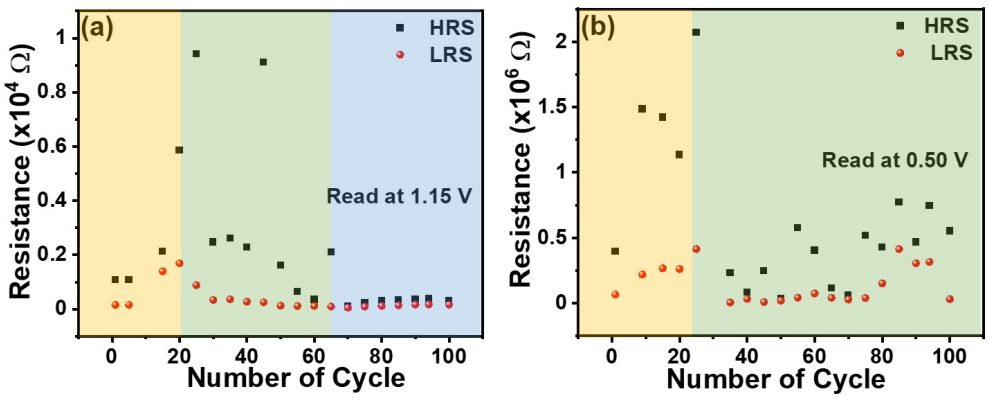

Figure 4.8: The endurance performance of the memristor associated with (a) pristine and (b) 350°C annealed sample.

The endurance properties of the RRAM device for pristine and annealed samples are tested up to 100 cycles, as shown in Figures 4.8(a) and 4.8(b), respectively. The HRS and LRS were measured at 1.15 and 0.50 V for pristine and annealed samples, respectively. The difference between HRS and LRS up to the 25th cycle is higher in the annealed sample compared to pristine (marked as a yellow region in Fig. 4.8). After that, this difference

is reduced for both samples. Pristine sustains the difference up to the 65th cycle (marked as green region) and nearly vanishes after the 70th cycle (blue region in Fig. 4.8(a)). In contrast, the annealed sample clearly holds the difference between the HRS, and LRS states up to the 100th cycle (a green region in Fig. 4.8(b)). Hence, an ON-OFF ratio is maintained in the annealed sample at the higher cycle, whereas the ratio is nearly one in pristine. This suggests that the endurability degrades more quickly in pristine with cycle, but it sustains in the annealed samples at the 100th cycle.

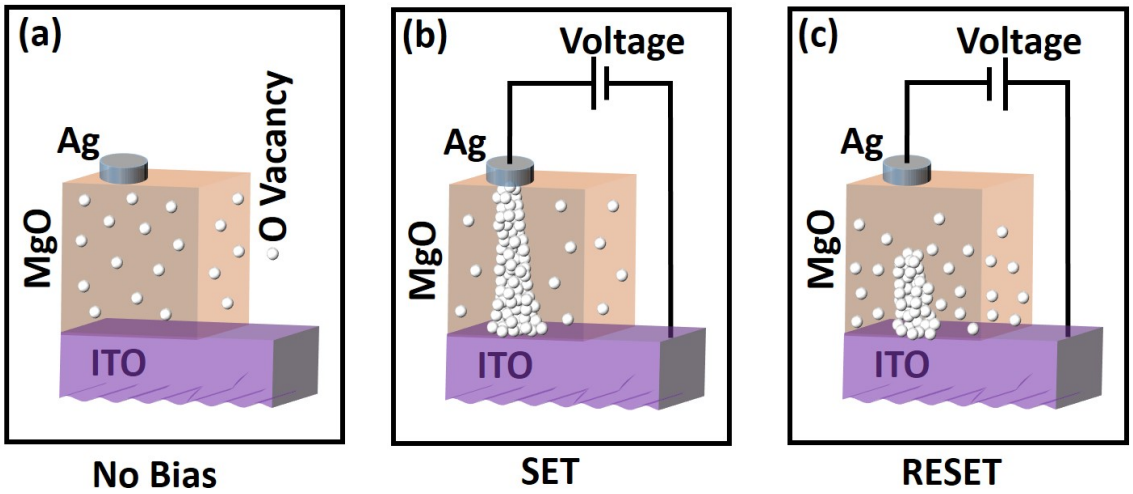

Figure 4.9: The schematic drawn of the filamentary model at (a) zero bias, (b) SET (complete filament formation), and (c) RESET (rupture of the filament) condition of the MgO-based RRAM device.

A higher fluctuation of HRS than the LRS is observed in both devices. This means that LRS is more stable than the HRS. In this case, more than 100 switching cycles are required to construct a stable switching state due to the high fluctuation in OFF states. The non-reproducibility of the structural changes after the forming process, the non-linearity in the RS ratio, and the sudden increase or decrease of the resistance state indicate that the rupture and formation of the vacancy filament in the bulk oxide control the resistive switching characteristics in the device. The filamentary model at zero bias, SET, and RESET process

are shown in Fig. 4.9(a-c), respectively. The conduction mechanism in HRS and LRS states implies that the current in the ON state is due to the local phenomenon in the bulk rather than uniform distribution. On the other hand, the hopping conduction mechanism gives the idea that traps in bulk can also assist in current flow in the formed conductive filaments. The sudden increase in current at SET voltage is due to the complete formation of filaments. In zero-bias conditions, no filament formation takes place rather, we assume that the vacancy centers (as seen in UV-Vis spectra) are randomly distributed in the films. In the annealed sample, when sufficient positive bias is applied on the top electrode, the oxygen vacancies and ions are formed. At the same time, the oxygen ions will attracted to the top electrode due to a higher drift velocity than vacancies. Hence, the accumulation of the vacancies starts to build a filamentary path inside the oxide layer. On the other hand, the formation energies of oxygen vacancies are less than the Mg vacancies [21]. So, it is energetically favorable to produce the oxygen vacancy enormously under bias voltage. Wang et al. [22] showed that the conductive path mainly consists of oxygen vacancy. The filament formation is completed between the top and bottom electrodes when the oxygen vacancy density is sufficiently high, and the applied voltage reaches the SET voltage, as shown in Fig. 4.9(b). At this SET condition, the current suddenly jumps. On the other hand, when the reverse electric field is applied on the top electrode, the oxygen ions are repelled out from the top electrode and migrate back towards the bottom electrode. During migration, the ions recombine with the vacancies, and the conductive filament is ruptured when the bias reaches the RESET voltage. Hence, at this RESET voltage, the resistance increases, and the current abruptly drops down. Pristine follows the opposite mechanism. The rupture of the filament depends on the magnitude of the applied field and the filament temperature that arises due to Joule heating. The low current flow in the annealed sample suggests the lower Joule heating during conduction to improve the device functionality. Hence, the current conduction in the ITO/MgO/Ag device occurs due to the formation and

rupture of the vacancy filament at the SET and RESET points. The above investigation suggests a better memory window for annealed samples till the 100th cycle, while this property degrades significantly in pristine at this cycle. The increase in the barrier height with annealing reduces the current, which suggests a lower Joule heating effect in the device for better switching applications.

4.6 Summary

In conclusion, we investigated the effect of annealing in improving the MgO-based digital bipolar resistive switching device where the oxide layer was sandwiched between the bottom ITO and top Ag electrode. We successfully demonstrated that the Schottky barrier developed at the ITO/MgO and MgO/Ag interface. The clockwise and anti-clockwise switching is observed in pristine and annealed samples, respectively. The increase in barrier height decreases the current conduction in the annealed sample for better device applications. The better reproducible memory window till the 100th cycle is sustained in the annealed sample, where this property reduces significantly in pristine. The OFF-ON ratio during the endurance test was observed in the annealed sample up to the 100th cycle. This ratio becomes nearly one in pristine at the higher cycles. The LRS shows more stability than the HRS in both samples. The current conduction in the device is proposed by a bulk-dominated vacancy filamentary model for the switching at the SET and RESET voltage. The probability of hopping conduction suggests the tunneling of the trapped electron from one trap site to another trap site. The sustainable endurance for higher cycles and stable resistive switching between HRS and LRS of the annealed sample can be suitable for storing data for long periods of time without losing information.

Bibliography

[1] Y. Arimoto, H. Ishiwara, *Mrs Bulletin* **29**, 823 (2004).

[2] S. Tehrani, *et al.*, *Proceedings of the IEEE* **91**, 703 (2003).

[3] O. Jambois, P. Carreras, A. Antony, J. Bertomeu, C. Martínez-Boubeta, *Solid state communications* **151**, 1856 (2011).

[4] H.-H. Huang, W.-C. Shih, C.-H. Lai, *Applied Physics Letters* **96**, 19 (2010).

[5] I. Baek, *et al.*, *IEDM Technical Digest. IEEE International Electron Devices Meeting, 2004.* (IEEE, 2004), pp. 587–590.

[6] P. Sun, *et al.*, *Scientific reports* **5**, 13504 (2015).

[7] A. Sawa, *Materials today* **11**, 28 (2008).

[8] S. Bhakta, P. K. Sahoo, *Applied Physics A* **128**, 990 (2022).

[9] S. Bhakta, S. Pradhan, A. K. Nandy, P. K. Sahoo, *Journal of Electronic Materials* **52**, 1937 (2023).

[10] M. Subramanian, R. Shannon, B. Chai, M. Abraham, M. Wintersgill, *Physics and chemistry of minerals* **16**, 741 (1989).

[11] F.-C. Chiu, S. Mondal, T.-M. Pan, *High-k Gate Dielectrics for CMOS Technology* pp. 111–184 (2012).

[12] Y. C. Yeo, *et al.*, *IEEE Electron Device Letters* **21**, 540 (2000).

[13] C. Chen, F. Pan, Z. Wang, J. Yang, F. Zeng, *Journal of Applied Physics* **111**, 1 (2012).

[14] Q. Liu, *et al.*, *Applied physics letters* **92**, 1 (2008).

[15] D. J. J. Loy, P. A. Dananjaya, X. L. Hong, D. Shum, W. Lew, *Scientific reports* **8**, 14774 (2018).

[16] N. Thankachen, U. Chhaya, A. Tripathi, U. Joshi, *Physica Scripta* **98**, 035829 (2023).

[17] S. Chang Lee, *et al.*, *Journal of Applied Physics* **114**, 6 (2013).

[18] J. Lee, F. Chiu, P. Juan, *Handbook of Nanoceramics and Their Based Nanodevices* **4**, 159 (2009).

[19] H. R. Day, *Physical Review* **91**, 822 (1953).

[20] U. Joshi, *et al.*, *Journal of Applied Physics* **105**, 7 (2009).

[21] A. Gibson, R. Haydock, J. P. Lafemina, *Physical Review B* **50**, 2582 (1994).

[22] Z. Wang, *et al.*, *IEEE electron device letters* **32**, 1442 (2011).

Chapter 5

Third order non-linear optical properties of NiO thin films

5.1 Introduction

The transparent conductive oxide (TCO) thin films, which have a meticulous combination of optical transparency and optical conductivity, attracted researchers due to low-cost optoelectronic devices [1]. Transparent semiconducting material has extensive application on architectural windows, solar cells, heat reflectors, light transparent electrodes, thin-film photovoltaics, etc. Among various TCO materials, NiO is one of the promising candidates for making optoelectronic devices due to (i) p-type semiconductor with transparent conductivity [2] and (ii) the modulation of conductivity by phase deviation from stoichiometry and/or adding a doping element in the material [3, 4]. Due to clear switching events, good reversibility, 3D staking compatibility, and simple constitution, NiO can be used as a resistive random access memory device [5]. NiO also exhibits various excellent properties, such as catalytic [6], magnetic [7], electrochromic [8], optical and electrochemical characteristics [9], transparent p-type semiconducting layer for applications in smart windows [10], electrochemical supercapacitors [11] and dye-sensitized photocathode [12]. Controlling the intensity of laser light and lowering the optical losses are major challenges in optical technology. High and low power illumination on NiO thin films can provide various kinds of nonlinear applications. Intense lasers with optical nonlinearity can be useful for optical bistability-based memory elements, switches, and saturable absorbers applications. Positive and negative nonlinear absorption coefficient-associated materials have huge potential

in optical limiting and saturable absorber device applications. Optical limiting material is transparent for low-input intensities and relatively opaque for high-level inputs. Optical limiters can provide safety to optical detectors, sensors, and human eyes. On the other hand, the saturable absorber is applied in passive mode-locking or Q-switching applications [13]. To achieve this, materials with absorption optical nonlinear behavior are required. Magnetically tuned absorptive nonlinear properties in NiO thin films and the consequence of sign reversal optical nonlinearity due to annealing in ion beam sputtered NiO are observed [13, 14]. The third-order nonlinearity (TONL) in Tin-doped NiO films is extensively investigated [15]. The TONL in spin-coated N doping NiO films is observed using the Z-scan technique [16]. So, the investigation of the threshold temperature in third-order optical nonlinearity of sputtered-grown NiO films for optical limiting applications needs to be explored.

In the present chapter, we demonstrated the variation in nonlinear properties of as-grown and 300-500°C annealed NiO thin films using the Z-scan technique. We successfully showed that SPR has no contribution to change in nonlinearity. On the other hand, we explained the SA and RSA on the basis of Ni d-d and Ni-d to O-p transition in the TPA process and correlated to the shifting of Ni-$d_{x^2-y^2}$ and Ni-d_{z^2} orbitals in CB (also responsible for increasing bandgap) using DFT calculations.

5.2 Experimental details

The RF sputtering technique was utilized to grow the 150 nm thick NiO thin films on the cleaned glass substrate (the cleaning process is described in Chapter 2) at room temperature. The 2-inch diameter of NiO target of purity 99.99% was used in the sputtering system to deposit the films. The substrates were kept at a distance of 7.5 cm from the target. The base pressure, working pressure, RF power, and reflectance were 6.57 $\times 10^{-6}$ mbar, 5 $\times 10^{-3}$

mbar, 80 W, and 0 W, respectively. We deposited NiO on the substrate for 30 min. The sputtering gas was high-purity Ar gas (99.99%) to react with the target at a flow rate of 15 sccm. Then, we anneal the sputtered grown NiO thin films at the temperature of 300, 350, 400, 450, and 500 °C (annealed samples) in a vacuum of pressure 2.13 $\times 10^{-2}$ mbar using the PECVD system. The surface morphology of as-grown and annealed samples was examined using the FESEM system. The crystal structure and phases of the thin films were investigated by analyzing the X-ray diffraction (XRD) spectra using the Rigaku Smartlab X-Ray diffractometer with Cu K_α source ($\lambda = 1.5418$ Å). The optical absorbance spectra for the as-grown and annealed samples were taken using the UV-Vis-NIR spectrometer. The spectra were taken at room temperature in transmission mode in the 300-800 nm wavelength range. The PL spectra were carried out at room temperature by He-Cd laser excited at 325 nm in the wavelength range of 330-700 nm. The steady-state spectra were collected through the same objective lens. The CL measurements were carried out at room temperature using the Monarc-P (GATAN) high-resolution CL detector integrated with the FESEM system. The scanning over the 1×1 μm area of NiO thin film was done with an accelerating voltage of 15 KV during CL measurements. The third-order non-linear optical properties of the thin films were investigated using the single-beam Z-scan technique. The schematic of the standard Z-scan experimental setup utilized for the measurement is shown in Fig. 2.17 in Chapter 2. In our case, the laser pulses were delivered from the fs-pulsed laser. To avoid the sample heating, we used the femtosecond laser at a repetition rate of 100 KHz with a pulse duration of 370 fs. The laser beam is brought to focus on the sample by a converging lens, which has a spot radius of w_0 = 32 μm with a power of 5 mW. The spectra were taken in two modes: open aperture (OA) and closed aperture (CA). In OA conditions, the photodetector directly collected the total transmitted power. The partial transmittance from the films was detected in CA conditions. The non-linear absorption coefficient and refractive index were calculated in OA and CA conditions, respectively. The sample was

translated across the focal point of the converging lens along the z-axis during the beam exposure by a motorized translation stage.

5.3 Computational Details

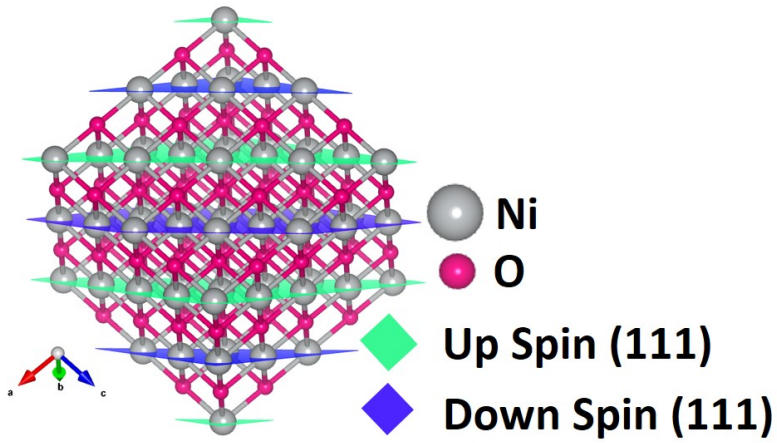

Figure 5.1: The NiO crystal structure of pristine, used in DFT calculation.

The DFT calculation of bandstructure and DOS of NiO is carried out with the VASP code [17] using the PAW potentials [18] and the semi-local PBE exchange-correlation functional [19]. In our case, we implemented the GGA along with onsite Coulomb repulsion corrections (Hubbard U correction) in Ni-d orbitals for all the calculations [20]. NiO is a rocksalt cubic structure with a space group of Fm$\bar{3}$m. A 64-atom supercell for the antiferromagnetic arrangement of NiO along the (111) plane was taken for the calculation, as shown in Fig. 5.1. The experimentally found lattice parameter was utilized for calculating band structure and DOS for pristine and annealed samples. The atomic configuration of NiO was optimized under a conjugate gradient scheme, and the only atomic position relaxation without changing cell shape and cell volume was completed when the force for each atom was less than 1×10^{-4} eV/Å. The relaxed structure was employed for the self-consistent calculation to attain the convergence result using the plane-wave basis set with a cutoff energy of

500 eV and a Monkhorst k-point mesh of $7 \times 7 \times 7$. The convergence was accomplished when the total energy approached the threshold of 1×10^{-7} eV. The tetrahedron method with Blochl corrections was applied for DOS calculations [21].

5.4 Surface Morphology and Structural Analysis

5.4.1 SEM study

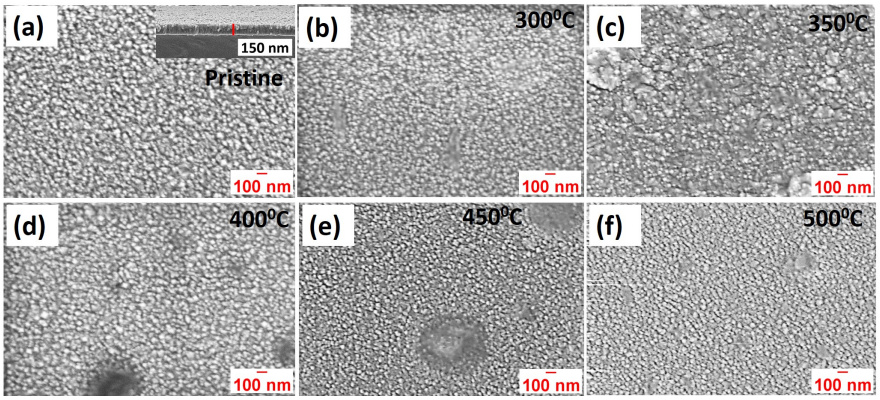

Figure 5.2: The surface morphology of (a) pristine and annealed samples at (b) 300, (c) 350, (d) 400, (e) 450 (f) 500°C. The inset of (a) shows the thickness of pristine sample.

The surface morphology of as-grown (pristine) NiO and the samples annealed at temperatures of 300, 350, 400, 450, and 500°C is shown in Fig. 5.2(a-f), respectively. The film thickness of pristine sample is found to be 150 nm, shown in the inset of Fig. 5.2(a). It has been observed that the surface of the samples is uniform, and small black spots appear in the annealed sample, which is not present in pristine. This black spot can originate as the nucleation center during annealing.

5.4.2 XRD Analysis

The XRD pattern of pristine and thermally annealed samples at a temperature of 300, 350, 400, 450, and 500°C are shown in Fig. 5.3(a). There is a peak shift in the annealed samples compared to pristine. The peaks observed for 500°C annealed sample at 37.24, 43.28,

62.84, 75.38, 79.46° matches well with the JCPDS number 780429. These peaks correspond to the 111, 200, 220, 311, and 222 planes with the FCC structures having a space group of Fm$\bar{3}m$. The corresponding peak position along these planes for pristine is identified at 36.41, 42.37, 61.50, 73.82, 77.71°. The shifting of the XRD peak position with the increase of annealing temperature happens due to the release of stress and strain in the system. Fig. 5.3(b) shows the variation of crystallite size and microstrain with annealing temperature. The temperature for pristine sample is considered as the room temperature (25°C) throughout the chapter. The crystallite size is calculated utilizing the Scherrer equation [22] by fitting the XRD peak using the Gaussian function.

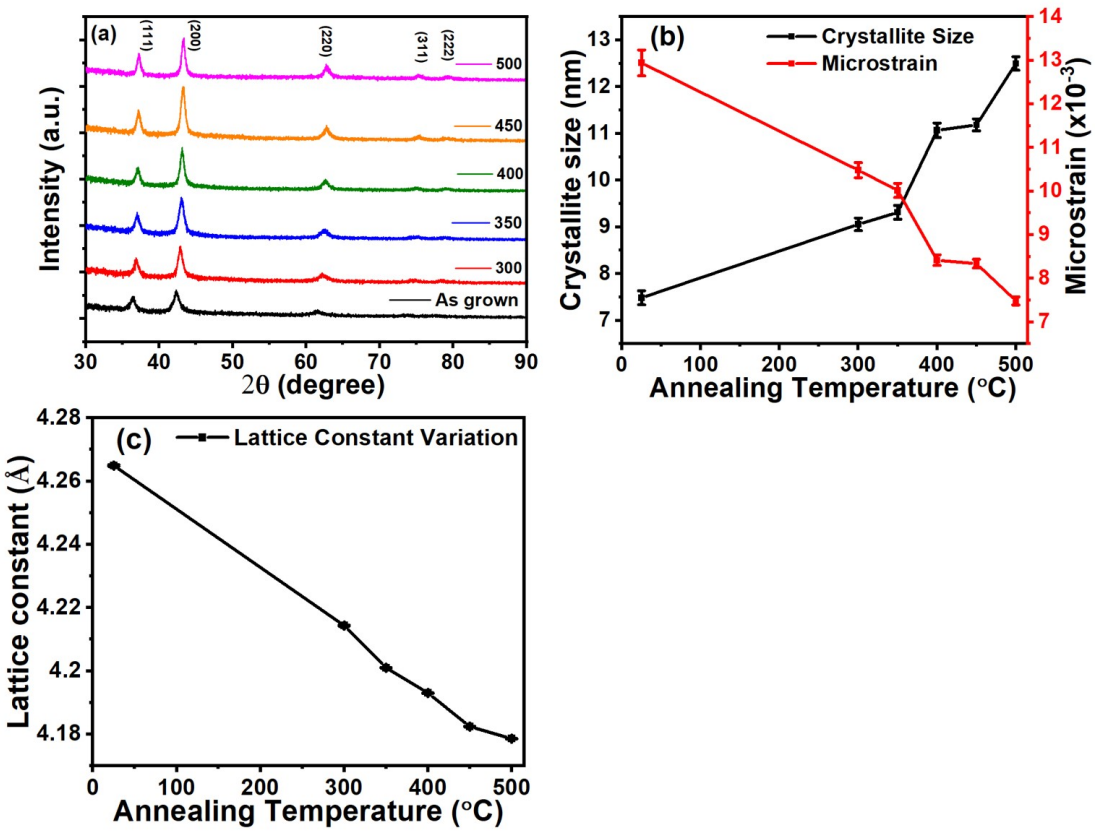

Figure 5.3: (a) The XRD patterns of pristine and annealed NiO thin film at 300, 350, 400, 450, and 500°C, (b) The variation of crystallite size and microstrain with annealing temperature, (c) The decrement of lattice constant with annealing temperature.

$$D = \frac{K\lambda}{\beta cos\theta} \tag{5.1}$$

Where, K = Scherrer constant (0.9), λ = Cu K_α radiation wavelength (0.154 Å), β = FWHM of the diffracted peak in radians, θ = Bragg's diffraction angle in radians. The strain (ϵ) is calculated using the following equation:

$$\epsilon = \frac{\beta}{4tan\theta} \tag{5.2}$$

Equation 5.2 indicates that strain depends on the diffraction peak position and FWHM of the peak. The crystallite size increases with annealing temperature while the strain decreases. The increment of crystallite size and decrement of strain affect in shifting the peak position toward the exactitude position of NiO than pristine. Since the strain decreases with annealing temperature, it is expected that the vacancy defects will decrease significantly at the highest annealing temperature [22]. The lattice constants (a) are evaluated using the following equation:

$$a = d_{hkl} \times (h^2 + K^2 + l^2)^{\frac{1}{2}} \tag{5.3}$$

Where d_{hkl} is the inter-planner distance, and h, k, l are the miller indices of the plane. d_{hkl} is calculated using Bragg's equation [23]. The variation of lattice constant with annealing temperature is presented in Fig. 5.3(c). The lattice constant decreases monotonically with the increase of annealing temperature. There is a drastic change in lattice constant from pristine (4.26 Å) to 300°C annealed sample (4.21 Å), which can also affect the shifting of the XRD peak position. The lattice constant for the 500°C annealed sample is 4.17 Å, matching exactly with the JCPDS file. The strain, shifting of peak position, and lattice parameters are improved greatly by increasing the annealing temperature of the grown films, which concur with the standard JCPDS. So, the amelioration of these parameters can affect

the optical and nonlinear properties of NiO thin films.

5.5 Optical Studies

5.5.1 UV-Vis Analysis

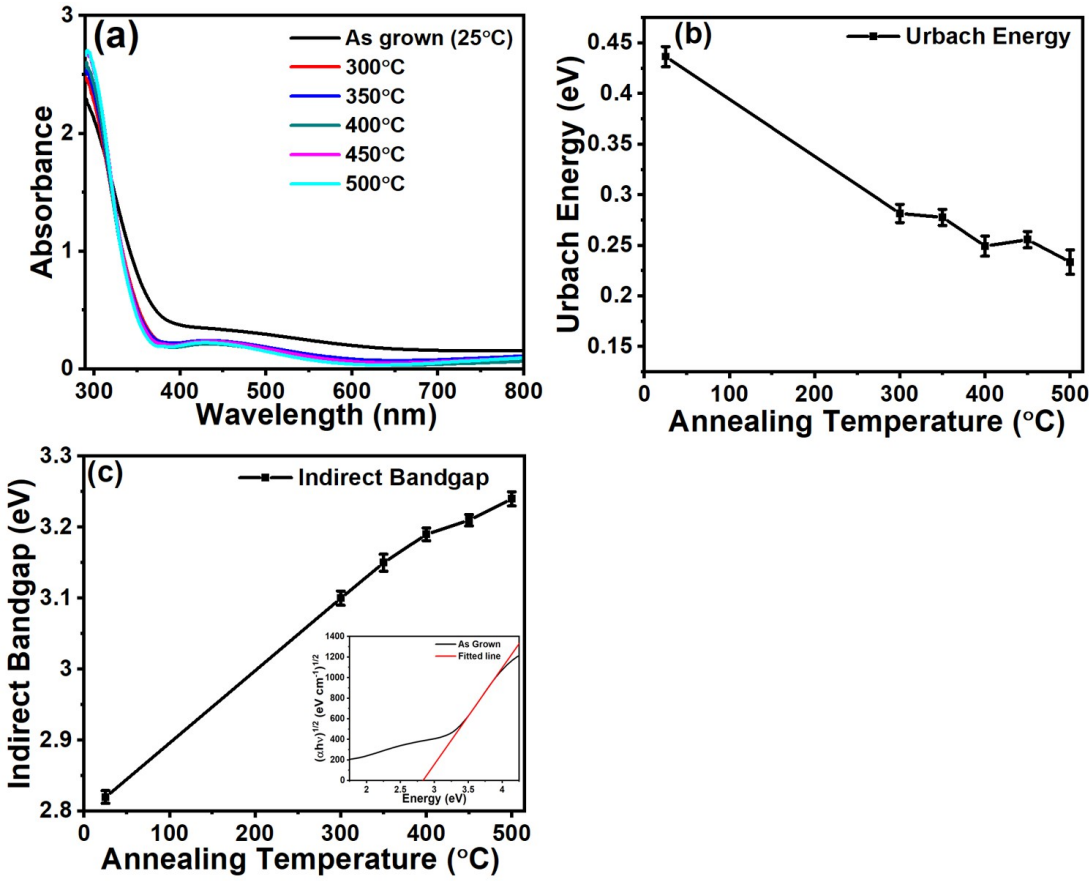

Figure 5.4: (a) The UV-Vis absorbance spectra for pristine and annealed samples, the variation of (b) Urbach energy, and (c) indirect bandgap of NiO with annealing temperature. Inset of (C) shows the typical Tauc plot of as-grown sample.

The UV-Vis absorption spectra are investigated in the wavelength range of 300 - 800 nm, shown in Fig. 5.4(a). The spectra show that the absorption edge for the bandgap of NiO is in the UV region. Another broad absorption peak is observed at 447 nm. The change in the Urbach energy with annealing temperature is shown in Fig. 5.4(b). The Urbach energy

is characterized using the following equation [24]:

$$ln(\alpha) = \frac{h\nu}{E_u} + ln(\alpha_0) \tag{5.4}$$

Where, α is the absorption coefficient, $h\nu$ is the incident photon energy, E_u is Urbach energy, α_0 is a constant. The reciprocal of the slope of the linear fitting of $ln(\alpha)$ vs energy will give the Urbach energy. The Urbach energy decreases with the increment of annealing temperature. The reduction of Urbach energy signifies that the lattice defects and disorders decrease with annealing temperature. The E_u value changes drastically from pristine to 300°C annealed sample. This means that pristine contains a lot of defects and disordered states. The lower value of E_u proposed the narrowing band tails and localized states within the conduction and valance band, predicting the increment of the bandgap. Furthermore, the lower value of Urbach energy signifies the lower amount of dislocation density within the system and vice versa. The decreasing of dislocation density can also be noticed from the increasing trend of crystallite size, calculated from XRD spectra. The variation of bandgap with annealing temperature is presented in Fig. 5.4(c). The bandgap increases with the increment of annealing temperature, as predicted. The bandgap is calculated using the Tauc equation (equation 3.4) [25]. The typical Tauc plotting for pristine is shown in the inset of Fig. 5.4(c). The indirect bandgap of pristine NiO is evaluated to 2.82 eV, which is increased to 3.24 eV for 500°C annealed sample. The decrease of defect, disorder, and dislocation density with the increment of annealing may be responsible for the increment of bandgap. The increase of crystallite size and reduction of lattice constant toward the standard value of NiO also play a crucial role in the increment of the bandgap of NiO.

5.5.2 PL Analysis

PL emission is very sensitive and depends on film quality and the presence of defects in the system. The PL spectra for pristine and thermally annealed samples are shown in Fig.

5.5(a). The typical deconvoluted spectra for pristine can be observed from Fig. 5.5(b). The spectra are deconvoluted into three peaks at 413, 524, and 572 nm.

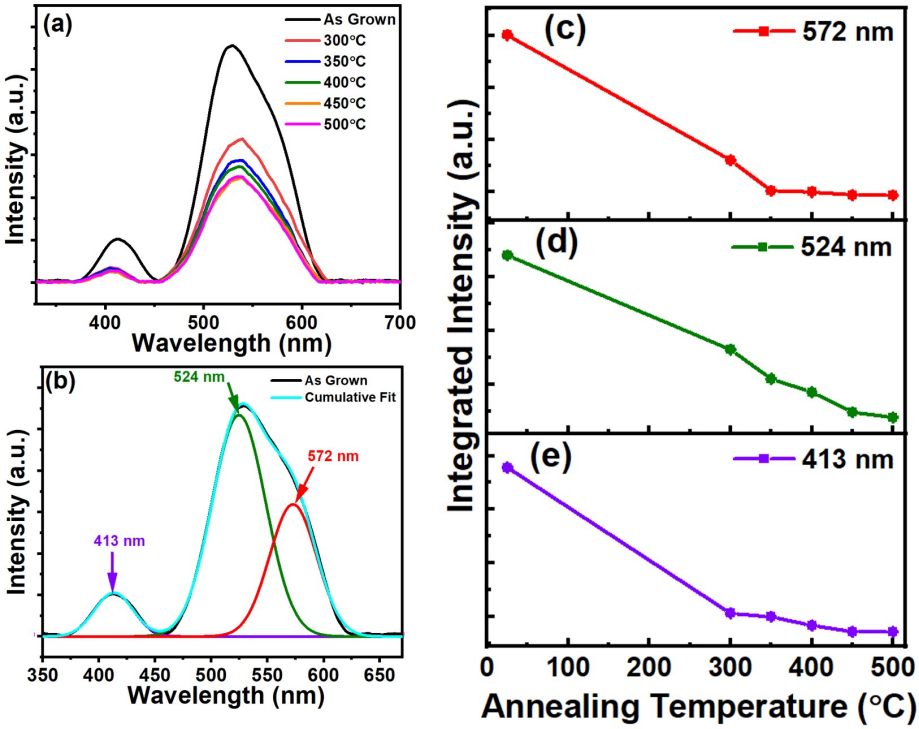

Figure 5.5: (a) The PL spectra of pristine and annealed samples, (b) The typical deconvoluted spectra of pristine, The integrated intensity variation with annealing temperature for (c) 572 nm, (d) 524 nm and (e) 413 nm, respectively.

The band emission peak at 413 nm (3.00 eV) can be attributed to defect-related deep-level emission due to oxygen vacancy [26]. The insignificant shifting of this emission peak is observed, and the disorder and defects reduce gradually with annealing associated with this peak, as seen in Fig. 5.5(e). The visible emission at 524 nm can correspond to the inter-band transition surface states due to oxygen vacancy, Ni interstitial defects, and incomplete bond formation [27]. The 572 nm peak also originated due to the presence of oxygen vacancies in NiO thin films [28]. The variation of the integrated intensity for the emission of 572, 524, and 413 nm are shown in Fig. 5.5(c-e), respectively. The integrated intensity decreases with annealing temperature for visible and blue emissions, signifying that the

defect states reduce with annealing temperature. This also concurs with the variation of Urbach energy evaluated from UV-Vis spectra. The drastic change in the integrated intensity from pristine to annealed samples occurred due to the rapid change in lattice parameters and Urbach energy.

5.5.3 CL Analysis

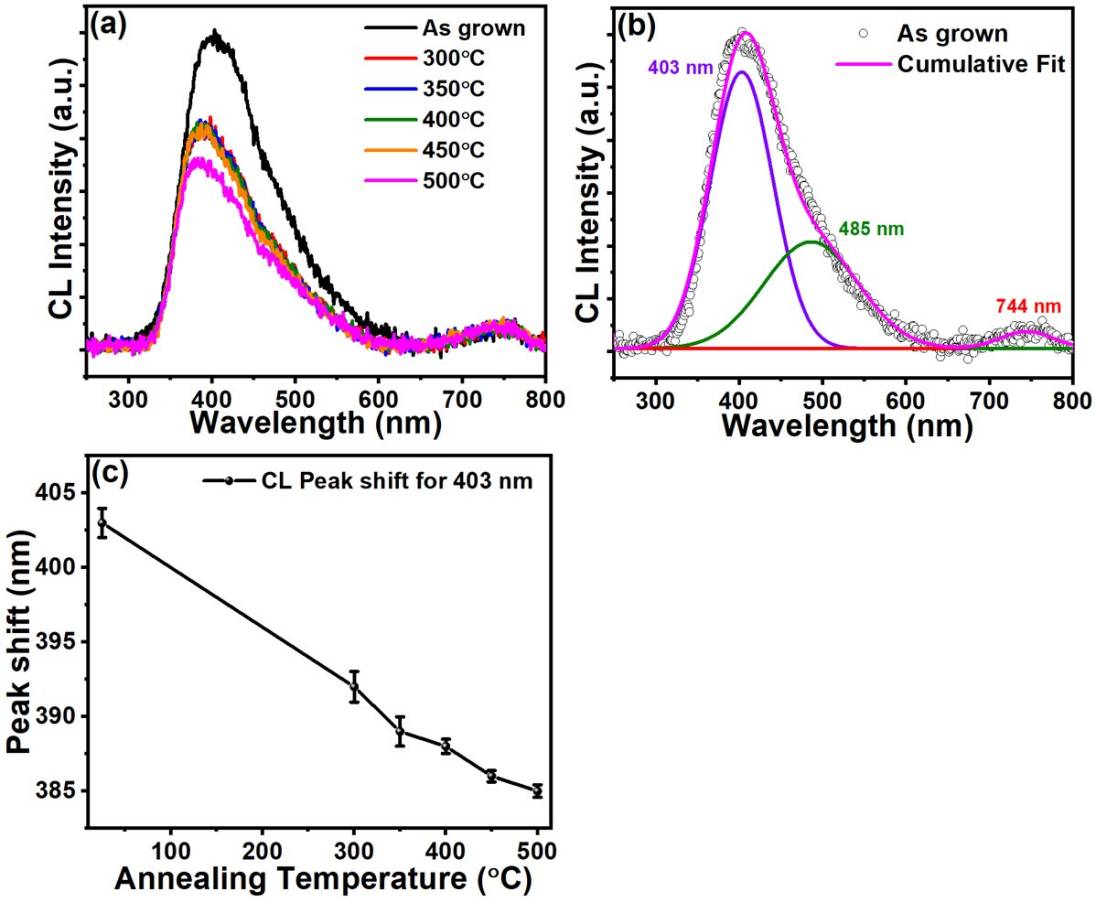

Figure 5.6: (a) The CL spectra of pristine and annealed samples, (b) The typical deconvoluted spectra of pristine, (c) The shifting of the 403 nm peak position with annealing temperature.

Fewer studies on CL signals have been done to analyze the defect-related properties of annealed NiO samples. Luminescence in NiO is correlated to different defects and impurities present between CB and VB. The CL spectra of pristine and annealed samples are

shown in Fig. 5.6(a). Two peaks are observed in the spectra, as seen in Fig. 5.6(a). The CL spectra are deconvoluted into three peaks at 403, 485, and 744 nm. The typical deconvoluted spectra for pristine are shown in Fig. 5.6(b). We have observed in Fig. 5.6(a) that there is a blue shift of the 403 nm peak position with annealing temperature with respect to pristine sample. The variation of this peak position with annealing temperature is shown in Fig. 5.6(c). The CL emission at 403 nm (3.07 eV) is attributed to the near-band emission due to the transition of electrons from CB to VB. The energy gap doesn't match exactly with the gap found from UV-Vis spectra. The peak position shifted to 385 nm (3.22 eV) for 500°C annealed samples. This value is quite close to the energy gap for this sample. The blue shift of this peak position agrees well with the increasing trend of the energy gap found from UV-Vis spectra. The visible emission at the 485 nm (2.55 eV) peak is attributed to the lattice defects in the matrix. Local noncubic distortion, which breaks the crystal symmetry, and the change in the native and surface-induced defects in NiO can be responsible for changes in emission intensity [29]. Again, Ni vacancies, which act as shallow acceptors in NiO, can vary with annealing temperature [30]. The crystal field d-d transition, Ni vacancies, and Ni^{2+} defect states can also be attributed to the visible emission peak at 485nm of NiO sample [31–33]. The small near-IR emission peak at 744 nm (1.66 eV) is associated with oxygen vacancies that can be formed during vacuum annealing due to the lack of oxygen supply [28].

5.5.4 Theoretical Analysis

The DFT calculation of band structure for pristine and 300, 350, 400, 450, and 500°C annealed samples are shown in Fig. 5.7(a-f), respectively. The spin-polarised magnetic calculation for the stable antiferromagnetic arrangement of NiO (along (111) plane) by taking the experimentally found lattice parameter value was accomplished for all the samples. The band structure in Fig. 5.7 shows that the up and down spin overlap with each other,

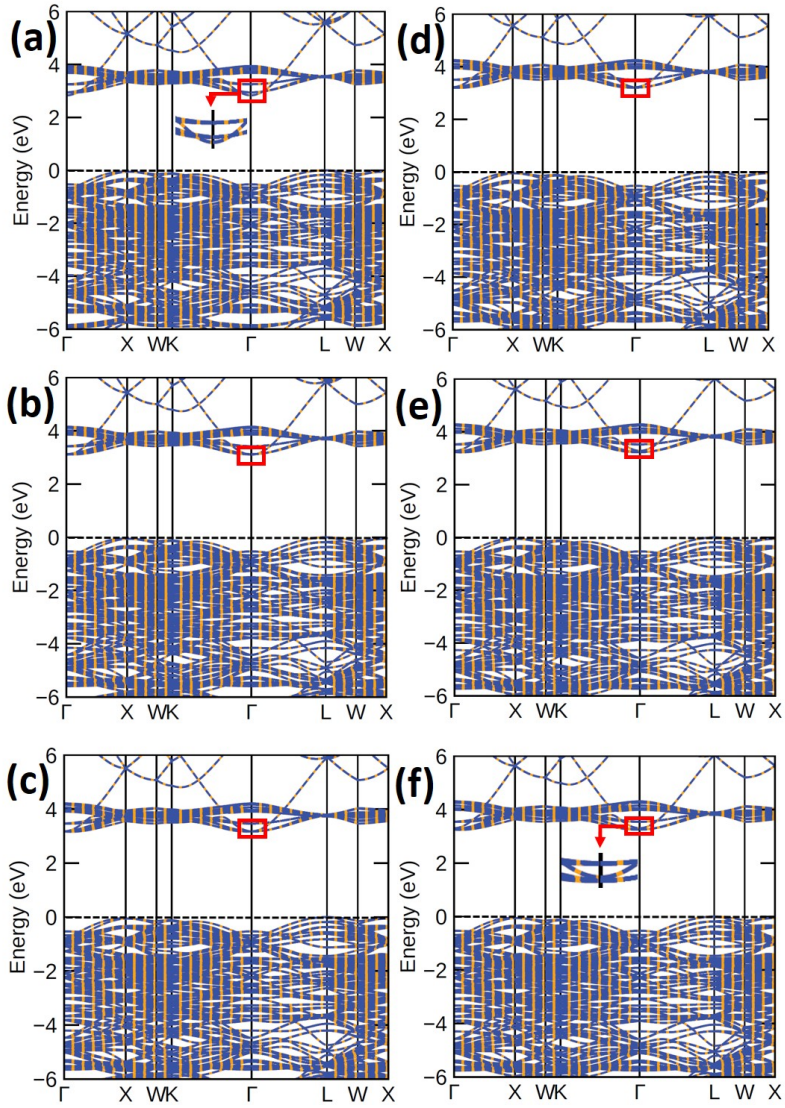

Figure 5.7: The electronic band structure calculation for (a) pristine, (b) 300, (c) 350, (d) 400, (e) 450, and (f) 500°C annealed samples. The black dashed line along zero indicates the Fermi level.

which leads to the total moment zero, as expected for the antiferromagnet NiO system. The calculated bandgap is found to be 2.83 eV for pristine by taking the Hubbered U value to 4.7 eV, which closely matches our experimental results (2.82 eV). As seen in Fig. 5.7(a) and Table 5.1. that the transition did not occur at the same gamma point. Rather, we found that the transition of electron happens from Γ (CB minimum) to L (VB maximum) for pristine.

The transition of electrons along different high symmetry points for other samples is listed in Table 5.1. This justifies the taking of n = 1/2 in the Tauc plot to find the indirect bandgap of NiO. It is noticed that the transition point differs after the 300°C annealed samples. The reason for this is that there is a shifting in the CB band along Γ points in annealed samples than pristine sample, as highlighted by the red square. The magnified view of CB around the Γ point for pristine and 500°C annealed samples is shown in the inset for clear vision. The upward shifting of the CB band may happen due to the decrease in the lattice parameter in the system. The theoretically calculated bandgap values with their corresponding U value are listed in Table 5.1. It is observed that the calculated bandgap increases with the increase of the U value and matches with the experimental value quite well. For further verification, we fixed the U value (taking pristine one, U = 4.7 eV) and took the varying experimental lattice parameter: we observed that the bandgap is also increasing (calculated values are listed in Table 5.1). From this, we can conclude that the gradually decreasing lattice parameter and increasing of the onsite Coulomb repulsion correction of Ni-d orbitals influence in increasing the bandgap in annealed samples.

To further understand the band structure, we calculated total, partial, and orbital DOS for pristine and 500°C annealed samples, shown in Fig. 5.8. The total and partial DOS for pristine and 500°C annealed samples in Fig. 5.8(a,d) shows that the CB is mainly formed by Ni-d orbital and VB by O-p and Ni-d orbitals. It is seen clearly from Fig. 5.8(a,d) that the O-p orbital has no contribution near the minimum of CB but rather Ni-d orbital has. So, the shifting in the CB minimum in the band structure is mainly occurring due to the Ni-d orbitals. The decomposed Ni-d and O-p orbital for these samples (Fig 5.8(b,e) and 5.8(c,f), respectively) clearly identified that the shifting of CB minimum is happening due to the shifting of Ni-$d_{x^2-y^2}$ and Ni-d_{z^2} orbitals with increasing U values which is causing the enhancement of the bandgap in the annealed samples.

Table 5.1: The DFT calculated bandgap values (with experimental lattice constant value) for different U values, matching with experimental values. The variation of calculated bandgap values for fixed U value.

Samples (°C)	IB (eV) (Exp.)	IB (eV) (Th.)	U value (eV)	IB (eV) (Th.), U = 4.7 eV	Lattice Constant (Å)
25	2.82	2.83, CB min = Γ, VB max = L	4.7	2.83, CB min = Γ, VB max = L	4.26
300	3.10	3.10, CB min = Γ, VB max = L	5.0	2.99, CB min = Γ, VB max = L	4.21
350	3.15	3.15, CB min = Γ-X, VB max = L	5.08	3.00, CB min = Γ-X, VB max = L	4.20
400	3.19	3.19, CB min = Γ-X, VB max = L	5.15	3.01, CB min = Γ-X, VB max = L	4.19
450	3.21	3.21, CB min = Γ-X, VB max = L	5.18	3.02, CB min = Γ-X, VB max = L	4.18
500	3.24	3.24, CB min = Γ-X, VB max = L	5.23	3.03, CB min = Γ-X, VB max = L	4.17

5.5.5 Non-linear Optical Properties

The normalized transmittance in OA and CA conditions as a function of distance in Z-scan measurements for pristine and annealed samples are shown in Fig. 5.9 and 5.10, respectively. The OA and CA normalized transmittance measurements are governed by [34],

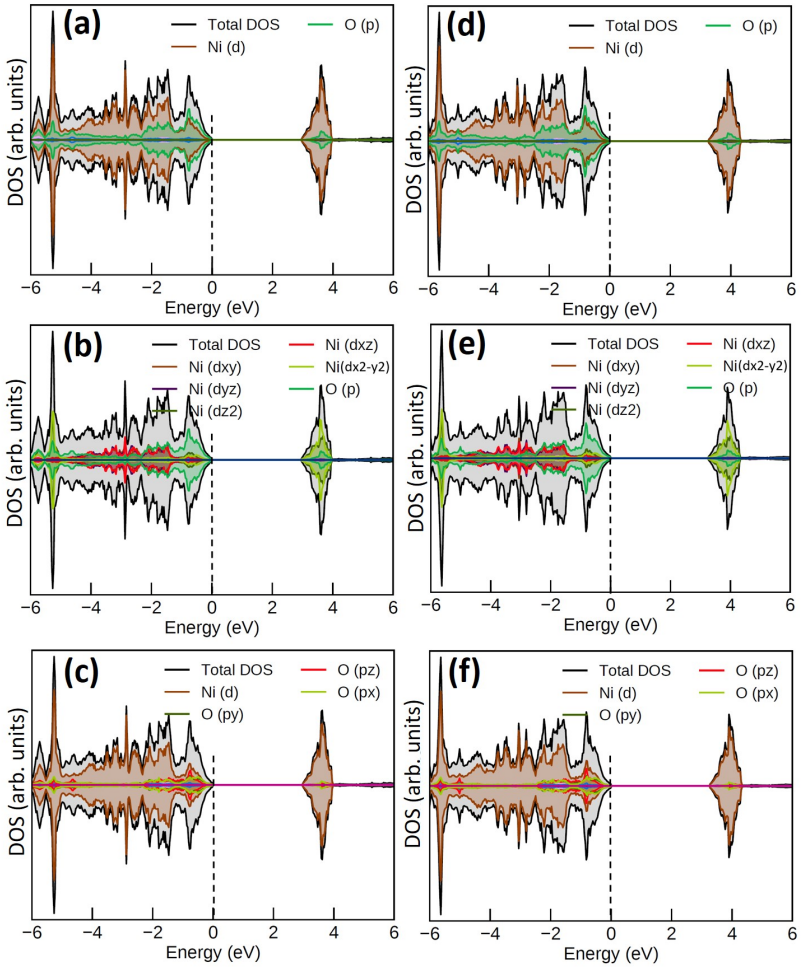

Figure 5.8: The total and partial (a and d), the Ni-d (b and e), and O-p (c and f) orbital decomposed DOS for pristine and 500°C annealed samples. The black dashed line along zero denotes the Fermi level.

$$T(z, S=1) = 1 - \frac{\beta I_0 L_{eff}}{2^{3/2}(1+x)^2} \tag{5.5}$$

$$T(z, \Delta\phi_0) = 1 - \frac{4\Delta\phi_0 x}{(x^2+9)(x^2+1)} - \frac{2(x^2+3)\Delta\psi_0}{(x^2+9)(x^2+1)} \tag{5.6}$$

where β = nonlinear absorption coefficient, I_0 = peak intensity at the focal point (z = 0), x = Z/Z_0, and $L_{eff} = \frac{1-e^{-\alpha L}}{\alpha}$, effective length of the sample, where α = absorption coefficient, and L = sample thickness. S = 1 for OA configuration measurements. $\Delta\phi_0 =$

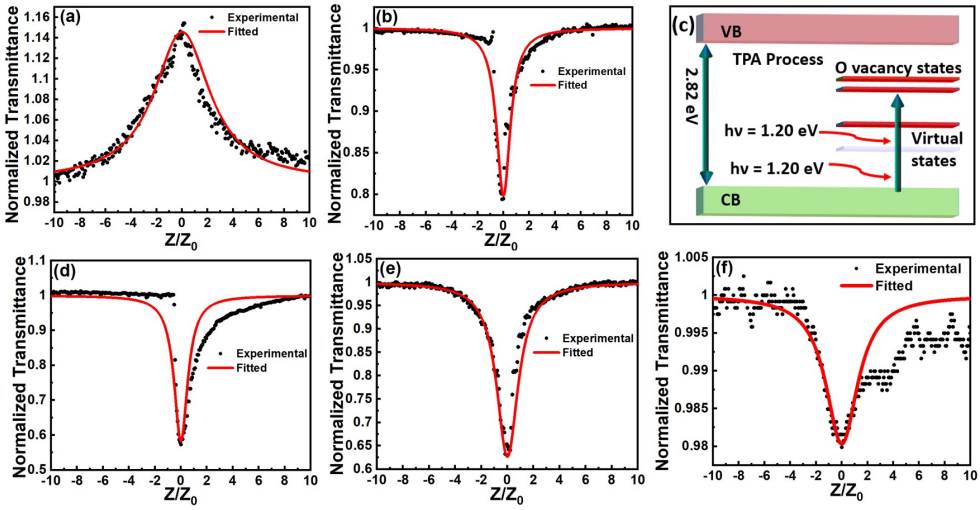

Figure 5.9: Open aperture Z-scan of normalized transmittance of (a) pristine and annealed samples at (b) 300, (d) 400, (e) 450, and (f) 500°C, respectively. (c) The schematic of the TPA process.

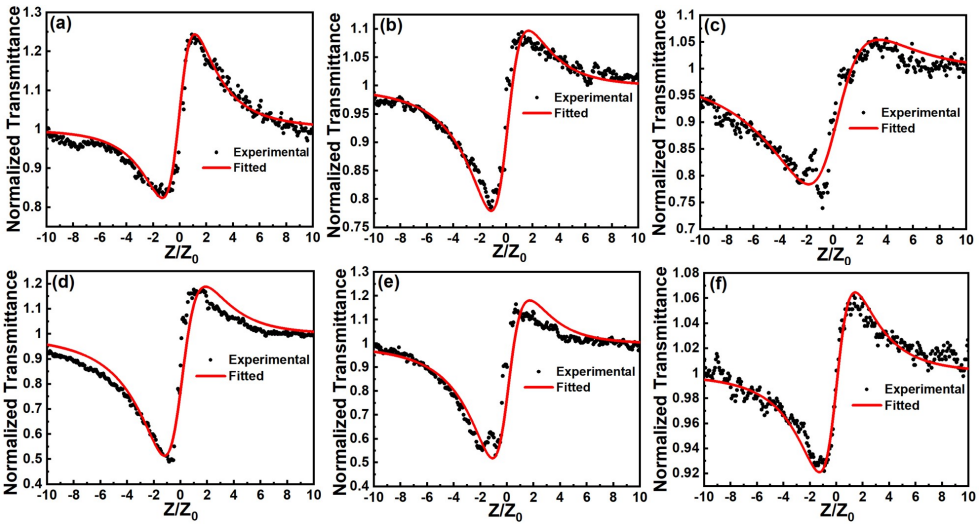

Figure 5.10: Closed aperture Z-scan of normalized transmittance of (a) pristine and annealed samples at (b) 300, (c) 350, (d) 400, (e) 450, and (f) 500°C, respectively.

$kn_2I_0L_{eff}$ and $\Delta\psi_0 = \beta I_0 L_{eff}/2$ = phase-change terms due to nonlinear refraction and nonlinear absorption, respectively, and k = $2\pi/\lambda$.

The β and n_2 values are evaluated by fitting the OA transmittance by equation 5.5 and CA by 5.6, listed in Table 5.2. The threshold value of annealing for enhancing the nonlinear

coefficient is found to the 400°C annealed sample, and after that, the nonlinearity decreases.

Table 5.2: The evaluated β and n_2 values for pristine and annealed samples

Sample	β (cm W^{-1})	n_2 (cm^2 W^{-1})
Pristine	-6.66×10^{-6}	2.68×10^{-10}
300	9.23×10^{-6}	1.99×10^{-10}
350	9.86×10^{-6}	1.64×10^{-10}
400	19.08×10^{-6}	4.21×10^{-10}
450	17.08×10^{-6}	4.11×10^{-10}
500	0.89×10^{-6}	0.92×10^{-10}

The OA curve in Fig. 5.9(a) shows that pristine exhibits the peak at the focal point. This indicates the signature of SA and is attributed to the negative sign of nonlinearity. The annealed samples exhibit a dip in the transmittance at the focus, revealing the RSA behavior with the positive sign of nonlinear absorption. One can notice that there is a rapid change in the sign reversibility between pristine and annealed samples in the nonlinear curve. The positive nonlinear absorption can be used for optical limiting applications. So, in this case, the annealed samples can be applied in optical limiting devices, which can provide safety to optical detectors, sensors, and even to human eyes, acting as transparent for low-level input intensity and relatively opaque to high-level inputs. Good optical limiting materials exhibit potential response in large nonlinearity, broad-band spectral response, fast response time, low limiting threshold, high linear transmittance, stability, etc. The negative nonlinear absorption is beneficial for Q switching. The RSA of nonlinear properties in semiconductor thin films can be assigned to TPA, Three-Photon Absorption (ThPA), Excited State Absorption (ESA), nonlinear scattering or free carrier absorption, etc. [35]. On the other hand, the SA absorption can be associated with the bleaching of the electronic ground state originated due to the effect of efficient plasmon adsorption [36]. The direct TPA is possible when the energy bandgap of the sample satisfies the following condition: $2h\nu < E_g < 3h\nu$.

The indirect TPA can also occur in the sample via intermediate energy level due to vacancy defect states [37]. In our case, E_g of NiO (2.82 - 3.24 eV) is larger than twice the excitation energy ($2h\nu$ = 2.40 eV), which signifies the possibility of occurring the direct TPA. The room temperature PL shows that oxygen vacancy can form inside the bandgap, suggesting the probability of indirect TPA also. Deng et al. and Li et al. already reported such indirect TPA due to defect and trap states in semiconducting materials [38, 39]. Since the TPA condition is satisfied, as shown in Fig. 5.9(c), it also occurs indirectly via the intermediate levels formed by vacancy. The RSA and SA are further examined by carefully analyzing the UV-Vis spectra. Fig. 5.4(a) shows that there is a clear broad hump centered at 447 nm (2.77 eV) appeared in annealed samples. This hump is also present but not prominent in pristine sample. This peak can be attributed to the partially filled d-band of Ni. The other possible reason for arising this hump is surface plasmon resonance (SPR) which is predicted to appear at 2.8 eV due to Ni nanoparticles [40]. In our case, since the crystallite size varies from 7.48 nm to 12.49 nm (as calculated from XRD spectra) and the presence of SPR peak (observed in UV-Vis spectra), the contribution of the SPR effect to optical nonlinearity can not be ruled out. Now, we need to check this plasmon effect to nonlinearity. It is found that at the resonance frequency ($\omega_p = \sqrt{2}\omega$), the surface plasmon significantly affects the nonlinear polarization [13]. In the present study, the excitation energy of the laser is 1.20 eV. The energy required to occur the resonance ($\sqrt{2}\hbar\omega$) is 1.70 eV, which is far lower than the SPR frequency (2.77eV). This justifies that, in our case, SPR has an almost insignificant role in optical nonlinearity. So, direct or indirect TPA is responsible for RSA.

In CA, the variation of beam intensity exhibits the pre-focal minima and post-focal maxima for all the samples. This valley-peak feature is the signature of the self-focusing effect and, hence, the positive value for the nonlinear refractive index (n_2). The real part of the non-linear susceptibility ($\chi_R^{(3)}$) is related to the n_2 values, as follows [14],

$$\chi_R^{(3)} = \frac{1.4cn_0^2n_2}{480\pi^2} \times 10^{-14} \tag{5.7}$$

Where c = speed of light, n_0 = background refractive index. The susceptibility shows a similar variation with the third-order nonlinear refraction coefficient. Such kind of highly significant response in the nonlinear coefficient (see Table 5.2) of NiO with annealing temperature can be suitable for various optoelectronic devices such as optical memory elements, etc. Various mechanisms have been proposed to explain the cause of the optical nonlinearity. Since the NiO samples are irradiated by the fs laser light with an energy of 1.20 eV, the following reasons may be responsible for the nonlinearity: (1) surface plasmon effect [13], (2) the effect of thermal lensing [41], and (3) the spin split d-d near resonant transition in sub-bandgap [14]. We have already explained on the basis of the UV-Vis spectra that the SPR effect has no role in the nonlinear effect as the excitation energy is not sufficient to occur the plasmon resonance. Again, the change in the path length within the illumination region leads to the thermal lensing effect. The negative or positive value of the path length change is associated with photo densification (PD) or photo expansion (PE). The PD and PE are related to the disorderness of the film [42]. The disorder reduces with thermal annealing, as observed from UV-Vis spectra. Since we are using the fs laser with low energy and the disorder of the annealed film reduces, we are assuming that the thermal lensing effect is negligible in this case. So, the sub-bandgap spin split in the d-d transition could be the reason for the nonlinear behaviors in the present study. The Ni-d orbital DOS (Fig. 5.8) showed that Ni-$d_{x^2-y^2}$ and Ni-d_{z^2} orbitals are mainly forming the CB minimum, which shifts with the increasing U values. The electron in Ni-d or O-p orbital in VB absorbs the two-photon and reaches one of the two orbitals of the CB. The d-d or p-d transition can give rise to changing the nonlinearity. Annealed samples are associated with direct or indirect TPA governing the RSA, which can be used as an auto-correlator and optical power limiter.

Since the bandgap increases in the annealed samples with temperature, the absorption in TPA is relatively low in the 300°C sample with respect to the higher annealed sample. So, the 400°C annealed sample can be used as a better optical limiter than pristine and the lower annealed samples due to having a high nonlinear absorption coefficient. Further annealing of the NiO samples degrades the optical limiting properties, and 400°C annealing is the threshold temperature for better optical limiting applications. The SA observed in pristine is useful for passive Q switching and passive mode locking, which can be utilized in generating nanosecond and femtosecond pulses, respectively. The modulation depth, which is proportional to the nonlinear absorption coefficient, is the key parameter for passive mode-locking [43]. Large modulation depth associated with SA can be used for generating short laser pulses and designing for self-starting mode-locked laser [44]. Pristine and annealed NiO can show different potential applications according to their nonlinear properties.

5.6 Summary

In summary, we have analyzed the NLOP of as-grown and annealed NiO thin films using the Z-scan technique. The structural and other optical properties are also discussed and correlated to the NLOP. The DFT calculation of band structure and DOS explain the electronic reason for increasing the bandgap with annealing temperature. We investigated that the upward shifting of Ni-$d_{x^2-y^2}$ and Ni-d_{z^2} orbitals in CB due to increasing U value with the decrease of lattice parameter causes the increase of bandgap. The theoretical calculation also gives the inner-sight reason for NLOP at the OA and CA measurements. In OA, SA and RSA are observed in pristine and annealed samples, respectively. The nonlinear absorption coefficient increases up to 400°C annealed sample and then decreases, resulting in the 400°C as the threshold temperature of NiO for achieving better optical limiter than the other annealed sample. In CA, the prefocal minima and postfocal maxima exhibit the

signature of a self-focusing effect. The spin split d-d or d-p transition is responsible for nonlinear behavior. PL and CL confirm the probability of the formation of an intermediate state between CB and VB. So, RSA is explained on the basis of direct and indirect TPA processes, taking into consideration the vacancy as intermediate states. The plasmonic effect is ruled out for altering NLOP, as the excitation energy is much less than the energy required for the resonant SPR.

Bibliography

[1] H. Kawazoe, *et al.*, *Nature* **389**, 939 (1997).

[2] S. Kerli, Ü. Alver, *et al.*, *Journal of Nanotechnology* **2016** (2016).

[3] M. Yang, *et al.*, *Thin Solid Films* **519**, 3021 (2011).

[4] A. Sreedhar, M. H. P. Reddy, S. Uthanna, *Physics Express* **3**, 15 (2013).

[5] P. Misra, V. Sahu, R. Ajimsha, A. Das, B. Singh, *Journal of Physics D: Applied Physics* **50**, 415106 (2017).

[6] Y. Wang, J. Zhu, X. Yang, L. Lu, X. Wang, *Thermochimica Acta* **437**, 106 (2005).

[7] Y. Uhm, J. Park, W. Kim, C.-H. Cho, C. Rhee, *Materials Science and Engineering: B* **106**, 224 (2004).

[8] S.-H. Lin, F.-R. Chen, J.-J. Kai, *Applied surface science* **254**, 3357 (2008).

[9] X. Wang, *et al.*, *Nanotechnology* **16**, 37 (2004).

[10] H. Sato, T. Minami, S. Takata, T. Yamada, *Thin solid films* **236**, 27 (1993).

[11] V. Srinivasan, J. W. Weidner, *Journal of the Electrochemical Society* **144**, L210 (1997).

[12] J. He, H. Lindström, A. Hagfeldt, S.-E. Lindquist, *The Journal of Physical Chemistry B* **103**, 8940 (1999).

[13] R. Chouhan, P. Baraskar, A. Agrawal, M. Gupta, P. Sen, *Optical Materials* **84**, 893 (2018).

[14] R. Chouhan, *et al.*, *Journal of Applied Physics* **122**, 2 (2017).

[15] T. Chtouki, *et al.*, *Optik* **136**, 237 (2017).

[16] V. Ganesh, *et al.*, *Solid State Sciences* **86**, 98 (2018).

[17] G. Kresse, J. Furthmüller, *Computational materials science* **6**, 15 (1996).

[18] P. E. Blöchl, *Physical review B* **50**, 17953 (1994).

[19] J. P. Perdew, K. Burke, M. Ernzerhof, *Physical review letters* **77**, 3865 (1996).

[20] S. L. Dudarev, G. A. Botton, S. Y. Savrasov, C. Humphreys, A. P. Sutton, *Physical Review B* **57**, 1505 (1998).

[21] P. E. Blöchl, O. Jepsen, O. K. Andersen, *Physical Review B* **49**, 16223 (1994).

[22] A. A. Ahmed, M. Devarajan, N. Afzal, *Surface Review and Letters* **24**, 1750096 (2017).

[23] C. G. Pope, *Journal of chemical education* **74**, 129 (1997).

[24] K. V. Chandekar, *et al.*, *Journal of Materials Research and Technology* **15**, 2584 (2021).

[25] S. Bhakta, S. Pradhan, A. K. Nandy, P. K. Sahoo, *Journal of Electronic Materials* **52**, 1937 (2023).

[26] K. Liang, X. Tang, W. Hu, *Journal of Materials Chemistry* **22**, 11062 (2012).

[27] S. I. Abbas, A. Q. Ubaid, *Journal of advances in Physics* **6**, 1 (2014).

[28] T. Potlog, L. Ghimpu, V. Suman, A. Pantazi, M. Enachescu, *Materials Research Express* **6**, 096440 (2019).

[29] M. Taeño, *et al.*, *Crystal Growth & Design* **20**, 4082 (2020).

[30] S. Jiang, B. Feng, P. Yan, X. Cai, S. Lu, *Applied surface science* **174**, 125 (2001).

[31] A. C. Gandhi, S. Y. Wu, *Nanomaterials* **7**, 231 (2017).

[32] C. Díaz-Guerra, A. Remón, J. Garcia, J. Piqueras, *physica status solidi (a)* **163**, 497 (1997).

[33] J. Gangwar, *et al.*, *Nanotechnology* **24**, 415705 (2013).

[34] A. Singh, S. Kumar, R. Das, P. K. Sahoo, *RSC advances* **5**, 88767 (2015).

[35] K. Nagaraja, S. Pramodini, P. Poornesh, H. Nagaraja, *Journal of Physics D: Applied Physics* **46**, 055106 (2013).

[36] M. Hari, *et al.*, *Optical and Quantum Electronics* **43**, 49 (2012).

[37] M. Sheik-Bahae, A. Said, T. Wei, D. Hagan, E. Van Stryland, *IEEE J. Quantum Electron* **26**, 760 (1990).

[38] S. Li, *et al.*, *Applied Physics Letters* **105**, 19 (2014).

[39] Y. Deng, Y. Du, M. Zhang, J. Han, Z. Yin, *Solid state communications* **135**, 221 (2005).

[40] H. Amekura, Y. Takeda, H. Kitazawa, N. Kishimoto, *Photon Processing in Microelectronics and Photonics II* (SPIE, 2003), vol. 4977, pp. 639–647.

[41] A. Agrawal, T. Ahmad Dar, R. Solanki, D. M. Phase, P. Sen, *physica status solidi (b)* **252**, 1848 (2015).

[42] L. Zou, B. Chen, L. Du, H. Hamanaka, M. Iso, *Journal of Applied Physics* **103**, 12 (2008).

[43] L. Gómez-Pavón, *et al.*, *Optics express* **26**, 1556 (2018).

[44] L. Cheng, *et al.*, *Results in Physics* **13**, 102282 (2019).

Chapter 6

Magnetocrystalline Anisotropy and Resistive Switching in 30 keV Au implanted NiO thin films

6.1 Introduction

TMO have gained considerable attention from researchers due to their versatile applications. Among these, NiO stands out as a promising TMO widely utilized in catalysis, battery cathodes, gas sensors, and electrochromic films [1–5]. In the realm of magnetic materials, NiO has garnered significant attention for applications in energy conversion, storage devices, antiferromagnetic layers, and transport conducting films [4, 6]. Notably, bulk NiO displays antiferromagnetic behavior with a Neel temperature of 573 K [7]. Despite its known properties, the magnetic effects of Au ion implantation in RF sputtered NiO thin films have not been thoroughly explored. The ferromagnetic (FM) dislocation in NiO and the origin of ferromagnetic fluctuations at the dislocation are attributed to the local non-stoichiometry with Ni deficiency [8]. The observed FM behavior is also investigated in Fe-doped NiO samples [9], and the hysteresis loop exhibits the remnant magnetization. The report concluded that the FM properties arise due to the introduction of Fe ions and defect states in the system. The co-doing of Li with V-, Mn-, and Fe-doped NiO exhibits the tunable FM properties [10]. The reason for observing the FM nature in 2% Fe-doped NiO is attributed to the presence of the $NiFe_2O_4$ phase [11]. On the other hand, the weak ferromagnetism in pure NiO nanorods at room temperature appears due to the existence of small hysteresis at the lower field [12]. The rising of a large amount of magnetization and exhibiting the

FM behavior in NiO nano-crystallite with a particle size of 5 nm are responsible for the broken bonds and lattice distortion in the system [13]. Hence, the magnetic properties are very complex because of the existence of defect states, various crystallite sizes, and surface and interface effects. Particle size-dependent study of magnetic properties, the effect of the substitution, and the room temperature magnetic cross-over have been investigated thoroughly for the past few years [14–20]. The study of NiO's magnetic behavior through the core-shell model of cation vacancy concentration emphasizes the role of interactions in vacancies [21].

Beyond its magnetic properties, NiO shows promise as a RRAM device [22–24], capable of switching between low and high resistance states. Various TMO (such as TiO_2, ZrO_2, CoO, $SrTiO_3$) materials have been found for constructing the RRAM device [25–30]. Compared to other TMO materials, NiO is deemed a superior choice for RRAM devices due to its simple rock-salt cubic structure with a bandgap of 3.6 eV. Between digital and analog-type memristors, the analog memristor has drawn interest in analog non-volatile memory, programmable analog circuits etc. [31–33]. The analog memristor, particularly in non-volatile memory devices, showcases unipolar and bipolar resistive switching in NiO depending on the top and bottom electrodes [34–36]. Hence, the working mechanism of the memristor depends on the type of electrodes and raises many controversies [37]. In fact, several models have been proposed based on bulk or interface effects like the filamentary model, charge trapping effect, defect state model, trap charge-driven space charge limited current, etc. [38–41]. The engineering of defects in tuning the RRAM devices has been investigated [42]. Point defects, such as vacancies in the matrix, play a role in filament formation, and ion implantation emerges as a suitable technique to manipulate RRAM device properties by introducing defects in cubic rock-salt structures [36, 43]. Hence, the investigation of the impact of various point defects motivates tuning the magnetic and electrical properties of NiO.

This chapter focuses on the generation of the FM response in NiO through the creation of various kinds of point defects by 30 keV Au ion implantation. The presence of defects in NiO leads to the formation of a short-magnetic domain with variable coercivity, allowing for the tuning of magnetization in the system. The study establishes a correlation between the induced defect states, the modulation of the magnetic environment around Ni ions, and, subsequently, the magnetocrystalline anisotropy. Additionally, this chapter investigates the impact of ion implantation on tuning the resistive switching behavior in Si/NiO/Au RRAM devices.

6.2 Experimental details

The NiO thin film of thickness 90 nm was grown on the clean Si substrate using the RF sputtering technique at room temperature. The single crystal NiO target (purity 99.99%) of 2-inch diameter was used as sputtering material to grow NiO thin film. The Si substrate was kept at a distance of 5 cm from the target. The base pressure, working pressure, sputtering power, and deposition time were maintained at 6.72 $\times 10^{-6}$ mbar, 5 $\times 10^{-3}$ mbar, 100 W, and 10 min, respectively. High purity (99.99%) Ar was used as a reactive gas with a flow rate of 15 sccm. After that, we anneal the as-grown sample under a vacuum of the pressure of 2.33×10^{-2} mbar at a temperature of 350° C. The annealed NiO thin films were implanted by 30 keV Au ions at room temperature in the fluence range of 5×10^{14} ions/cm^2 to 1×10^{16} ions/cm^2. We kept the ion flux low of 1×10^{12} ions/cm^2/s to avoid beam heating during irradiation. The projected range of 30 keV Au ion is 10 nm in rocksalt cubic structure of NiO with a space group of Fm$\bar{3}$m, calculated from SRIM [44]. The option " Detailed Calculation with full Damage Cascades" was implemented for simulation in the version 'SRIM 2013'. The FESEM was utilized to observe the surface morphology and measure the thickness of the thin film. The crystal structure and phases of the thin films were identified using

the Rigaku Smartlab X-Ray diffractometer with Cu K_α source (λ = 1.5418 Å). We have used a UV-Vis-NIR spectrometer to measure the optical absorption spectra of the implanted samples. The absorption spectra were taken in diffuse reflection mode. The 325 nm He-Cd laser was used at room temperature to collect the PL spectra in the wavelength range of 330-800 nm. The magnetic moment vs. applied field measurement was done using the vibrating sample magnetometer-based SQUID system. The magnetic measurement was performed by applying the magnetic field in the range of -5000 Oe to 5000 Oe with varying temperatures between 5K and 300K. For I-V measurement, we deposited a 25 nm thick Au layer on top of the implanted NiO film by the thermal evaporation technique. Before and during the deposition, the chamber vacuum was kept at 2.14×10^{-7} mbar and 4.2×10^{-7} mbar, respectively. The deposition rate was fixed at 0.1 Å/sec. The rotation of the sample holder was kept at 20 rpm for the uniform deposition of Au. The I-V measurement was done by applying a bias voltage between the top and bottom electrodes and measuring the current at the same point.

6.3 Ion Beam Simulations

Fig. 6.1(a) shows the SRIM simulation of 30 keV Au ions distribution in 90 nm NiO thin film and their corresponding energy deposition with depth from the surface. We used the SRIM-TRIM code [45] to calculate the ion range, deposited energy, Au atomic percentage, and displacement per atom (dpa). The simulated range of Au ions in NiO is 18 nm, and the deposited energy (F_d) by the ion is maximum near the depth of 6 nm. The energy deposition reduces gradually as the ions penetrate the depth above 6 nm, and it is zero near the end of the ion range. The energy deposition depends on the electronic (S_e) and nuclear (S_n) energy loss of the incident ion in the target material. The S_e and S_n values of 30 keV Au ion in NiO are 0.37 and 4.80 keV/nm, calculated using the SRIM-TRIM code. As nuclear

energy loss dominates over electronic energy loss for low-energy ion implantation, the ion will transfer its energy to the target NiO nuclei through elastic collision. So, the target atom will be displaced from its lattice site and create the Ni and O vacancy defect in the matrix. The size of the Au^{+} (137 pm) and Au^{3+} (85 pm) ion is much larger than the size of the Ni^{2+} ions (69 pm). So, the Au ion preferably occupies the interstitial position. The variation of atomic percentage of Au ions with target depth in the film is calculated and shown in Fig. 6.1(b). The percentage of Au implantation is maximum at a depth of 10 nm. The increase of fluence increases the percentage of Au implantation in the films, indicating an increase in damage. The Monte Carlo computer simulation was used to get a better damage profile. The option "Detailed calculation with Full Damage cascades" in the SRIM-TRIM code was used to calculate the dpa. This option includes all collisional damage to the target.

The following equation is used to calculate the dpa:

$$dpa = \frac{Fluence(\frac{ions}{cm^2}) \times \left(\frac{Vacancies}{ions-\text{Å}}\right) \times 10^8(\frac{\text{Å}}{cm})}{atomic\ density\ of\ target\ material(\frac{atoms}{cm^3})} \tag{6.1}$$

Where, $\frac{Vacancies}{ions-\text{Å}}$ is the vacancy creation per ion per Å. The atomic density of NiO is 5.38×10^{22} $\frac{atoms}{cm^3}$. Fig. 6.1(c) shows the damage profile with depth for different ion fluences. The displacement of the Ni and O atoms increases with the increment of incident ion fluences. The displacement of atom per incident ion is less than 13 for the fluence of 5×10^{14} and 1×10^{15} ions/cm^2, where it is more than 125 for the fluence of 1×10^{16} ions/cm^2. So, the damage production by lower fluence is insignificant compared to higher fluences. The dpa is maximum at a depth of 6 nm, and it starts to drop off at 8 nm because the deposited energy by the ions is maximum at 6 nm, and then it decreases, as seen in Fig. 6.1(a).

The dynamic simulation of surface recession, partial sputtering yield, and surface atomic fraction with ion fluences calculated using TRIDYN code are shown in Fig. 6.1(d-f), re-

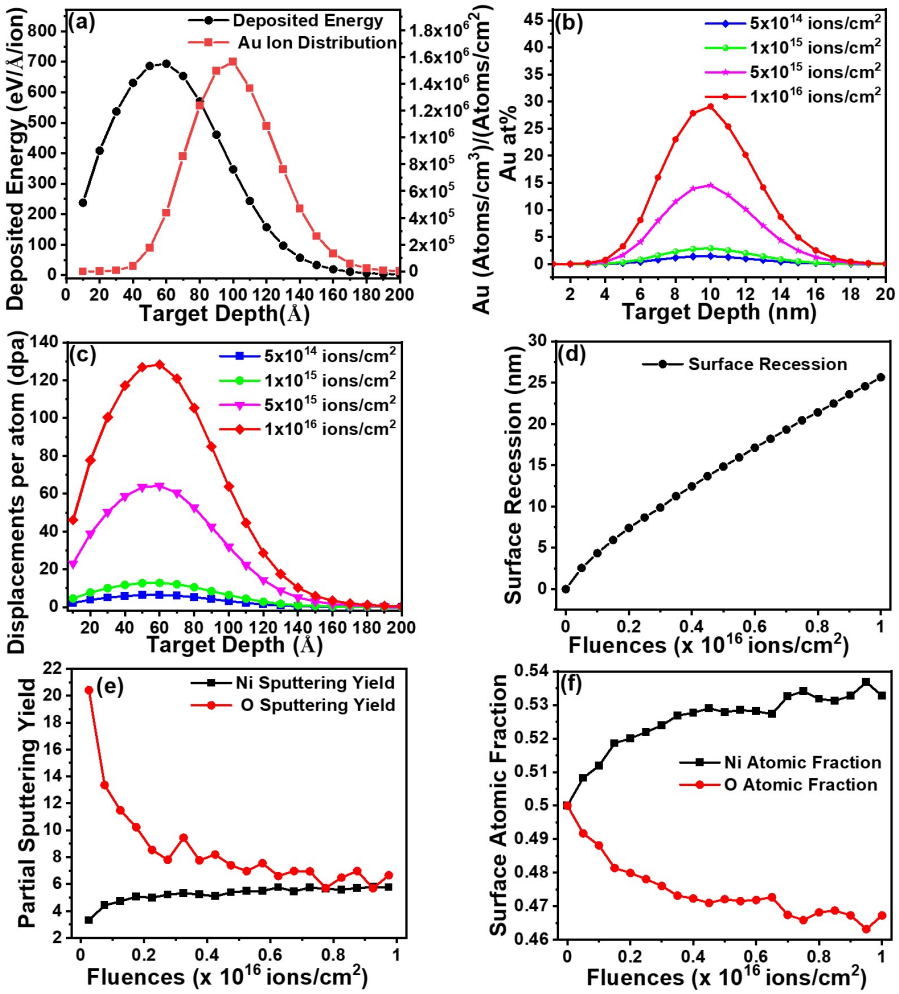

Figure 6.1: (a) The SRIM simulation of deposited energy and ion range vs. target depth, (b) The distribution of Au atomic percentage with target depth for different ion fluences, (c) The variation of dpa with sample depth for different ion fluences, calculated from SRIM simulations. The TRIDYN simulation for (d) surface recession, (e) partial sputtering yield, and (f) surface atomic fraction with ion fluences.

spectively. The surface recession linearly increases with ion fluences, which indicates that there are non-proportionate Ni and O atoms at the surface. The atomic fraction calculation of Ni and O atoms at the surface shows that the atomic fraction of Ni and O atoms is equal (0.5) at lower fluences. O atom is lighter than Ni and can be removed easily from the surface by ion implantation rather than Ni atom. This is reflected in partial sputtering

yield and surface atomic fraction calculation. The partially sputtering yield of O is higher initially for the lower fluences than Ni atoms, as seen in Fig. 6.1(e). However, the sputtering approaches a steady state condition for higher fluences where the sputtering of both the Ni and O atoms converges. This indicates that the relative atomic fraction of Ni will be more than the O atom for higher fluences, which is also seen in Fig. 6.1(f). The atomic fraction of the Ni atom compared to O atoms increases with ion fluences and becomes 0.53 for the fluence of 1×10^{16} ions/cm^2. It decreases for O atoms, as expected, and becomes 0.47 at 1×10^{16} ions/cm^2. So, the sputtering results in the reduction of the relative O atomic fraction and increases the Ni atomic fraction.

6.4 Morphological and structural studies

6.4.1 FESEM

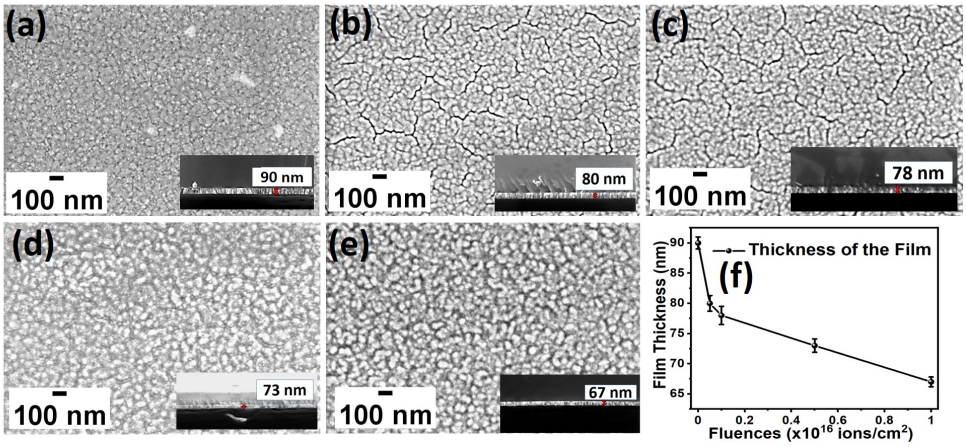

Figure 6.2: The surface morphology of (a) pristine, (b) 5×10^{14} ions/cm^2, (c) 1×10^{15} ions/cm^2, (d) 5×10^{15} ions/cm^2, (e) 1×10^{16} ions/cm^2, The inset shows the film thickness of the corresponding sample from (a-e), respectively, (f) The variation of NiO film thickness with ion fluences.

The surface morphology of pristine NiO and the implanted samples with different ion fluences in the range of 5×10^{14} - 1×10^{16} ions/cm^2 are shown in Fig. 6.2(a-e), respectively.

Pristine shows no fracture on the surface and the film is homogeneous, as seen in Fig. 6.2(a). For the fluence 5×10^{14} and 1×10^{15} ions/cm^2, the surface starts to show tiny fractures. The damage is low at lower fluences. The sputtering of O atoms is much higher than Ni atoms at these fluences. So, the fracture observed (Fig. 6.2(b,c)) over the surface may be due to oxygen deficiency. But, the fracture disappears for the fluence 5×10^{15} - 1×10^{16} ions/cm^2 since the sputtering yield tends to approach a steady state condition for higher fluence. It is seen that the surface is not smooth for these fluences as compared to the fluence 5×10^{14} - 1×10^{15} ions/cm^2 because the dpa is relatively huge for higher fluences. The thickness of the film decreases with the increase of ion fluences, as shown in Fig. 6.2(f). It is expected because the surface recession increases with ion fluences, and at the highest fluence, the recession is nearly 25 nm, as shown in Fig. 6.1(d). This TRIDYN simulation suggested that 65 nm NiO film should remain at the highest fluences. We observed that the film thickness is nearly 67 nm at a fluence of 1×10^{16} ions/cm^2. Hence, the simulation agrees well with the experimental results.

6.4.2 XRD Spectra

The XRD pattern for pristine and implanted samples is shown in Fig. 6.3(a). The XRD peak observed at 43.24° corresponds to the (200) plane of the cubic structure of NiO (JCPDS number 780429). In order to understand the structural properties of NiO with ion fluences, the different parameters such as Peak position (2θ), full-width half maxima (FWHM), lattice constant (a), crystallite size (D), strain (ϵ), and dislocation density (δ) along (200) planes were calculated and listed in Table 6.1. The table shows that the FWHM has decreased from 1.44 to 1.36 for lower fluences, but it increases to 1.60 for the highest fluences. The lattice constant (calculated using equation 5.3) variation is also shown in Table 6.1. The Scherer equation is utilized to calculate the crystallite size and strain (Eq. 5.1 and 5.2, respectively).

The dislocation density is calculated using the following equation: $\delta = \frac{1}{D^2}$

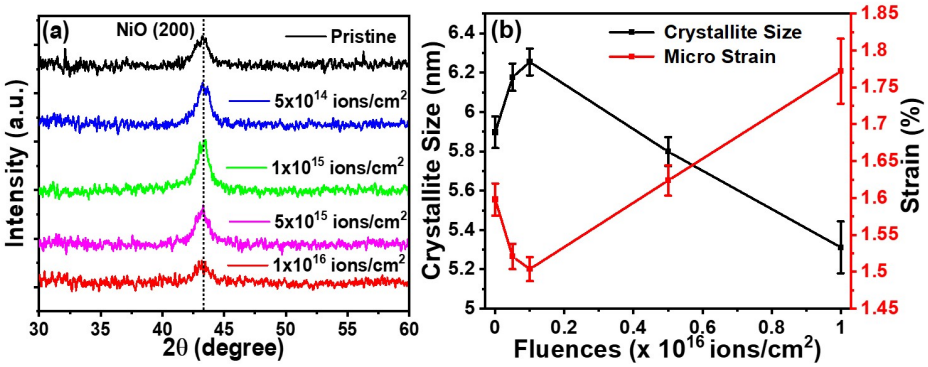

Figure 6.3: (a) The XRD pattern of pristine and ion implanted samples with fluences 5×10^{14} ions/cm^2 - 1×10^{16} ions/cm^2. The dashed line is for guiding the eye. (b) A plot of variation of crystallite size and strain with ion fluences.

Fig. 6.3(b) shows the variation of crystallite size and percentage of strain with ion fluences. The crystallite size increases for lower fluences and then decreases for higher fluences. The strain is low for lower fluences and increases for higher fluences. The lower value of strain indicates the lesser amount of defects in the sample [46]. The crystallinity of the film is enhanced for lower fluences, whereas it decreases for higher fluence due to containing higher strain and defects in the samples. The dislocation density also shows a similar trend to that of the micro-strain. A small amount of intrinsic defect is expected to be produced in pristine during crystal growth. The intrinsic defect influences the lattice strain. In static SRIM simulation, the damage due to lower fluence is minimal compared to the higher fluences. Besides, the dynamic sputtering simulation shows that the sputtering yield of O is very high at lower fluences and tends to steady-state at higher fluences. This means that there is a competition between defect creation (small amount) and defect annihilation (due to high sputtering at low ion energy) at lower fluences. At a fluence of 1×10^{15} ion/cm^2, the total sputtering yield is 17. On the other hand, the value of dpa is 12. Hence, the defect annihilation is higher than the defect creation. This yields the decrease of strain up to a fluence of 1×10^{15} ion/cm^2 due to the significant amount of defect annihilation in

the matrix. However, at higher fluences ($> 1 \times 10^{15}$ ion/cm^2), the sputtering of the host atom is much less compared to the damage production in NiO, which increases the strain significantly.

Table 6.1: Structural parameters: Peak position (2θ), full-width half maxima (FWHM), lattice constant (a), crystallite size (D), strain (ϵ), and dislocation density (δ)

Sample	2θ (°)	FWHM (°)	a (Å)	D (nm)	ϵ (%)	δ (10^{-2} nm^{-2})
Pristine	43.17	1.44 ± 0.02	4.18	5.89	1.59	2.88
5×10^{14} ions/cm^2	43.31	1.38 ± 0.02	4.17	6.17	1.52	2.62
1×10^{15} ions/cm^2	43.26	1.36 ± 0.01	4.17	6.25	1.50	2.55
5×10^{15} ions/cm^2	43.20	1.47 ± 0.02	4.18	5.79	1.62	2.97
1×10^{16} ions/cm^2	43.22	1.60 ± 0.04	4.18	5.31	1.77	3.54

6.5 Optical studies

6.5.1 UV-visible spectroscopy

The UV-Vis absorption spectra in the wavelength range of 200-550 nm with Au ion fluences are shown in Fig. 6.4(a). The absorption spectra were taken in diffuse reflectance mode. Kubelka-Munk function [47] ($F(R_\infty)$) is utilized in Tauc equation[48] to calculate the bandgap of NiO. The Tauc equation follows as [48]:

$$(F(R_\infty \times h\nu))^{\frac{1}{\gamma}} = D(h\nu - E_g) \tag{6.2}$$

Where, $h\nu$ is the incident photon energy. γ determines the nature of electron transition from the conduction band to the valence band. For the direct transition of the electron, $\gamma = \frac{1}{2}$. D is a constant. E_g is the bandgap of the material. Fig. 6.4(b) shows the variation of bandgap with ion fluences. The typical Tauc plot for pristine is shown in the inset of Fig. 6.4(b). The bandgap for pristine NiO is estimated to be 3.61 eV. The bandgap decreases

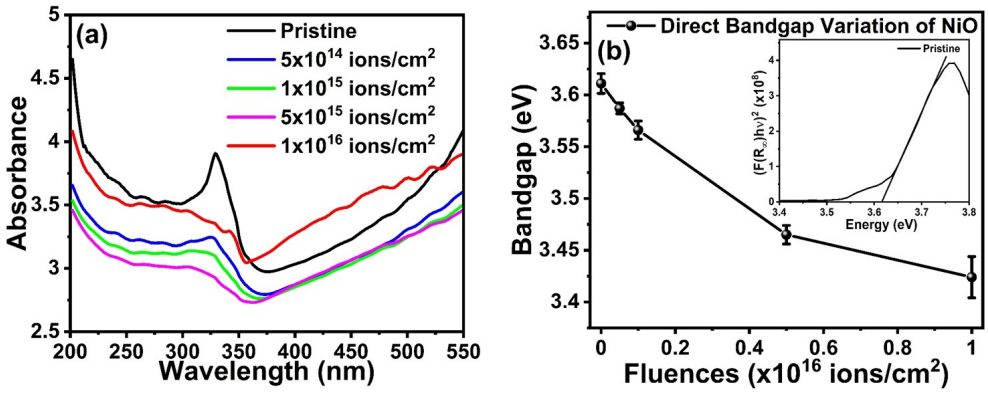

Figure 6.4: (a) The UV-Vis absorption spectra of pristine and implanted samples in the wavelength range of 200-550 nm for different ion fluences. (b) The variation of bandgap with ion fluences. A typical Tauc plot of pristine in the inset.

with Au ion fluences. The bandgap for the highest fluence (1×10^{16} ions/cm^2) is 3.42 eV. The bandgap reduction can occur due to the production of defect states in the system [49]. The damage is very high for the highest fluence, as seen in SRIM simulations. So, ion implantation induces a large number of interstitials and vacancy defect states between the CB and VB of NiO. The number of defects in the NiO matrix increases with the increase of ion fluences, which introduce intermediate defect bands between CB and VB. The increase of intermediate defect states with the increase of ion fluences causes the decrease of the bandgap of NiO.

6.5.2 PL spectroscopy

The PL spectra of NiO in the wavelength range of 330 - 800 nm with different ion fluences are shown in Fig. 6.5(a). Fig. 6.5(b) shows the typical deconvoluted spectra of pristine sample. The PL spectra are deconvoluted into four peaks with the wavelengths of 428, 507, 579, and 753 nm. The three emission band peaks at 428, 507, and 579 nm can be attributed to defect-related deep-level emissions that arise due to oxygen vacancies [50]. The emission peak near 753 nm (1.64 eV) is much lower than the band energy. This band

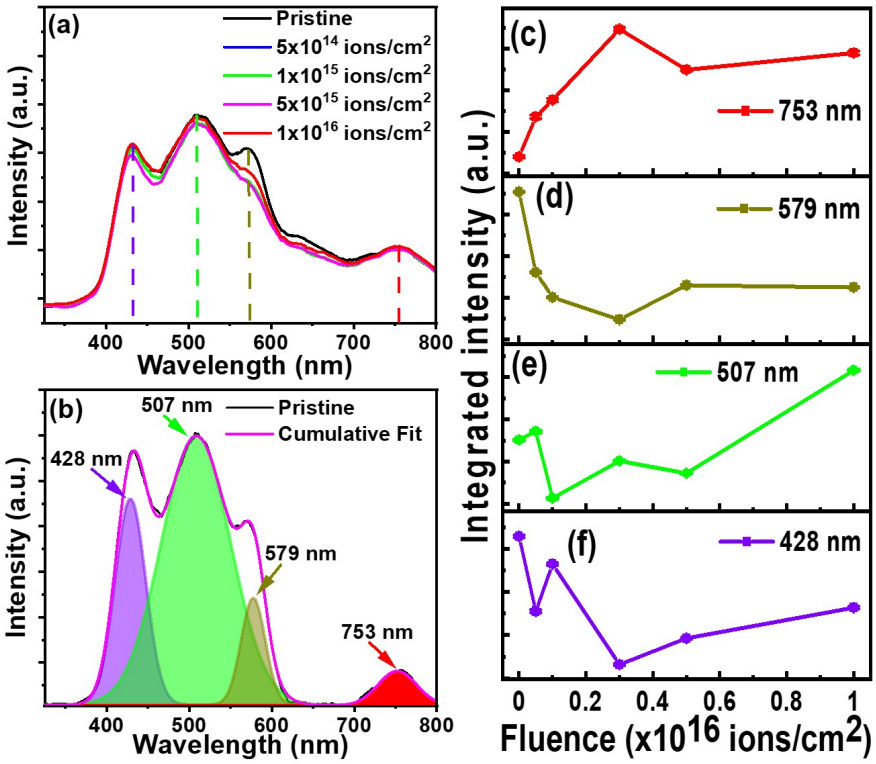

Figure 6.5: (a) The room temperature PL spectra in the wavelength range of 330 - 800 nm of pristine and Au ion implanted samples with different fluences. (b) The typical deconvoluted PL spectra of pristine. (c-f) The variation of integrated intensity with ion fluences for the deconvoluted peaks at 753 nm, 579 nm, 507 nm, and 428 nm.

peak could correspond to the O vacancy defects in NiO [50]. The variation of the integrated intensity with ion fluences of the defect peak at 753, 579, 507, and 428 nm is shown in Fig. 6.5(c-f), respectively. The integrated intensity of the peak at 753 nm increases with ion fluences. This means that the oxygen vacancies increase with fluences. This result corroborates with the simulated calculations. The intensity of the weak band peak at 579 nm slightly decreases and then saturates for higher fluence. The integrated intensity of the broad emission band peak at 507 nm increases with ion fluences. This result signifies that a large number of oxygen vacancy defects are boosted in NiO at higher fluences. The vacancy defects decrease initially and then tend to escalate the defects in the system at higher fluence,

as shown in Fig. 6.5(f).

6.6 Magnetic Properties

The variation of magnetization with the applied magnetic field for pristine and ion-implanted samples at different fluences is measured at the temperatures of 5K, 10K, 50K, 100K, 200K, and 300K. The magnetic moment vs. field (M-H) plots at 5K, 100K, and 300K (RT-Room Temperature) are shown here in Fig. 6.6(a-c), respectively. The magnified hysteresis loops are shown in the inset of the respective graph. Since NiO is antiferromagnetic (AFM) in nature, the FM behavior dominates over the antiferromagnetic (AFM) nature from 5K to RT, as shown in Fig. 6.6. In this case, pristine sample shows the hysteresis loop at all temperatures with remanence magnetization, finite coercivity, and saturation magnetization, indicating that pristine sample may process FM behavior. This magnetic behavior in pristine sample arises due to the presence of intrinsic defects during the crystal growth. Another reason may be the lack of super-exchange interaction between Ni-O-Ni in pristine samples [7]. The magnetization of the implanted sample is much greater than pristine sample. Since the vacancy and interstitial defects are induced by ion implantation and the magnetization is also increased in the implanted sample, it elucidates that defects play a role in inducing the FM nature in the samples [7]. In Fig. 6.6, the magnetization decreases for the fluence greater than 5×10^{15} ions/cm^2 at 5K, 100K, and RT. The sputtering yield of Ni and O tends to steady-state conditions (Fig. 6.1(e)), and the crystallite size decreases in these fluences. Neel found that crystal structure and particle morphology impact the uncompensated spins, and hence, three models are considered [51, 52]. If the uncompensated spins (p) are randomly assigned in the particles, it is expected that $p \propto n_s^{1/2}$ (where n_s is the total number of spins). But $p \propto n_s^{2/3}$ when the uncompensated spins are ordered to parallel to each other in an odd number of layer stakes in the cube. In the third case, $p \propto n_s^{1/3}$ when the core of

the particles is defect-free, and the uncompensated spins are randomly distributed around the surface. So, the expansion of defects with fluences plays a crucial role in controlling the interaction between uncompensated surface spins and the core of the particles. On the surface, the sputtering of O is higher than Ni at lower fluences, as shown in Fig. 6.1(e).

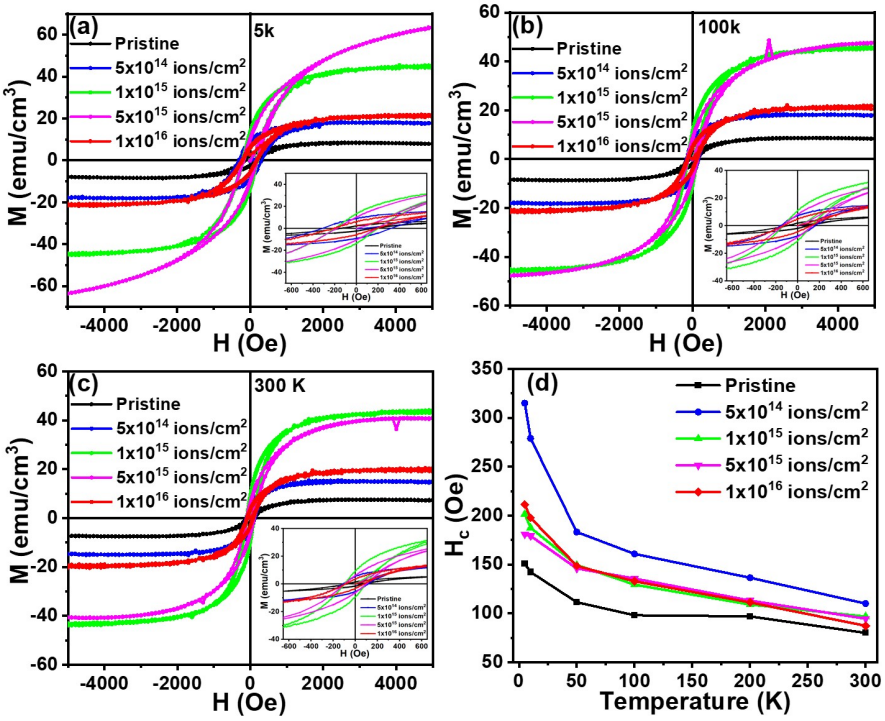

Figure 6.6: The magnetic moment vs. field with ion fluences at (a) 5 K (b) 100 K, and (c) 300 K, respectively. The inset shows the magnified hysteresis in the respective plot. (d) The variation of coercivity with temperature for different ion fluences.

So, it can change the defect states of oxygen more than Ni. So, the Ni and O vacancy defect states and the interaction in the uncompensated spins induce the FM nature in AFM NiO. At higher fluences, there may be a saturation of defects to arrange the moment in such a way that the uncompensated spins are reduced and decrease the magnetization. The magnetic parameters found from the M-H plot are listed in Table 6.2. The coercivity decreases with the temperatures for pristine and implanted samples, as shown in Fig. 6.6(d). The re-

manent magnetization decreases with the increase of temperature in pristine and implanted samples.

Table 6.2: Magnetic parameters: Magnetic coercivity (H_c), Remanence (M_r), Saturation magnetization (M_s)

Samples	H_c (Oe)	M_r (emu/cm^3)	M_s (emu/cm^3)	Temperature (K)
Pristine	80.15	1.40	7.21	300
	97.06	1.70	7.55	200
	98.14	1.81	8.40	100
	111.42	1.98	8.39	50
	142.25	2.24	8.09	10
	150.75	2.27	7.92	5
5×10^{14} ions/cm^2	110.13	5.49	14.72	300
	136.53	6.27	15.14	200
	160.90	7.28	18.17	100
	183.19	7.58	17.86	50
	278.85	8.97	17.82	10
	314.86	9.27	17.74	5
1×10^{15} ions/cm^2	96.84	9.53	43.91	300
	109.06	9.90	44.68	200
	129.46	11.09	45.85	100
	149.51	11.81	45.39	50
	187.54	13.20	44.55	10
	201.44	13.22	44.18	5
5×10^{15} ions/cm^2	94.69	6.25	40.67	300
	113.20	7.08	45.48	200
	135.63	8.37	47.66	100
	145.99	8.79	57.36	50
	179.18	10.10	62.64	10
	180.96	10.38	63.65	5
1×10^{16} ions/cm^2	87.37	3.71	20.27	300
	111.25	4.32	20.83	200
	132.88	4.66	21.92	100
	148.59	5.04	21.77	50
	197.79	6.35	21.69	10
	211.23	5.90	21.58	5

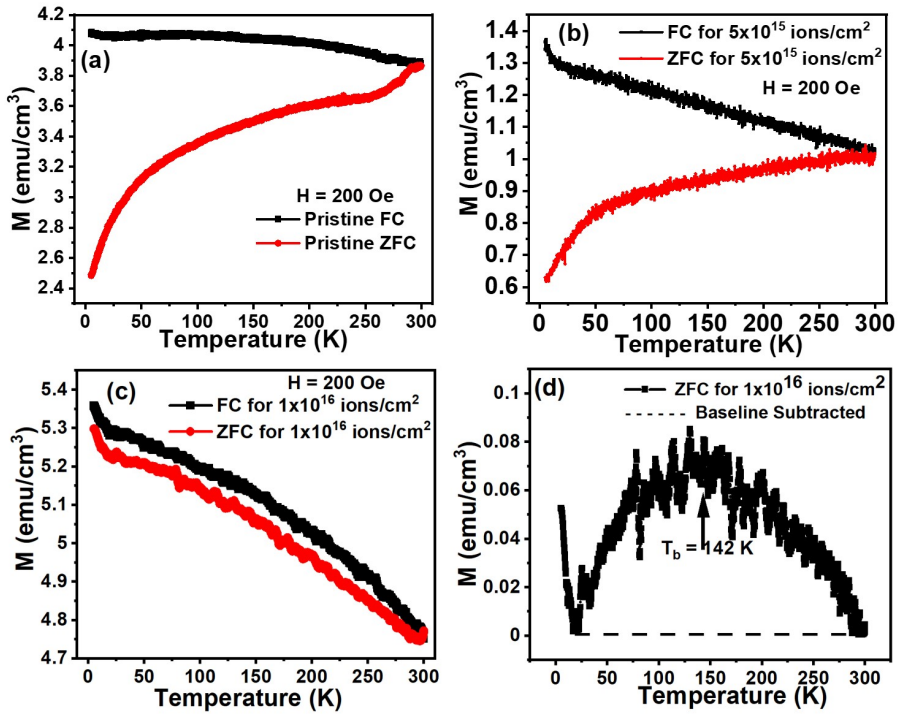

Figure 6.7: The magnetic moment vs. temperature at a fixed field of 200 Oe for (a) pristine, (b) 5×10^{15} ions/cm^2, and (c) 1×10^{16} ions/cm^2. (d) shows the typical baseline corrected ZFC curve of the fluence 1×10^{16} ions/cm^2 to find the blocking region.

Fig. 6.7 (a-c) shows the zero field cooled (ZFC) and field cooled (FC) magnetization curve with temperature at a fixed magnetic field of 200 Oe for pristine, 5×10^{15} and 1×10^{16} ions/cm^2, respectively. During ZFC measurement, the sample was cooled down to 5K without any external field, and the measurement was taken during the warming (5K-300K) at 200 Oe. During FC measurement, the samples were cooled down to 5K with a field of 200 Oe, and the moment was measured during warming at the same field. The bifurcation temperature (T_{irr}) between ZFC and FC curve is near 300K for all the samples. The T_{irr} is related to the largest particle in size distribution, indicating that all spins are unblocked above this temperature [17]. The baseline subtraction of the ZFC curve for all the samples is performed to determine the blocking temperature [53]. The typical subtraction for the sample of fluence 1×10^{16} ions/cm^2 is shown in Fig. 6.7(d). The blocking temperature (T_b) for

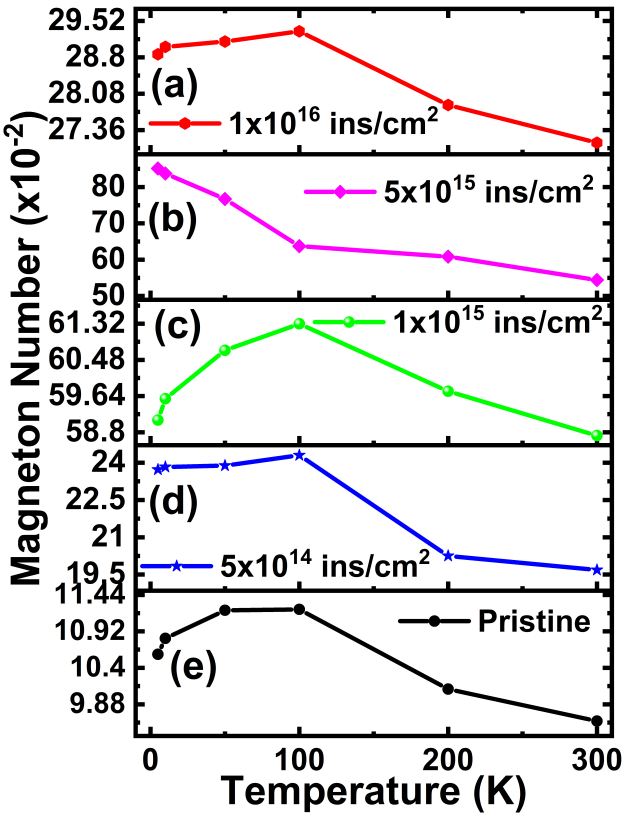

Figure 6.8: The variation of magneton number with temperature for (a) 1×10^{16} ions/cm^2, (b) 5×10^{15} ions/cm^2, (c) 1×10^{15} ions/cm^2, (d) 5×10^{14} ions/cm^2, and (e) pristine samples.

pristine, 5×10^{15} and 1×10^{16} ions/cm^2 samples are 75, 84, and 142 K, respectively. So, T_b increases with ion fluences, and there is a certain jump after the fluence 5×10^{15} ions/cm^2. T_b is incorporated with the modified magnetic environment of Ni^{2+} ions around the surface [54]. Oxygen ions mediate the exchange interaction between the two neighboring Ni^{2+} ions. The oxygen vacancy breaks the exchange bond between the Ni^{2+} ions. This yields to arise the uncompensated spins. SRIM simulations show that the damage increases with ion fluences and leaps up after the fluences of 5×10^{15} ions/cm^2. PL spectra also agree that the oxygen vacancy defect is more at higher fluences. So, this suggests that the uncompensated spins should be higher at higher fluences, and hence, T_b increases suddenly at a fluence of

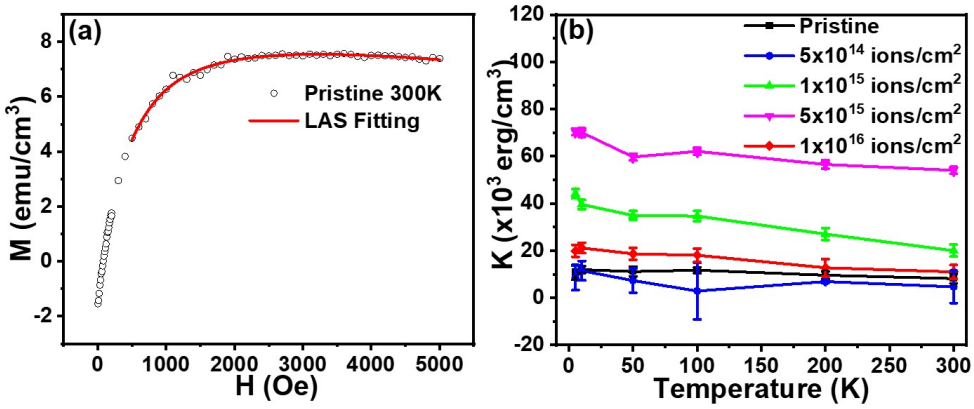

Figure 6.9: (a) A typical M-H curve of pristine at 300 K with LAS fitting at the higher field region. (b) The variation of magnetocrystalline anisotropy constant with temperature (5K to 300K) for different incident ion fluences.

1×10^{16} ions/cm^2. At low temperatures below 23 K, the sharp increase in the moment in FC indicates the paramagnetic (PM) behavior in NiO [15]. The PM tail is associated with an incomplete compensation of the AFM sublattice at the surface. This can be attributed to the presence of uncorrelated PM spins near the surface. This low-temperature behavior also suggests that the large magnetization values are related to the broken exchange bonds and reduced coordination at the surface [54].

The variation of magneton number with temperature for pristine and implanted samples is shown in Fig. 6.8. The value of the magneton number (n_b) is calculated using the following equation [55]:

$$n_b = \frac{Molar\ weight \times M_s}{5585} \tag{6.3}$$

The saturation magnetization decreases for all samples at higher temperatures, which is reflected in the magneton number. The larger magnetic moment induction in implanted samples than in pristine suggests that a strong interaction is involved in the implanted samples. Usually, saturation magnetization increases with the increase of crystalline particle

size and vice versa [56, 57]. The increasing trend of crystallite size and defects increases the saturation magnetic moment per cm^3. But, at the highest fluences, the crystallite size decreases in a significant amount, which decreases the amount of magneton number enormously in the sample of fluence 1×10^{16} ions/cm^2. So, the systematic effect of crystal defects, dislocation, lattice strain, crystallite size, disordered surface spins, broken bonds, and redistribution of cations could result in variation of saturation magnetization and hence magneton number with ion fluences [58].

Since the magnetic material exists in a single domain in the crystallite size, the magnetization reversal mechanism of these materials is related to magnetocrystalline anisotropy. Magnetocrystalline anisotropy is expressed in terms of anisotropy constant, which is anisotropy energy per unit volume. Magnetocrystalline anisotropy and its role in magnetic interaction can be investigated by M-H curve. So, the law of approach to saturation (LAS) formula is used to fit the magnetization vs. magnetic field curve to extract the anisotropy constant. LAS shows the dependency of M on the applied field (H), where H is much higher than H_c. The parameter related to saturation magnetization and magnetocrystalline anisotropy energy, found from LAS fitting, is associated with the anisotropy constant K [59], which is as follows,

$$K = M_s\sqrt{\frac{105b}{8}} \tag{6.4}$$

Where b is the fitting parameter related to magnetocrystalline anisotropy energy with cubic symmetry. The typical LAS fitting for pristine at RT is shown in Fig. 6.9 (a). The variation of K with temperature for different ion fluences is shown in Fig. 6.9 (b). The anisotropy gradually decreases with increasing temperature for all the samples. The value of anisotropy increases to near 60 erg/cm^3 for the fluence 5×10^{15} ions/cm^2, and it reduces to near 20 erg/cm^3 at the highest fluence sample at low-temperature region. The energy

loss through elastic collision will knock out the host atoms from the lattice site, as S_n dominates over S_e at lower ion energy. Besides, the sputtering of oxygen atoms is higher at lower fluences. So, this can yield the breaking of the translational symmetry near the surface of the polycrystalline sample. As an effect, the bond breaking has happened near the surface, leading to the additional contribution of anisotropy [60]. The enhancement of anisotropy with ion fluences might be associated with translational bond breaking at the surface due to the production of defect states, increment of crystallite size, spin-orbit interaction, and lack of super-exchange interaction [60, 61]. Besides, T_b is also related to the magnetocrystalline anisotropy. So, the increment of blocking temperature may escalate the anisotropy in the system, and the sudden increase in T_b leads to the decrease in anisotropy at the highest fluences, which may be due to the oversaturation of uncompensated spins. The decrease of magnetocrystalline anisotropy at the highest fluence also occurred due to decreased crystallite size and weakened magnetic interaction due to excessive defect states. The anisotropy becomes maximum at 5 K, where the coercive field is maximum. The number of defects increases with ion fluences. In contrast, the moment around the defect states try to align themselves according to their preferential direction due to the adequate spin-orbit interaction at lower temperatures. The alignment is disrupted at high temperatures because thermal agitation increases with increasing temperature. This weakens the spin-orbit interaction. On the other hand, the coercive field decreases with temperature, which also signifies that more energy is required to saturate the moment at the higher temperature. Hence, the anisotropy decreases with temperature due to a lack of sufficient spin-orbit interaction and a coercive field around the defect states in competition with thermal energy to stabilize the moments. Hence, various defect states, spin-orbit interaction, coercive field, magnetization, and blocking temperature of the material play a significant role in changing the magnetocrystalline anisotropy of the system.

6.7 Resistive Switching studies

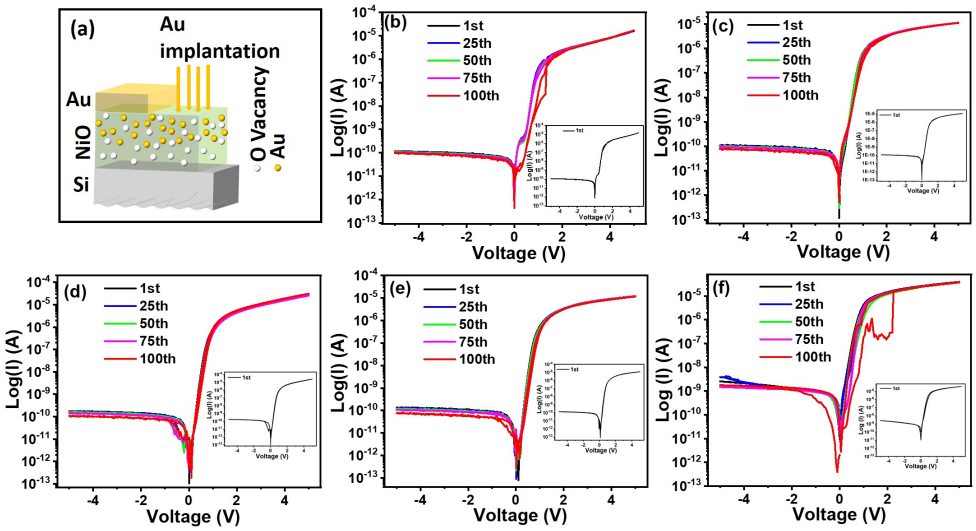

Figure 6.10: (a) Schematic of NiO-based RRAM device. The Current vs. voltage (I-V) graph of (b) pristine, (c) 5×10^{14} ions/cm^2, (d) 1×10^{15} ions/cm^2, (e) 5×10^{15} ions/cm^2, and (f) 1×10^{16} ions/cm^2 for 1st, 25th, 50th, 75th and 100th cycle at a compliance current of 20 mA. The inset in (b-f) shows I-V variation for the 1st cycle for pristine and 5×10^{14} - 1×10^{16} ions/cm^2 fluence samples for clear vision, respectively.

The schematic of the RRAM device for current vs. voltage measurement is shown in Fig. 6.10(a). The NiO (200) film of a thickness of 90 nm was sandwiched between the bottom Si substrate and the top Au electrode (25 nm). The n-Si and p-NiO formed a p-n junction at the bottom electrode, and a Schottky barrier was established at the NiO/Au interface. The variation of current with voltage sweep for 1st, 25th, 50th, 75th and 100th cycles for pristine (Fig. 6.10(b)) and different ion fluences of 5×10^{14}, 1×10^{15}, 5×10^{15} and 1×10^{16} ions/cm^2 are shown in Fig. 6.10(c-f), respectively. The inset in Fig. 6.10(b-f) shows the variation of current vs. voltage for the 1st cycle. The top Au electrode was stressed by applying a bias voltage, and the bottom n-type Si was grounded during the measurement. The I-V curve shows the asymmetry characteristics for pristine and all the implanted samples for the 1st-100th cycles. This indicates that a Schottky-like barrier is

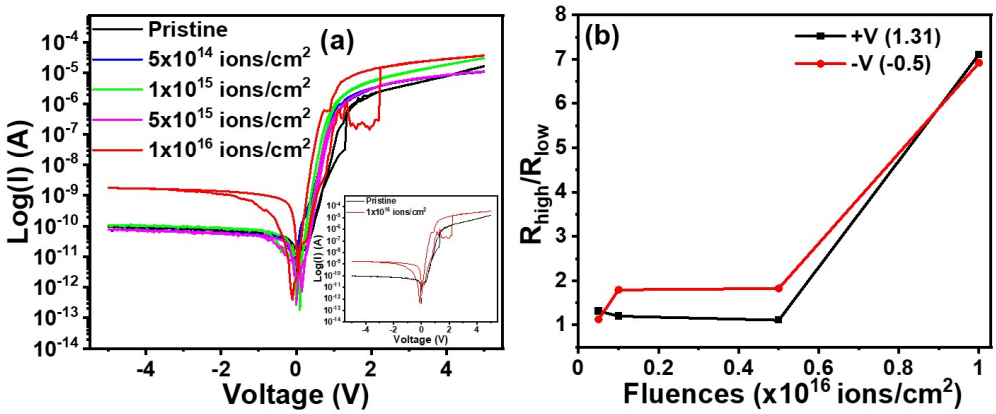

Figure 6.11: (a) The current vs. voltage graph of pristine, 5×10^{14} ions/cm^2, 1×10^{15} ions/cm^2, 5×10^{15} ions/cm^2, and 1×10^{16} ions/cm^2 for 100th cycle. Inset shows the current vs. voltage graph for pristine and 1×10^{16} ions/cm^2 fluence sample for better comparison. (b) Fluence-dependent RS ratio of the memristor.

formed at the NiO/Au interface. The hysteresis loop tends to develop with the increase of the cycle in positive voltage sweep (0V-5V-0V) in pristine. The high current conduction is observed in the positive voltage sweep compared to the negative voltage sweep for both pristine and implanted samples. At positive bias, the significant hysteresis is observed at the 100th cycle for the fluence of 1×10^{16} ions/cm^2 (highest fluence sample), which is not the case for other samples. But, in contrast, the hysteresis began to develop in the implanted samples at the negative bias sweep and became significantly large at the 100th cycle of the highest fluence sample. On the other hand, pristine, even at the 100th cycle, doesn't exhibit any significant hysteresis at negative bias.

The I-V curve for the 100th cycle with various ion fluences is shown in Fig. 6.11(a). The typical I-V curve of the 100th cycle for pristine and highest fluence samples is shown in the inset for clear vision. The figure shows that hysteresis starts at 1.31 V in pristine at positive bias and insignificant hysteresis at negative bias. But, the lowest fluence sample (5×10^{14} ions/cm^2) exhibits the formation of hysteresis at 0.77 V at positive bias, and a tiny hysteresis began to develop at -0.04 V with a current value of 7.3 pA at negative bias.

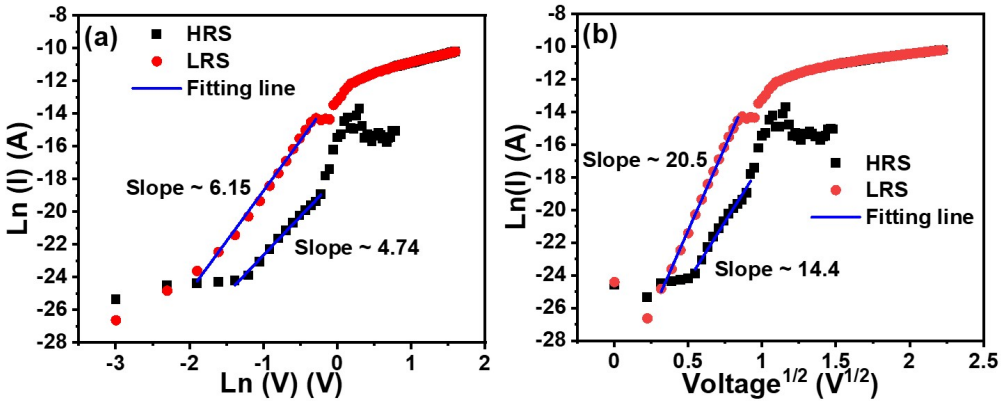

Figure 6.12: The typical (a) ln (I) vs. ln (V) and (b) ln (I) vs. $V^{1/2}$ plot with linear fitting for the fluence of 1×10^{16} ions/cm^2 of 100th cycle.

Similarly, the I-V hysteresis loop starts at 0.17 V (I= 25 pA) at positive bias, whereas at negative bias, the hysteresis appears at -0.13 V (15 pA). The 5×10^{15} ions/cm^2 fluence sample shows the I-V hysteresis loops at 0.25 V (20 pA) and -0.1 V (8.6 pA) for positive and negative bias, respectively. A drastic change in the hysteresis is perceived at positive bias with the increment of the cycle of the highest fluence sample with a sudden jump in the current at a voltage of 2.21 V. At negative bias, a significant hysteresis loop is seen in the sample compared to the other fluence samples. This hysteresis undergoes at a voltage of -0.01 V (24 pA). The current conduction at negative bias increases from pA to nA at the highest fluence compared to other samples. The fluence dependence resistance switching (RS) ratio of the implanted samples at the 100th cycle (read at 1.31 V and -0.5 V) is shown in Fig. 6.11(b). The non-linear behavior of the RS ratio with ion fluences is observed. The RS doesn't change rapidly up to the fluence 5×10^{15} ions/cm^2. However, the RS ratio leaps up at the highest fluence sample due to huge damage creation in the NiO thin film around the surface compared to the lower ion fluences. So, the hysteresis loop is induced by the bulk vacancy defects in the vicinity of the NiO/Au interface and p-n junction. The resistive switching in polycrystalline NiO due to the formation and rupture of filament has been

proposed by several authors [40, 62, 63]. The filamentary model is a local phenomenon at the metal/oxide/metal interface. The change in the defect density in an oxide matrix can change the switching behavior in the RRAM device [64]. In this case, the higher S_n value than the S_e value leads to creating a lot of vacancies and interstitial defects in the matrix, which affects the RS behavior.

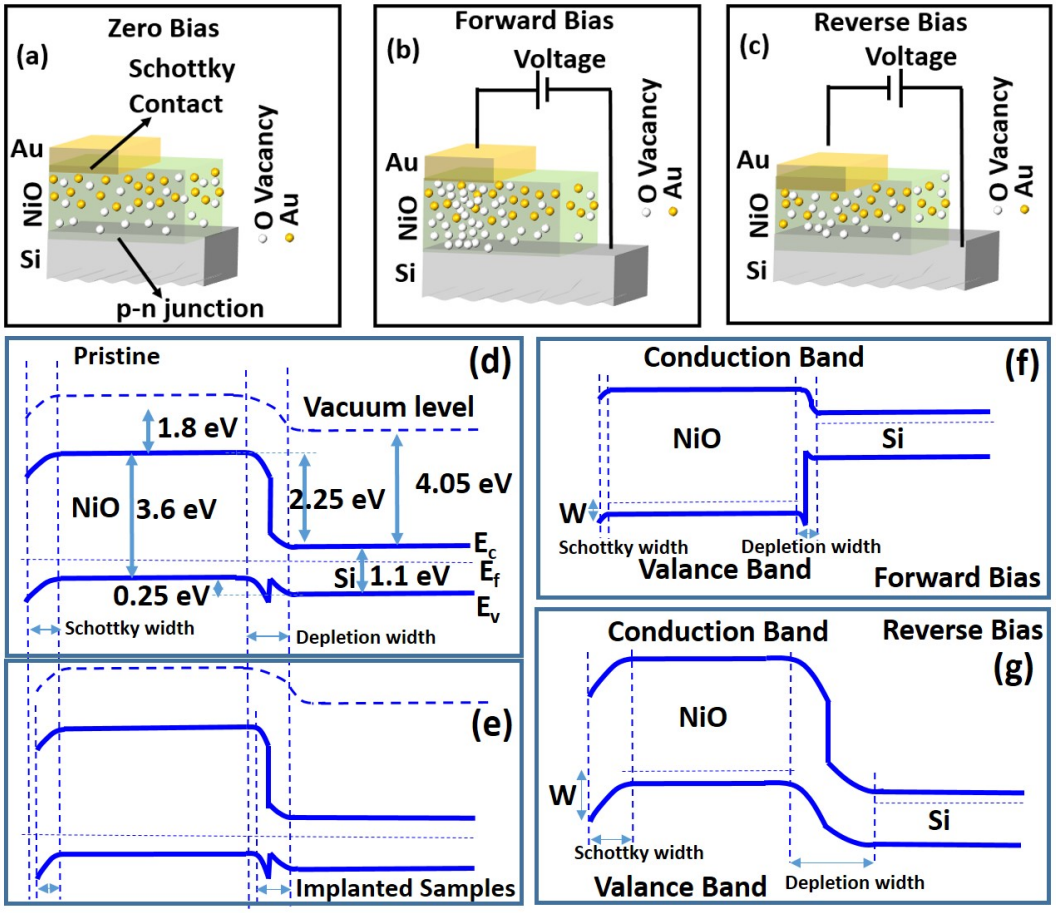

Figure 6.13: Schematic of conduction mechanism of the Si/NiO/Au memristor of (a) zero bias, (b) forward bias, and (c) reverse bias. The band diagram of (d) pristine, (e) implanted samples at zero bias, (f) forward bias, and (g) reverse bias.

Fig. 6.12(a) and 6.12(b) show the linear fitting of the ln (I) vs. ln (V) and ln (I) vs. $\sqrt{V}$ graph at the 100th cycle of the highest fluence sample, respectively. The LRS or HRS will show the Ohmic behavior if the slope is one. In our case, the LRS and HRS don't fit

linearly with a slope of one (Fig. 6.12(a)). So, the deviation from ohmic behavior can be explained by other conduction mechanisms. The main conductive mechanisms are Schottky emission [65], space charge limited conduction [66], F-N tunneling [67], and P-F emission [68]. The Schottky emission, space charge, F-N, and P-F emission may be responsible for the deviation from Ohmic behavior. We have checked the possibility of other conduction mechanisms by a similar process explained in section 4.5 in Chapter 4 and found the dominance of Richardson-Schottky behavior. The asymmetry in I-V curves and semiconductor (NiO)/metal (Au) junction at the top electrode signify that the Schottky barrier plays a crucial role in RS over the other conduction mechanisms. To describe the I-V characteristics, we took the Richardson-Schottky equation as follows:

$$I = AA^{*}T^{2}e^{(-q(\phi_B - \sqrt{qE/4\pi\epsilon_i})/KT)} \tag{6.5}$$

Where, A = conduction area, A^* = effective Richardson constant, T is the absolute temperature, k is the Boltzmann constant, q is the electric charge, E is the electric field, d = spacing between top and bottom electrode, ϕ_B = Schottky barrier and ϵ_i = dielectric constant of the material. We are taking the Richardson constant of A^* = 119.8 A/K^2·cm2, calculated with m_n^* = 1.0 m_0 = 9.1 × 10^{-31} Kg^3. After taking logarithm at both sides of equation 6.5, follows as:

$$ln(I) = (ln(AA^{*}T^{2}) - q\phi_B/KT) + q/KT(\sqrt{q/4\pi\epsilon_i d}\sqrt{V}) \tag{6.6}$$

The slope of LRS and HRS is found to be 6.15 and 4.74, respectively, as shown in Fig. 6.12(a). So, the Ohmic behavior is ruled out at the NiO/Au interface. The LRS and HRS in ln (I) vs. $\sqrt{V}$ graph are fitted linearly with a slope of 20.5 and 14.4, respectively. This further confirms the formation of the Schottky barrier at the top interface, affecting the hysteresis and RS with ion fluence at various cycles. So, we can suggest that current conduction in the memristor can be interfered by the Schottky barrier at the NiO/Au interface and the

p-n junction at the bottom electrode. The schematic of the current conduction mechanism of the Si/NiO/Au device is shown in Fig. 6.13. The n-type Si has the majority carriers of electrons. Under forward bias, the Si/NiO interface behaves as a classical p-n junction diode where the electrons in Si move to the depletion region, but the oxygen vacancies in implanted samples move away from the NiO/Au interface at the high electric field. At this bias, the recombination of e^- and hole at the p-n junction and to minimize the field strength developed at the Si/NiO interface decreases the depletion width above a threshold electric field, resulting in a sudden increase in current. At positive bias, the Schottky barrier decreases at the NiO/Au interface (Fig. 6.13(f)) than the zero bias condition (Fig. 6.13(d,e)), helping in increasing the current conduction. Furthermore, NiO is a p-type semiconductor whose minority carriers are electrons [69]. Again, the formation energy for oxygen vacancies is less than the Ni vacancies [70]. So, it is energetically more favorable to create oxygen vacancies than Ni during ion implantation. The highest fluence will create more oxygen vacancies in the matrix due to having high damage capability, as seen in ion beam simulations. The vacancies act as e^- trap centers. The thermally excited electrons from the bottom electrode can move to CB or trap states, respectively. Under forward bias, the reduced depletion width of the p-n junction helps the thermally excited electrons in the bottom electrode overcome the potential barrier to move to the CB or to the trap center by tunneling of the oxide layer easily. The trapped e^- then transmits to other trap states via hopping conduction. Since the highest fluence sample has an enormous number of trap states compared to the low fluence sample, the current conduction and hysteresis should be improved, as in this sample, the conduction is governed by the thermionic emission along with increased hopping conduction through increased trap center. Finally, the carriers move to the upper electrode by overcoming the reduced Schottky barrier at forward bias. Hence, the vacancy defects formation through ion implantation mainly influences the high current conduction and bigger hysteresis loop at the highest fluence sample after overcoming the

threshold voltage at forward bias, as described in Fig. 6.13. Under reverse bias, the recombination of oxygen vacancies happens inside the NiO and is distributed in the matrix. At this bias, the depletion width at the interfaces increases (Fig. 6.13(g)). Hence, the current conduction is relatively poor in reverse bias compared to forward bias for all the samples. Again, the density of trap centers (vacancies) increases in NiO with ion fluences, whereas no excess vacancies are induced externally in pristine to act as extra trap centers for charge carriers to improve the current conduction. So, the excess vacancy induction in implanted samples plays a crucial role in electrons getting a pathway to pass through easily to improve current and hysteresis. Hence, negligible hysteresis is observed in pristine. However, current and hysteresis increase with ion fluence in reverse bias conditions. The improvement of current from pA to nA for the highest fluence (Fig. 6.11(a)) has been observed in reverse bias because of the induction of a sufficient amount of excess vacancies in NiO.

6.8 Summary

In summary, 30 keV Au ions introduced defects in the NiO matrix, and dpa increases with ion fluences. The sputtering of the surface atom causes the reduction of the thickness with ion fluences, which agrees well with the dynamic TRIDYN simulations. The increased vacancy defects in the matrix introduced intermediate bands that reduce the bandgap with increased ion fluences. The intrinsic Ni and O defects during crystal growth induced FM property in pristine sample. The FM behavior is further tuned by creating various vacancies and interstitial defects in NiO by ion implantation. The FM can originate from the interaction of uncompensated surface spins and the core of the particles. The magneton number exhibits a variation pattern similar to that of saturation magnetization. The magnetization mechanism, blocking temperature, and bond breaking due to defects at the surface tune the magnetocrystalline anisotropy in the system, which has a vital role in permanent magnets

and magnetic data storage applications.

On the other hand, the tuning in resistive switching behavior of the implanted films with ion fluences is also investigated. Pristine doesn't show significant hysteresis in negative bias, but the hysteresis is developed with ion fluences. The value of the current improved from pA to nA at the highest fluence at negative bias due to the generation of excess vacancies during ion implantation. In positive bias, the hysteresis doesn't change significantly up to a fluence of 5×10^{15} ions/cm^2, but it shows a drastic change at the highest fluence. In forward and reverse bias, the induction of excess oxygen vacancies in NiO and the changing of depletion width and Schottky barrier height at the p-n junction and NiO/Au interface plays a role in the variation of hysteresis and current in the memristor with ion fluences.

Bibliography

[1] M. Yoshio, *et al.*, *Journal of power sources* **74**, 46 (1998).

[2] R. Gabr, A. EI-Naimi, M. AI-Thani, *Thermochim. Acta* **197**, 307 (1992).

[3] S. Ikeda, *et al.*, *Physical Chemistry Chemical Physics* **1**, 4485 (1999).

[4] H. Steinebach, S. Kannan, L. Rieth, F. Solzbacher, *Sensors and Actuators B: Chemical* **151**, 162 (2010).

[5] A. Sonavane, *et al.*, *Journal of Alloys and Compounds* **489**, 667 (2010).

[6] H. Guan, *et al.*, *Inorganic Chemistry Communications* **6**, 1302 (2003).

[7] P. Ravikumar, B. Kisan, A. Perumal, *Aip Advances* **5**, 087116 (2015).

[8] I. Sugiyama, *et al.*, *Nature nanotechnology* **8**, 266 (2013).

[9] Y.-H. Lin, *et al.*, *Physical Review B* **73**, 193308 (2006).

[10] Y.-H. Lin, *et al.*, *Journal of Applied Physics* **110**, 4 (2011).

[11] A. Douvalis, L. Jankovic, T. Bakas, *Journal of Physics: Condensed Matter* **19**, 436203 (2007).

[12] S. Manna, A. Deb, J. Jagannath, S. De, *The Journal of Physical Chemistry C* **112**, 10659 (2008).

[13] H. Bi, S. Li, Y. Zhang, Y. Du, *Journal of magnetism and magnetic materials* **277**, 363 (2004).

[14] R. H. Kodama, S. A. Makhlouf, A. E. Berkowitz, *Physical Review Letters* **79**, 1393 (1997).

[15] E. Winkler, R. Zysler, M. V. Mansilla, D. Fiorani, *Physical Review B* **72**, 132409 (2005).

[16] S. Tiwari, K. Rajeev, *Physical Review B* **72**, 104433 (2005).

[17] M. Peck, *et al.*, *Journal of Applied Physics* **109**, 07B518 (2011).

[18] L. Li, L. Chen, R. Qihe, G. Li, *Applied physics letters* **89**, 134102 (2006).

[19] N. H. Hong, J. Sakai, N. Poirot, V. Brizé, *Physical Review B* **73**, 132404 (2006).

[20] X. Wang, *et al.*, *Nanotechnology* **16**, 37 (2004).

[21] S. Mandal, S. Banerjee, K. S. Menon, *Physical Review B* **80**, 214420 (2009).

[22] S.-H. Phark, S. C. Chae, *Journal of Physics D: Applied Physics* **48**, 155102 (2015).

[23] U. Russo, D. Ielmini, C. Cagli, A. L. Lacaita, *IEEE Transactions on Electron Devices* **56**, 193 (2009).

[24] C. Cagli, F. Nardi, D. Ielmini, *IEEE Transactions on electron devices* **56**, 1712 (2009).

[25] K. A. Bogle, M. N. Bachhav, M. S. Deo, N. Valanoor, S. B. Ogale, *Applied Physics Letters* **95**, 203502 (2009).

[26] X. Wu, *et al.*, *Applied Physics Letters* **90**, 183507 (2007).

[27] H. Shima, *et al.*, *Applied Physics Letters* **91**, 012901 (2007).

[28] K. Shibuya, R. Dittmann, S. Mi, R. Waser, *Advanced materials* **22**, 411 (2010).

[29] S. Lee, *et al.*, *Applied Physics Letters* **91**, 202115 (2007).

[30] J. Gibbons, W. Beadle, *Solid-State Electronics* **7**, 785 (1964).

[31] W. Lu, K.-H. Kim, T. Chang, S. Gaba, *16th Asia and South Pacific Design Automation Conference (ASP-DAC 2011)* (IEEE, 2011), pp. 217–223.

[32] Y. V. Pershin, M. Di Ventra, *IEEE Transactions on Circuits and Systems I: Regular Papers* **57**, 1857 (2010).

[33] E. Chicca, *et al.*, *IEEE Transactions on Circuits and Systems I: Regular Papers* **54**, 981 (2007).

[34] Y. Sharma, P. Misra, S. P. Pavunny, R. S. Katiyar, *Applied Physics Letters* **104**, 7 (2014).

[35] S. Chang, *et al.*, *Applied Physics Letters* **92**, 18 (2008).

[36] U. Joshi, *et al.*, *Journal of Applied Physics* **105**, 7 (2009).

[37] T. Ishihara, *et al.*, *Materials Science and Engineering: B* **148**, 40 (2008).

[38] C. J. Kim, B. I. Kim, I.-W. Chen, *Japanese journal of applied physics* **44**, 1260 (2005).

[39] Y. Watanabe, *et al.*, *Applied Physics Letters* **78**, 3738 (2001).

[40] S. Seo, *et al.*, *Applied Physics Letters* **85**, 5655 (2004).

[41] I. H. Inoue, S. Yasuda, H. Akinaga, H. Takagi, *Physical Review B* **77**, 035105 (2008).

[42] W. Banerjee, Q. Liu, H. Hwang, *Journal of Applied Physics* **127**, 5 (2020).

[43] R. Elliman, *et al.*, *Nuclear Instruments and Methods in Physics Research Section B: Beam Interactions with Materials and Atoms* **307**, 98 (2013).

[44] J. F. Ziegler, M. D. Ziegler, J. P. Biersack, *Nuclear Instruments and Methods in Physics Research Section B: Beam Interactions with Materials and Atoms* **268**, 1818 (2010).

[45] R. E. Stoller, *et al.*, *Nuclear instruments and methods in physics research section B: beam interactions with materials and atoms* **310**, 75 (2013).

[46] A. A. Ahmed, M. Devarajan, N. Afzal, *Surface Review and Letters* **24**, 1750096 (2017).

[47] P. Kubelka, F. Munk, *Z. Tech. Phys* **12**, 193 (1931).

[48] P. Makuła, M. Pacia, W. Macyk, *The journal of physical chemistry letters* **9**, 6814 (2018).

[49] P. Salunkhe, M. A. AV, D. Kekuda, *Applied Physics A* **127**, 1 (2021).

[50] T. Potlog, L. Ghimpu, V. Suman, A. Pantazi, M. Enachescu, *Materials Research Express* **6**, 096440 (2019).

[51] C. R. H. Bahl, *et al.*, *Journal of Physics: Condensed Matter* **18**, 4161 (2006).

[52] L. Néel, *Comptes Rendus Hebdomadaires Des Seances De L Academie Des Sciences* **252**, 4075 (1961).

[53] G. Madhu, K. Maniammal, V. Biju, *Physical Chemistry Chemical Physics* **18**, 12135 (2016).

[54] D. Liu, D. Li, D. Yang, Size-dependent magnetic properties of branchlike nickel oxide nanocrystals, aip adv. 7 (1)(2017) 015028.

[55] M. Srivastava, A. K. Ojha, S. Chaubey, P. K. Sharma, A. C. Pandey, *Materials science and engineering: B* **175**, 14 (2010).

[56] R. Malik, S. Annapoorni, S. Lamba, P. Sharma, A. Inoue, *Journal of Applied Physics* **104**, 064317 (2008).

[57] R. B. Kamble, V. Varade, K. Ramesh, V. Prasad, *AIP Advances* **5**, 017119 (2015).

[58] L. Kumar, M. Kar, *Journal of Magnetism and Magnetic Materials* **323**, 2042 (2011).

[59] K.-Y. Ho, X.-Y. Xiong, J. Zhi, L.-Z. Cheng, *Journal of applied physics* **74**, 6788 (1993).

[60] S. Mitra, K. Mandal, P. A. Kumar, *Journal of magnetism and magnetic materials* **306**, 254 (2006).

[61] G. Muscas, *et al.*, *IEEE Magnetics Letters* **10**, 1 (2019).

[62] S. C. Chae, *et al.*, *Advanced Materials* **20**, 1154 (2008).

[63] I. H. Inoue, S. Yasuda, H. Akinaga, H. Takagi, *Physical Review B* **77**, 035105 (2008).

[64] N. Das, S. Tsui, Y. Xue, Y. Wang, C. Chu, *Physical Review B* **78**, 235418 (2008).

[65] K. P. Biju, *et al.*, *Journal of Applied Physics* **110**, 064505 (2011).

[66] J. Won Seo, *et al.*, *Applied Physics Letters* **95**, 133508 (2009).

[67] S. Chang Lee, *et al.*, *Journal of Applied Physics* **114**, 064502 (2013).

[68] K. Park, J.-S. Lee, *Nanotechnology* **27**, 125203 (2016).

[69] M. D. Irwin, D. B. Buchholz, A. W. Hains, R. P. Chang, T. J. Marks, *Proceedings of the National Academy of Sciences* **105**, 2783 (2008).

[70] H. D. Lee, B. Magyari-Köpe, Y. Nishi, *Physical Review B* **81**, 193202 (2010).

Chapter 7

Resistive switching and Terahertz conductivity in 100 keV Cu ion implanted NiO thin films

7.1 Introduction

Antiferromagnets can be a suitable replacement for ferromagnets in spintronic applications for their faster terahertz operations compared to gigahertz speed in ferromagnets [1–3]. The next generation of technological advancement and complex computation capabilities demand high data processing in miniaturized storage devices. RRAM exhibits the potential interest to replace the limitations of conventional CMOS technology due to its simple structure, rapid operation, high-density integration, clear switching events, good reversibility, 3D staking compatibility, neuromorphic computing, etc. [4–8]. Among various binary metal oxides such as TiO_2 [9], ZnO [10], HfO_2 [11], CeO_2 [12], Cu_xO [13], NiO is one of the suitable candidates due to having simple cubic rack salt structure and intrinsic wide gap (3.70 eV) for RRAM applications [14]. The digital RRAM stored information in terms of resistance state by switching resistance abruptly in the oxide layer from a high resistance state (HRS) to a low resistance state (LRS) and vice versa. On the other hand, analog switching shows a gradual change in conductance with the bias, which has drawn enormous interest among researchers due to its intrinsic analogy to biological synapses for implementing brain-inspired neuromorphic computing applications. Besides RRAM applications, NiO can be utilized for various THz applications since antiferromagnetic materials process the resonant frequency in the THz region. Antiferromagnets are good passive microwave com-

ponents, such as inductors and microwave absorbers in the THz range, predicting the need beyond the post 5G technology, while ferromagnet works for these components in the GHz range [15, 16]. The recent development of active THz devices, such as ultrafast memory devices [17] and THz spin oscillators [18], motivated the researcher to put forward the THz spintronics and NiO can be one of the promising candidates for THz radiation. In NiO, the Ni^{2+} sites in the adjacent (111) planes aligned antiferromagnetically in the ground state below Neel temperature, yielding no net magnetic moments. Such spin alignment can be applied to a high-density spintronic memory application [1, 2]. The dynamics of free carriers in materials can control the transport and optical transparency. The physical and optical properties are greatly affected by the growth condition and extrinsic defect states induced by doping or ion implantation in the system. Moriyama et al. investigated the THz antiferromagnetic resonance properties in Mn, Mg, and Li-doped NiO [19]. The enhanced damping in NiO/heavy metal (Pt, Pd) at THz resonance frequency was also reported by Moriyama et al. [20]. Using the THz probe, Ha et al. showed the free carrier charge dynamics in NiO_x [21]. Wang et al. discussed THz transmission from Ni ion implanted single crystal $LiNbO_3$ [22]. THz spectroscopy analysis of 3.1 MeV Au ion implanted MgO has been reported by Ogiso et al. [23]. Wang et al. investigated the THz emission in Cu ion implanted lithium niobate single crystal at a fluence of 1.2×10^{17} ions/cm^2 [24]. Various approaches, such as doping, interface engineering, implantation, etc., have been adopted to improve the memristor parameter and THz transmission to realize the high-performance device functionality [25, 26]. However, ion implantation emerges as the suitable technique over other conventional methods to introduce defects at precise depth with appropriate amounts in the system to vary the RRAM and THz transmission properties with various ion fluences.

The first part of this chapter investigates the impact of 100 keV Cu ion implantation in ITO/NiO/Ag memristor for the transformation from analog to digital switching. We correlate the effect of defect with increasing ion fluence for such transformation. The sec-

ond part comprises the effect of defects in THz transmission in 100 keV Cu ion-implanted $Si/SiO_2/NiO$ thin films with various ion fluences. The THz results are correlated with the ion beam simulations and theoretical DFT calculations.

7.2 Experimental Details

Cleaned (cleaning process discussed in Chapter 2) ITO and Si/SiO_2 substrates were mounted in the RF sputtering system in front of the NiO target (2-inch diameter, 99.99% purity). The substrate-to-target distance was kept fixed at 6.5 cm during the deposition time. The sputtering parameters, such as RF power, reflectance, Ar gas flow rate, base pressure, and deposition pressure, were 100 W (for Si/SiO_2 substrate) and 80 W (for ITO substrate), 0 W, 15 sccm, 6.77 $\times 10^{-6}$ mbar, and 5 $\times 10^{-3}$ mbar, respectively. After deposition, we annealed all the samples under a vacuum of pressure of 3.23 $\times 10^{-2}$ mbar at a temperature of 350° C using the PECVD system. The annealed NiO sample (pristine) grown on ITO and Si/SiO_2 substrates were implanted by 100 keV Cu ions in the fluence range of 5×10^{14} ions/cm^2 to 2×10^{16} ions/cm^2 at room temperature. The phase identification of pristine and implanted samples was done using a Rigaku Smartlab X-Ray diffractometer with Cu K_α source ($\lambda = 1.5418$ Å). The thickness and surface morphology of the samples are investigated using cross-sectional FESEM and AFM images. The top electrode on the NiO sample was accomplished by conducting Ag paste. The two-terminal Keithley 2450 source meter was used to apply the bias voltage. The current was measured in an ITO/NiO/Ag memory cell with a voltage sweep step of 40 mV. The room temperature PL spectra were carried out using the 325 nm He-Cd laser source in the wavelength range of 350-650 nm through an achromatic UV objective (LMU-UVB). The PL emissions were detected using a CCD detector incorporated into the spectrometer through the same objective lens. The room temperature CL spectra were collected using the Monarc-P (GATAN) high-resolution CCD

detector integrated into the FESEM system. During CL measurement, the electron accelerating voltage was 20 KV, and irradiated over 1×1 μm area of NiO film. The self-designed THz time-domain spectrometer (TDTS) was utilized to measure the THz transmission for all the samples.

7.3 Computational Details

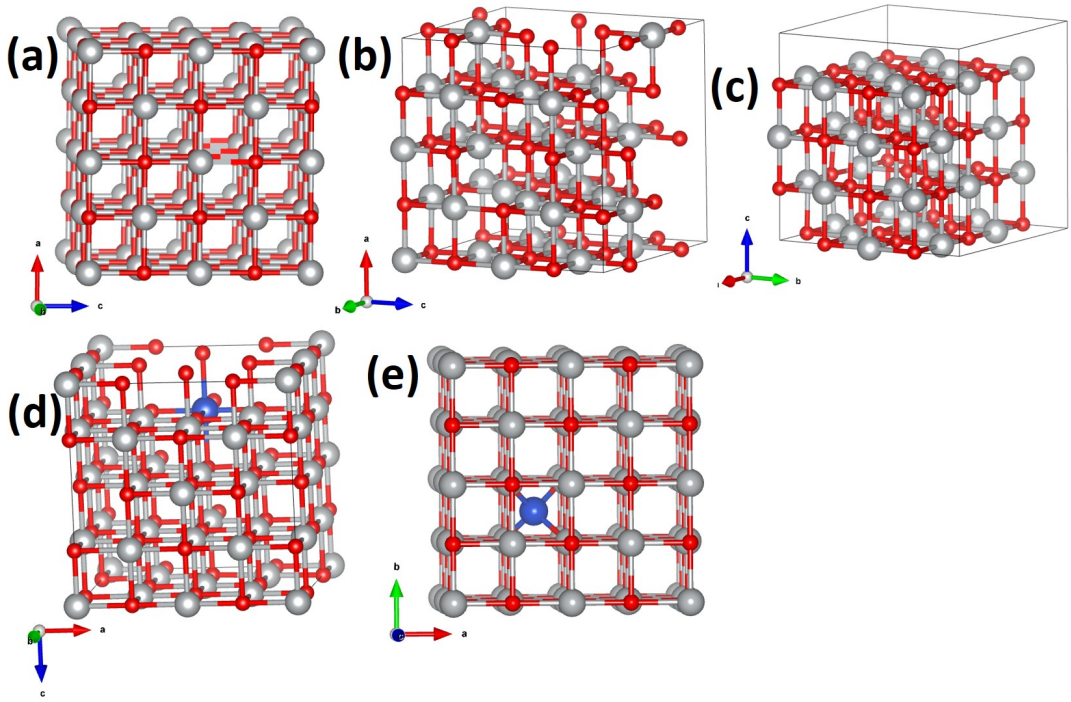

Figure 7.1: The crystal structure of (a) pristine NiO, (b) O vacancy, (c) Ni vacancy, (d) Ni substitution by Cu, and (e) Cu interstitial associated NiO, used for theoretical calculations.

The theoretical calculation of band structure and DOS was performed using the VASP code [27] with PAW method [28] for pristine and implanted samples. The exchange-correlation interaction implemented in the PBE functional was treated using the GGA scheme [29]. The supercell NiO structure, which contains 32 formula units, is subjected to onsite Coulomb repulsion correction (Hubbard U correction) along with GGA-PBE functional to imply the effect of strong electron correlation [30]. In this case, the implementation of the effective

electron interaction will reproduce the correct ground state. The antiferromagnetic arrangement along (111) plane for pristine, O vacancy, Ni vacancy, Ni substituted by Cu, and Cu interstitial associated NiO for spin polarised calculation are shown in Fig. 7.1(a-e), respectively. All the structures are relaxed using the GGA+U scheme. The values for U are 5 eV and 2 eV, which are used to apply the onsite Coulomb repulsion correction to the electrons in the Ni-d and Cu-d orbitals, respectively. The volume, cell, and shape relaxation was completed when the force was less than 1×10^{-4} eV/Å. The convergence calculation was done using the relaxed structure with a plane wave basis set (cut-off energy = 500 eV) and a Monkhorst k-point mesh of $7 \times 7 \times 7$. The threshold energy for achieving the convergence criteria was set to 1×10^{-7} eV per atom. The linear tetrahedron method with Blochl corrections was implemented in convergence and DOS calculations [31].

7.4 First Part: Resistive Switching

The XRD spectra of the ITO substrate, pristine, and implanted NiO sample are shown in Fig. 7.2. The dashed line in Fig. 7.2 corresponds to the peak position of ITO substrate. The solid line corresponds to the NiO peak position. The NiO peaks are observed at 37.31, 43.30, 62.73, 75.37, and 79.40° for all the samples. These peaks agree well with the JCPDS card number 780429, which identifies the space group of $Fm\bar{3}m$ with the cubic phase of NiO. The XRD spectra confirm that the grown NiO is polycrystalline in nature.

The thickness of the as-grown film is evaluated using the crossectional FESEM images. Fig. 7.3(a) shows that the film thickness of pristine sample is found to be 185 nm. The surface morphology of pristine, the implanted samples with fluences 5×10^{15} (sample B) and 2×10^{16} (sample C) ions/cm^2 are examined by AFM images, as shown in Fig. 7.3(b-d), respectively. Pristine sample shows the continuous growth of the NiO thin films. The surface of the implanted samples doesn't show a drastic variation compared to pristine sample,

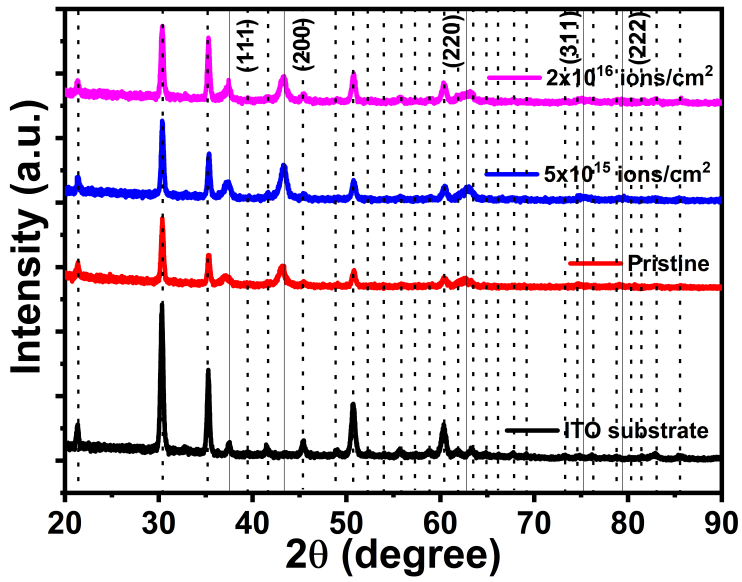

Figure 7.2: The X-ray diffraction spectra of ITO substrate, pristine, and implanted samples.

rather than the roughness. The rms surface roughness of pristine sample is 8.82 nm, and it increases to 9.02 and 9.38 nm in samples B and C, respectively, due to Cu ion implantation.

The schematic of the NiO-based ITO/NiO/Ag memristive device is shown in Fig. 7.4(a). The bias voltage is stressed between the top Ag electrode and the bottom ITO substrate. Fig 7.4(b) and 7.4(c) shows the variation of current with applied voltage of NiO memristor of pristine and sample B of the 1st, 25th, 50th, 75th, and 100th cycles for positive and negative bias sweeping. The I-V curve of the 1st cycle with the variation of ion fluences is demonstrated in Fig. 7.4(d). An abrupt change of current at a particular voltage signifies the digital switching in sample C, which will be discussed later. In contrast, pristine and sample B show the bipolar analog switching in the -2 to +2 voltage sweep range. The small-scale asymmetry is observed in pristine. This indicates the formation of the Schottky barrier at the NiO/Ag interface, with NiO being a p-type semiconductor and Ag an n-type metal. The ITO/NiO junction also forms the Schottky barrier, as reported by Swathi and No et al.

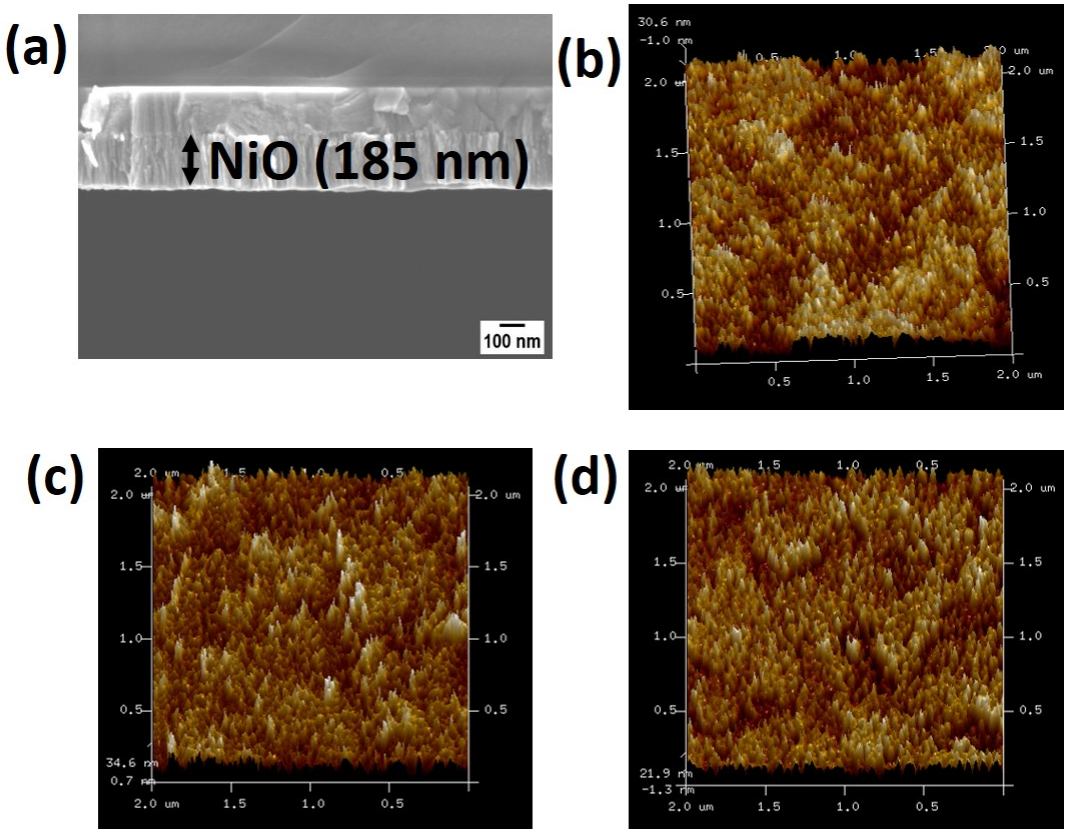

Figure 7.3: (a) Crossectional FESEM images of pristine sample. The AFM images of the (b) pristine, (c) sample B, and (d) sample C.

[32, 33]. The Schottky barrier at both interfaces is crucial for analog switching. The anti-clockwise hysteresis is observed for both the samples in both positive (0 V $\rightarrow$ 2 V $\rightarrow$ 0 V) and negative voltage sweep regions (0 V $\rightarrow$ -2 V $\rightarrow$ 0 V). In pristine, the current increases with increasing cycles at both the positive and negative bias sweeping region. In contrast, the opposite scenario is observed in sample B. The decrease of the current in sample B may be attributed to the defect formation in the system. Cu implantation creates a lot of vacancies, interstitial, and substitutional defect states in the film, and the damage increases with ion fluences. When these defect states are stressed by sufficient fields for a long period, the carrier's movement may be disrupted. This can yield a change in the Schottky barrier height and Fermi level, which is responsible for decreasing the current with consecutive increasing

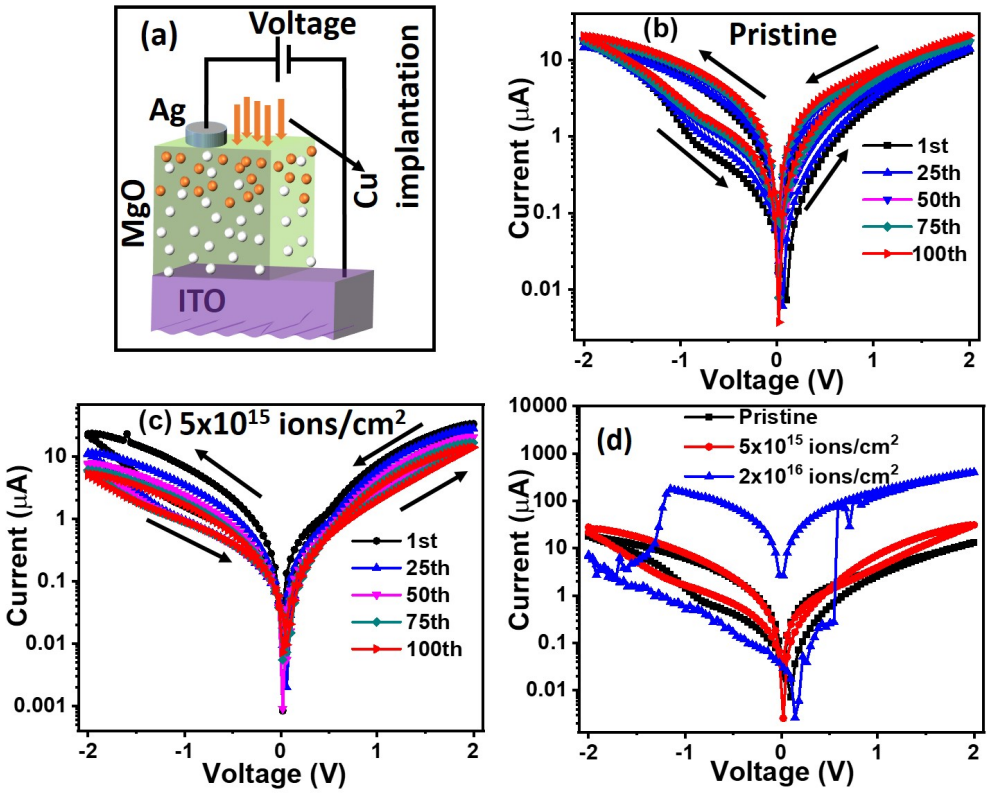

Figure 7.4: (a) Schematic of ITO/NiO/Ag RRAM device for I-V measurements. The current-voltage curve of the 1st, 25th, 50th, 75th, and 100th cycles of (b) pristine and (c) sample B. (d) The variation of the current (1st cycle) with an applied bias voltage of pristine and implanted samples with increased ion fluences

in the number of cycles. The negative voltage sweep exhibits a bigger hysteresis compared to the positive voltage sweep. The increase and decrease in conductance in pristine and sample B can be useful for biological synapses [34]. In biological systems, presynaptic and postsynaptic neurons communicate themselves through the synaptic node. The variation in the concentration of the synapses plays a key role in the brain's memory and learning process [35]. The short-term memory (STM) followed by long-term memory (LTM) is one of the basis of human memory loss, according to Psychological studies [36]. The frequent stimulation of the biological system can transform the STM into LTM [37]. In this work, the increasing or decreasing current of the NiO-based memristor can be modulated gradu-

ally with the number of cycles by taking the combination of pristine and sample B. Hence, using this analog resistive switching of NiO, synaptic learning and forgetting characteristics can be stimulated and employed in neuromorphic systems. The increasing current with consecutive pulses in pristine can be assigned as a learning process, and the decreasing current in sample B is analogous to the forgetting process. Now, to investigate the mechanism of analog switching at the interface, we fitted the double logarithmic I-V curve of the 1st positive cycle linearly. Fig. 7.5(a) and 7.5(b) show the linear fitting of double logarithmic I-V curve and ln(I) vs $V^{1/2}$ plot (Schottky plot) of the 1st positive cycle for pristine, respectively. The Ohmic condition is satisfied under the applied low bias voltage (0 V $\rightarrow$ 0.9 V), as the curve is fitted well linearly with a slope of 1.09, as seen in Fig. 7.5(a). But, under a high bias voltage, the deviation of slope from 1 indicates other conductive mechanisms, such as Schottky emission [38], space charge limited conduction [39], Fowler Nordheim tunneling [40], and Poole Frenkel emission [41] that can dominate over Ohmic conduction. The good linear fitting observed in Fig. 7.5(b) at a high bias voltage region suggests the formation of Schottky contact at both interfaces. The good linear fitting of the Schottky plot at the high bias voltage region and the asymmetry characteristic signifies the domination of Schottky emission compared to the other conduction mechanism. We used the following Richardson-Schottky equation to understand the I-V characteristics [42]:

$$I = AB^{*}T^{2}exp[-q\phi_{B} + \frac{q}{kT}\sqrt{\frac{qE}{4\pi\epsilon_{i}}}] \tag{7.1}$$

Where, A = Conduction area, B^{*} = Effective Richardson constant ($\frac{4\pi q m_{n}^{*} k_{0}^{2}}{h^{3}}$), T = Absolute Temperature, k = Boltzmann constant, q = electric charge, E = $\frac{V}{d}$, d = NiO film thickness, ϕ_{B} = Schottky barrier, ϵ_{i} Dielectric constant of NiO.

After taking logarithm on both sides, the equation 7.1 reflect as:

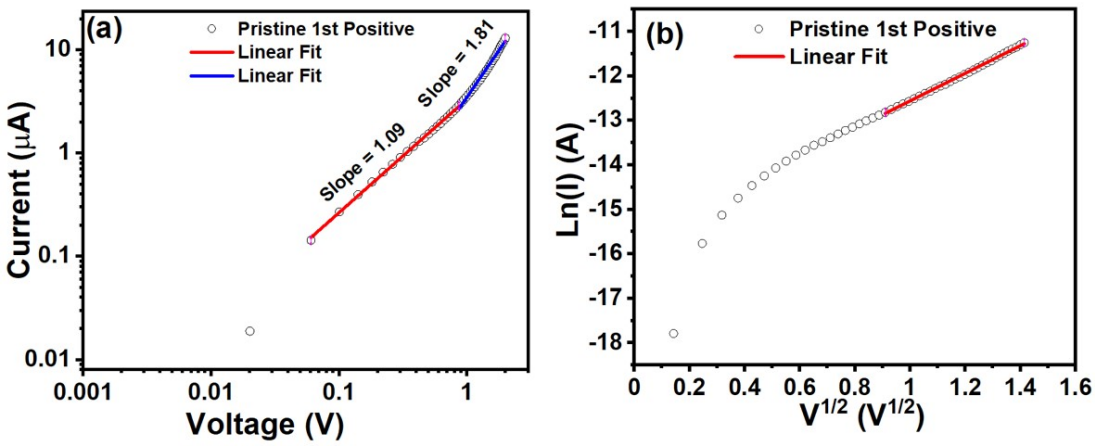

Figure 7.5: (a) The double logarithmic I-V plot and (b) ln(I) vs $V^{1/2}$ plot with liner fitting for first positive voltage scan of pristine.

$$ln(I) = ln(AB^*T^2) - \frac{q\phi_B}{kT} + \frac{q}{kT}\sqrt{\frac{q}{4\pi\epsilon_i d}}\sqrt{V} \tag{7.2}$$

The intercept value at the ln (I) axis after linear fitting of the Schottky plot in positive and negative bias at higher field region (Fig. 7.5(b)) (0.9 V $\rightarrow$ 2 V) provides the Schottky barrier height. In this case, we used the Richardson constant as B^* = 119.8 K/$K^2.cm^2$ by considering m_n^* = 1.0 and m_0 = 9.1 $\times$ 10^{-31} Kg. The variation of the Schottky barrier with the number of cycles for positive and negative voltage sweep of pristine and sample B is shown in Fig. 7.6(a) and 7.6(b), respectively. The energy band diagram of Schottky contact is illustrated in Fig. 7.6(c). In pristine, the Schottky barrier decreases with the increase of the number of cycles for both positive and negative bias. The obstruction for the carrier reduces due to the decrease in the Schottky barrier at the interface. Hence, the reduction of ϕ_B with increasing cycle increases the conduction in pristine for both positive and negative voltage sweep. In contrast, the decrease of the current with the number of cycles in sample B is due to the increase of the Schottky barrier at the interface for both positive and negative voltage sweep. The increase in the barrier height may be attributed to the creation of defects by Cu ion implantation in the NiO thin films. The carriers need more energy to overcome

the barrier height, which yields a decrease in the current conduction in sample B. Hence, the prevailing conduction mechanism in analog RRAM devices is governed by the interface-dominant Schottky effect rather than filament formation.

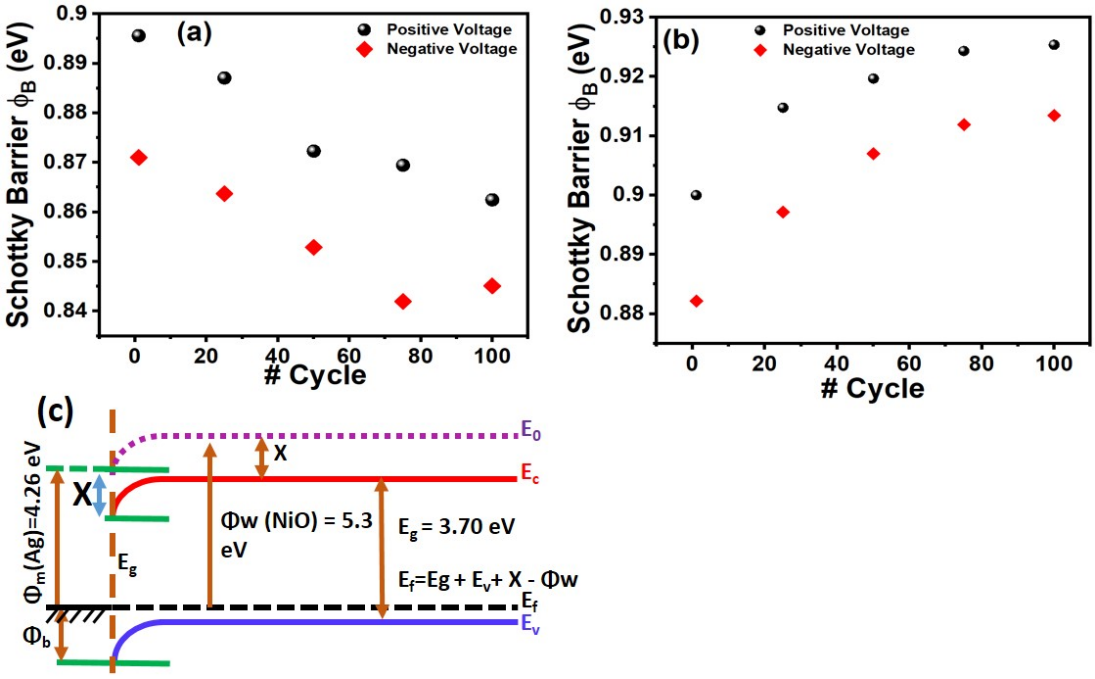

Figure 7.6: The variation of Schottky barrier with the increase of number of cycles in (a) pristine, (b) sample B for positive and negative voltage scan. (c) The schematic of Schottky contact at NiO/Ag interface.

Sample C shows the digital bipolar resistive switching in the same voltage sweeping range (-2 V → 0 V →2 V and 2 V → 0 V → -2 V), as shown in Fig. 7.7(a). An electroforming process was observed at the lower voltage region due to the presence of high vacancy defect concentration in the sample, induced at high Cu ion fluences. The higher fluence sample is transformed into a digital RRAM device through the electroforming process, whereas pristine and lower fluence samples (sample B) show the signature of analog switching. After electroforming, the current jumps at 0.54 V for the first cycle and reaches the LRS state, defining it as a SET process. The device moves from LRS to the HRS at -1.15 V by dropping the current abruptly, defining the RESET process. The SET and RESET

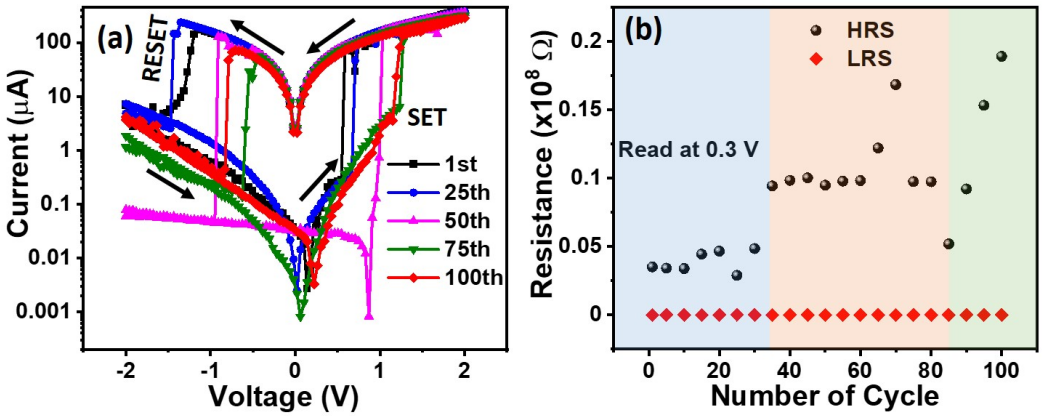

Figure 7.7: (a) The current-voltage curve of the 1st, 25th, 50th, 75th, and 100th cycles of sample C, (b) The LRS and HRS state with an increasing number of cycles for the endurance test of sample C. The HRS and LRS was read at 0.3 V.

cycles of the memristor (sample C) are clearly observed in Fig. 7.7(a). The SET voltage increases with increasing the number of cycles, while the RESET voltage reduces for the higher one with respect to the initial cycle. The hysteresis developed drastically in sample C compared to pristine sample and sample B. The mechanism of such an abrupt change of current at the SET and RESET point is understood in the next section through the vacancy filamentary model. Now, the endurance of the device is examined by plotting the HRS and LRS with the increasing number of cycles, as shown in Fig. 7.7(b). The current was read at 0.3 V. The graph shows that HRS exhibits a fluctuation with the number of cycles, indicating the requirement of more cycles for stability, whereas the LRS is relatively stable. The clear ON-OFF is sustained up to the 100th cycle. The gradual increase in the gap between LRS and HRS (as shown in different color regions) suggests that the device can store information for a long period of time. Hence, ion implantation with proper ion energy and species can be an alternate technique to improve the endurance capability of RRAM devices.

The schematic of the filamentary model through oxygen vacancy for understanding the

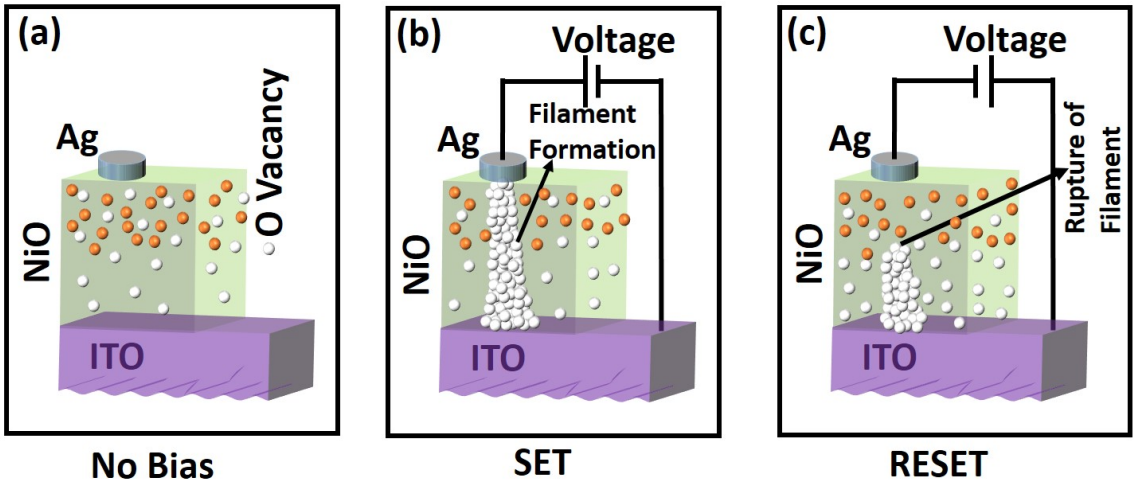

Figure 7.8: The schematic of the proposed filamentary model for the (a) zero bias, (b) SET, and (c) RESET process in digital resistive switching of sample C.

current conduction mechanism in sample C is shown in Fig. 7.8. Lee et al. [43] reported that lower formation energy is required for oxygen vacancy than Ni vacancy, and the certain configured oxygen vacancies form clusters help to form the conducting path. In sample C, high fluence boosts the sufficient number of vacancies in the matrix, which helps in filament formation. In zero bias condition (Fig. 7.8(a)), no vacancy filament formed, although a lot of vacancy defects are already present in the system. After applying the sufficient positive bias voltage, the vacancies and oxygen ions are generated. The oxygen ions will migrate toward the Ag electrode due to high drift velocity compared to vacancies. The existing large amount of induced and generated vacancies in the matrix accumulate to form the vacancy filament. The path between the top and bottom electrode is completed through the formation of vacancy filament at the SET point (Fig. 7.8(b)), and the current jumps abruptly to reach the LRS state. In the RESET process, the oxygen ions migrate back toward the bottom electrode. During migration, they recombine with the oxygen vacancies. The quick annihilation of the vacancies will rupture the filament (Fig. 7.8(c)), and the current will drop sharply at the RESET voltage. Hence, the formation and rupture of the vacancy filament explain the

SET and RESET process of the ITO/NiO/Ag device (implanted with a sufficient high fluence of 2×10^{16} ions/cm^2). The analog switching is modulated by the interface-dominated Schottky effect at the NiO/Ag and ITO/NiO interface, whereas the bulk-dominated vacancy filamentary model influences the digital switching in sample C. The NiO film is modified by the creation of a lot of vacancy defects using Cu ion implantation, which plays the underlying role of transforming analog to digital switching of ITO/NiO/Ag device after the threshold fluence.

7.5 Second Part: Optical Properties and THz Dynamics

To understand the THz dynamics of 100 keV Cu ion-implanted Si/SiO_2/NiO thin films, we first do ion beam simulations to understand the effect of implantation in the matrix. Then, subsequently observing the surface morphology, phase identification, and optical properties through PL and CL spectra to identify various kinds of defects, we analyze the nature of THz optical conductivity with ion fluences and correlate them with defects.

7.5.1 SRIM and TRIDYN Simulations

The variation of dpa with target depth, calculated from SRIM simulations [44], are shown in Fig. 7.9(a). The option " Detailed Calculation with full Damage Cascades" was implemented for simulation in the version 'SRIM 2013'. The inset of Fig. 7.9(a) shows the simulation result of deposited energy and Cu ion range vs target depth. dpa is calculated using the Eq. 6.1, as presented in chapter 6. Fig. 7.9(a) shows that the damage increases with ion fluences, and maximum displacement of the host atoms occurs at a depth of 20 nm for all the fluences. The maximum dpa is observed in 2×10^{16} ions/cm^2 fluence (highest fluence) sample. The projected range of Cu ions is around 35 nm, where the maximum ions deposit their energy at a depth of 20 nm, as shown in the inset of Fig. 7.9(a). The energy deposition depends on the S_e and S_n value of the incident ions. The SRIM-TRIM [45] cal-

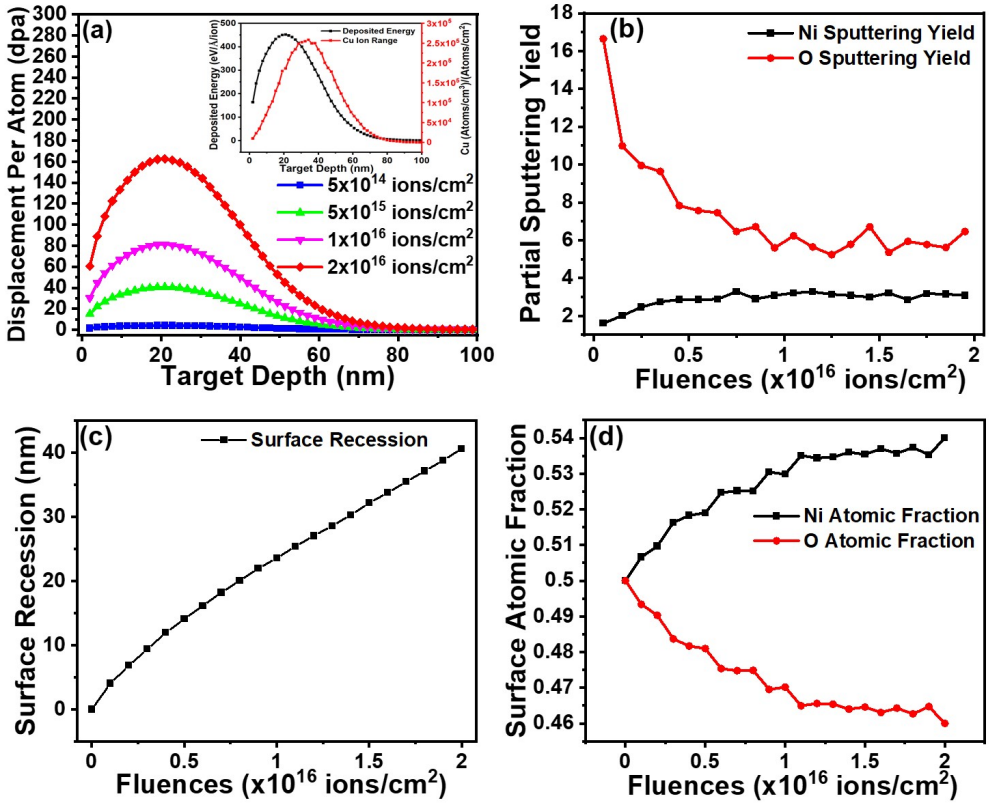

Figure 7.9: (a) The variation of displacement per atom with respect to target depth for different ion fluence, calculated using SRIM simulations. The inset shows the SRIM simulated deposited energy and ion range vs. target depth. The TRIDYN simulation for (b) partial sputtering yield, (c) surface recession, and (d) surface atomic fraction with ion fluences.

culated S_e and S_n values for 100 keV Cu ions in NiO are 203.8 keV/μm and 2286 keV/μm, respectively. Nuclear energy loss dominates over electronic energy loss: more than 11 times of S_e. So, it is more probable to displace the host atoms through elastic collisions from their lattice site to create vacancy defects. The ionic radius of Cu^{2+} (0.73 Å) is comparable to the ionic radius of Ni^{2+} (0.69 Å) . It is also possible that Cu can substitute the Ni atoms and occupy the substitutional site. Cu can also sit at the interstitial site. The ions are more capable of displacing the host atom at a depth of 20 nm, as deposited energy is maximum at this depth, as seen in Fig 7.9(a). After this depth, dpa gradually decreases

with the decreasing of the deposited energy up to the depth of the ion range. The dynamic simulation of partial sputtering yield, surface recession, and surface atomic fraction with increasing ion fluences are shown in Fig. 7.9(b-d), respectively. The sputtering yield of O is significantly higher than Ni up to the fluence of 5×10^{15} ions/cm^2. The sputtering of Ni and O atoms reaches a steady state for the higher fluence (1-2$\times10^{16}$ ions/cm^2). This yields that there might be non-proportionate Ni and O atoms near the surface. The surface recession increases with ion fluences. The recession is nearly 40 nm at the highest fluence (Fig. 7.9(c)). This indicates that the sputtering dominates up to this depth. Further, the atomic fraction of Ni and O atoms is equal for pristine sample, but the atomic fraction of Ni increases with respect to the O atom with the increasing of ion fluences. This verifies the non-proportionate atomic elements near the surface due to sputtering. As O is lighter than the Ni atom, the relative decrease of O atomic fraction with fluences occurs due to higher sputtering than the Ni atom.

7.5.2 Surface Morphology and Structural Analysis

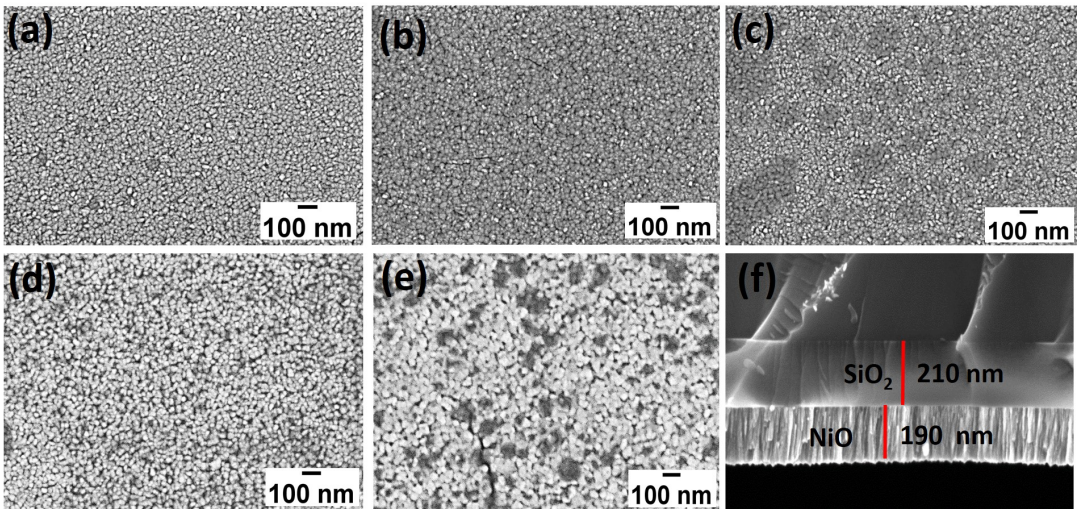

Figure 7.10: The surface morphology of (a) pristine, (b) 5×10^{14} ions/cm^2, (c) 5×10^{15} ions/cm^2, (d) 1×10^{16} ions/cm^2, and (e) 2×10^{16} ions/cm^2. (f) shows the cross-sectional FESEM to get the thickness of pristine.

The surface morphology for pristine and implanted samples is shown in Fig 7.10(a-e), respectively. The thickness of pristine sample is measured to be 190 nm, as shown in Fig. 7.10(f). Fig. 7.10(b-e) for the implanted samples reveal that the NiO film remains nearly uniform all over the surface even after implantation. The particles on the surfaces become loosely bound to each other with increasing ion fluences compared to pristine sample.

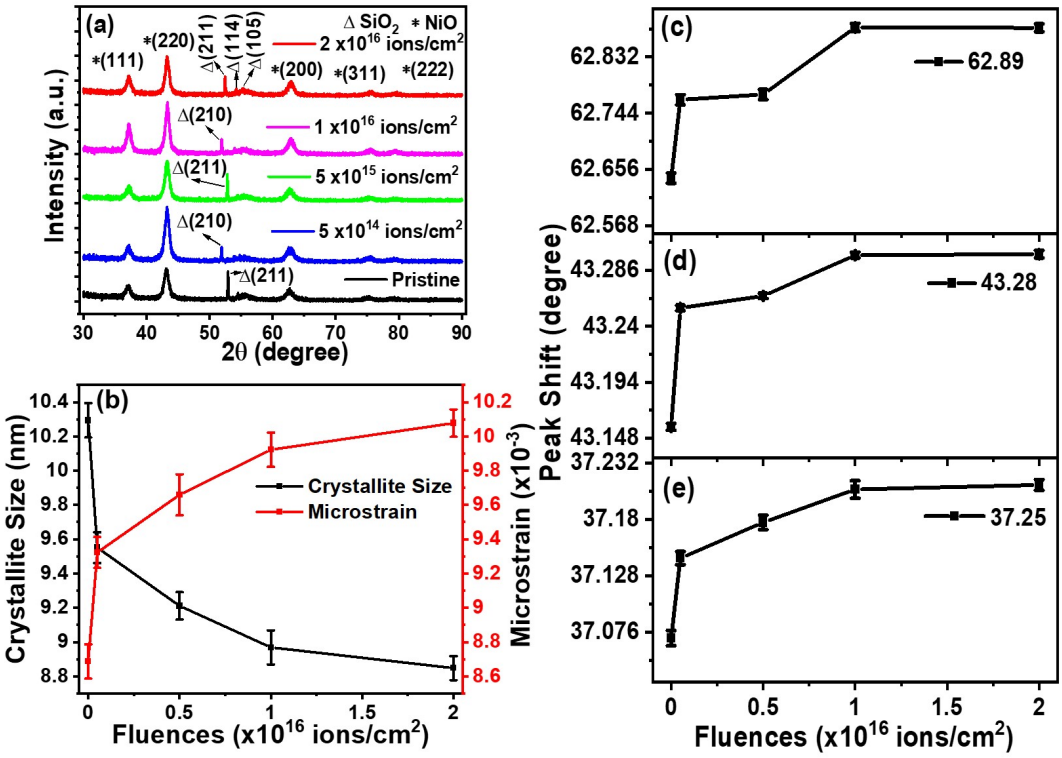

Figure 7.11: (a) The XRD spectra of pristine and implanted samples in the fluence range of 5×10^{14} ions/cm^2 - 2×10^{16} ions/cm^2, (b) The variation of crystallite size and microstrain with ion fluences, (c-e) The shifting of the XRD peak position of 62.89°, 43.28°, and 37.25° with increasing ion fluences, respectively.

The XRD pattern for pristine and implanted samples is shown in Fig. 7.11(a). The peaks observed for the highest fluence are 37.21, 43.29, 62.87, 75.41, and 79.49°, matching well with the standard JCPDS number 780429. These peaks correspond to the (111), (200), (220), (311), and (222) planes, respectively, of the face-centered cubic structure of

NiO with a space group of $Fm\bar{3}m$. The peaks at 51.98, 53.10, 54.02, and 56.10° (211), (corresponding planes (210), (211), (114) and (105), respectively) of SiO_2 substrate also appeared in the spectra (JCPDS number 893608). The variation in crystallite size and microstrain is shown in Fig. 7.11(b). The crystallite size and microstrain are calculated using the Scherrer equation as mentioned in equation 5.1 and 5.2, respectively. The crystallite size decreases with increasing Cu ion fluences, whereas the microstrain increases with fluences. The decreasing crystallite size occurs due to the increase in the defect states (such as vacancy, interstitial, and substitutional defects) in the matrix. The significant XRD peak shifting with ion fluences of the intense peak at 62.89, 43.28, and 37.25° are shown in Fig. 7.11(c-e), respectively. The peak shifting improved towards the exactitude peak position referenced in the standard JCPDS. This means that the increasing defects, resulting in the increase of damage and strain, play a role in shifting the peak positions with ion fluences.

7.5.3 Optical Properties

PL Studies

PL emission is very sensitive and responds differently depending on the structure of the material and the presence of defects in the matrix. The PL spectra at room temperature for pristine and implanted samples for different ion fluences in the wavelength range of 350 -650 nm are shown in Fig 7.12(a). The typical deconvoluted PL spectra for pristine are presented in Fig 7.12(b). The spectra are deconvoluted into three peaks at 429, 510, and 574 nm, and their corresponding variation of integrated intensity with ion fluences are illustrated in Fig. 7.12(c-e), respectively. The violet emission at 429 nm is attributed to the electronic transition of the trapped electron from the Ni interstitial (Ni_i) state to the valence band [46]. The increasing trend of integrated intensity suggests that the Ni interstitial defect states increase with ion fluences. Jiang et al. [47] reported that the 510 nm green emission corresponds to the Ni vacancy related to deep-level emission. The probability of

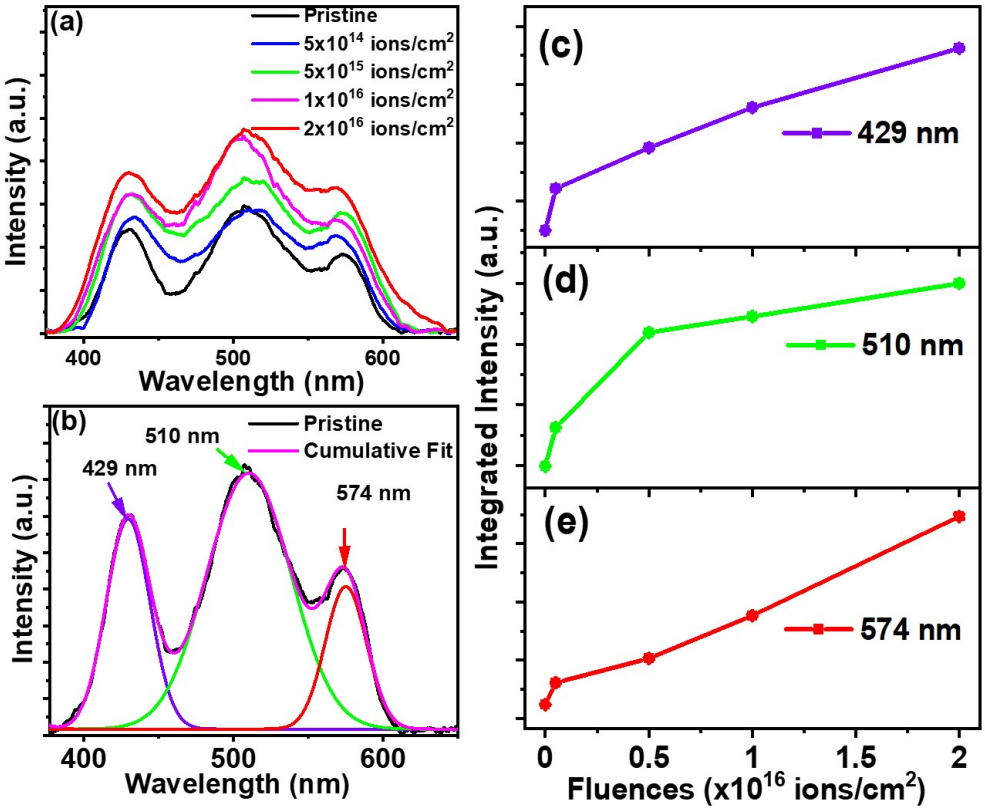

Figure 7.12: (a) The PL spectra of pristine and implanted samples, (b) The typical deconvoluted PL spectra of pristine, The variation in integrated intensity with ion fluences for the peak position at (c) 429, (d) 510 and (e) 574 nm.

the origination of this green emission due to O vacancy can not be neglected [46, 48]. The intensity of the green emission largely depends on the concentration of Ni or O vacancy. During vacuum annealing, the production of vacancy is more favorable than interstitial defect. From our sputtering simulation (Fig. 7.9(b)), we observed that the Ni and O atoms are sputtered out from the surface, contributing to forming the corresponding vacancies. So, the presence of Ni and O vacancies may be responsible for this emission. The recombination between the electrons trapped at the shallow level seated just below the CB and holes trapped in deep-level O vacancies can be attributed to this emission [46]. The integrated in-

tensity for the visible emission band increases with ion fluences, which suggests that the Ni and O vacancies also increase with fluences. The 574 nm emission band is also attributed to oxygen vacancies [49], and the vacancy defects are increased with ion fluences, as seen in Fig. 7.12(e). From PL, we observed that O vacancies dominate over Ni vacancies, as the sputtering of O is higher than Ni. So, the vacancy and interstitial defects can affect the THz transmission and the optical conductivity of the samples.

CL Studies

The luminescence signals based on CL have been reported hardly for NiO. The CL spectra for pristine and implanted samples with the variation of the ion fluences are shown in Fig. 7.13(a). The spectra of pristine sample are deconvoluted into three peaks at 445 (2.78 eV), 481 (2.57 eV), and 652 nm (1.90 eV), as shown in Fig. 7.13(b). The corresponding change in the integrated intensity of the CL peaks with fluences is exhibited in Fig. 7.13(c-e), respectively. The luminescence emission of metal oxide is generally of two kinds: (i) near-band edge emission due to electron-hole recombination between CB and VB and (ii) deep-level defect emission in the visible region. The emission peak at 445 nm is attributed to the transition of $T_{2g}^{1} \rightarrow A_{2g}^{3}$, Ni interstitials, or double ionized Ni vacancies, as reported by Taeno et al. [50]. The parity and spin consideration forbids the d-d transition, but the presence of different defect states allows them by lowering the symmetry [51]. The lowering of crystal symmetry due to local noncubic distortions and surface-induced defects (as seen in SRIM and TRIDYN simulations) is also responsible for the enhancement of luminescence in NiO sample. The intense visible CL emission band peak at 481 nm can be associated with defect-induced states such as Ni vacancies, Ni^{2+} defect states, or crystal field d-d transition [50]. This emission arises from the inter-band transition due to defects such as O vacancies, Ni interstitials, or other impurities with incomplete bonding [52]. The direct electron-hole recombination of Ni-d orbital in CB to O-p orbital in the vacancy state is also another pos-

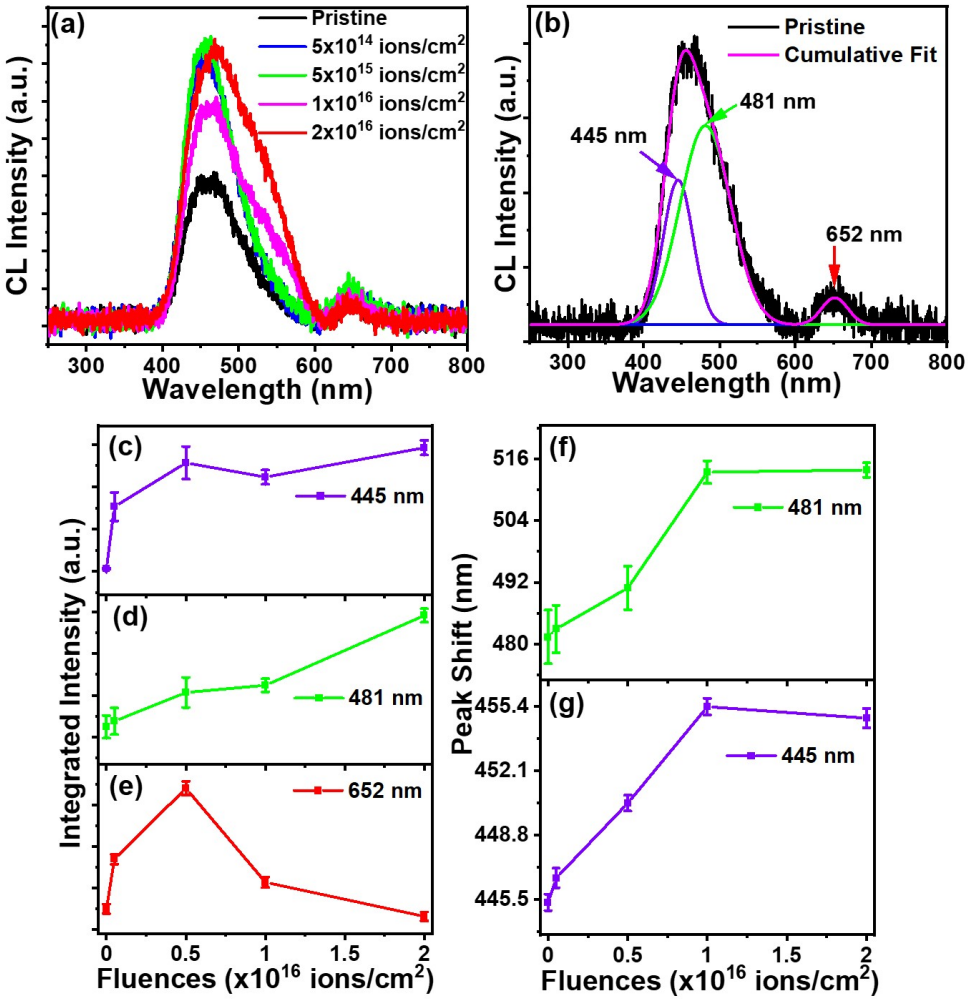

Figure 7.13: (a) The CL spectra for pristine and implanted samples, (b) The typical deconvoluted CL spectra for pristine, (c-e) The integrated CL intensity of the deconvoluted peak at 445, 481, and 652 nm, respectively, The shifting of intense CL peak at (f) 481 and (g) 445 nm with ion fluences.

sible transition for this emission. The band emission at 652 nm is related to the presence of oxygen vacancies [49], which is induced with ion fluences in the matrix. The integrated intensity of 445 and 481 nm peaks increases with ion fluences, whereas the 652 nm peak shows a decreasing trend after the fluence of 5×10^{15} ions/cm^2. The enhancement of the integrated intensity of the blue and green emissions signifies that the Ni interstitials, Ni,

and O vacancy defects increase with ion fluences. The peak shifting of the green and blue emission with fluences are shown in Fig. 7.13(f) and 7.13(g), respectively. The green emission shifts to 513 nm for the highest fluences, which lies in the visible PL band emission (510 nm). For blue emission, it shifts to 454 nm. Ashish et al. reported that the blue emission at 454 nm is responsible for the radiative electronic transition from doubly ionized Ni vacancy states to holes in VB [46].

Raman Studies

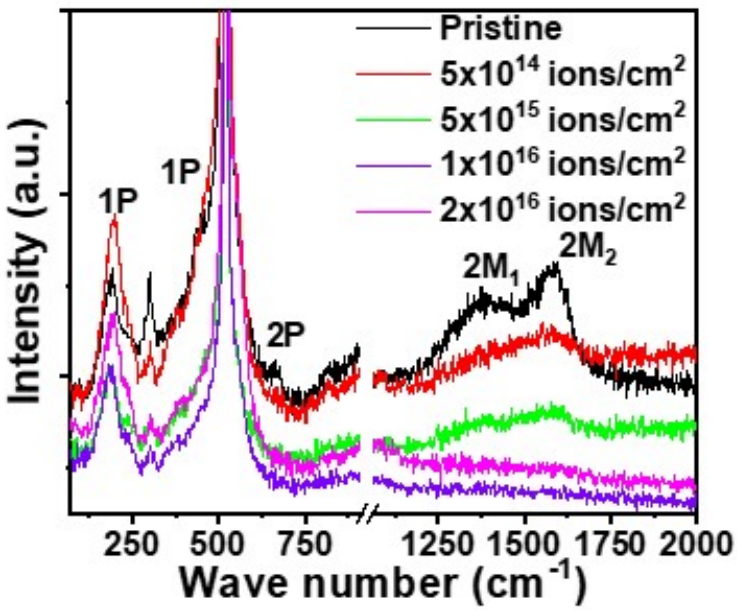

Figure 7.14: The room temperature Raman spectra of pristine and Cu ion implanted samples in the fluence range of 5×10^{14} ions/cm^2 to 2×10^{16} ions/cm^2.

The room temperature Raman spectra of pristine and Cu ion-implanted NiO are shown in Fig. 7.14. The Raman active modes are found at 193 (1P), 450 (1P), 670 (2P), 810 (2P), 1367 ($2M_1$), and 1585 ($2M_2$) cm^{-1}. The defects due to oxygen vacancies, which lowered the symmetry of the lattice, are attributed to the arising of the 1P mode at 193 cm^{-1} [53].

The TO phonon mode occurs at 450 cm^{-1} [54], which is gradually abolished with ion fluences. This peak arises due to the magnetostriction effect. The weak peak observed in pristine at 670 cm^{-1} is attributed to TO(X)+LA(X) mode [55]. The two broad peaks at 1367 and 1585 cm^{-1} corresponds to two-magnon (2M, we call it $2M_1$ and $2M_2$, respectively) mode [55]. The 2M modes gradually decrease with ion fluences. Fig. 7.14 shows that the two modes apparently merged into one mode to the fluence 5×10^{15} ions/cm^2 and completely broadened at the highest fluences. The disappearance of this mode suggested the destruction of the magnetic ordering. Since the defect states increase with ion fluences, there will be a change in the spin alignment around the defects, resulting in the net moment in antiferromagnetic NiO. This 2M scattering in NiO, which is related to Brillouin zone-edge magnons, interacts weakly with phonons. The broadening of this mode involves the substitutional disorder in the matrix [54]. The probability of substitution of Ni by Cu is higher at the highest fluence sample due to the increase of a huge number of Cu implantation in NiO than the lower fluence samples. Hence, the broadening of 2M mode appears in NiO due to the induction of substitutional disorder in the matrix by Cu ions.

7.5.4 THz Properties

Figure 7.15(a) shows the THz transmittance at room temperature as a function of frequency for pristine NiO and implanted samples. Pristine shows the transmission dip (absorption) at a frequency of 1.09 THz, while it is shifted to 1.16 THz for the highest fluence sample. The increasing of vacancies, Ni substituted by Cu, and Cu interstitial defect states in the matrix (which led to the shift of diffraction peak to the exactitude position with ion fluences) may be responsible for such kind of THz absorption shifting. For further understanding, real conductivity is calculated from the THz transmittance signal. The higher real conductivity at a certain THz frequency signifies that at that frequency, the interaction of the THz pulse with the material is high. In the lower frequency region of real conductivity spectra,

the Drude characteristic is present, which is due to mainly free carriers. The peak at resonance frequency indicates a Lorentzian behavior due to mainly bound carriers. Hence, to understand the interaction of THz pulse with free and carriers of the sample, we fit the real conductivity with the Drude-Lorentz (D-L) model (shown in Figs. 7.15(b)) as follows [56]:

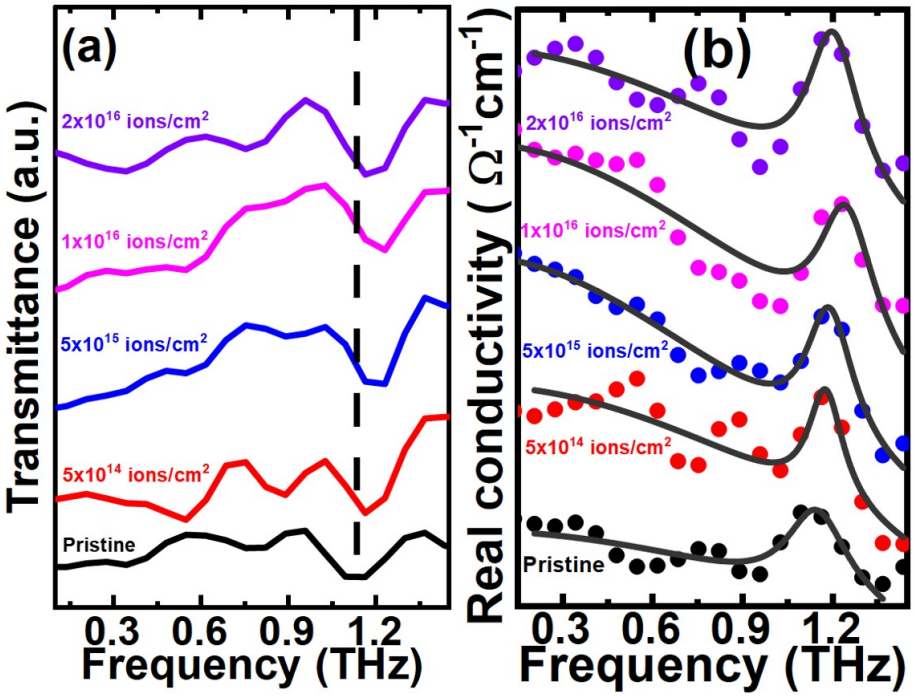

Figure 7.15: (a) The THz transmission spectra for pristine and implanted samples in the fluence range of 5×10^{14} - 2×10^{16} ions/cm^2 at room temperature, (b) The real optical conductivity with THz frequency for pristine and implanted samples, found from transmission spectra.

$$\sigma^{\mathrm{r}}_{\mathrm{DL}}(\omega) = \epsilon_0[\frac{\omega_{p1}^2\tau_1}{(1+\omega^2\tau_1^2)} + \frac{\omega_{p2}^2\tau_2\omega^2}{\omega^2+\tau_2^2(\omega^2-\omega_0^2)^2}] \tag{7.3}$$

The first term in Eq. 7.3 signifies the Drude term, which is related to free charge carriers, and the second part is the Lorentzian term. Here, ω_{p1} and ω_{p2} are the plasma frequencies for free and bound charge densities, respectively. τ_1, and τ_2 are the scattering time of free and bound charges, and ω_0 is the peak frequency.

The peak of the real part of the optical conductivity shifts from 1.13 THz to 1.2 THz for

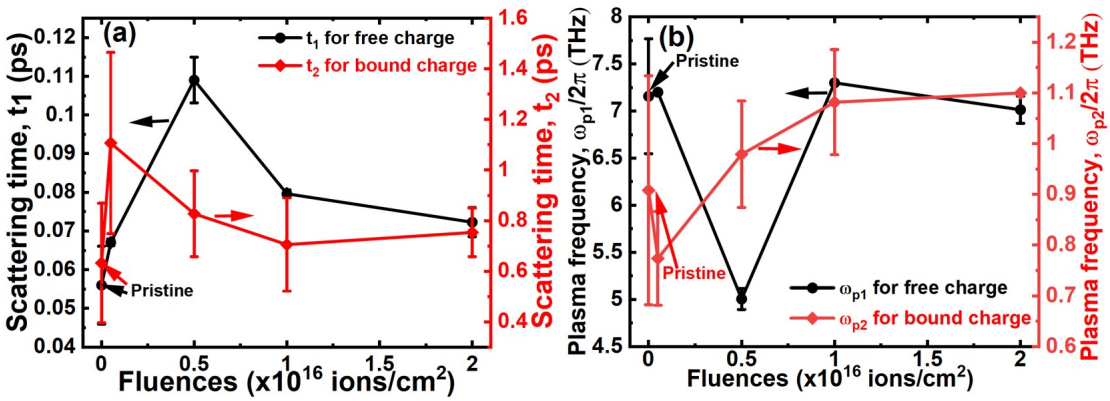

Figure 7.16: The variation of (a) scattering time and (b) plasma frequency for free and bound charges with ion fluences

pristine to highest fluence sample. This shifting may be attributed to the creation of defects in the matrix due to implantation.

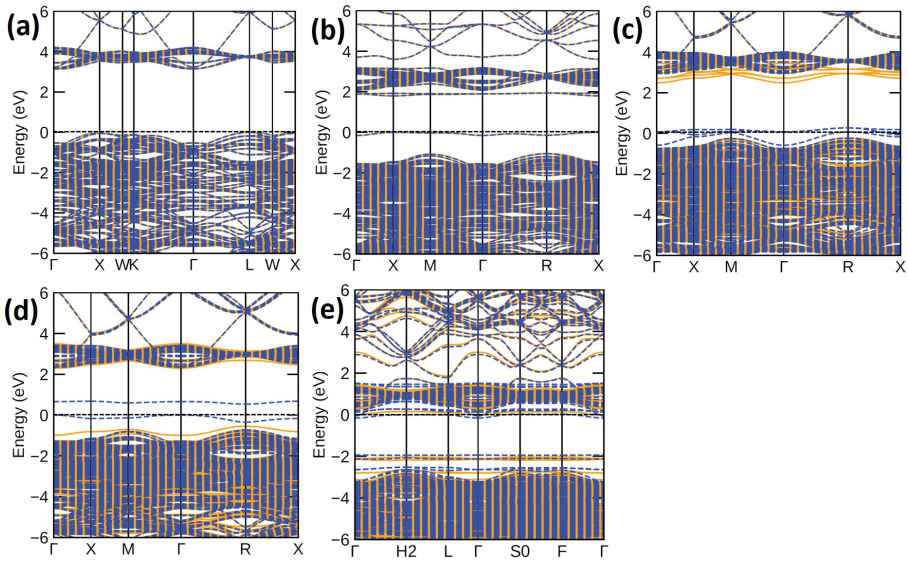

Figure 7.17: The calculated band structure of (a) pristine, (b) O vacancy, (c) Ni vacancy, (d) Ni substituted by Cu, and (e) Cu interstitial associated NiO, respectively. The black dashed line along zero is the Fermi level.

It is observed that the real conductivity (RC) peak around the THz region is well simulated using the D-L model. The implantation of Cu ions creates a large number of defects in the system. We observed from the simulation that the damage significantly increases with

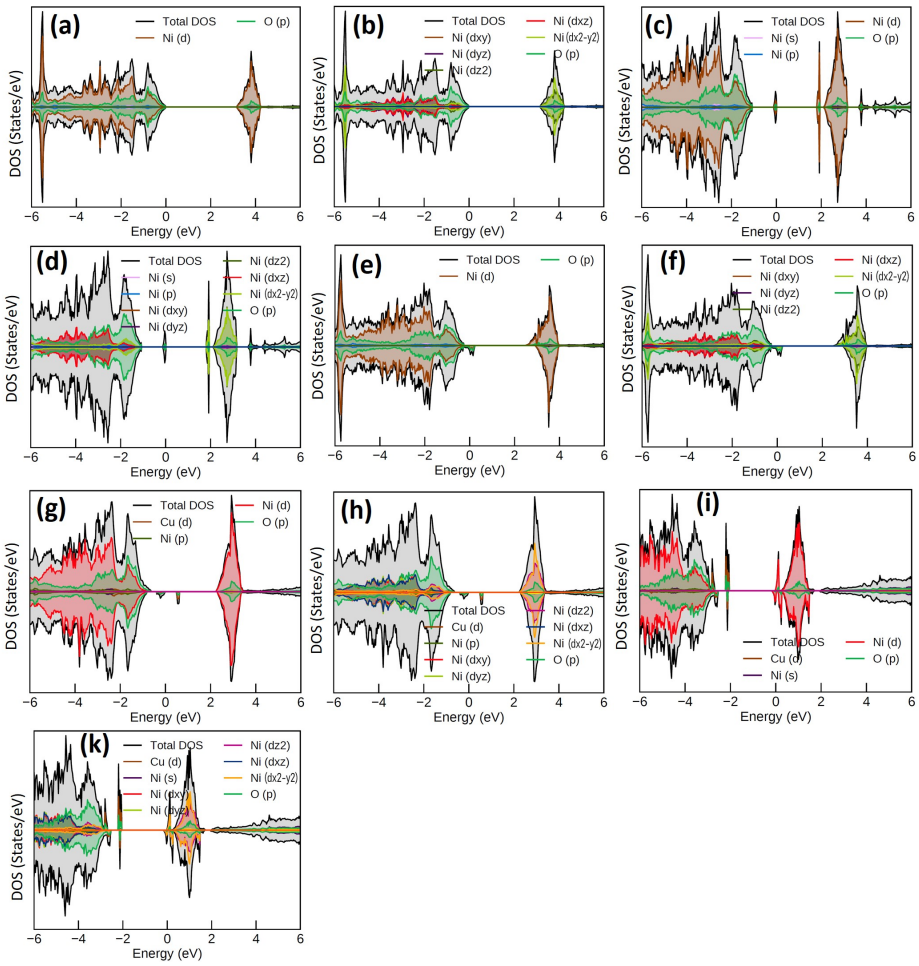

Figure 7.18: The calculated total, orbital, and Ni-d orbital decomposed DOS of (a,b) pristine, (c,d) O vacancy, (e,f) Ni vacancy, (g,h) Ni substituted by Cu, and (i,k) Cu interstitial associated NiO, respectively.

increasing ion fluences, which affects the crystal quality. The crystallite size decreases with fluences. The enhanced strain and defects with ion fluences shift the optical conductivity and THz transmittance [21]. Optical conductivity is associated with carrier density, which can give an idea about scattering time and plasma frequency with ion fluences. The variation of scattering time and plasma frequency for free and bound charges with ion fluences can be seen in Fig. 7.16(a) and 7.16(b), respectively. The scattering time for free and bound charges increases for lower fluences and decreases for higher fluences. The carrier density

is low for lower fluences and relatively high for higher fluences as damage and various defect states increase with Cu ion fluences. Hence, the interaction frequency between THz signal and defect states is low for lower fluences and high at higher fluences. The plasma frequency depends on carrier density (n) and effective mass (m^*) (as, $\omega_p^2 = \frac{ne^2}{\epsilon_0 m^*}$). The competition between carrier density and effective mass influences the variation of plasma frequency. The low carrier density and high effective mass decrease the plasma frequency at lower fluence samples and increase it at higher fluence samples due to significantly increasing carrier density with increasing defects in the matrix.

Now, we need to understand such kind of THz interaction through theoretical band structure and DOS for pristine and defect-associated structures, calculated and shown in Fig. 7.17 and 7.18, respectively. The bandgap of pristine is 3.28 eV (Fig. 7.17(a)), close to the indirect bulk bandgap of antiferromagnetic NiO. The spin-polarized calculation with Hubbered onsite Coulomb repulsion correction between the electrons of Ni-d orbital shows that the up and down spin bands overlap each other, indicating no net moment. Oxygen vacancy also doesn't generate moments (Fig. 7.17(b), but it creates a vacancy state between CB and VB, which narrows down the gap. The moment generation is associated with Ni vacancy (Fig. 7.17(c)), Ni substitution by Cu (Fig. 7.17(d)), and Cu interstitial (Fig. 7.17(e)) defects. The Fermi level remains near the VB for Ni vacancy and substitutional defects, but it shifts to near the CB for Cu interstitial defects. An extra moment (-0.929 μ_b) is generated due to Cu interstitial. The combined effect of Cu interstitial, substitutional, and vacancies greatly increases the carrier density through the generation of defect states in the matrix, which helps to increase the plasma frequency for higher fluence than the lower fluences. The increased carrier concentration at the highest fluence increases the collision frequency and hence reduces the scattering time. Now, the electron density of states can give a clear picture of orbital information of the carrier density. The VB mainly consists of O-p and Ni-d orbitals; in contrast, the Ni-d orbital has a major contribution to forming the CB in

pristine (Fig. 7.18(a and b)) and all the defect-associated structures. The defect states of oxygen vacancies (Fig. 7.18(c and d))(equal contribution from up and down spin), Ni substitution (Fig. 7.18(g and h)), and Cu interstitial (Fig. 7.18(i and k)) contribute to creating the disorder in the system. The Ni vacancy (Fig. 7.18(e and f)) and Ni substitution by Cu show significant defect states near the VB around the Fermi level. So, their role in affecting the scattering can not be neglected. The defect in the system is related to the D-L model. So, the frequency of carrier scattering events increases for higher fluences, resulting in a decrease in the scattering time. The O vacancy is related to the narrowing of the gap. The production of O and Ni vacancies (as evidenced by PL and CL spectra) is low in the lower fluence region, which can lead to the lowering of the plasma frequency in this fluence. On the other hand, the increased strain with the increase of interstitial and substitutional defects with ion fluences mainly increases the carrier concentration and hence increases the plasma frequency at higher fluences.

7.6 Summary

In summary, we investigated the analog to digital transformation of bipolar resistive switching in 100 keV Cu-implanted ITO/NiO/Ag devices. Pristine and sample B show analog switching, but the digital switching characteristic developed in sample C. The Schottky barrier is formed at the NiO/Ag and ITO/NiO interfaces. The observed analog switching in pristine and sample B is interface barrier dominant due to the Schottky effect rather than the bulk domination. The decrease and increase of ϕ_B for both the polarity increases and decreases the current conduction in pristine and sample B with the increase of number of the cycle, respectively. The sudden jump of current from OFF to ON and ON to OFF state at SET and RESET voltage in sample C is elucidated by the formation and rupture of bulk-dominated vacancy filamentary model. In this case, the high Cu ion fluence boosts the

vacancies in sample C above the threshold vacancy concentration level, playing a crucial role in exhibiting such digital switching.

On the other hand, the variation of THz transmission in the 100 keV Cu ion implanted NiO samples with various ion fluences is observed due to the variation of vacancy, interstitial, and substitutional defect states between CB and VB. These defects increase with ion fluences, yielding a decrease in crystallite size and an increase in strain. The shifting of the THz transmission dip and optical conductivity peak is associated with the shifting of the XRD peak position towards the exactitude values with ion fluences. The shifting is also affected by the increase of defects in the matrix. The carrier concentration tunes the scattering time and plasma frequency for free and bound charges. The DOS calculation shows that the strengthening of disorder with the presence of O vacancy (narrows the gap), Ni substitution, and Cu interstitial increases the carrier concentration between CB and VB with ion fluences. This increases the scattering frequency and hence decreases the scattering time for higher fluences. The increased strain and carrier density due to increased defect states is responsible for increasing the plasma frequency at higher fluences.

Bibliography

[1] T. Jungwirth, X. Marti, P. Wadley, J. Wunderlich, *Nature nanotechnology* **11**, 231 (2016).

[2] V. Baltz, *et al.*, *Reviews of Modern Physics* **90**, 015005 (2018).

[3] T. Jungwirth, *et al.*, *Nature Physics* **14**, 200 (2018).

[4] K. M. Kim, D. S. Jeong, C. S. Hwang, *Nanotechnology* **22**, 254002 (2011).

[5] R. Waser, M. Aono, *Nature materials* **6**, 833 (2007).

[6] I. Baek, *et al.*, *IEDM Technical Digest. IEEE International Electron Devices Meeting, 2004.* (IEEE, 2004), pp. 587–590.

[7] P. Sun, *et al.*, *Scientific reports* **5**, 13504 (2015).

[8] D. Marković, A. Mizrahi, D. Querlioz, J. Grollier, *Nature Reviews Physics* **2**, 499 (2020).

[9] X. Cao, *et al.*, *Journal of alloys and compounds* **486**, 458 (2009).

[10] G. Chen, *et al.*, *Advanced Materials* **24**, 3515 (2012).

[11] S. Privitera, *et al.*, *Microelectronic Engineering* **109**, 75 (2013).

[12] A. Younis, D. Chu, I. Mihail, S. Li, *ACS applied materials & interfaces* **5**, 9429 (2013).

[13] R. Dong, *et al.*, *Applied physics letters* **90**, 4 (2007).

[14] S. Seo, *et al.*, *Applied Physics Letters* **85**, 5655 (2004).

[15] K. David, H. Berndt, *IEEE vehicular technology magazine* **13**, 72 (2018).

[16] A. Yusoff, *et al.*, *Journal of Applied Physics* **92**, 876 (2002).

[17] K. Olejník, *et al.*, *Science advances* **4**, 3566 (2018).

[18] R. Cheng, D. Xiao, A. Brataas, *Physical review letters* **116**, 207603 (2016).

[19] T. Moriyama, *et al.*, *Physical Review Materials* **4**, 074402 (2020).

[20] T. Moriyama, *et al.*, *Physical Review B* **101**, 060402 (2020).

[21] T. Ha, *et al.*, *2009 34th International Conference on Infrared, Millimeter, and Terahertz Waves* (IEEE, 2009), pp. 1–2.

[22] Y.-h. Wang, H.-w. Ni, W.-t. Zhan, J. Yuan, R.-w. Wang, *Optics Communications* **291**, 334 (2013).

[23] H. Ogiso, M. Nakada, S. Nakano, J. Akedo, *Nuclear Instruments and Methods in Physics Research Section B: Beam Interactions with Materials and Atoms* **257**, 545 (2007).

[24] Y. Wang, R. Wang, J. Yuan, Y. Wang, *Journal of luminescence* **147**, 242 (2014).

[25] T. Shi, *et al.*, *Small Structures* **2**, 2000109 (2021).

[26] N. Deng, H. Pang, W. Wu, *Chinese Physics B* **23**, 107306 (2014).

[27] G. Kresse, J. Furthmüller, *Physical review B* **54**, 11169 (1996).

[28] P. E. Blöchl, *Physical review B* **50**, 17953 (1994).

[29] J. P. Perdew, K. Burke, M. Ernzerhof, *Physical review letters* **77**, 3865 (1996).

[30] S. L. Dudarev, G. A. Botton, S. Y. Savrasov, C. Humphreys, A. P. Sutton, *Physical Review B* **57**, 1505 (1998).

[31] P. E. Blöchl, O. Jepsen, O. K. Andersen, *Physical Review B* **49**, 16223 (1994).

[32] S. Swathi, S. Angappane, *Japanese Journal of Applied Physics* **61**, 1009 (2022).

[33] Y. S. No, *et al.*, *Japanese Journal of Applied Physics* **52**, 051102 (2013).

[34] Z. Q. Wang, *et al.*, *Advanced Functional Materials* **22**, 2759 (2012).

[35] R. Yang, *et al.*, *Nanotechnology* **24**, 384003 (2013).

[36] J. T. Wixted, E. B. Ebbesen, *Psychological science* **2**, 409 (1991).

[37] J. L. McGaugh, *Science* **287**, 248 (2000).

[38] K. P. Biju, *et al.*, *Journal of Applied Physics* **110**, 6 (2011).

[39] J. Won Seo, *et al.*, *Applied Physics Letters* **95**, 13 (2009).

[40] S. Chang Lee, *et al.*, *Journal of Applied Physics* **114**, 6 (2013).

[41] K. Park, J.-S. Lee, *Nanotechnology* **27**, 125203 (2016).

[42] L. Zhong, L. Jiang, R. Huang, C. De Groot, *Applied Physics Letters* **104**, 9 (2014).

[43] H. D. Lee, B. Magyari-Köpe, Y. Nishi, *Physical Review B* **81**, 193202 (2010).

[44] J. F. Ziegler, M. D. Ziegler, J. P. Biersack, *Nuclear Instruments and Methods in Physics Research Section B: Beam Interactions with Materials and Atoms* **268**, 1818 (2010).

[45] R. E. Stoller, *et al.*, *Nuclear instruments and methods in physics research section B: beam interactions with materials and atoms* **310**, 75 (2013).

[46] A. C. Gandhi, S. Y. Wu, *Nanomaterials* **7**, 231 (2017).

[47] D. Jiang, *et al.*, *Vacuum* **86**, 1083 (2012).

[48] G. Madhu, V. Biju, *Physica E: Low-dimensional Systems and Nanostructures* **60**, 200 (2014).

[49] T. Potlog, L. Ghimpu, V. Suman, A. Pantazi, M. Enachescu, *Materials Research Express* **6**, 096440 (2019).

[50] M. Taeño, *et al.*, *Crystal Growth & Design* **20**, 4082 (2020).

[51] J. Gangwar, *et al.*, *Nanotechnology* **24**, 415705 (2013).

[52] S. I. Abbas, A. Q. Ubaid, *Journal of advances in Physics* **6**, 1 (2014).

[53] H. Ramachandran, M. M. Jahanara, N. M. Nair, P. Swaminathan, *RSC advances* **10**, 3951 (2020).

[54] N. Mironova-Ulmane, *et al.*, *Journal of Physics: Conference Series* (IOP Publishing, 2007), vol. 93, p. 012039.

[55] D. Wang, *et al.*, *Journal of Applied Physics* **128**, 13 (2020).

[56] J. Lloyd-Hughes, T.-I. Jeon, *Journal of Infrared, Millimeter, and Terahertz Waves* **33**, 871 (2012).

Chapter 8

Summary and future prospects

8.1 Summary

This thesis delves into the diverse electronic and optical properties of rock salt crystals, specifically focusing on MgO and NiO with low-energy ion-induced defects. The impact of point defects within rock salt structures is explored, examining their influence on memristive, THz, and nonlinear optical devices. Point defects can be created in two ways: ion implantation and chemical doping. Chemical doping results the randomly distributed defects that cannot be precisely controlled externally. However, ion implantation offers a more controlled approach to introduce defects at desired depths and areas in the target materials, depending on the incident ion species and energy. Hence, point defects are introduced in the rock salt structures using ion implantation rather than chemical doping. During low-energy ion implantation, considerable heat is generated along the ion track due to both elastic and inelastic energy loss. Elastic energy loss involves an increase in lattice temperature, while the inelastic energy loss process raises the system's temperature through electron-phonon coupling. Given the significant heat generation associated with ion implantation, the thesis also explores the impact of thermal heating on rock salt crystals concerning variations in electronic and optical properties for improving various device functionalities. This chapter summarizes the aforementioned findings and outlines potential future directions for research.

Chapter 1 elucidates a concise introduction to existing research in this domain and an exploration of the pivotal role played by ion implantation in managing defects to enhance

device functionalities. Chapter 2 gives a brief outline of the experimental method and characterization technique utilized in this thesis work. The chapter-wise summary and future prospects are as follows:

Ni and Co Ion Implanted MgO Single Crystal

The one MeV Ni and Co ions are implanted in a rock salt single crystal MgO to study the effect of point defects on modulating the optical and electronic properties. The MgO single crystal was implanted in the fluence range of 5×10^{14} ions/cm^2 to 1×10^{16} ions/cm^2. The SRIM simulations show that the maximum number of Ni and Co ions modify MgO up to the depth of 574 and 577 nm, whereas the maximum energy depositions occur at 470 and 478 nm, respectively. In TRIDYN simulations, no signature of the saturation of sputtering is observed at the highest fluences for both ions. The UV-Vis absorption spectra confirmed the presence and evolution of F, F_2, other O_2 vacancy centers, and V-type color centers in the matrix. The PL spectra also support the existence of vacancy and metal-assisted defect centers in the matrix. The Ni and Co ion act as a controlling knob to induce these defects to decrease the bandgap of MgO with increasing ion fluences. A band model is proposed to understand various defect states. We also demonstrate the electronic transition between CB and defect states and from defect states to VB using the band and DOS calculation with the help of DFT to support the proposed band model. The Raman and FTIR spectra were collected to study the induced vibrational modes in implanted samples. The Raman mode is absent in pristine. The observed defect peaks in UV-Vis and PL spectra induce the vibrational modes with ion fluences. We noticed that the overlapping of D and G bands evolves with Ni and Co ion fluences. The calculated phonon band and DOS under the framework of DFPT with the help of VASP find the origin of observed Raman scattering at 237, 346, 409, 444, 499 cm^{-1} in the implanted samples. These peaks are originated due to the vibration of Mg, O vacancy, and Mg substitution by Ni and Co-associated defect states. The FTIR spectra identify the presence of functional groups due to the chemisorption

of atmospheric constituents with MgO, stretching and bending vibration between host and implanted ions.

RRAM of ITO/MgO/Ag Device

In this part, the effect of thermal annealing is employed to investigate the altering of the RRAM properties of ITO/MgO/Ag devices. The FESEM micrographs show the cluster-type surface morphology in pristine and 350°C annealed samples. The AFM images exhibit a similar kind of surface morphology with increasing roughness from 81 to 110 nm. The peak at 42.86° in XRD spectra identifies the rock salt cubic phase of the MgO (200) plane with a space group of $Fm\bar{3}m$. The formation of native Mg and O vacancy centers during crystal growth is confirmed by UV-Vis spectra. The MgO-based RRAM device is constructed by sandwiching the oxide layer between the bottom ITO substrate and the top Ag electrode. Schottky barriers are established at both interfaces, and annealing contributes to a substantial increase in barrier height. The increment of height reduces the current conduction in annealed samples, signifying the low Joule heating effect. The annealed sample exhibits a good memory reproducible window till the 100th cycle, whereas this property lags behind in pristine. The endurance of pristine sustain till the 70th cycle, whereas in comparison, the annealed sample shows the switching property even at the 100th cycle. The bulk-dominated vacancy filamentary model with hopping conduction is adopted to explain the conduction mechanism in the memristive device.

Temperature Dependent NLOP of NiO Thin Films

This part of the thesis explores the nonlinear optical properties of pristine and thermally annealed NiO thin films. The NLOP measurements were conducted using the Z-scan technique. The FESEM images exhibit the surface morphology of the samples. The XRD pattern identifies the rock salt cubic phase of NiO. The micro-strain and lattice constant decrease with increasing annealing temperature. Annealing reduces disorder in the system, leading to an increase in the bandgap. PL and CL spectra identify the defects and suggest

a decrease in defects in the matrix with temperature. The increased bandgap is further discussed through theoretical band structure and DOS calculations. The upward shifting of Ni-$d_{x^2-y^2}$ and Ni-d_{z^2} orbitals in CB increase the bandgap. The 400°C annealed sample is considered a better optical limiter compared to other annealed samples. The OA and CA of NLOP are correlated with DFT calculations. Pristine and annealed samples exhibit the SA and TPA in OA conditions. On the other hand, a self-defocusing effect with prefocal minima and postfocal maxima is observed in CA conditions. The spin split d-d or d-p transition in the sub-bandgap is responsible for such nonlinear behavior. The observed plasmonic effect in UV-Vis spectra is excluded due to the lack of sufficient excitation energy for the resonant SPR to explain the NLOP.

Magnetocrystalline Anisotropy and RRAM of Au Implanted NiO Thin Films

This section studies the magnetocrystalline anisotropy and RRAM characteristics of 30 keV Au ion-implanted NiO thin films. The electronic energy loss dominates over the nuclear loss for low-energy ions, leading to the creation of numerous defects due to the dominant elastic collisions. SRIM simulations illustrate that the ion range is 18 nm, and the maximum energy is deposited near 6 nm. Moreover, damage increases with ion fluences in the system. The dynamic TRIDYN simulation findings indicate that the sputtering of Ni and O atoms reaches a steady-state condition at higher ion fluences. The modification of the surface morphology with ion fluences is examined using FESEM images. The thickness of the film reduces with the increasing ion fluences, which agrees well with the surface recession calculations. XRD patterns reveal the preservation of the NiO (200) rock salt structure with a cubic phase under the space group of $Fm\bar{3}m$, even under low-energy ion bombardment. The bandgap narrowing with ion fluences is incorporated with damage production during implantation. Intrinsic defect production during crystal growth induces FM properties in pristine sample. FM properties are further manipulated by the introduction of various vacancies and interstitial defects in NiO through ion implantation. The origin of FM properties

lies in the interaction energy between uncompensated surface spins and the particle core. The magnetization mechanism, blocking temperature, and bond disruptions caused by defect production at the surface contribute to the modulation of magnetocrystalline anisotropy in the system. Additionally, the RS properties of the constructed Si/NiO/Au RRAM device are investigated. The Schottky barrier and p-n junctions form at NiO/Au and Si/NiO interfaces, respectively. In negative bias conditions, the hysteresis is insignificant in pristine sample but evolves in the implanted sample with ion fluences. Also, at the 100th cycle, the current suddenly improved from pA to nA at the highest fluence sample because of overcoming the threshold vacancies by ion implantation. On the other hand, in positive bias, a drastic change of hysteresis at the highest fluence is observed at the 100th cycle. In our proposed model, the variation of hysteresis and current in the memristor with ion fluences for both forward and reverse bias is explained through the modulation in the depletion width and Schottky barrier at the p-n junction and NiO/Au interface, respectively.

Analog to Digital RRAM, and THz Spectroscopy of Cu implanted NiO Thin Films

In this section, we investigated the Cu ion implantation effect in ITO/NiO/Ag devices, specifically focusing on the transition from analog to digital bipolar resistive switching. The crystal structure and phase identification of pristine and implanted samples are accomplished using the XRD spectra. The surface morphology is examined using AFM images. The RRAM device is constructed by sandwiching NiO between the top Ag and bottom ITO substrate. The Schottky barrier is developed at the NiO/Ag and ITO/NiO interfaces. We found analog switching characteristics in pristine and sample B. However, in contrast, sample C exhibits the digital bipolar RRAM behavior. The interface-dominated Schottky effect influences the analog switching. The reduction of the Schottky barrier with the number of cycles is responsible for increasing current conduction in pristine sample. Conversely, the decrease in current flow in sample B is attributed to the rising of the Schottky barrier height with the increasing number of cycles. In contrast, the complete transformation of the current

conduction mechanism, i.e., sudden jump and drop of current at SET and RESET point, in sample C is associated with a bulk-dominated vacancy filamentary model. This is because high Cu ion fluences boost the vacancies in the matrix above the threshold value for such transformation.

This segment of the thesis also discusses the THz conductivity in 100 keV Cu ion implanted NiO thin films. The low energy ion implantation modulates the crystal defect concentration to tune the THz optical properties of the films. SRIM simulations were employed to calculate damages in NiO thin films, revealing an increase in damages with ion fluences. PL and CL measurements identified the presence of various kinds of defects in the system. Concerning optical properties, Raman spectra revealed a gradual diminishment of magnon modes in the NiO film due to the increase of defects with ion fluences. The modulation of THz transmission and optical conductivity with ion fluences is associated with increasing defect concentration in the films. The variation of carrier density tunes the scattering time and plasma frequency for free and bound charges. The theoretical band and DOS calculations for vacancy, substitutional, and interstitial defect-associated NiO show that the tuning of defect states between CB and VB addresses the electronic reason for the variation of scattering time and plasma frequency with ion fluences.

8.2 Future prospects

1. The correlation of band engineering with defect concentration between CB and VB of MgO felicitates the electronic transition states to improve the conductivity of MgO from its insulating state. Further exploration is required to understand the improvement of optical and electronic properties of MgO through extended defects, chemical doping by Ni and Co, and ion implantation with other ion species and energies.

2. Annealing of MgO improves the endurance and RS property of the ITO/MgO/Ag

devices. The swift heavy ion irradiation in MgO can give rise to the local heating around the ion track for a very short period of time. The investigation of RRAM device functionality with ion-irradiated MgO can be interesting.

3. The thermal annealing at different temperatures modulates the NLOP of NiO. The heat generation by low or high-energy ion implantation through election phonon coupling can tune the NLOP of NiO. Hence, the NLOP of NiO thin films with different ion species and energies must be explored.

4. NiO, as another rock salt candidate for RRAM devices, exhibits altered magnetic properties with varying crystal defects. The swift heavy ion irradiation, which involves dominant electron-phonon coupling and local heating effects, can be applied to tune both magnetic and RS properties in NiO.

5. Low-energy ion implantation effectively induces defects in NiO thin films, resulting in altering the optical properties in the THz time domain. This concept can be extended by exploring different ion species and energies to investigate the THz properties of NiO.

6. The low-energy Cu ion implantation demonstrates the analog-to-digital switching in NiO-based RRAM devices. Such transition should be investigated using other ion implantation, spanning various ion energies from low to swift heavy ions.